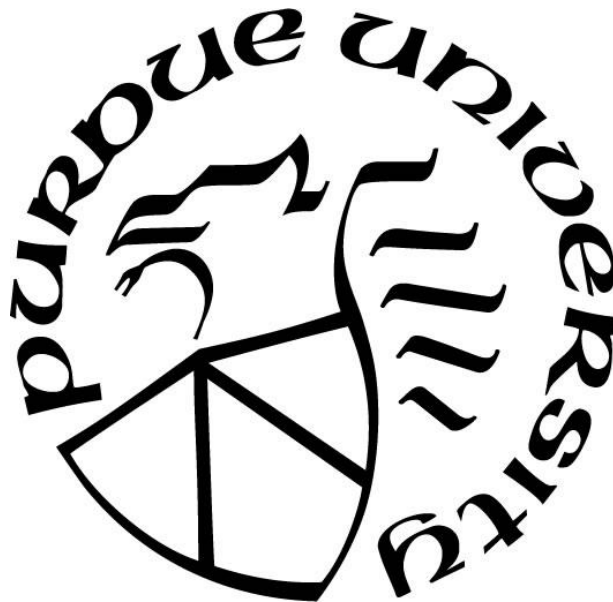# ULTRASOUND IMAGING OF TISSUE REMODELING IN MURINE MODELS OF VASCULAR DISEASE AND REPAIR

by

Alycia G. Berman

A Dissertation

Submitted to the Faculty of Purdue University

In Partial Fulfillment of the Requirements for the degree of

Doctor of Philosophy

Weldon School of Biomedical Engineering

West Lafayette, Indiana

December 2021

THE PURDUE UNIVERSITY GRADUATE SCHOOL
STATEMENT OF COMMITTEE APPROVAL

Dr. Craig J. Goergen, Co-Chair

Weldon School of Biomedical Engineering

Dr. Joseph M. Wallace, Co-Chair

School of Engineering & Technology, IUPUI

Dr. Abigail D. Cox

College of Veterinary Medicine

Dr. Adrian Buganza-Tepole

School of Mechanical Engineering

Approved by:

Dr. Tamara L. Kinzer-Ursem

ACKNOWLEDGMENTS

There's a saying that it takes a village to raise a child, but I would assert that it also takes a village to make a PhD graduate. In the five years that I have been a graduate student, I am honored to have had so many people come alongside me. The journey has been long, but it would not have happened at all if not for the sheer number of people to encourage and support me. I hope that this acknowledgement is a small way to say thank you, even though I know that it does not do justice to the years of support.

First, I would like to thank my co-advisors, Drs. Craig Goergen and Joseph Wallace. Joey, I first joined your lab after my sophomore year. I came as an overeager undergrad with no experience, and yet, you gave me a chance. You gave me the opportunity to see how cool research could be, and you supported me every step of the way. I doubt that I would have pursued graduate education if not for my experience in your lab. So thank you. Then, after doing a Master's degree with Joey, I entered the PhD program at Purdue. I had told Joey that I wanted to experience another lab for a year to provide me a broader view of research. And with that, enter Craig. Craig, when we first started discussing a rotation in your lab, my only experience was in bone biomechanics, which is a far cry from the cardiovascular imaging that your lab focuses on. And yet, here I am, writing a dissertation on vascular imaging. As it so happened, I did stay for a year as a lab rotation…but then I stayed four more. Thank you for taking a chance on me and giving me the opportunity to explore vascular imaging. And I thank both of you for your flexibility and support over these years, especially as I have navigated two labs with very different foci. To my committee members, Drs. Abigail Cox and Adrian Buganza-Tepole, thank you for the discussions and advice on both research and career. I so appreciate your support.

To the members of the Bone Biology and Mechanics Lab (BBML) and the CardioVascular Imaging Research Lab (CVIRL – i.e. Craig's Very Interesting Research Lab), thank you. Graduate school is so much more than just the research, and I have you to thank for that. Thank you for the game nights and potlucks and holiday parties and golf outings. Thank you for exploring different cities with me during conferences. Thank you for being a group that I could talk with and laugh with and (at times) even bemoan research with. Thank you for the Lab Olympics and the numerous other things that made graduate school so much more than just school.

To my Upper Room family, thank you for not being school. Thank you for being a group where I could set aside the craziness of grad school and just be me. You welcomed me in and adopted me into the Upper Room family. Thank you for the friendships – weekend trips and game nights and conversations and walks. Without my time at Purdue University, I may not have become the graduate student that I was, but without you, I would not have become the person that I am.

And last but certainly not least – To my family, how do I thank you for all your support throughout the years? Thank you for encouraging me, supporting me, and believing in me. Thank you for always being there for me, every step of the way. You all mean the world to me.

TABLE OF CONTENTS

LIST OF TABLES

LIST OF FIGURES

ABSTRACT

An abdominal aortic aneurysm (AAA) is a pathological dilation of the abdominal aorta, as defined by a 50% increase in diameter or a diameter greater than 3 cm. While typically asymptomatic, there is a risk that the AAA will rupture, causing massive hemorrhaging and high mortality rates. Thus, once detected, the clinician must choose between surveillance and elective surgical repair. The first option carries the risk of rupture; the second risks complications and graft failure. Currently, clinical metrics of rupture risk are dependent on diameter and growth rate. However, a number of studies have indicated that, although rupture risk does increase with increased diameter, there are also a large number of patients with aneurysms for which the diameter criteria is insufficient. There remains a strong need to 1) determine better estimates of rupture risk in order to accurately assess the need for surgery and 2) improve surgical treatment to reduce perioperative risk.

Herein, we use ultrasound in mice to address these two prevalent uncertainties in aneurysm development and treatment. First, we further develop a murine aneurysm model that forms large aneurysms with distal thrombus. To increase the applicability of the model, we modulate aneurysm growth by altering elastase concentration and lysyl oxidase inhibition. We show that initial elastase concentration impacts aneurysm size, which is driven in part by a change in the degree of initial degradation of the aortic wall. We also demonstrate that lysyl oxidase inhibition (via BAPN) remains necessary for expansion even after the initial aneurysm formation and that removal of the lysyl oxidase inhibitor effectively stops growth in this model. As a final point, we show that female mice develop larger aneurysms than the males using this model. Then, with the aim of improving surgical treatment options, we explore the patency of various design parameters involved in tissue-engineered vascular grafts. To do so, we assess the allowable parameter design space of murine textile arterial grafts, so as to lead to better selection of key design components. Overall, the findings in this thesis demonstrate the applicability of ultrasound in small animals to improve aneurysm diagnostic and treatment options.

1. INTRODUCTION

Abdominal aortic aneurysms are inherently a degenerative disease, predominately characterized by extracellular matrix (ECM) degradation, vascular smooth muscle cell (vSMC) apoptosis, inflammation, and, in some cases, thrombus. While current clinical metrics focus on diameter and growth rate to assess rupture risk, the complex pathophysiology of this disease make it difficult to accurately determine rupture risk using these metrics alone. Development of improved metrics is necessary, but success in this field is highly dependent on our enhanced understanding of the disease.

While human studies have provided a wealth of information regarding AAA progression, they are limited as baseline data is often absent and controlled manipulation of experimental variables can be difficult. To this end, experimental animal models have been widely utilized, but their usefulness is often dependent on the degree to which they mimic the human condition. Many of the current animal models of AAA are limited by the fact that they naturally stabilize after formation, making it difficult to assess growth dynamics. In one more recently developed murine model, this barrier was overcome by the addition of a lysyl oxidase inhibitor to mice that underwent a topical elastase administration procedure. Of note, this murine model also formed intraluminal thrombus (ILT), which is of particular interest given the small number of murine aneurysm models that develop ILT, despite its prevalence in many AAA patients. While still a relatively new model, the combined advantages of a large growing aneurysm and intraluminal thrombus make it a strong contender for use in assessing the applicability of novel diagnostic metrics to detect AAA growth. However, much work remains to further develop the model and understand the influencing role of elastase and lysyl oxidase on aneurysm growth. These areas of research are necessary in the ultimate goal of improving diagnostic metrics.

In addition to improving diagnostic metrics, it is also necessary to improve vascular grafts and surgical techniques for those patients elected to undergo AAA repair. Graft failure is one complication, which may be improved by better graft design. Current decisions on how to improve graft designs are often empirically determined, and could be improved by a more formal analysis. While not currently used clinically for AAA repair, tissue engineered vascular grafts are particularly interesting due to the insight that they provide into vascular tissue remodeling, and in

the future they may even improve endovascular stent grafts through the use of biodegradable materials.

Thus, this thesis probes these two areas: 1) murine model development and AAA morphology assessment so as to improve disease diagnostic capabilities, and 2) tissue engineered vascular graft design so as to increase our understanding of vascular tissue remodeling and improve grafts for surgical repair. To address these issues, in Chapter 2, we first provide a background on the general structure and function of the artery, aneurysm pathology and clinical management, and then the preclinical methods used to further our understanding of the disease. In Chapter 3, we focus on further developing a murine aneurysm model that forms large aneurysms with distal thrombus. We then increase the applicability of the model by modulating aneurysm growth, and we probe the relative impacts of elastase concentration and lysyl oxidase inhibition. In Chapter 4, we shift focus slightly to assess vascular remodeling after implantation of a tissue engineered vascular graft. We consider the influencing role of graft braiding pattern on its patency. Overall, the findings in this thesis demonstrate the applicability of ultrasound in small animals to improve aneurysm diagnostic and treatment options.

2. BACKGROUND

The cardiovascular system is, in a word, amazing. One of this system's primary goals is to transport gases and nutrients, and remove wastes, which it does from each of the ~37 trillion cells that make-up the human body.[1] It does this through a series of vascular conduits, with diameters ranging across ~3-4 orders of magnitude. The largest of the arteries—the ascending aorta—is ~3 cm in diameter and receives blood directly from the heart.[2] As blood travels through the aorta, it branches into smaller and smaller arteries, eventually becoming arterioles. Even then, the vessels continue to branch until they become capillaries. Capillaries are the smallest of the vessels, with an average diameter of ~5 µm.[3] While the diameter decreases from the arteries to the arterioles to the capillaries, the number of vessels increases, resulting in a net increase in surface area. In fact, capillaries are estimated to have a total surface area of ~6000 cm^2 which enables the exchange of gases, nutrients, and wastes to occur primarily through diffusion.[4] On the return to the heart, capillaries combine to form venules which combine to form veins. Two veins, the superior and inferior vena cava, then lead back to the heart, completing the systemic circulation. This complete circuit takes approximately 1 min when at rest, and even less time during exercise.[5]

As expected, this intricate system is dependent on appropriate functioning of the vascular conduits (arteries, arterioles, capillaries, venules, and veins). While there are a number of diseases that can plague the cardiovascular system, herein we focus on abdominal aortic aneurysms, which are pathological dilations of the abdominal aorta. In this chapter, the general structure and function of the artery is discussed, followed by a discussion of aneurysm pathology and clinical management. Lastly, we discuss preclinical methods used to further our understanding of the disease.

2.1 Arterial Structure and Function

Arteries are the blood vessels that carry blood away from the heart. They are typically comprised of 3 layers: the tunica intima, tunica media, and tunica adventitia or externa (**Figure 2.1**). The innermost layer, the tunica intima, interfaces with the blood in the lumen and is usually comprised of a single layer of endothelial cells attached to a basement membrane. These cells form a barrier, creating a dividing line between blood and vessel wall, but they also contribute

to a variety of other functions, such as vascular tone, thrombosis, and inflammation.[6] The importance of the endothelium in normal homeostasis is highlighted by the fact that its dysfunction has been associated with increased risk of cardiovascular disease.[6]
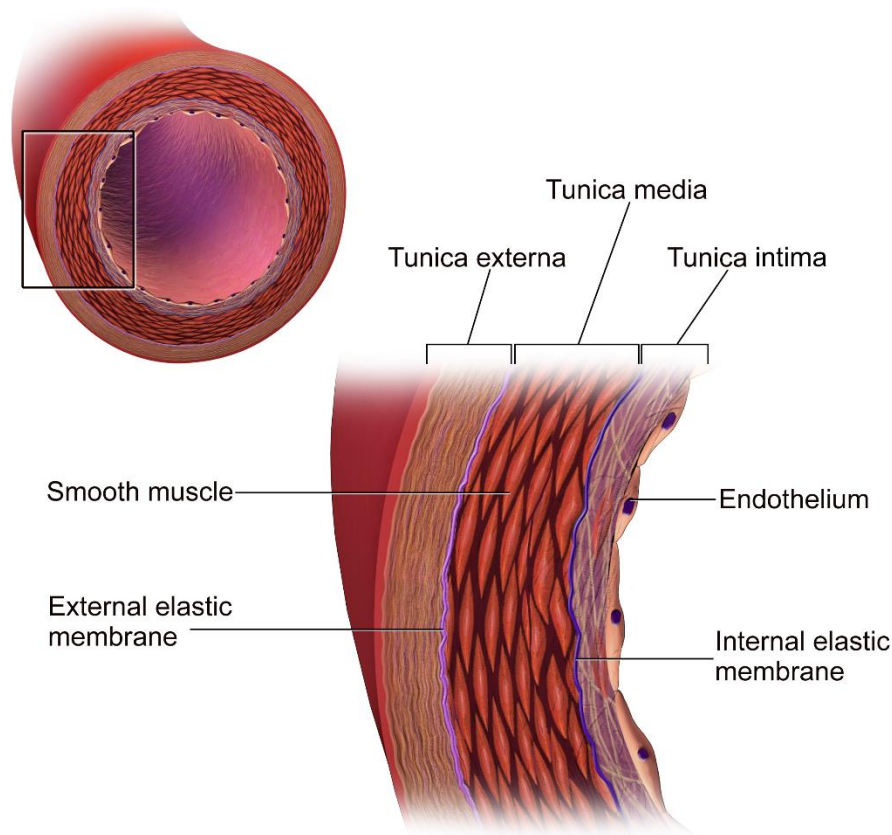
Figure 2.1. Arterial structure showing the three layers: tunica intima, media and externa. Adapted from Blausen.com[7]

Beneath the basement membrane is an elastic-like sheet, called the internal elastic lamina, which separates the tunica intima and media. The tunica media is by far the thickest of the layers, occupying ~80% of the wall.[8] It is comprised primarily of elastin, collagen, smooth muscle cells, and proteoglycans.[9] In elastic arteries, the elastin form in sheets, called lamina, which enable the artery to recoil when pressurized. In the ascending aorta of humans, where blood volume fluctuates considerably, there are ~80 elastic lamina[10] which allows the wall to dampen the oscillation. Further down the aorta, where oscillations in volume are less severe, the number of elastic lamina are reduced, such that the infrarenal aorta only has ~30 lamina.[10] In contrast to the elastin, the collagen is much stiffer, more akin to that of a rope rather than a rubber band, and serves to provide

added structural stiffness. The presence of collagen is sparse in the medial layer but, it does make up the majority of the adventitial layer. Within the medial layer, smooth muscle cells are integral to maintain vascular tone. In addition, as the primary cell type in the tunica media, it also helps to organize the repair of ECM through release of chemokines, and its apoptosis is one hallmark of aneurysms.

The outermost layer in the aorta is the tunica adventitia. As noted, collagen is the primary component of this layer, though there are some elastic fibers and fibroblasts.[8] At normal physiologic pressures, the tunica media bears much of the load. However, in diseases such as aneurysms, the elastin is degraded which causes a greater load on the outer collagen sheath.

2.2   Abdominal Aortic Aneurysms

An abdominal aortic aneurysm (AAA) is a pathological dilation of the abdominal aorta, as defined by a 50% increase in diameter or a diameter greater than 3 cm (**Figure 2.2**).[11,12] Although only affecting ~1.4% of the US population aged 50 to 84,[13] additional factors such as advanced age, male sex, hypertension, cigarette smoking, and a family history of AAAs all increase risk.[13-16] Despite an increased prevalence of AAAs in males than in females,[17,18] females who have an AAA are at greater risk of rupture than males.[19,20] In addition, other rupture risks include large initial aneurysm diameter, cigarette smoking, and hypertension.[16] Given the prevalence and risk of AAAs, it is increasingly important to understand and thereby improve diagnosis and treatment of aneurysms. In the following sections, we briefly review the disease pathology and current clinical assessment.

Figure 2.2. CT image (left) and volume reconstruction (right) of an abdominal aortic aneurysm. Adapted from Sangha et al.[12]

2.2.1 General Disease Pathology

Abdominal aortic aneurysms are inherently a degenerative disease, predominately characterized by extracellular matrix (ECM) degradation, vascular smooth muscle cell (vSMC) apoptosis, and inflammation. The first of these—degradation of the extracellular matrix—occurs initially through elastin fragmentation and degeneration within the medial layer, which continues to degrade as aneurysm size increases.[21,22] Since elastin is the primary component to provide elasticity and recoil, the loss of elastin results in a stiffened and weakened medial layer that is unable to support the engendered forces. As a result, greater load is placed on the adventitial collagen. Thus, it is not surprising that concomitant with the reduction in elastin is an increase in collagen,[22] perhaps as a mechanism to maintain structural integrity in the absence of elastin. Collagen half-life is 60-70 days,[23] while elastin has a half-life of 40 to 70 years,[24] making collagen more prone to remodeling. Further work has suggested that while elastin degradation is key in aneurysmal growth, collagen failure may be the primary factor in rupture.[25] Rupture eventually occurs when there is an imbalance of collagen proteolysis and synthesis during remodeling.

This degradation is driven, in large part, by matrix metalloproteinases (MMPs). MMPs are zinc-metalloproteinases capable of degrading a variety of ECM proteins. Studies have indicated that MMPs are elevated in aneurysms, and that their deficit can prevent aneurysm formation in mice.[26,27] Interestingly, although doxycycline – a broad spectrum MMP inhibitor – does prevent

21

aneurysm development, it seems to have little effect on the growth of pre-established aneurysms,[28] suggesting that there may be a time course in which MMP inhibition is most effective. These results are corroborated by Lu *et al*. who showed in a murine aneurysm model that both inactive and active forms of MMP9 – which displays significant elastase activity – were most elevated during the first two weeks post-aneurysm induction, but then returned to a much lower (though still elevated) level for the remainder of the study.[29] Taken together, these data suggest an early role of MMPs (especially MMP9) on aneurysm formation, but potentially a reduced role as the aneurysm progresses.[30]

In addition to ECM degradation, aneurysms are marked by apoptosis of vascular smooth muscle cells[31-33] as indicated by increased levels of p53 and p21 – two molecular markers of apoptosis – in aneurysmal tissue.[34] Moreover, light and electron microscopy have shown decreased density of vSMCs, with ~30% of the cells showing fragmented DNA.[35] Since the vSMCs are the main cells within the wall of the aorta, this reduction in vSMCs destroys the very cells that can enable ECM repair, further exacerbating the condition.

The last primary hallmark of the disease is inflammation, which both drives and is driven by the changes in the ECM and the apoptosis of vSMCs. During vSMC apoptosis, monocyte-chemoattractant protein-1 and cytokine-induced neutrophil chemoattractant are released.[31] Similarly, the products of ECM degradation (elastin degradation products) are chemotactic for monocytes.[36] Thus, as the ECM and vSMCs are affected, they in turn drive increased inflammation, as demonstrated by the increased numbers of neutrophils, mast cells, macrophages, and T and B lymphocytes in aneurysmal tissue.[28] As these inflammatory cells increase, they further the degradation of the ECM and vSMC apoptosis.[37] This has led some to hypothesize that aneurysm development is an autoimmune disorder driven by a sustained positive feedback mechanism involving the ECM, vSMCs, and inflammation.[38]

Over time, the degeneration of the aortic wall, apoptosis of vSMCs, and increased inflammation results in a severely weakened wall that is unable to repair itself. Rupture occurs when the forces on the wall exceed the material strength of the wall, leading to a break in the tissue and resulting in internal hemorrhaging. An overview of disease progression is shown in **Figure 2.3**.[39]
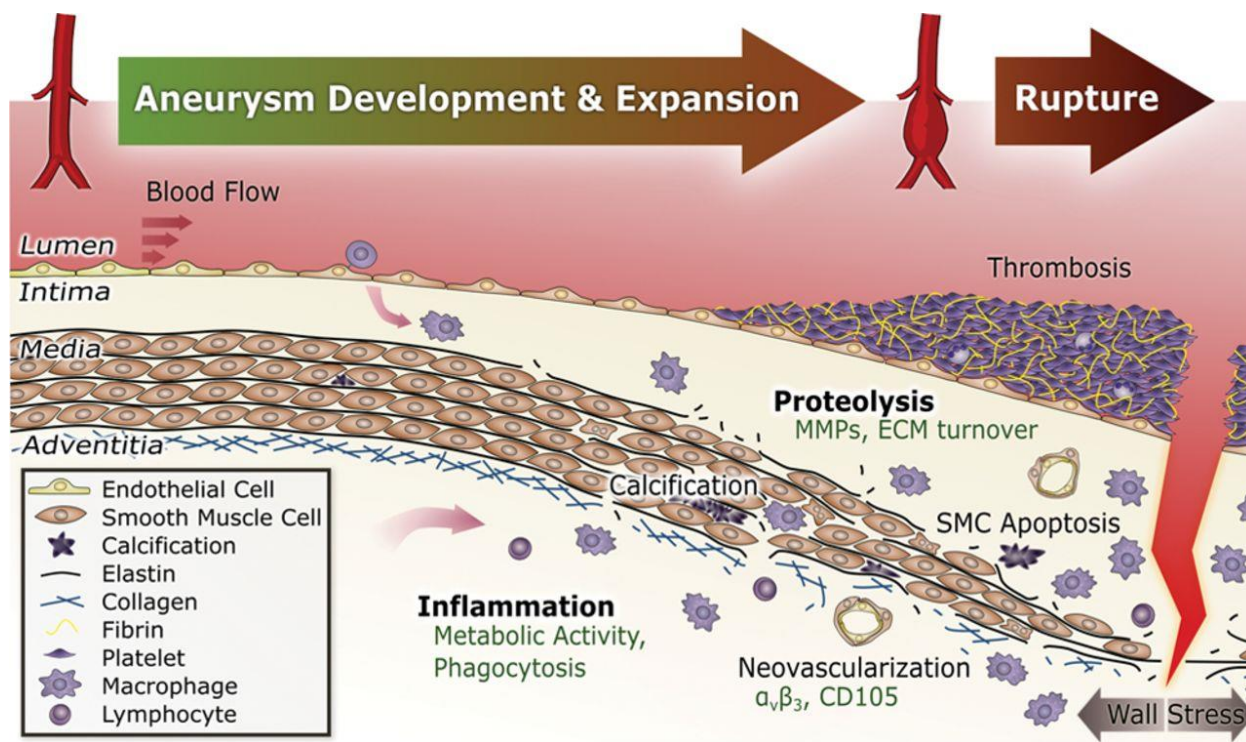
Figure 2.3. Schematic of aneurysm development and expansion. Although the initiating event is unknown, disease progression is marked by degeneration of the extracellular matrix, smooth muscle cell apoptosis, and inflammation. This deleterious remodeling of the aortic wall eventually results in an ECM that is unable to support the engendered load, leading to rupture.[39]

Role of Thrombus

In addition to the three hallmarks noted above, abdominal aortic aneurysms often contain intraluminal thrombus, with an estimated prevalence of 70-80% in humans,[40,41] though some studies have even shown a prevalence up to 95%.[42] Despite its prevalence, its role in aneurysm development is unclear. As such, this section is devoted to providing background on the topic.

Thrombus formation is hypothesized to be driven by high shear stress in the proximal neck portion,[43] causing endothelial dysfunction and platelet activation, followed by low flow in the distal aneurysmal portion which allows adhesion of the platelets and formation of the thrombus.[44,45] Indeed, this hypothesis would help explain why thrombus often forms in the distal portion of the aneurysm.[46] Further accumulation and growth of the thrombus may be driven by either a continuous deposition or a more "staccato" based layering of the thrombus.[47] In the more layered thrombus, the thrombus may have mini-breaks that cause immediate inflow of blood and

secondary clotting, leading to a layered look. In contrast, the continuous deposition of thrombus leads to a more uniform appearance.

Independent of the type of deposition, the composition of thrombus is primarily a fibrin mesh with aggregated platelets and red blood cells, and is typically divided into three radial layers: luminal, medial, and abluminal (**Figure 2.4**).[48] The luminal layer interfaces with the blood and is characterized by a thick fibrin mesh. Moving from luminal to medial to abluminal layers, the mesh becomes more and more degraded, ultimately resulting in near-complete degeneration of the fibers in the abluminal layer.[48,49] At times, the abluminal-wall interface is so degraded that it is no longer even a solid, but instead a liquid phase that lacks all structure.[50] Porosity also varies per layer, with the largest cavities observed in the abluminal layer. This porosity creates a large canaliculi network within the ILT (across all three layers) that enables free diffusion.[49]
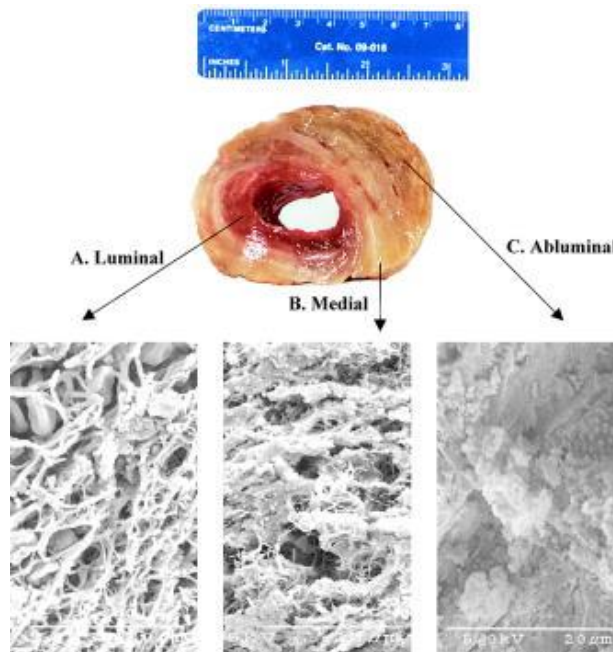
Figure 2.4. Cross-section of a human aneurysm containing intraluminal thrombus. Scanning electron microscopy of the A) luminal, B) medial, and C) abluminal layers show distinct microstructure.[48]

Given the microstructural differences in layers, it is reasonable that the mechanics also varies relative to layer. While ILT is isotropic in the medial and abluminal layers, it is anisotropic within the luminal layer,[51,52] and radially and regionally heterogeneous throughout.[48,52,53] For example, Tong *et al*. found that the strength of an ILT decreased while moving from the luminal to abluminal

surface, with older thrombus contributing to wall weakness.[54] Thrombus also appears to have regional differences, with the posterior region stronger than the anterior region.[53] Additional work by Gasser *et al*. suggested that microstructural pores may be a key driver of observed differences in macroscopic mechanical strength.[52] Also of note, ILT is highly vulnerable to fatigue loading, with a cyclic load level of 60% ultimate strength causing failure within an hour, suggesting that fatigue may be a leading cause of thrombus and potentially even aneurysm failure.[54] These and other mechanical assessments of ILT, in conjunction with computational analyses, have led some researchers to conclude that ILT is beneficial in that it is able to protect the aneurysm wall.[55-59] Namely, thrombus may act to mechanically shield the wall,[60-62] reducing aneurysmal wall stress and thus decreasing rupture risk.

However, thrombus is also biologically active. Kazi *et al.* compared the wall of aneurysms in regions with and without thrombus, and found that the walls with thrombus had greater inflammation, apoptosis of vascular smooth muscle cells, and degradation of the extracellular matrix (e.g. fewer and more fragmented elastin).[63] Interestingly, while plasminogen was only detected in the thrombus and its activator was only in the wall, activated plasmin was prevalent throughout,[50,64] which may be driven by activation at the wall/thrombus interface[64] followed by distribution through a canaliculi network.[49] Despite this prevalence of plasmin throughout the thrombus and wall, fibrin degradation was found to occur primarily at the abluminal surface,[49] giving further credence to the idea that the thrombus-wall interface may be a key site of plasmin activation and thrombus-wall stability. Moreover, Fontaine *et al*. demonstrated that polymorphonuclear leukocytes are co-localized with MMP-9 storage in the luminal region of intraluminal thrombus in human AAAs, suggesting that these trapped leukocytes may be a source of proteases that exacerbate aneurysmal growth.[50] Thus, thrombus is not merely an inert structure, but a biologically active secretor of proteases and chemokines that can heavily influence aneurysm development.

Given this balance of mechanical integrity and inflammatory response, it may be that the shoulder region of the thrombus—where the thrombus is thin and therefore provides little mechanical integrity but still has increased inflammation because the lumen is close to the adventitia—may be particularly prone to rupture. In addition, to further confound factors, the aforementioned difference in formation (continuous vs. layered) may also play a large role in the

stability of the aneurysm (**Figure 2.5**). However, much remains unknown about thrombus deposition, the biochemomechanics of its formation and growth, and its role in aneurysm rupture.
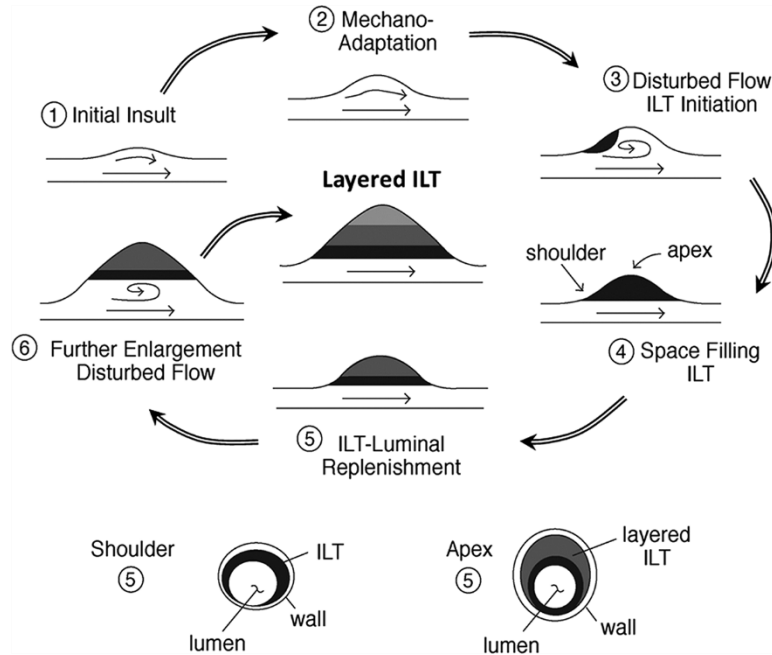
Figure 2.5. Schematic depicting a potential mechanism for the layering of ILT. An initial insult, followed by ECM remodeling causes the initial formation of the aneurysm. Then, due to the shape of the aneurysm, flow is disturbed, creating regions of low wall shear stress which are ideal for thrombus deposition. The thrombus fills that region; however, as the aneurysm continues to grow, there are new regions of disturbed flow, causing more thrombus deposition. This process creates a layered appearance within the thrombus.[47]

2.2.2 Clinical Management

Aneurysms are often asymptomatic. At times, these aneurysms are discovered as an incidental finding during an imaging examination,[65] but many remain undetected until rupture. In an effort to improve detection, large-scale population-based ultrasound screenings have been proposed. Three large randomized clinical trials in men over the age of 65 (n=127,891) have shown the efficacy of screening to reduce aneurysm-related mortality.[66-69] Moreover, a 10-year follow-up found that the early benefit of screening was maintained in the later years.[67] These studies led the Society for Vascular Surgery to recommend a one-time ultrasound screening for all men aged 65+, or even earlier if they have a family history of AAA.[16] Unfortunately, for women, the dearth of clinical studies have made it difficult to assess efficacy. One randomized clinical trial in women

(n=9,342) suggested that screening was unable to reduce aneurysm mortality.[70] However, due to the small number of patients, the Society for Vascular Surgery still recommends ultrasound screening in women older than 65 who have a family history of AAA or a history of smoking.[16]

Once the aneurysm is detected, the clinician must choose between surveillance—and potentially risk rupture—or elective repair—and risk complications and graft failure. Unfortunately, the cost of an incorrect choice is severe. If the clinician chooses surveillance and the aneurysm does rupture, it causes massive hemorrhaging and high mortality rates. Many patients die prior to reaching a hospital[71] and even among those who make it to the hospital, perioperative mortality rates can be as high as 50%.[19,72] In contrast, if elective surgical repair is performed before rupture, survival rates are better than surgery due to rupture; however, this too has risk, with perioperative mortality rates ranging from 0.5-5% based on the study and type of repair.[73-75] Although the continuous improvement of grafts and surgical techniques will likely improve those statistics, surgical risk remains a consideration, especially in older patients who also have co-morbidities. In addition, an autopsy study revealed that approximately 75% of AAAs never rupture,[76] and in those cases, elective surgery would have been an unnecessary risk.

In the next section, we will discuss current surgical interventions. However, for the current discussion, it is apparent that there remains a strong need to determine better estimates of rupture risk in order to accurately assess the need for surgery. Current clinical metrics of rupture risk primarily focus on aortic diameter[66,77] and expansion rate,[20,78] as determined by yearly imaging check-ups. The current paradigm is that, as the aneurysm steadily increases in size, the aneurysm wall weakens, and rupture risk correspondingly increases. Thus, a large diameter and fast growth rate implies a high rupture risk whereas a small diameter and slow growth rate implies a low rupture risk. Current guidelines by the Society for Vascular Surgery recommend elective surgical repair at a diameter >5.4 cm as it is assumed that rupture risk exceeds surgical risk.[16] However, in a seminal work by Darling *et al*., review of 24,000 autopsies over 23 years showed that nearly 13% of "small" aneurysms ruptured, while nearly 60% of the "large" aneurysms did not.[76] Thus, although rupture risk does increase with increased diameter, there are also a large number of patients with aneurysms for which the diameter criteria is insufficient.

For this reason, researchers have begun to explore other predictors of rupture. Given that rupture occurs when the stress on the wall exceeds its material strength, AAA wall stress has become a prime focus in this assessment.[79-90] For example, using finite element analysis, Fillinger

et al. found that peak wall stress was better than diameter at differentiating the symptomatic or ruptured AAAs from the AAAs that underwent elective repair.[79] Venkatasubramaniam *et al.* corroborated these results, even after normalizing blood pressure, suggesting that the geometry itself plays an integral role in rupture risk. Moreover, the location of rupture correlated with the location of peak stress, providing further credence to the role of FEA-measured stress on rupture.[81] Further work has attempted to improve the accuracy of the models by assessing the role of anisotropy,[82] asymmetry,[83,84] wall thickness,[83] calcification,[85,86] and thrombus.[86-91] Despite the increasing number of studies on the topic, FEA has remained primarily a research tool, potentially due to the lack of standardization and guidelines that prevent widespread clinical utility. In addition, models are heavily influenced by the accuracy of material properties and constitutive assumptions,[92] making widespread implementation difficult. Further simplification and refinement of the technique, as well as development of guidelines delineating rupture risk, will be necessary before clinics are able to reliably use this method.

Other predictors of rupture risk have also been explored, including thrombus burden,[91,93,94] tortuosity,[91,94-97] volume,[98] and surface area.[97] For example, Stenbaek *et al.* demonstrated that a rapid increase in thrombus area, as measured by CT at the maximum diameter location, was a better predictor of rupture than diameter.[93] In addition, clinically, tortuosity has been associated with increased rupture risk[95,96] and higher rates of graft-related complications after repair.[94] According to Parikh *et al.*, surface area and tortuosity were the most important indices in predicting whether AAAs would be electively or emergently repaired,[97] while according to Hatakeyama *et al.*, diameter expansion rate, diameter per length, and diastolic blood pressure were most important predictors of diameter growth rate.[99] However, in general, traction of these metrics within the clinic remain lacking, and further studies on both these and future metrics will be needed to enable movement of clinical assessment beyond that of diameter and growth rate alone.

2.2.3   Surgical Intervention

While the accurate determination of rupture risk is important, equally important is the improvement of clinical treatment options. Currently, treatment relies on surgical repair, which can be divided into two main categories: open repair and endovascular repair.

In open repair, either a midline or transverse laparotomy is performed. Vascular control is often obtained by clamping, after which the diseased aneurysm is resected and replaced with a

vascular graft. The graft—which is typically made of either a textile polyester synthetic graft such as Dacron[100] or a non-textile synthetic graft such as PTFE[101,102]—is sewn into the aorta and sealed with either collagen or albumin.[103] Blood flow is then restored to the area, the incisions are sutured, and the patient allowed to recover. This procedure is considered a major surgery, and has a perioperative mortality rate of ~3-5%[73,74] and a 5-year survival rate of ~70%.[104] Thus, although it is considered the standard for aortic repair, the procedure is not without risk.

More recently, endovascular aortic repair (EVAR) was designed as a minimally invasive surgical repair technique.[105] Rather than perform a laparotomy, in this procedure, the surgeon gains access to the aneurysm via cannulation of the common femoral artery. The graft is then balloon-expanded, and held in place by stents at either end. While the perioperative mortality for this procedure is lower than that of open repair,[74,75] long-term results were worse due to graft-related complications (such as endoleaks) and required re-interventions.[106] Further developments to surgical technique and graft design are will be necessary to improve these outcomes.

2.3   Murine Models of AAAs

Although clinical studies have provided a wealth of information regarding AAA formation, growth, and surgical repair, the preclinical realm affords researchers the ability to manipulate experimental variables in a highly controlled manner, which is often difficult to do in the clinic. Within the realm of preclinical research, the complexities of aneurysm development necessitates the use of animal models to recapitulate aspects of the human condition.[107] No animal model is perfectly able to do so, and as such, a myriad of models have been developed, each with their own advantages and disadvantages.[107] Herein, we discuss three common murine aneurysm models (Angiotensin II, Calcium Chloride, and Elastase), as well as more recent work that has combined elastase with a lysyl oxidase inhibitor (BAPN) to create a combination model.

2.3.1   Angiotensin II Model

The Angiotensin II (AngII) model, first described by Daugherty *et al.*,[108] is created by subcutaneously implanting an AngII-filled mini-osmotic pump into the dorsal flank of apolipoprotein E-deficient (*apoE*-/-) mice. The *apoE*-/- mice are genetically predisposed to form atherosclerotic lesions, which when combined with AngII infusion, typically forms aneurysms in

within the first 14 days. However, not all mice form aneurysms. In a meta-analysis by Trachet *et al.*, only 60% of mice form aneurysms. Another 20% die, typically within the first few days, and for the remaining 20%, there are no gross changes in morphology.[109] While the lower incidence of aneurysm formation could be seen as a challenge to some studies due to the necessity to use more mice, it also provides the distinct opportunity to assess why there is a discrepancy in the animal-to-animal response so as to elucidate mechanisms of disease.[110]

For the mice that do form an aneurysm, the aneurysm typically forms in the suprarenal aorta due to a tear separating the medial and adventitial layers of the aorta.[109,111] This tear is rapid, occurring on the order of minutes to hours[112] and results in a variety of severities. In many of the mice, the aneurysmal dissection often has both a true and false lumen, with the false lumen filled with intramural thrombus. While there is some growth after the initial onset, it is modest relative to the initial expansion.[111,113] In addition, given its formation and development, the model may better depict that of an aortic dissection[111] rather than the fusiform aneurysms that are more commonly observed in the infrarenal abdominal aorta of humans.

2.3.2   Calcium Chloride Model

In contrast to the AngII model, the calcium chloride and elastase models are both surgically induced. For the calcium chloride model, the model is formed by topically applying calcium chloride to the aorta peri-adventitially, causing calcium precipitations that disrupt the elastin and lead to an inflammatory response.[114] However, even though this is surgically induced, not all mice form aneurysms and among those that do, maximum diameter remains small, even after 10 weeks.[115] In addition, the chemical burn caused by the treatment may not be the best representation of human pathology. As such, although this is a well-known model, it has not garnered the same enthusiasm as the AngII and elastase models.

2.3.3   Elastase Model

Similar to the calcium chloride model, the elastase model is surgically induced. Initially, this model was developed in rats[116] but later expanded to include mice.[26] In this model, porcine pancreatic elastase is perfused into the aorta, causing an immediate increase in diameter due to the

inflation pressure. Post-surgery, the aortic wall remains stable for the first week, after which the aorta begins to dilate, typically resulting in an aneurysm by the second week (**Figure 2.6**).[26,117]
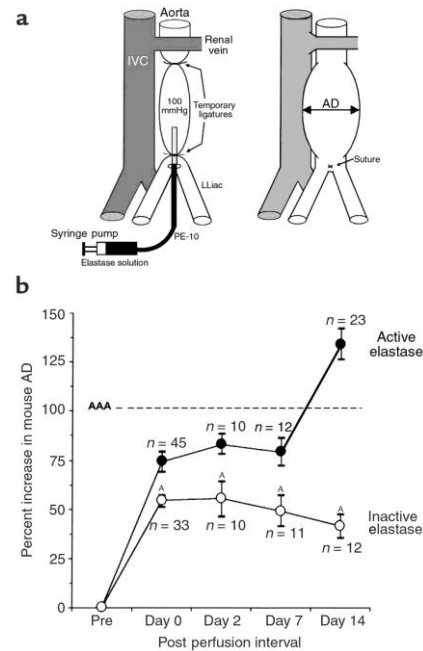
Figure 2.6. In the elastase model, the elastase is perfused into the aorta, resulting in an aneurysm by the second week.[26]

One of the primary problems with this surgery is its technical difficulty. As a result, Bhamidipati *et al.* adapted the elastase perfusion model by applying peri-adventitial elastase.[118] Although this model does form aneurysms, they typically stabilize by day 14,[29,119] which is atypical in the human condition. Given that much of the research is dedicated to understanding why human aneurysms continue to grow, the small size and stability of this model are significant disadvantages. Even so, the elastase model remains a popular choice for researchers due to its medial elastin degradation and inflammatory cell recruitment.

2.3.4   Addition of BAPN to the Elastase Model

Recently, Lu *et al.* combined this topical elastase surgery with continuous oral administration of BAPN, a lysyl oxidase (LOX) inhibitor, to create a continuously expanding aneurysm (**Figure 2.7**).[29] LOX is produced by vascular smooth muscle cells and is the primary

enzyme involved in the formation and maturation of irreducible cross-links in collagen and elastin.[120] By inhibiting LOX and reducing the cross-linking of collagen and elastin, the elastase-treated vessel is unable to resolve and stabilize, creating a large aneurysm. In addition, Lu and colleagues noted the presence of intraluminal thrombus in some animals, which is of particular interest given the small number of animal models that have thrombus, despite its prevalence in the human condition. While still a relatively new model, the combined advantages of a large growing aneurysm and intraluminal thrombus make it a strong contender for future studies.
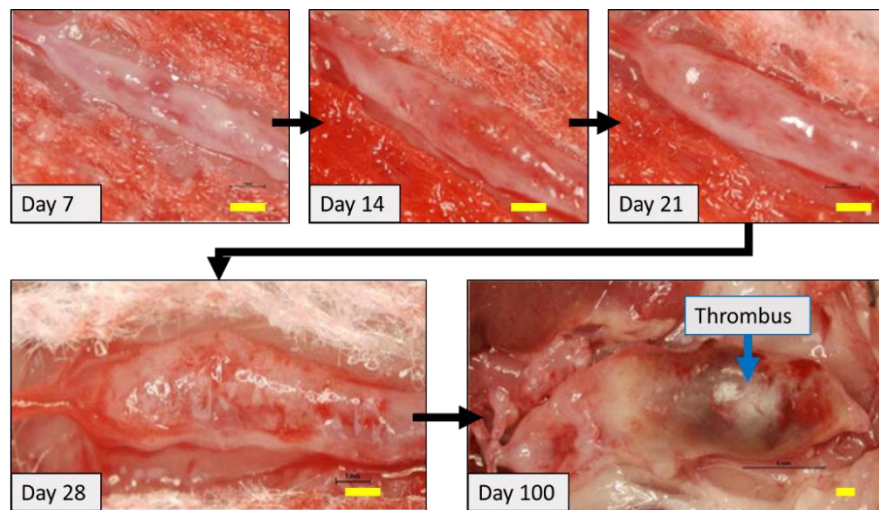
Figure 2.7. Combination of elastase with BAPN results in continuously growing aneurysms with distal thrombus in some of the mice.[29]

2.4   Ultrasound Imaging

Ultrasound is a non-invasive, non-ionizing way to view internal body structures in real-time. As such, it is an important technique to explore disease development. The term ultrasound comes from its use of ultrasonic waves, which are sound waves that are above the audible range of humans (>20,000 Hz). In essence, ultrasound imaging works by sending out short acoustical pulses and listening for a response. The acoustical pulses are formed by applying a short electrical current to a piezoelectric crystal. The crystal expands and contracts due to the current, thus creating a pressure wave that propagates through the tissue. Only ~0.1% of the time is spent emitting a sound wave; the rest is spent listening for the echo response.[121]

As the sound wave travels through tissue, it does so at a velocity (c) dependent on the density (ρ) and compressibility of the material (K):

$$c \propto \frac{1}{\sqrt{K\rho}}$$

Although acoustic velocity varies slightly among soft tissues, these differences are modest and sound is assumed to travel at an average of ~1540 m/s for soft tissues.

When the sound waves reach an interface between two tissue types, some sound is transmitted while some is reflected, dependent on the relative acoustic impedance of the two tissues:

$$\%R = \left(\frac{Z_2 - Z_1}{Z_2 + Z_1}\right)^2 \times 100$$

where $\%R$ is the percent that is reflected, and Z is the acoustical impedance, which is calculated as the product of the tissue density (ρ) and the speed of sound (c):

$$Z = \rho c$$

Thus, a high density tissue will have a high acoustic impedance and a low density tissue will have a low acoustic impedance. If the acoustic impedance between two tissues is similar, most of the wave will continue to propagate and very little will be reflected. In contrast, if the acoustic impedance is very different, most will be reflected and very little will be transmitted. That is why the interface between soft tissue and bone is so bright, but it is hard to see anything below the interface. Namely, at the interface, the acoustical impedance between soft tissue and bone is so different that most of the sound is reflected, causing a bright interface. However, because most of the sound is reflected, there is very little sound is left to transmit, making it difficult for an operator to see anything below the interface.

It is these reflected sound waves that the ultrasound system uses to construct a grayscale image. Since the acoustic velocities of various soft tissues are similar, we can assume that the speed of sound is ~1540 m/s. Based on this information, the machine can calculate the depth at which a sound wave is reflected based on the time-delay between emitting and receiving a signal.

In addition to reflection, there are a few other ways that sound interacts with tissue: scatter, absorption, and refraction.[121] In scatter, sound waves encounter small objects that cause a diffuse reflection. This is what gives different tissue types their distinctive "look" in an ultrasound image. Absorption is the energy that is lost through friction as the sound travels through tissue. And lastly,

refraction can occur when sound does not perpendicularly approach a tissue interface. This can distort the location at which the ultrasound machine "thinks" the sound is coming from, resulting in imaging artefacts.

2.4.1 Image Resolution

The spatial resolution of an ultrasound image is not isotropic, and is given in the axial, lateral, and elevational directions.[122] The axial direction has the best resolution, and is equal to half of the spatial pulse length (SPL):

$$Res_{axial} = \frac{1}{2}SPL = \frac{1}{2}n\lambda = \frac{1}{2}n\left(\frac{c}{f}\right)$$

In the above equation, n is the number of cycles emitted during a pulse sequence, c is the speed of sound described previously, λ is the wavelength of the sound wave, and f is the frequency of the sound wave. From the above equation, frequency is inversely related to axial resolution. For this reason, small animal imaging systems are often called High Frequency Ultrasound systems because they use a much higher center frequency than is used clinically so as to improve resolution enough to view the small structures in mice and rats.

The primary disadvantage to using higher frequencies is the lower depth of penetration. Attenuation is proportional to the frequency of ultrasound. Thus, as the frequency increases, the resolution increases, but so does the attenuation, resulting in lower viewable depths.

The lateral and elevational resolutions are almost always worse than in the axial direction. The lateral resolution is dependent on the beam width, which is about half of the transducer width within its focal zone. The elevational resolution is defined by the height of the transducer and is the slice thickness of an image.

In addition to spatial resolution, the temporal resolution is also important, especially in small animal imaging because of the fast heartrates of rodents (typically 500-600 beats/min). For an image with a single focus, the temporal resolution is the inverse of the frame rate (FR) and can be given as:

$$Res_{time} = \frac{1}{FR_{max}} = \frac{2Rn}{c}$$

where c is the speed of sound, R is the maximum imaging depth, and n is the number of lines per frame.

The Vevo2100 (VisualSonics, Toronto, Ontario, Canada) is a small animal imaging system that uses a high frequency probe to improve spatial and temporal resolutions. A summary of resolutions for one of their probes is shown in **Table 2.1**:

Table 2.1. Ultrasound probe specifications and resolutions

Specifications	MS550D Probe
Frequency Bandwidth	22-55 MHz
Center Frequency	40 MHz
Axial Resolution	40 μm
Lateral Resolution	90 μm
Elevational Resolution	180 μm
Temporal Resolution	1 ms

2.4.2   Imaging Modes

Three of the main imaging modes are brightness (B-), motion (M-), and pulsed wave (PW) Doppler modes (**Figure 2.8**).
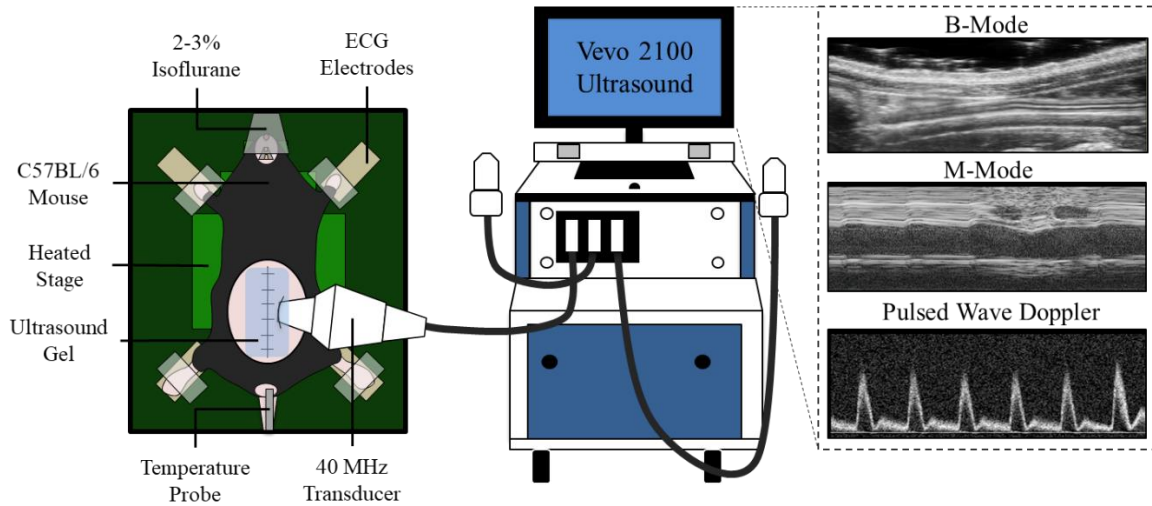
Figure 2.8. Murine imaging setup for the Vevo2100 ultrasound system. Representative images of B-mode, M-mode, and Pulsed Wave Doppler demonstrate three of the main imaging modes.[12]

The first mode, B-mode, creates a real-time 2D image by using an array of transducers to scan a plane of the body.[123,124] This is one of the most common imaging modalities. In contrast to B-mode that creates an entire 2D image, the M-mode examines how a single axial location changes over time.[123] As noted earlier, temporal resolution is inversely related to the number of lines per frame. Because M-mode only images a single line, temporal resolution is much higher than that of B-mode, making it ideal for assessing the pulsatility of the aorta. From aortic images, the mean systolic and diastolic diameters can be used to calculate Green-Lagrange circumferential strain:[125]

$$E_{\theta\theta} = \frac{1}{2}\left[\left(\frac{D_{sys}}{D_{dia}}\right)^2 - 1\right]$$

The last main imaging mode is PW Doppler Imaging which uses the Doppler Effect to determine the velocity of a very small portion of blood within a vessel.[126] Due to the Doppler Effect, in order to obtain accurate measurements, the probe must be approximately parallel to the blood flow. An angle ±60° from parallel can be corrected; however, anything larger results in inaccurate values.

In addition to these modes, adaption to B-mode has enabled two other acquisitions: ECG-gated Kilohertz Visualization (EKV) images and 3D datasets. For the EKV images, VisualSonics developed a strategy for creating high temporal resolution images by first collecting respiratory- and cardiac-gated B-mode images. The B-mode images are collected and tagged at various locations across the cardiac cycle. These images can then be used to create a high temporal resolution image across a single cardiac cycle.

Lastly, 3D datasets can be acquired a number of different ways,[127] one of which involves collecting B-mode images and then translating the probe. In this method, the ultrasound probe is attached to a linear stepper motor. After collecting a single B-mode image, the probe is translated by a specific step size after which it collects another image. This process continues to create a 3D dataset. These datasets are particularly useful in assessing disease development because morphology can change drastically from location to location.

2.5   Conclusion

The previous sections, although brief, demonstrates a clear need to improve diagnostic and treatment options for aneurysms. Small animal research affords the opportunity to assess new options in a very controlled manner, using both *in vivo* and *ex vivo* techniques. As such, in the next

chapters we use ultrasound in mice to address two prevalent uncertainties in aneurysm development and treatment.

First, although a number of studies have tried to improve risk stratification, current clinical metrics are primarily restricted to measures of diameter and growth rate. This may be driven, in part, by discrepancies in study outcomes that make clinical integration challenging. One key variable that may influence these discrepancies is thrombus, but information on thrombus growth and development is lacking. Understanding the morphology and growth of aneurysms using *in vivo* assessment can enable better construction of diagnostic metrics.

Second, even after risk is deemed severe enough to warrant treatment, current surgical risks suggest a need for improvement. Graft failure is one complication, which may be improved by better graft design. Current decisions on how to improve graft designs are often empirically determined, and could be improved by a more formal analysis. In this regard, a secondary objective is to assess the allowable parameter design space of murine textile arterial grafts, which could lead to better selection of key design components. The use of tissue engineered vascular grafts are particularly interesting due to the insight that they provide into the vascular tissue remodeling, and in the future, they may even improve endovascular stent grafts through the use of biodegradable materials. In the next chapters, we consider these two main areas.

2.6   References

1.   Bianconi E, Piovesan A, Facchin F et al. 2013. An estimation of the number of cells in the human body. Ann Hum Biol. 40(6):463-471.

2.   Campens L, Demulier L, De Groote K et al. 2014. Reference values for echocardiographic assessment of the diameter of the aortic root and ascending aorta spanning all age categories. The American Journal of Cardiology. 114(6):914-920.

3.   Potter RF, Groom AC. 1983. Capillary diameter and geometry in cardiac and skeletal muscle studied by means of corrosion casts. Microvasc Res. 25(1):68-84.

4.   Sherwood L. 2015. Human physiology: From cells to systems. Cengage learning.

5.   Vogel S. 1993. Vital circuits: On pumps, pipes, and the workings of circulatory systems. Oxford University Press, USA.

6.   Lerman A, Zeiher AM. 2005. Endothelial function. Circulation. 111(3):363-368.

7. Blausen.com. 2014. Medical gallery of blausen medical 2014. WikiJournal of Medicine. 1(2).

8. Humphrey JD. 2013. Possible mechanical roles of glycosaminoglycans in thoracic aortic dissection and associations with dysregulated transforming growth factor-β. J Vasc Res. 50(1):1-10.

9. Dingemans KP, Teeling P, Lagendijk JH, Becker AE. 2000. Extracellular matrix of the human aortic media: An ultrastructural histochemical and immunohistochemical study of the adult aortic media. The Anatomical Record: An Official Publication of the American Association of Anatomists. 258(1):1-14.

10. Annambhotla S, Bourgeois S, Wang X et al. 2008. Recent advances in molecular mechanisms of abdominal aortic aneurysm formation. World J Surg. 32(6):976-986.

11. Johnston KW, Rutherford RB, Tilson MD et al. 1991. Suggested standards for reporting on arterial aneurysms. J Vasc Surg. 13(3):452-458.

12. Sangha GS, Busch A, Acuna A et al. 2019. Effects of iliac stenosis on abdominal aortic aneurysm formation in mice and humans. J Vasc Res. 56(5):217-229.

13. Kent KC, Zwolak RM, Egorova NN et al. 2010. Analysis of risk factors for abdominal aortic aneurysm in a cohort of more than 3 million individuals. J Vasc Surg. 52(3):539-548.

14. Lederle FA, Johnson GR, Wilson SE et al. 2000. The aneurysm detection and management study screening program: Validation cohort and final results. Aneurysm detection and management veterans affairs cooperative study investigators. Arch Intern Med. 160(10):1425-1430.

15. Brady AR, Thompson SG, Fowkes FG et al. 2004. Abdominal aortic aneurysm expansion: Risk factors and time intervals for surveillance. Circulation. 110(1):16-21.

16. Chaikof EL, Dalman RL, Eskandari MK et al. 2018. The society for vascular surgery practice guidelines on the care of patients with an abdominal aortic aneurysm. J Vasc Surg. 67(1):2-77 e72.

17. Singh K, Bønaa KH, Jacobsen BK et al. 2001. Prevalence of and risk factors for abdominal aortic aneurysms in a population-based study : The tromsø study. Am J Epidemiol. 154(3):236-244.

18. Vardulaki K, Walker N, Day N et al. 2000. Quantifying the risks of hypertension, age, sex and smoking in patients with abdominal aortic aneurysm. Br J Surg. 87(2):195-200.

19. Brown LC, Powell JT. 1999. Risk factors for aneurysm rupture in patients kept under ultrasound surveillance. Uk small aneurysm trial participants. Ann Surg. 230(3):289-296; discussion 296-287.

20. Brown PM, Zelt DT, Sobolev B. 2003. The risk of rupture in untreated aneurysms: The impact of size, gender, and expansion rate. J Vasc Surg. 37(2):280-284.

21. Baxter BT, McGee GS, Shively VP et al. 1992. Elastin content, cross-links, and mrna in normal and aneurysmal human aorta. J Vasc Surg. 16(2):192-200.

22. Sakalihasan N, Heyeres A, Nusgens BV et al. 1993. Modifications of the extracellular matrix of aneurysmal abdominal aortas as a function of their size. Eur J Vasc Surg. 7(6):633-637.

23. Nissen R, Cardinale GJ, Udenfriend S. 1978. Increased turnover of arterial collagen in hypertensive rats. Proceedings of the National Academy of Sciences. 75(1):451-453.

24. Shah PK. 1997. Inflammation, metalloproteinases, and increased proteolysis: An emerging pathophysiological paradigm in aortic aneurysm. Circulation. 96(7):2115-2117.

25. Dobrin P, Mrkvicka R. 1994. Failure of elastin or collagen as possible critical connective tissue alterations underlying aneurysmal dilatation. Cardiovasc Surg. 2(4):484-488.

26. Pyo R, Lee JK, Shipley JM et al. 2000. Targeted gene disruption of matrix metalloproteinase-9 (gelatinase b) suppresses development of experimental abdominal aortic aneurysms. J Clin Invest. 105(11):1641-1649.

27. Longo GM, Xiong W, Greiner TC et al. 2002. Matrix metalloproteinases 2 and 9 work in concert to produce aortic aneurysms. The Journal of clinical investigation. 110(5):625-632.

28. Davis FM, Rateri DL, Daugherty A. 2014. Mechanisms of aortic aneurysm formation: Translating preclinical studies into clinical therapies. Heart. 100(19):1498-1505.

29. Lu G, Su G, Davis JP et al. 2017. A novel chronic advanced stage abdominal aortic aneurysm murine model. J Vasc Surg. 66(1):232-242. e234.

30. Petersen E, Wagberg F, Angquist KA. 2002. Proteolysis of the abdominal aortic aneurysm wall and the association with rupture. Eur J Vasc Endovasc Surg. 23(2):153-157.

31. Fries DM, Lightfoot R, Koval M, Ischiropoulos H. 2005. Autologous apoptotic cell engulfment stimulates chemokine secretion by vascular smooth muscle cells. Am J Pathol. 167(2):345-353.

32. Rowe VL, Stevens SL, Reddick TT et al. 2000. Vascular smooth muscle cell apoptosis in aneurysmal, occlusive, and normal human aortas. J Vasc Surg. 31(3):567-576.

33. Ailawadi G, Moehle CW, Pei H et al. 2009. Smooth muscle phenotypic modulation is an early event in aortic aneurysms. The Journal of Thoracic and Cardiovascular Surgery. 138(6):1392-1399.

34. Thompson RW, Liao S, Curci JA. 1997. Vascular smooth muscle cell apoptosis in abdominal aortic aneurysms. Coron Artery Dis. 8(10):623-631.

35. Lopez-Candales A, Holmes DR, Liao S et al. 1997. Decreased vascular smooth muscle cell density in medial degeneration of human abdominal aortic aneurysms. The American journal of pathology. 150(3):993.

36. Hance KA, Tataria M, Ziporin SJ et al. 2002. Monocyte chemotactic activity in human abdominal aortic aneurysms: Role of elastin degradation peptides and the 67–kd cell surface elastin receptor. J Vasc Surg. 35(2):254-261.

37. Henderson EL, Geng Y-J, Sukhova GK et al. 1999. Death of smooth muscle cells and expression of mediators of apoptosis by t lymphocytes in human abdominal aortic aneurysms. Circulation. 99(1):96-104.

38. Pearce WH, Shively VP. 2006. Abdominal aortic aneurysm as a complex multifactorial disease. Ann N Y Acad Sci. 1085(1):117-132.

39. Toczek J, Meadows JL, Sadeghi MM. 2016. Novel molecular imaging approaches to abdominal aortic aneurysm risk stratification. Circ Cardiovasc Imaging. 9(1):e003023.

40. Harter LP, Gross BH, Callen PW, Barth RA. 1982. Ultrasonic evaluation of abdominal aortic thrombus. J Ultrasound Med. 1(8):315-318.

41. Piechota-Polanczyk A, Jozkowicz A, Nowak W et al. 2015. The abdominal aortic aneurysm and intraluminal thrombus: Current concepts of development and treatment. Frontiers in cardiovascular medicine. 2:19.

42. Hans SS, Jareunpoon O, Balasubramaniam M, Zelenock GB. 2005. Size and location of thrombus in intact and ruptured abdominal aortic aneurysms. J Vasc Surg. 41(4):584-588.

43. Biasetti J, Gasser TC, Auer M et al. 2010. Hemodynamics of the normal aorta compared to fusiform and saccular abdominal aortic aneurysms with emphasis on a potential thrombus formation mechanism. Ann Biomed Eng. 38(2):380-390.

44. . A haemodynamic predictor of intraluminal thrombus formation in abdominal aortic aneurysms. Proc R Soc A; 2014: The Royal Society.

45. Di Achille P, Tellides G, Humphrey JD. 2016. Hemodynamics-driven deposition of intraluminal thrombus in abdominal aortic aneurysms. Int J Numer Method Biomed Eng.

46. Biasetti J, Spazzini PG, Swedenborg J, Gasser TC. 2012. An integrated fluid-chemical model toward modeling the formation of intra-luminal thrombus in abdominal aortic aneurysms. Front Physiol. 3:266.

47. Wilson JS, Virag L, Di Achille P et al. 2013. Biochemomechanics of intraluminal thrombus in abdominal aortic aneurysms. J Biomech Eng. 135(2):021011.

48. Wang DH, Makaroun M, Webster MW, Vorp DA. 2001. Mechanical properties and microstructure of intraluminal thrombus from abdominal aortic aneurysm. J Biomech Eng. 123(6):536-539.

49.   Adolph R, Vorp DA, Steed DL et al. 1997. Cellular content and permeability of intraluminal thrombus in abdominal aortic aneurysm. J Vasc Surg. 25(5):916-926.

50.   Fontaine V, Jacob MP, Houard X et al. 2002. Involvement of the mural thrombus as a site of protease release and activation in human aortic aneurysms. Am J Pathol. 161(5):1701-1710.

51.   Tong J, Cohnert T, Regitnig P, Holzapfel GA. 2011. Effects of age on the elastic properties of the intraluminal thrombus and the thrombus-covered wall in abdominal aortic aneurysms: Biaxial extension behaviour and material modelling. Eur J Vasc Endovasc Surg. 42(2):207-219.

52.   Gasser TC, Martufi G, Auer M et al. 2010. Micromechanical characterization of intra-luminal thrombus tissue from abdominal aortic aneurysms. Ann Biomed Eng. 38(2):371-379.

53.   O'Leary SA, Kavanagh EG, Grace PA et al. 2014. The biaxial mechanical behaviour of abdominal aortic aneurysm intraluminal thrombus: Classification of morphology and the determination of layer and region specific properties. J Biomech. 47(6):1430-1437.

54.   Gasser TC, Görgülü G, Folkesson M, Swedenborg J. 2008. Failure properties of intraluminal thrombus in abdominal aortic aneurysm under static and pulsating mechanical loads. J Vasc Surg. 48(1):179-188.

55.   Wolf YG, Thomas WS, Brennan FJ et al. 1994. Computed tomography scanning findings associated with rapid expansion of abdominal aortic aneurysms. J Vasc Surg. 20(4):529-538.

56.   Satta J, Läärä E, Juvonen T. 1996. Intraluminal thrombus predicts rupture of an abdominal aortic aneurysm. J Vasc Surg. 23(4):737-739.

57.   Faggioli GL, Stella A, Gargiulo M et al. 1994. Morphology of small aneurysms: Definition and impact on risk of rupture. The American journal of surgery. 168(2):131-135.

58.   Inzoli F, Boschetti F, Zappa M et al. 1993. Biomechanical factors in abdominal aortic aneurysm rupture. Eur J Vasc Surg. 7(6):667-674.

59.   Mower WR, Quiñones WJ, Gambhir SS. 1997. Effect of intraluminal thrombus on abdominal aortic aneurysm wall stress. J Vasc Surg. 26(4):602-608.

60.   Wang DH, Makaroun MS, Webster MW, Vorp DA. 2002. Effect of intraluminal thrombus on wall stress in patient-specific models of abdominal aortic aneurysm. J Vasc Surg. 36(3):598-604.

61.   Vorp DA. 2007. Biomechanics of abdominal aortic aneurysm. J Biomech. 40(9):1887-1902.

62.   Vorp D, Mandarino W, Webster M, Gorcsan III J. 1996. Potential influence of intraluminal thrombus on abdominal aortic aneurysm as assessed by a new non-invasive method. Cardiovasc Surg. 4(6):732-739.

63. Kazi M, Thyberg J, Religa P et al. 2003. Influence of intraluminal thrombus on structural and cellular composition of abdominal aortic aneurysm wall. J Vasc Surg. 38(6):1283-1292.

64. Carrell TW, Burnand KG, Booth NA et al. 2006. Intraluminal thrombus enhances proteolysis in abdominal aortic aneurysms. Vascular. 14(1):9-16.

65. Akkersdijk G, de Vries A, Puylaert J. 1991. Abdominal aortic aneurysm as an incidental finding in abdominal ultrasonography. Br J Surg. 78(10):1261-1263.

66. Scott R, Group MASS. 2002. The multicentre aneurysm screening study (mass) into the effect of abdominal aortic aneurysm screening on mortality in men: A randomised controlled trial. The Lancet. 360(9345):1531-1539.

67. Thompson SG, Ashton HA, Gao L, Scott RAP. 2009. Screening men for abdominal aortic aneurysm: 10 year mortality and cost effectiveness results from the randomised multicentre aneurysm screening study. BMJ. 338:b2307.

68. Lindholt JS, Juul S, Fasting H, Henneberg EW. 2002. Hospital costs and benefits of screening for abdominal aortic aneurysms. Results from a randomised population screening trial. Eur J Vasc Endovasc Surg. 23(1):55-60.

69. Norman PE, Jamrozik K, Lawrence-Brown MM et al. 2004. Population based randomised controlled trial on impact of screening on mortality from abdominal aortic aneurysm. BMJ. 329(7477):1259.

70. Scott R, Bridgewater S, Ashton H. 2002. Randomized clinical trial of screening for abdominal aortic aneurysm in women. Br J Surg. 89(3):283-285.

71. Mealy K, Salman A. 1988. The true incidence of ruptured abdominal aortic aneurysms. Eur J Vasc Surg. 2(6):405-408.

72. Johnston KW. 1994. Ruptured abdominal aortic aneurysm: Six-year follow-up results of a multicenter prospective study. Canadian society for vascular surgery aneurysm study group. J Vasc Surg. 19(5):888-900.

73. Schermerhorn ML, Buck DB, O'Malley AJ et al. 2015. Long-term outcomes of abdominal aortic aneurysm in the medicare population. N Engl J Med. 373(4):328-338.

74. Lederle FA, Freischlag JA, Kyriakides TC et al. 2009. Outcomes following endovascular vs open repair of abdominal aortic aneurysm: A randomized trial. JAMA. 302(14):1535-1542.

75. Paravastu SC, Jayarajasingam R, Cottam R et al. 2014. Endovascular repair of abdominal aortic aneurysm. Cochrane Database Syst Rev. (1):CD004178.

76. Darling RC, Messina CR, Brewster DC, Ottinger LW. 1977. Autopsy study of unoperated abdominal aortic aneurysms. The case for early resection. Circulation. 56(3 Suppl):II161-164.

77. Powell JT, Brady AR. 2004. Detection, management, and prospects for the medical treatment of small abdominal aortic aneurysms. Arterioscler Thromb Vasc Biol. 24(2):241-245.

78. Limet R, Sakalihassan N, Albert A. 1991. Determination of the expansion rate and incidence of ruptur of abdominal aortic aneurysms. J Vasc Surg. 14(4):540-548.

79. Fillinger MF, Marra SP, Raghavan ML, Kennedy FE. 2003. Prediction of rupture risk in abdominal aortic aneurysm during observation: Wall stress versus diameter. J Vasc Surg. 37(4):724-732.

80. Fillinger MF, Raghavan ML, Marra SP et al. 2002. In vivo analysis of mechanical wall stress and abdominal aortic aneurysm rupture risk. J Vasc Surg. 36(3):589-597.

81. Venkatasubramaniam A, Fagan M, Mehta T et al. 2004. A comparative study of aortic wall stress using finite element analysis for ruptured and non-ruptured abdominal aortic aneurysms. Eur J Vasc Endovasc Surg. 28(2):168-176.

82. Geest JPV, Schmidt DE, Sacks MS, Vorp DA. 2008. The effects of anisotropy on the stress analyses of patient-specific abdominal aortic aneurysms. Ann Biomed Eng. 36(6):921-932.

83. Scotti CM, Shkolnik AD, Muluk SC, Finol EA. 2005. Fluid-structure interaction in abdominal aortic aneurysms: Effects of asymmetry and wall thickness. Biomedical engineering online. 4(1):64.

84. Doyle BJ, Callanan A, Burke PE et al. 2009. Vessel asymmetry as an additional diagnostic tool in the assessment of abdominal aortic aneurysms. J Vasc Surg. 49(2):443-454.

85. Speelman L, Bohra A, Bosboom EMH et al. 2007. Effects of wall calcifications in patient-specific wall stress analyses of abdominal aortic aneurysms.

86. Li Z-Y, U-King-Im J, Tang TY et al. 2008. Impact of calcification and intraluminal thrombus on the computed wall stresses of abdominal aortic aneurysm. J Vasc Surg. 47(5):928-935.

87. Speelman L, Schurink GWH, Bosboom EMH et al. 2010. The mechanical role of thrombus on the growth rate of an abdominal aortic aneurysm. J Vasc Surg. 51(1):19-26.

88. Polzer S, Gasser TC, Swedenborg J, Bursa J. 2011. The impact of intraluminal thrombus failure on the mechanical stress in the wall of abdominal aortic aneurysms. Eur J Vasc Endovasc Surg. 41(4):467-473.

89. Bluestein D, Dumont K, De Beule M et al. 2009. Intraluminal thrombus and risk of rupture in patient specific abdominal aortic aneurysm – fsi modelling. Computer Methods in Biomechanics and Biomedical Engineering. 12(1):73-81.

90. Polzer S, Gasser TC, Markert B et al. 2012. Impact of poroelasticity of intraluminal thrombus on wall stress of abdominal aortic aneurysms. BioMedical Engineering OnLine. 11(1):62.

91. Georgakarakos E, Ioannou C, Kamarianakis Y et al. 2010. The role of geometric parameters in the prediction of abdominal aortic aneurysm wall stress. Eur J Vasc Endovasc Surg. 39(1):42-48.

92. Polzer S, Christian Gasser T, Bursa J et al. 2013. Importance of material model in wall stress prediction in abdominal aortic aneurysms. Med Eng Phys. 35(9):1282-1289.

93. Stenbaek J, Kalin B, Swedenborg J. 2000. Growth of thrombus may be a better predictor of rupture than diameter in patients with abdominal aortic aneurysms. Eur J Vasc Endovasc Surg. 20(5):466-469.

94. Wyss TR, Dick F, Brown LC, Greenhalgh RM. 2011. The influence of thrombus, calcification, angulation, and tortuosity of attachment sites on the time to the first graft-related complication after endovascular aneurysm repair. J Vasc Surg. 54(4):965-971.

95. Pappu S, Dardik A, Tagare H, Gusberg RJ. 2008. Beyond fusiform and saccular: A novel quantitative tortuosity index may help classify aneurysm shape and predict aneurysm rupture potential. Ann Vasc Surg. 22(1):88-97.

96. Fillinger MF, Racusin J, Baker RK et al. 2004. Anatomic characteristics of ruptured abdominal aortic aneurysm on conventional ct scans: Implications for rupture risk. J Vasc Surg. 39(6):1243-1252.

97. Parikh SA, Gomez R, Thirugnanasambandam M et al. 2018. Decision tree based classification of abdominal aortic aneurysms using geometry quantification measures. Ann Biomed Eng. 46(12):2135-2147.

98. Kontopodis N, Metaxa E, Papaharilaou Y et al. 2014. Value of volume measurements in evaluating abdominal aortic aneurysms growth rate and need for surgical treatment. Eur J Radiol. 83(7):1051-1056.

99. Hatakeyama T, Shigematsu H, Muto T. 2001. Risk factors for rupture of abdominal aortic aneurysm based on three-dimensional study. J Vasc Surg. 33(3):453-461.

100. Cooke PA, Nobis PA, Stoney RJ. 1974. Dacron aortic graft failure. Arch Surg. 108(1):101-103.

101. Friedman SG, Lazzaro RS, Spier LN et al. 1995. A prospective randomized comparison of dacron and polytetrafluoroethylene aortic bifurcation grafts. Surgery. 117(1):7-17.

102. Prager MR, Hoblaj T, Nanobashvili J et al. 2003. Collagen-versus gelatine-coated dacron versus stretch ptfe bifurcation grafts for aortoiliac occlusive disease: Long-term results of a prospective, randomized multicenter trial. Surgery. 134(1):80-85.

103. Sakalihasan N, Limet R, Defawe OD. 2005. Abdominal aortic aneurysm. The Lancet. 365(9470):1577-1589.

104. Norman PE, Semmens JB, Lawrence-Brown MMD. 2001. Long-term relative survival following surgery for abdominal aortic aneurysm: A review. Cardiovasc Surg. 9(3):219-224.

105. Parodi J, Palmaz JC, Barone H. 1991. Transfemoral intraluminal graft implantation for abdominal aortic aneurysms. Ann Vasc Surg. 5(6):491-499.

106. Investigators UKET. 2010. Endovascular versus open repair of abdominal aortic aneurysm. N Engl J Med. 362(20):1863-1871.

107. Poulsen JL, Stubbe J, Lindholt J. 2016. Animal models used to explore abdominal aortic aneurysms: A systematic review. Eur J Vasc Endovasc Surg. 52(4):487-499.

108. Daugherty A, Manning MW, Cassis LA. 2000. Angiotensin ii promotes atherosclerotic lesions and aneurysms in apolipoprotein e–deficient mice. The Journal of clinical investigation. 105(11):1605-1612.

109. Trachet B, Fraga-Silva RA, Jacquet PA et al. 2015. Incidence, severity, mortality, and confounding factors for dissecting aaa detection in angiotensin ii-infused mice: A meta-analysis. Cardiovasc Res. 108(1):159-170.

110. Phillips EH, Lorch AH, Durkes AC, Goergen CJ. 2018. Early pathological characterization of murine dissecting abdominal aortic aneurysms. APL Bioengineering. 2(4):046106.

111. Trachet B, Aslanidou L, Piersigilli A et al. 2017. Angiotensin ii infusion into apoe-/-mice: A model for aortic dissection rather than abdominal aortic aneurysm? Cardiovasc Res. 113(10):1230-1242.

112. Saraff K, Babamusta F, Cassis LA, Daugherty A. 2003. Aortic dissection precedes formation of aneurysms and atherosclerosis in angiotensin ii-infused, apolipoprotein e-deficient mice. Arteriosclerosis Thrombosis and Vascular Biology. 23(9):1621-1626.

113. Adelsperger AR, Phillips EH, Ibriga HS et al. 2018. Development and growth trends in angiotensin ii-induced murine dissecting abdominal aortic aneurysms. Physiological reports. 6(8):e13668.

114. Chiou AC, Chiu B, Pearce WH. 2001. Murine aortic aneurysm produced by periarterial application of calcium chloride. J Surg Res. 99(2):371-376.

115. Wang Y, Krishna S, Golledge J. 2013. The calcium chloride-induced rodent model of abdominal aortic aneurysm. Atherosclerosis. 226(1):29-39.

116. Anidjar S, Salzmann JL, Gentric D et al. 1990. Elastase-induced experimental aneurysms in rats. Circulation. 82(3):973-981.

117. Thompson RW, Curci JA, Ennis TL et al. 2006. Pathophysiology of abdominal aortic aneurysms: Insights from the elastase-induced model in mice with different genetic backgrounds. Ann N Y Acad Sci. 1085:59-73.

118. Bhamidipati CM, Mehta GS, Lu G et al. 2012. Development of a novel murine model of aortic aneurysms using peri-adventitial elastase. Surgery. 152(2):238-246.

119. Romary DJ, Berman AG, Goergen CJ. 2019. High-frequency murine ultrasound provides enhanced metrics of bapn-induced aaa growth. American Journal of Physiology-Heart and Circulatory Physiology. 317(5):H981-H990.

120. Kagan HM, Li W. 2003. Lysyl oxidase: Properties, specificity, and biological roles inside and outside of the cell. J Cell Biochem. 88(4):660-672.

121. Powles AEJ, Martin DJ, Wells ITP, Goodwin CR. 2018. Physics of ultrasound. Anaesthesia & Intensive Care Medicine. 19(4):202-205.

122. Ng A, Swanevelder J. 2011. Resolution in ultrasound imaging. Continuing Education in Anaesthesia Critical Care & Pain. 11(5):186-192.

123. Carovac A, Smajlovic F, Junuzovic D. 2011. Application of ultrasound in medicine. Acta Inform Med. 19(3):168-171.

124. Harvey CJ, Pilcher JM, Eckersley RJ et al. 2002. Advances in ultrasound. Clin Radiol. 57(3):157-177.

125. Goergen CJ, Azuma J, Barr KN et al. 2011. Influences of aortic motion and curvature on vessel expansion in murine experimental aneurysms. Arterioscler Thromb Vasc Biol. 31(2):270-279.

126. Allan PL. 2006. Clinical doppler ultrasound. Elsevier Health Sciences.

127. Huang Q, Zeng Z. 2017. A review on real-time 3d ultrasound imaging technology. BioMed research international. 2017.

3. ULTRASOUND IMAGING OF VASCULAR TISSUE REMODELING DURING ANEURYSMAL DISEASE

The previous chapter highlights the need to improve diagnostic and treatment options for aneurysms, both of which are highly dependent on our understanding of disease pathology. In this chapter, we further develop a murine model of aneurysmal disease and probe the role of elastin degradation and ECM cross-linking on aneurysm stability.

3.1 Abstract

Abdominal aortic aneurysm (AAA) formation and expansion is highly complex and multifactorial, and the improvement of animal models is an important step to enhance our understanding of AAA pathophysiology. In this study, we explore our ability to influence aneurysm growth in a topical elastase plus β-Aminopropionitrile (BAPN) mouse model by varying elastase concentration and by altering the cross-linking capability of the tissue. To do so, we assess both chronic and acute effects of elastase concentration using volumetric ultrasound. Our results suggest that the applied elastase concentration affects initial elastin degradation, as well as long-term vessel expansion. Additionally, we assessed the effects of BAPN by 1) removing it to restore the cross-linking capability of tissue after aneurysm formation and 2) adding it to animals with stable aneurysms to interrupt cross-linking. These results demonstrate that, even after aneurysm formation, lysyl oxidase inhibition remains necessary for continued expansion. Removing BAPN reduces the aneurysm growth rate to near zero, resulting in a stable aneurysm. In contrast, adding BAPN causes a stable aneurysm to expand. Altogether, these results demonstrate the ability of elastase concentration and BAPN to modulate aneurysm growth rate and severity. The findings open several new areas of investigation in a murine model that mimics many aspects of human AAA.

3.2 Introduction

An abdominal aortic aneurysm (AAA) is a pathological dilation of the abdominal aorta defined by a 50% increase in diameter or a diameter greater than 3 cm in humans.[1] While aneurysm severity is often defined based on measures of diameter and growth rate, a large variance in patient-

to-patient outcomes suggests a complex disease pathophysiology. Broadly, aneurysm progression includes proteolytic degradation of the extracellular matrix (ECM), smooth muscle cell apoptosis, and chronic inflammation of the aortic wall,[2] though the relative contributions of each remains unclear. To further confound factors, 70-80% of patients exhibit intraluminal thrombus (ILT) within their aneurysms,[3,4] but the role of thrombus is still controversial. Given this multifactorial nature of AAA progression and rupture, developing appropriate clinical metrics and new therapies is difficult.

While human studies have provided a wealth of information regarding AAA progression, they are limited as baseline data is often absent and controlled manipulation of experimental variables can be difficult. To this end, experimental animal aneurysms have been used to recapitulate aspects of the human condition.[5] One common model is the elastase perfusion model, which was initially developed in rats[6] and later optimized for mice.[7] In this model, porcine pancreatic elastase is pressure-perfused into the aorta, which causes an immediate increase in diameter due to the inflation pressure and typically results in an aneurysm by the second week. Bhamidipati et al. adapted the elastase perfusion model by applying peri-adventitial elastase, avoiding the need for cannulation of the aorta.[8] Although this model does form aneurysms, they typically stabilize by day 14,[9,10] making it difficult to assess growth dynamics.

Recently, Lu et al. combined this topical elastase surgery with continuous oral administration of β-Aminopropionitrile (BAPN), a lysyl oxidase (LOX) inhibitor, to create continuously expanding aneurysms.[10] LOX is produced by vascular smooth muscle cells and is the primary enzyme involved in the formation and maturation of irreducible cross-links in collagen and elastin.[11] By inhibiting LOX and reducing collagen and elastin cross-linking, elastase-treated vessels were unable to stabilize, leading to progressive damage and expansion of the arterial wall, thus creating large aneurysms. In addition, Lu and colleagues noted the presence of ILT in some animals, which is of particular interest given the small number of murine aneurysm models that develop ILT, despite its prevalence in many AAA patients.

Given the ability of combined BAPN and topical elastase to recapitulate continuous infrarenal AAA growth and development of ILT, we utilized this model to further explore the role of elastin degradation and cross-linking on continued aortic expansion. By utilizing high frequency volumetric ultrasound to acutely and longitudinally assess the development of aneurysms, we demonstrate that vessel expansion varies with elastase concentration. Further, by altering the

timeline of BAPN application, we show that, while initial elastase degradation strongly influences final aneurysm size and presence of ILT, LOX inhibition also remains necessary for continued aneurysm expansion.

3.3 Materials and Methods

3.3.1 General Experimental Setup

Data in this study is available on request from the authors. All procedures were performed with approval from the Purdue University Institutional Animal Care and Use Committee (Protocol 1305000869), in accordance with relevant guidelines and regulations, and in compliance with the ARRIVE guidelines. In addition, prior to performing any procedures, mice were acclimated to the facility for a minimum of 3 days. Similar to a previously published protocol,[10] 10-week-old C57BL/6J mice (Jackson Laboratories, Bar Harbor, ME) were given drinking water with 0.2% BAPN fumarate salt (A3134; Sigma-Aldrich, St. Louis, MO), beginning two days before surgery and extending through the duration of the study, unless otherwise noted. The majority of these mice were male as was used previously;[9,10] however, a subset (n=5) of mice were female to assess effects of sex. All mice then underwent topical elastase surgery.[10] Briefly, mice were anesthetized with 2-3% isoflurane and a laparotomy was performed to expose the infrarenal aorta. After blunt dissection to expose the infrarenal aorta, 5 µL of either 2.5 mg/ml, 5 mg/ml, or 10 mg/ml porcine pancreatic elastase (E7885, Sigma Aldrich, St. Louis, MO) was applied directly on the aortic adventitia via a pipette and allowed to remain for 5 minutes before triple rinsing with saline.[12] To ensure appropriate location of the elastase, only the section of the aorta that was to receive elastase was bluntly dissected. The psoas muscle and inferior vena cava (IVC) also ensured that the elastase remained on top of the aorta for the entire 5 minutes. After rinsing, the incision was sutured closed and the mice recovered. To track aneurysm progression, mice were imaged with a high-frequency ultrasound system (Vevo 2100 or Vevo 3100, FUJIFILM VisualSonics, Toronto, ON, Canada) before surgery and then regularly afterward (timeline and imaging details below; **Figure 3.1**). At end-of-study, mice were euthanized by isoflurane overdose and bilateral pneumothorax. Cardiac puncture was then performed on a subset of mice, and the systemic vasculature was flushed with saline, paraformaldehyde, and agarose. All aortas were then fixed in paraformaldehyde for

histological analysis (details below). Analysis was performed without blinding. A summary of the experiments is shown schematically in **Figure 3.1**.
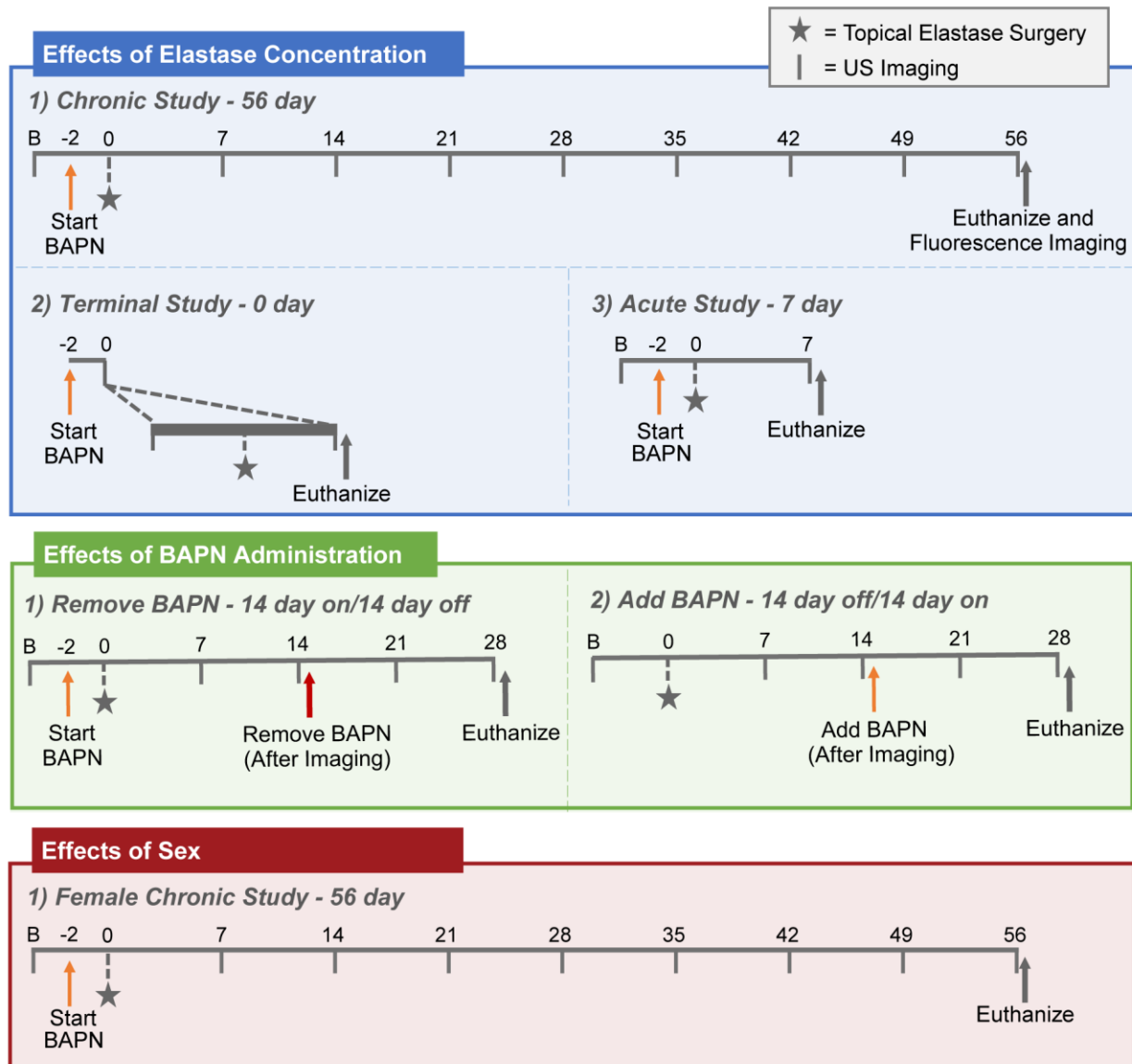
Figure 3.1. Experimental Overview. Schematic depicts the timelines of BAPN administration, elastase surgery, ultrasound imaging, fluorescence imaging, and euthanasia for each sub-experiment.

3.3.2   Experiment 1 – Chronic Effects of Elastase Concentration

During surgery, mice were randomly allocated to receive one of three concentrations of elastase: 2.5, 5, or 10 mg/ml (n=8/group, based on prior work[10]). Male mice were imaged with

ultrasound at baseline, as well as weekly post-surgery. After 8 weeks, mice were euthanized, near infrared (NIR) imaging was performed on explanted aortas (details below), and aortas were subsequently fixed for histology. In addition to the three elastase concentrations, 5 additional mice received elastase that had been inactivated by heating to 100°C for 30 min (heat-inactivated negative controls) and were imaged at baseline and again at weeks 1, 2, 4, and 8 post-surgery.

3.3.3   Experiment 2 – Short-term Effects of Elastase Concentration

Similar to Experiment 1, three concentrations of elastase were used: 2.5, 5, or 10 mg/ml (n=5/group per timepoint), as well as heat-inactivated elastase as a negative control (n=5 per timepoint). To assess the surgical effects of elastase administration, mice were imaged by ultrasound immediately after surgery and then euthanized. To assess acute effects, mice were imaged and euthanized 1 week after surgery. At both timepoints, aortic tissue was fixed for histology.

3.3.4   Experiment 3 – Effects of LOX Inhibition on Aneurysm Growth

Surgery was performed on male mice with an elastase concentration of 10 mg/ml (n=6). Two sub-experiments were performed. In the first, BAPN was added to the animals' drinking water two weeks after surgery to assess if adding BAPN after the aortic tissue had begun to stabilize would still result in aneurysmal growth. In the second sub-experiment, BAPN was removed from the animals' drinking water two weeks after surgery to assess if LOX inhibition continued to be necessary even after aneurysm formation. For both sub-experiments, mice were imaged before surgery and weekly after surgery. Four weeks post-surgery (2 weeks after either removing or adding BAPN), mice were euthanized, and aortic tissue fixed for histology. Mice with 10 mg/mL elastase and continuous BAPN administration (n=6) were used for comparator data.

3.3.5   Experiment 4 – Chronic Effects in Females

To assess the chronic effects of sex on AAA progression, five female mice were treated with 10 mg/ml of elastase concentration. As was done for the chronic male study, female animals were imaged with ultrasound at baseline, as well as weekly post-surgery. After 8 weeks, mice were euthanized and aortic tissue fixed for histology.

3.3.6 Ultrasound Imaging

High frequency ultrasound imaging (Vevo 2100; FUJIFILM VisualSonics) was performed on anesthetized mice (1-3% isoflurane). The mice were placed in supine position on a heated stage, connected to electrodes to measure both cardiac and respiration rates. Depilatory cream (Nair, Church & Dwight, Ewing, NJ) was applied to the abdomen to remove hair prior to imaging. Using a MS550D/MX550D linear transducer (22-50 MHz bandwidth; 40 MHz center frequency, FUJIFILM VisualSonics), long- and short-axis brightness (B-) mode and ECG-gated Kilohertz Visualization (EKV) images of the aorta were acquired, in addition to motion (M-) mode at the proximal, maximum diameter, and distal portions of the infrarenal aorta. Lastly, using a linear step motor, sequential 2D short-axis images were collected to create a 3D ultrasound dataset.[13,14]

Effective maximum diameters of the lumen and outer wall were measured at systole using short-axis images. The perimeter of the vessel was hand-drawn to obtain the cross-sectional area (VevoLab 5.5.0, FUJIFILM VisualSonics), and the effective diameter was back calculated by assuming a circular cross-section. In addition, using the M-mode images at the maximum diameter location, we measured systolic and diastolic diameters in triplicate. Systolic and diastolic diameters were then used to calculate Green-Lagrange circumferential strain[15]:

$$E_{\theta\theta} = \frac{1}{2}\left[\left(\frac{D_{sys}}{D_{dia}}\right)^2 - 1\right]$$

The 3D datasets were manually segmented utilizing the SimVascular platform [16] to create volumetric segmentations of the aneurysms.

3.3.7 NIR Imaging for MMP Activity

A fluorescent probe was used to measure matrix metalloprotease (MMP) activity in the region of the aneurysm. MMPSense 680 (150 μL; PerkinElmer, Waltham, MA) was injected via tail vein approximately 24 hours prior to euthanasia. After harvesting the aorta, the specimen was exposed to NIR light at 625 nm to obtain fluorescent images from both the dorsal and ventral sides. For each image, an intensity ratio was calculated as the average pixel intensity of the aneurysm relative to that of healthy thoracic aortic tissue.[15] More specifically, the mean signal intensity was measured for the AAA, the thoracic aorta, and the background using ImageJ (National Institutes of Health, Bethesda, MD).[17] The intensity ratio was calculated as:

$$Intensity\ Ratio = \frac{I_{AAA} - I_{Background}}{I_{Thoracic} - I_{Background}}$$

The intensity ratio was calculated for dorsal and ventral images and then averaged to get a single intensity ratio per animal. A representative schematic showing the analysis method is included in **Appendix A Figure 1**.

3.3.8   Histology

Specimens were fixed in 4% paraformaldehyde for at least 24 hours. Fixed samples were grossly sectioned in ~4 mm increments and embedded in paraffin. Sections (4 µm thick) were stained with hematoxylin and eosin (H&E) and Movat's Pentachrome (MPC). Microscopic examination of the H&E slides was performed by a board-certified pathologist using a semi-quantitative scoring system (**Appendix A Methods**). Additionally, MPC stained slides were digitally scanned with a Leica Biosystems Versa scanner (Aperio Technologies, Vista, CA). For the terminal and acute studies, the most severely degraded histological section was annotated using Aperio ImageScope software (v12.4.3.50008) to assess elastin degradation in the terminal and acute studies. If no slice had degradation (such as in the heat-inactivated group), a single slice at the mid-infrarenal region was selected instead. The number of dark pixels in the wall was divided by the total number of pixels as a measure of percent elastin in the wall.

3.3.9   Statistical Analyses

Analyses were performed in Prism 9.0 (GraphPad Software, CA) and figures compiled in Adobe Illustrator 2019 (Adobe Inc., CA). Data were checked for normality (Shapiro-Wilk test) and homogeneity of variance (Brown-Forsythe test), and violations were corrected with appropriate transformations. The ultrasound data were analyzed using a two-way repeated measures ANOVA to assess main effects of time and elastase concentration ($p<0.05$). For the female mice, a two-way repeated measures ANOVA assessed the main effects of time and sex ($p<0.05$). Within each time point, a post-hoc Tukey HSD was performed to assess differences between groups. In addition, within each group, a post-hoc Dunnett's test was used to assess significant differences relative to baseline data. MMP activity and histology were analyzed using a one-way ANOVA with a post-hoc Tukey HSD ($p<0.05$). Correlation of thrombus and MMP

activity was assessed using Pearson's correlation. Lastly, thrombus prevalence was measured using a Fisher's exact test ($p<0.05$). All data are plotted as mean ± std dev.

3.4 Results

3.4.1 Elastase concentration influences aneurysm size and growth, but has minimal effect on strain.

Following the topical elastase surgery, mice in the 2.5, 5, and 10 mg/ml groups showed reduced strain relative to both baseline values and to the heat-inactivated group, and these strain values continued to remain low for the remainder of the study ($p<0.05$; **Figure 3.2A-B**). In addition, this reduction in strain was accompanied by a significant increase in diameter, beginning at day 14 for the 5 and 10 mg/ml groups, and at day 21 for the 2.5 mg/ml group ($p<0.05$; **Figure 3.2C-D**). Of particular interest, elastase concentration clearly influenced final aneurysm size, with the 2.5 mg/ml elastase application resulting in moderately sized aneurysms and the 5 and 10 mg/ml elastase application resulting in significantly larger aneurysms (**Figure 3.3A-D**; **Appendix A Figure 2-11**). By day 56, the diameters of the heat-inactivated, 2.5, 5, and 10 mg/ml groups were 0.74±0.04, 3.0±1.3, 5.3±1.0, and 4.3±0.9 mm, respectively ($p<0.01$ for all comparisons; **Figure 3.3E**). Interestingly, some of the mice in the 5 mg/ml and 10 mg/ml groups formed thrombus. In the 5 mg/ml group, thrombus was first observed on day 28 and had a final prevalence of 2 in 7 mice (28.6%), while in the 10 mg/ml group, thrombus was first observed between days 28 and 42, and had a final prevalence of 5 of 8 mice (62.5%; $p=0.31$). While diameter showed a graded effect with elastase concentration, circumferential strain did not. The strain in all three groups was significantly reduced compared to the heat-inactivated group ($p<0.001$ for all comparisons) but not significantly different from each other ($p=0.98$ for 2.5 vs 5 mg/ml; $p=0.93$ for 2.5 vs 10 mg/ml; $p>0.99$ for 5 vs 10 mg/ml; **Figure 3.3F**).

Further, measures of MMP activity at day 56 were increased in aneurysmal mice and correlated with diameter ($p<0.01$; **Figure 3.3G-H**). We were unable to obtain MMP data for two of the mice in the 10 mg/ml group due to difficulties with the injections. We also note that one mouse from the 5 mg/ml elastase group in Experiment 1 died on day 42 before the end of the 56-day study and was excluded from all analyses. During necropsy, we observed blood in the

abdomen, suggesting aneurysm rupture as the cause of death, although visualization of a rupture site was not possible.
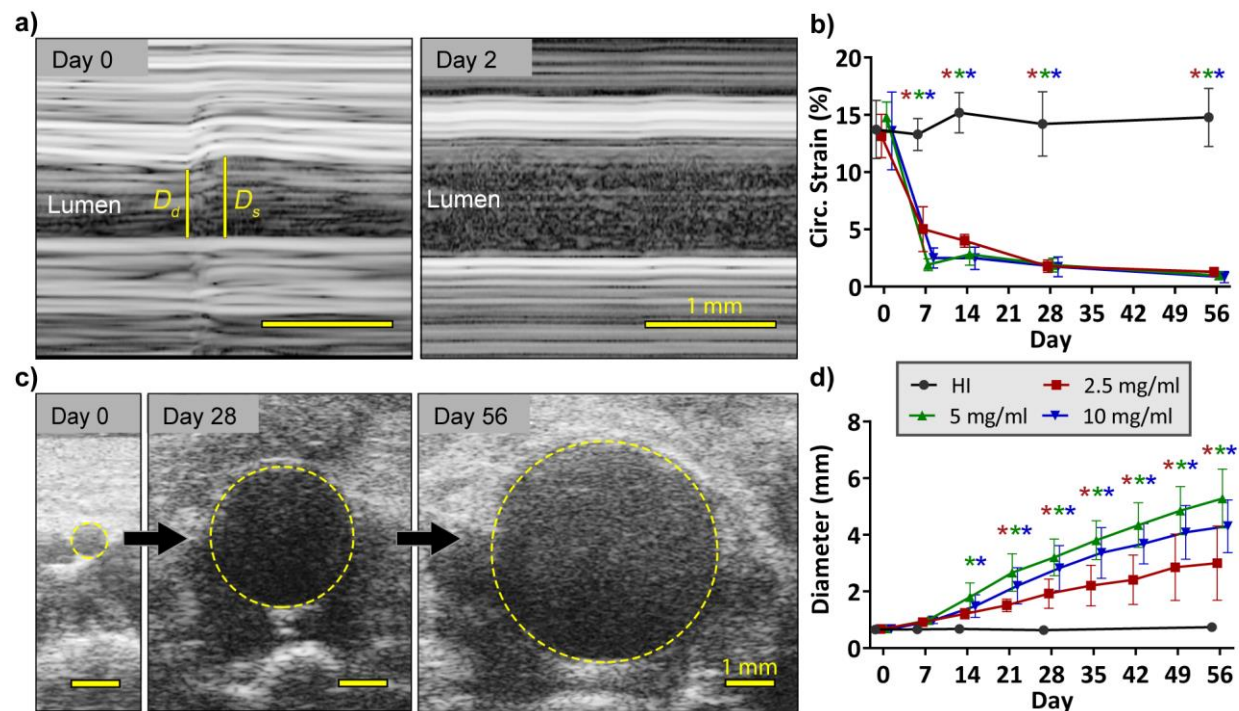
Figure 3.2. Longitudinal ultrasound imaging of elastase-treated mice. A) Measurements of diastolic and systolic diameters from ultrasound M-mode images were used to calculate Green-Lagrange circumferential strain. B) Post-elastase application, mice showed significantly reduced circumferential strain compared to both baseline measurements and to the heat-inactivated group. In addition, mice treated with 2.5 mg/ml (red) elastase had significantly higher strain than the 5 (green) and 10 mg/ml (blue) groups on day 7. By day 14, measures of strain were indistinguishable among the elastase-treated groups, and remained low for the remainder of the study. C) Short-axis measures of diameter show a continuously increasing aneurysm. D) While all mice had aneurysms, the mice treated with 5 and 10 mg/ml elastase had significantly larger aneurysms than the mice treated with 2.5 mg/ml, beginning at days 21 and 28, respectively. Scale bars are 1 mm. Note that for clarity, the only statistical comparison shown in the graphs are relative to the baseline within each group ($p<0.05$ with the color of the '*' indicating the group).
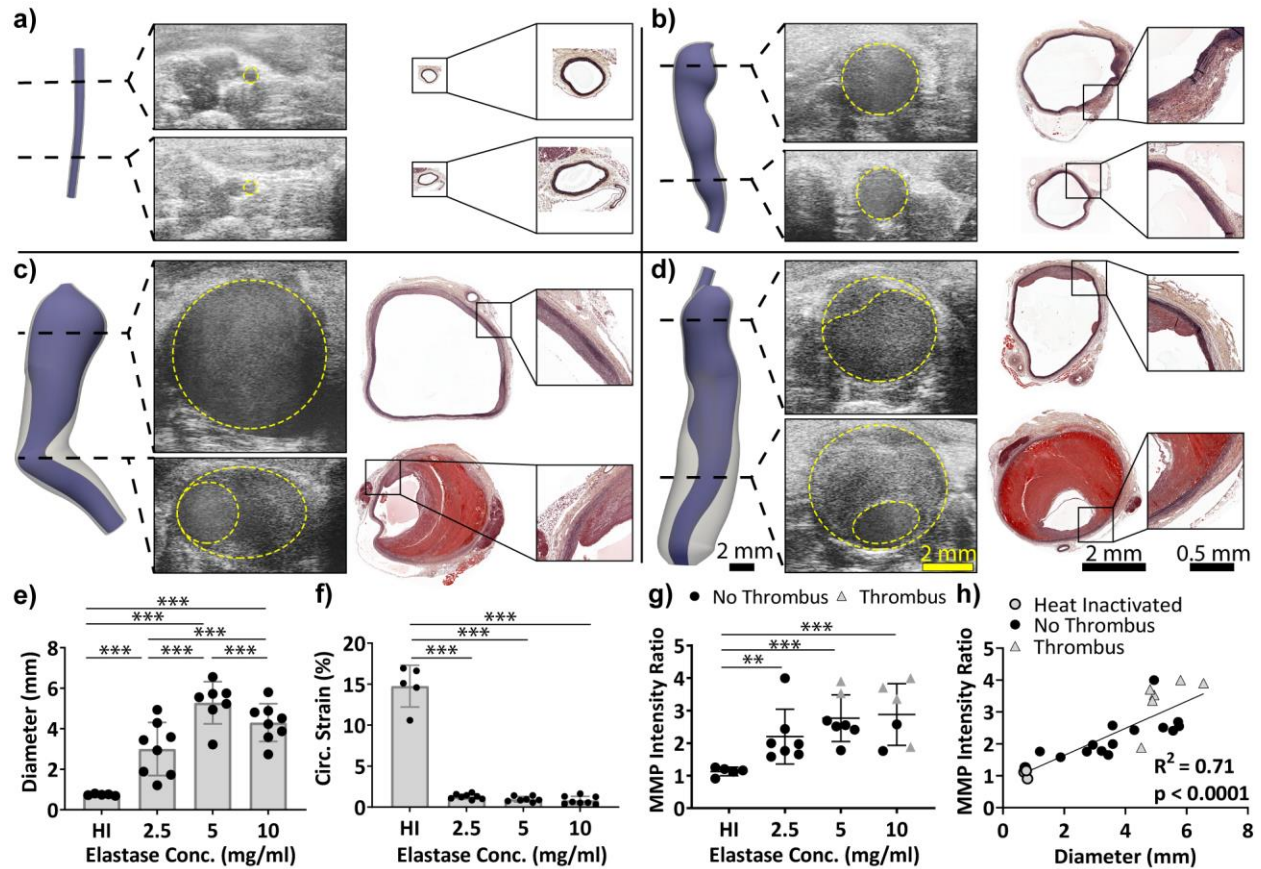
Figure 3.3. Chronic effects in mice treated with varied elastase concentrations. Ultrasound-based 3D segmentations at day 56 compare well with end-of-study histology (MPC shown). A) In mice treated with heat-inactivated elastase, the aortas showed no degradation of the elastin and remained the same size throughout the study. In contrast, mice treated with B) 2.5 mg/ml, C) 5 mg/ml, and D) 10 mg/ml elastase-treated groups had fragmented elastin and varying-sized aneurysms. In addition, although not all mice in the 5 and 10 mg/ml groups had thrombus, those that did have thrombus tended to have a thin proximal wall and a thrombus-laden distal portion. E) Diameter measurements indicated a graded effect of elastase concentration, with the 2.5 mg/ml group having moderately-sized aneurysms, and the 5 and 10 mg/ml groups having large aneurysms. F) Despite differences in diameter, circumferential strain was statistically indistinguishable among elastase-treated groups, and was only different from the heat-inactivated control. G) MMP activity was also increased in aneurysmal mice, which correlated linearly with diameter (H). Of interest, mice with thrombus tended to have higher MMP activity (not statistically assessed). *p<0.05; **p<0.01; ***p<0.001 with lines indicating the comparison.

56

3.4.2 Elastase application causes immediate reduction in elastin.

To assess if the chronic differences observed among the elastase-treated groups were driven by observable acute effects, we performed terminal (euthanize immediately after surgery) and acute (euthanize on day 7) experiments (**Figure 3.4** and **Appendix A Figures 12-15**). In the terminal group, the 5 and 10 mg/ml elastase-treated mice had an immediate reduction in elastin as quantified with histology (p=0.04 and p=0.01 compared to heat-inactivated, respectively; **Figure 3.4A-D**). The elastin in the 2.5 mg/ml group, although reduced, was not significantly different than that of the heat-inactivated group (p=0.2; **Figure 3.4I**). Noteworthy is that, in all three elastase-treated groups, the destruction of elastin appears heterogeneous, with some regions showing healthy elastin and other regions showing near-complete degradation.

Concomitant with the reduction in elastin content was a reduction in circumferential strain. Immediately post-surgery, all three elastase-treated groups had significantly lower circumferential strain compared to the heat-inactivated mice (p<0.001 for all) but were not significantly different from each other (p=0.16 for 2.5 vs 5 mg/ml; p=0.05 for 2.5 vs 10 mg/ml; p=0.93 for 5 vs 10 mg/ml; Fig. 4J). In addition, diameter was greater in the elastase-treated mice, though it only reached significance in the 5 mg/ml group (p=0.03 vs heat-inactivated; **Figure 3.4K**).

By day 7, much of the outer wall in the elastase-treated aortas lacked clear delineation. Instead, the wall appeared to diffuse into the surrounding tissue (**Figure 3.4E-H**), with mononuclear and polymorphonuclear leukocytes infiltrating into the wall (**Appendix A Figure 16**). Per histology, the elastin content in the 5 and 10 mg/ml groups remained low, and were significantly lower than the heat-inactivated group (p<0.001 for both). In addition, by day 7, the elastin content in the 5 and 10 mg/ml groups were also significantly lower than the 2.5 mg/ml group (p=0.03 and p=0.04, respectively). For the 2.5 mg/ml group, although some images showed severe degradation, quantification of elastin suggested that it was non-significantly different than that of the heat-inactivated mice (p=0.13; **Figure 3.4I**). Between days 7 and 56, the elastin in the elastase treated mice continued to degrade, to such a degree that a semi-quantitative scoring by a board-certified pathologist (**Appendix A Methods**) showed that all mice in the 2.5 mg/ml, 5 mg/ml, and 10 mg/ml groups had the highest score in terms of disorderly arrangement of fibers, disruption in continuity, and distorted form.

Circumferential strain in all three elastase-treated groups remained significantly lower than heat-inactivated (p<0.001; **Figure 3.4J**). In addition, by day 7, the three elastase-treated groups

began to differentiate from each other, with the 5 and 10 mg/ml groups showing significantly lower strain than the 2.5 mg/ml group (p=0.02 for both comparisons). Also by day 7, the 2.5, 5, and 10 mg/ml groups had significantly larger diameters than heat-inactivated (p=0.01, p<0.001, and p<0.01, respectively), but were not significantly different from each other (p=0.42 for 2.5 vs 5 mg/ml; p=0.97 for 2.5 vs 10 mg/ml; p=0.67 for 5 vs 10 mg/ml; Fig. 4J).
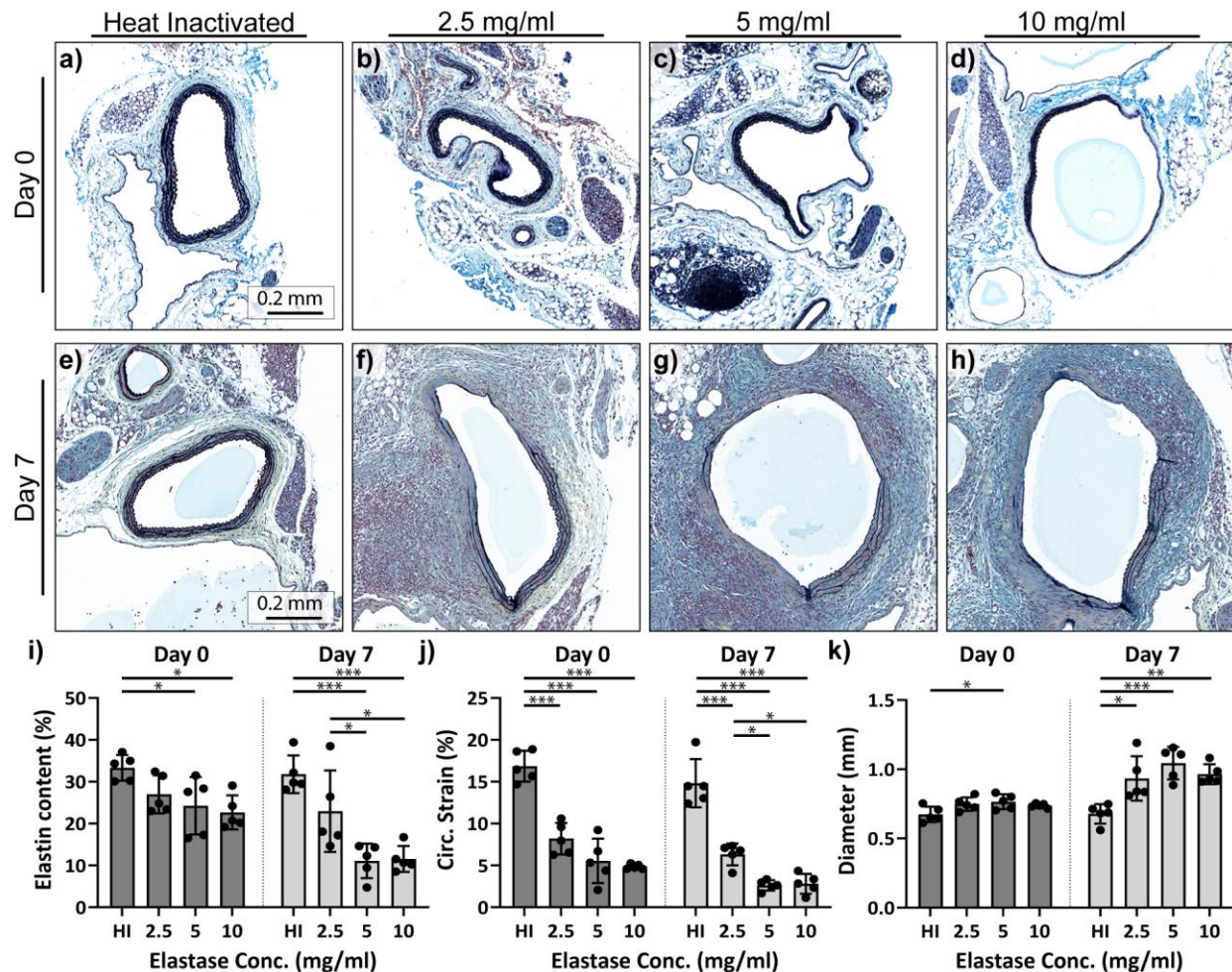
Figure 3.4. Short-term effects in mice treated with varied elastase concentrations. Terminal and acute MPC and ultrasound results of the topical elastase procedure revealed an immediate reduction in elastin integrity compared to the heat-inactivated group. A) Heat-inactivated elastase-treated mice qualitatively showed no damage post-surgery compared to the B) 2.5 mg/ml, C) 5 mg/ml, and D) 10 mg/ml groups. E) By day 7, heat-inactivated elastase-treated mice similarly showed no damage, but the F) 2.5 mg/ml, G) 5 mg/ml, and H) 10 mg/ml groups also showed diffuse damage. Quantification of intact elastin showed similar results. In addition, ultrasound was used to quantify J) strain and K) diameter. *p<0.05; **p<0.01; ***p<0.001

3.4.3 LOX inhibition drives continued aneurysm progression.

To probe the effects of BAPN, mice were either 1) given BAPN continuously for 28 days, 2) given regular water for 14 days followed by BAPN for 14 days, or 3) given BAPN water for 14 days followed by regular water for 14 days (**Figure 3.5A-C**). Results demonstrate the necessity of BAPN for aneurysmal growth. Mice given regular water for the first two weeks had aortic diameters that increased from day 0 to 7 (due to the elastase treatment); however, after 7 days, the aortic growth stabilized, resulting in very little growth from day 7 to day 14 (**Figure 3.5D**). Then, after day 14, BAPN was added, and the aneurysms began to expand again.

In a similar manner, the removal of BAPN after aneurysm formation caused stabilization of the aneurysm. Two weeks post-elastase surgery, all mice in the Remove BAPN group had aneurysms, with an average maximum diameter of 2.0±0.8 mm (**Figure 3.5E**). However, after BAPN was removed, the aneurysms stabilized and ceased to expand. Two weeks after removing the BAPN treatment, the average diameter growth in the Remove BAPN group was reduced to 0.03±0.08 mm/week (**Figure 3.5F**). In contrast, mice that continued to be treated with BAPN had an average diameter growth of 0.39±0.21 mm/week at the same time point (p<0.01; **Figure 3.5F**).

3.4.4 Female mice tend to have larger aneurysms.

Five female mice were treated with 10 mg/ml elastase and BAPN (**Figure 3.6A** and **Appendix A Figure 17**), and compared to the eight 10 mg/ml elastase-treated male mice from the concentration study. Of the female mice, two died prior to end-of-study, with one dying on Day 10 and the other dying on Day 32 (**Figure 3.6B**). For the Day 10 mouse, necropsy showed no blood in the abdomen. For the Day 32 mouse, blood was observed in the abdomen, presumably due to aneurysm rupture, although visualization of the location of vessel wall failure was not possible. These two female mice were removed from all subsequent analysis. The three female mice had significantly larger diameters than the male mice, beginning at Day 21 and extending through the rest of the study. At end-of-study, the average maximum diameter of the female mice was 7.3±0.3 mm, compared to average male diameter of 4.3±0.9 mm (p<0.001; **Figure 3.6C**).
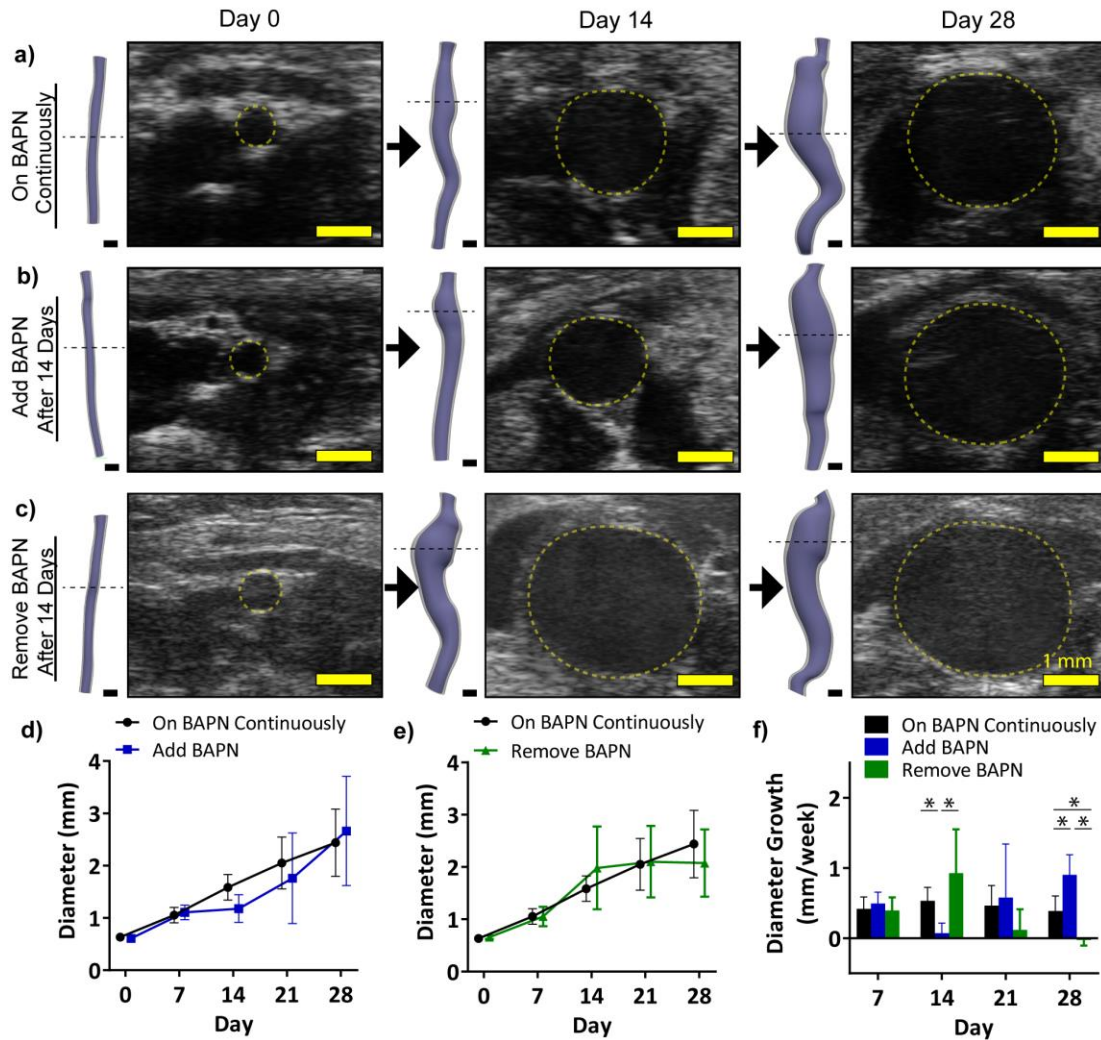
Figure 3.5. Effects of altering timeline of BAPN administration. Even after aneurysm formation, BAPN administration was necessary for continued aneurysmal expansion. Representative ultrasound and volumetric segmentations demonstrate the lack of growth from Day 14 to Day 28 observed in A) the mice treated with BAPN continuously compared to B) the Add BAPN group and C) the Remove BAPN group. Quantification of maximum effective diameter demonstrates that D) the addition of BAPN causes growth and E) the removal of BAPN inhibits growth. F) Growth rate shows similar results. Scale bars are 1 mm. *p<0.05 with the lines indicating comparison.
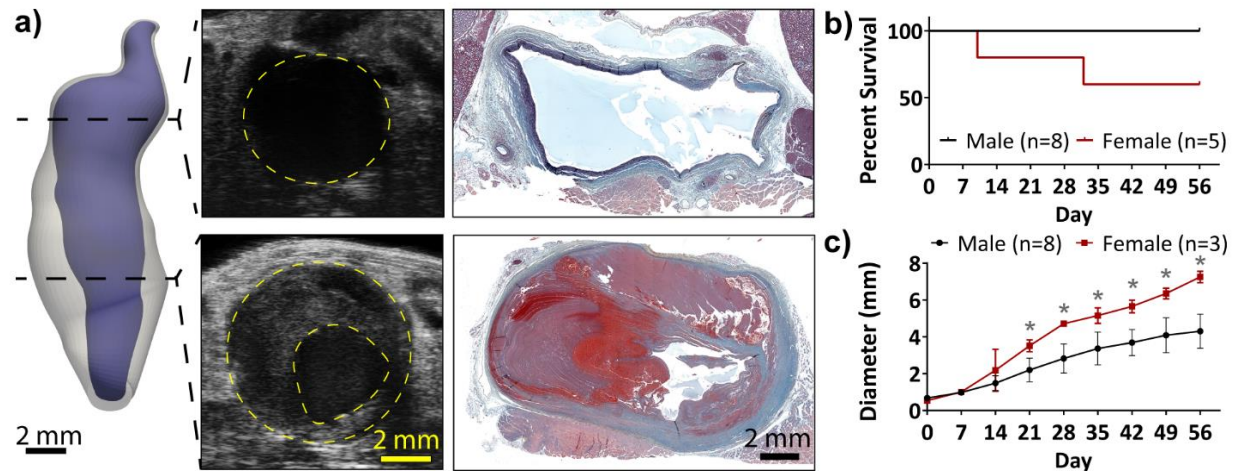
Figure 3.6. Female elastase-treated mice. Combined treatment of elastase and BAPN in female mice resulted in large aneurysms. A) Similar to the male mice, these aneurysms tended to have a thin, proximal region and a thick, thrombus-laden distal region. B) In addition, two of the five female mice died before end-of-study. C) Among the remaining female mice, maximum diameter was significantly larger than that of the males, beginning on Day 21. *p<0.05 for male and female comparison within each time point.

3.5   Discussion

The formation and expansion of an AAA is highly complex and multifactorial, and the ability to improve patient care is heavily dependent on increasing our understanding of aneurysm pathophysiology. In this study, we assessed aneurysm growth in a relatively new BAPN+Elastase mouse model[9,10] by varying elastase concentration and BAPN timing, thus altering the cross-linking capability of the aortic wall tissue. Our results suggest that initial elastin degradation and ultimate vessel expansion is dependent on the concentration of elastase. In addition, we demonstrate that even after aneurysm formation, LOX inhibition remains necessary for continued aneurysmal growth. Namely, removing BAPN, and thus enabling LOX activity, caused stability of the aneurysm. In contrast, adding BAPN caused growth in a previously stable aneurysm. Collectively, these results demonstrate the ability of elastase concentration and BAPN to modulate aneurysm severity.

While the purpose of animal models is to recapitulate aspects of the human condition, no animal model is perfectly able to accomplish this. As such, a myriad of murine models have been developed, each with their own advantages and disadvantages.[5,18] Some of the more established chemical aneurysm animal models include the angiotensin II (AngII) dissection model, the calcium

chloride model, and the elastase model. The AngII dissecting AAA model, first described by Daugherty et al.,[19] is created by subcutaneously implanting an AngII-filled mini-osmotic pump into apolipoprotein E-deficient (apoE-/-) mice. The resulting aneurysm, which occurs in ~60% of the mice, is typically formed due to a tear separating the medial and adventitial layers of the suprarenal aorta.[20,21] The aneurysmal dissection often has both a true and false lumen, with the false lumen filled with intramural thrombus. While there is some growth after the initial onset, it is modest, and aneurysm typically plateaus in size.[13,21] In addition, given its formation and development, the model may better depict an aortic dissection[21] rather than the fusiform aneurysms that are more commonly observed in the human infrarenal abdominal aorta.

In contrast, both the calcium chloride and elastase models form infrarenal, fusiform aneurysms. The calcium chloride model is formed by topically applying calcium chloride to the adventitial surface of the aorta, causing calcium precipitations that disrupt the elastin and lead to an inflammatory response.[22] However, not all mice form aneurysms and among those that do, maximum diameter remains small, even after 10 weeks.[23] In addition, the chemical burn caused by the treatment is likely not the best representation of the human pathology. Similar to the calcium chloride model, the elastase model can be created by a peri-adventitial application,[8] although initial studies were performed with a more technically challenging intraluminal perfusion procedure.[6,7] Also similar to the calcium chloride model, the resulting aneurysms are small and stable,[9] though prevalence and size are often greater than that of calcium chloride-induced AAAs.[7-9]

While each of these models have their advantages, one common issue is the lack of chronic growth that is typically observed in humans. To counter this, more recent studies have begun to add BAPN to these "classic" models in order to block LOX activity, thus preventing cross-linking of elastin and collagen, and increasing the incidence and/or severity of the disease.[9,10,24-28] In the present work, we used the BAPN+Elastase model, mostly because it resulted in continuously growing aneurysms. Compared to the work of Lu et al., we similarly observed the development of large aneurysms. However, since we concluded our study at Day 56 and not Day 100, we did not observe nearly as many late-stage deaths as they did. We also did not see any early-stage deaths (by Day 8), which may be driven by variations in elastase application and surgical techniques. Building on the work that they had performed, of particular interest to us was the ability to modulate aneurysm severity, which would increase the versatility of this model given the large range of diameters observed in human AAAs.[29] By varying elastase concentration, we were able

to modify the maximum aneurysm diameter from ~350% increase in the 2.5 mg/ml group to large ~500-650% increase in the 5 and 10 mg/ml groups. Presumably, the elastase concentration could be even further reduced to create small but slowly expanding aneurysms.

Although maximum AAA diameter is often used for clinical decisions, 3D imaging and segmentation may provide a more holistic understanding of progression.[30] To this end, we used high frequency ultrasound to obtain 3D datasets from which we created volumetric segmentations of both luminal and adventitial boundaries (**Appendix A Figure 2-3**). One striking feature is the wide variation in shape and degree of tortuosity observed with this model. In general, the proximal portion tended to be larger, potentially driven by differences in mechanics and blood flow in the region near the renal arteries. With that in mind, in an additional experiment, we applied the elastase either closer to the renal arteries or closer to the trifurcation (**Appendix A Figure 18**). Although the 3D segmentations suggest an increase in aneurysm size in the mice that received a more proximal elastase treatment, maximum diameter results were highly variable and therefore non-significant (p=0.09 at day 28).

While the proximal portion of the aneurysm tended to be larger, it was the distal portion where we more often observed thrombus formation. Interestingly, this thrombus was intraluminal as has also been noted in human AAAs,[31] and not intramural as is the case in the AngII dissection model. This presence of ILT in a mouse model is noteworthy in that it opens avenues for further exploration of ILT composition, growth, and impact on AAA rupture risk. Such analyses have already begun, with the recent work by Weiss et al. who combined histological and biomechanical information in a computational model to provide insight on ILT growth and remodeling.[32]

In the current study, in 10 mg/ml group, thrombus was observed in 62.5% of the mice, which compares well with the ~70% of human cases that develop thrombus[3] and also matches well with previous data in this model.[10] In contrast, the thrombus frequency in the 5 mg/ml group was only 28.6%. The Fisher exact test was not significantly different between the 5 mg/ml and 10 mg/ml groups, and further studies would be required to explore if this slight variation is consistent; however, it may suggest that initial elastase concentration has some effect on eventual ILT formation independent of vessel diameter since both the 5 and 10 mg/ml groups had similar-sized aneurysms. As a simple metric, we found that diameter growth rate in the week prior to thrombus may be a better predictor of initial thrombus deposition than diameter itself (**Appendix A Figure 19**). We also observed a highly tortuous region within the non-aneurysmal proximal aorta in some

mice that formed thrombus, which then caused a small inflow jet of blood (**Appendix A Figure 20**). In addition, some of the thrombus was layered (e.g. M8 in **Appendix A Figure 5**) suggesting a staccato process, while other thrombus appeared more homogenous (M1 in **Appendix A Figure 5**). Future work utilizing computational fluid dynamic or fluid-structure interaction simulations will be necessary to add mechanistic insight regarding the relationship between flow profiles and ILT. Even so, these preliminary observations provide further support for the idea that flow-induced activation of platelets in the proximal region, followed by stagnant flow in the distal region, may be correlated with ILT formation and warrants further investigation.[33-35]

Tortuosity also varied considerably in the BAPN+Elastase model, with some mice in the 5 and 10 mg/ml elastase groups showing highly tortuous distal sections (**Appendix A Figure 3**). Clinically, tortuosity has been associated with increased rupture risk[36,37] and higher rates of graft-related complications after repair.[38] In our study, increased tortuosity occurred early in some of the mice as also shown previously,[9] but tended to become more exacerbated as aneurysms continued to grow (**Appendix A Figure 2**). We also observed that most complex geometries with the highest level of tortuosity were found in the 5 and 10 mg/ml groups, suggesting the vessel was also lengthening as it was expanding radially. This tortuosity seemed to occur independent of thrombus formation, with increased tortuosity noted in both thrombus-laden and non-thrombus-laden aneurysms. Further work will be needed to determine if these severe BAPN+Elastase AAA tortuosities develop in a consistent pattern, as has been previously reported in the AngII dissecting AAA model that commonly expands leftward directly above the right renal artery.[15,39]

Given the difference in chronic aneurysm size among the 2.5, 5, and 10 mg/ml groups, we wanted to explore if these variations were driven by early-stage differences. Indeed, we found an immediate reduction in strain in all three elastase-treated groups compared to the heat-inactivated group. Moreover, quantification of elastin content suggested that the 5 and 10 mg/ml groups had significantly less elastin than the heat-inactivated group, while degradation of elastin in the 2.5 mg/ml group seemed to be more moderate and was not significantly different from either the heat-inactivated group or the 5 and 10 mg/ml groups. This suggests that even at these early stages, the various elastase concentrations cause differing amounts of elastin degradation, which over the course of 8 weeks, results in varying-sized aneurysms. By day 7, these results are more pronounced, demonstrating a graded effect of elastase concentration.

In addition to understanding the role of elastase concentration, we also studied the impacts of LOX inhibition after aneurysm formation. The importance of LOX in the cardiovascular system has become increasingly apparent.[40] In humans, a LOX missense mutation was discovered in a family with autosomal dominant thoracic aortic dissection.[41] Homozygous mice with the same mutation died of perineonatal aortic aneurysms and hemorrhaging.[41] Similarly, Guo et al. found specific rare variants of the LOX gene in humans with enlarged aortic root and ascending aortic dissections.[42] Further study in the smooth muscle cells of humans indicated that in those taken from human AAAs, LOX gene expression was higher, but the LOX functional activity was significantly reduced compared to healthy controls.[43] These all suggest the importance of LOX clinically. However, understanding its role in aneurysm progression is limited. For example, previous work in mice has only assessed the continual presence or absence of BAPN on AAA formation and growth.[9,10] Namely, the question remained: does the aneurysm ever become self-sustaining, whether that be due to hemodynamic, inflammatory, or other reasons? To address this question, we removed BAPN from the animals' drinking water after an aneurysm had formed by day 14, and noted a near complete stoppage in expansion (**Figure 3.5C**). These results suggest that the influence of hemodynamics and inflammation are secondary to the role of LOX inhibition on continued aneurysmal growth in this animal model.

This influence of BAPN works both ways. Removal of BAPN stabilizes the aneurysm while addition of BAPN can cause growth. In a second sub-experiment, we waited two weeks post-surgery to add BAPN to the water. We chose this time point because previous studies demonstrated that the elastase-only aneurysm stabilizes by day 14.[9] Similar to what was shown previously, there was steady growth between baseline and day 7, followed by minimal expansion from day 7 to 14, suggesting stability. However, after BAPN was added on day 14, the aneurysm began to grow rapidly again. These data demonstrate that LOX inhibition can cause aneurysm growth in previously stabilized AAAs. We do know that this result is not driven by BAPN-induced changes in blood pressure, as mice were normotensive (**Appendix A Figure 21**). Instead, we postulate that these effects of BAPN are driven, at least in part, by a reduction of ECM cross-linking[44] combined with residual inflammation from the elastase treatment.[10] It is also likely that the reduction of LOX by BAPN alters the inflammatory response[45] and impacts endothelial function,[40] both of which are also key contributors to vascular disease. Further work will be needed to assess the specific effects of BAPN and how effects lead to aneurysm growth observed in this study.

A last component of this study was to explore the effects of sex. Clinically, although men have a higher incidence of aneurysm formation, the rupture rate among women is greater than that of men.[46-49] Since these AAA formed by elastase administration which causes severe elastin degradation in all mice, we had hypothesized that both male and female mice would form similar large aneurysms. Both sexes did form large aneurysms; however, the female mice had significantly larger aneurysms than those of the males at the same timepoint, suggesting that there may be hormone-specific effects on aneurysmal growth.[50] While this likely does not fully explain the size discrepancies noted, further investigation would be necessary to provide additional mechanistic insight. Such an exploration is beyond the scope of the current study; even so, our results do suggest that there are sex-based differences in this model.

One clear difference of this murine model compared to human pathology is the observation that topical application of elastase caused rapid, severe, and heterogeneous degradation of elastin immediately post-surgery, as demonstrated both by the reduction of in vivo strain and by ex vivo histological analysis. This regional degradation is consistent with the topical (and therefore regional) administration of elastase. While these results were expected given the nature of the surgery, the abrupt change in elastin contrasts with the more gradual reduction that is likely to occur clinically. Clinically, reductions in strain can be indicative of decreased elastin content and increased collagen deposition, which occur during remodeling of the aneurysmal tissue and can result in a stiffer vessel.[51] Unfortunately, once elastin is degraded, it can rarely be recovered, though advances in tissue-engineered solutions may provide avenues that lead to functional elastin deposition and return strain to normal levels. In the current study, while we do observe the concomitant reduction in strain and decreased elastin content, it occurs much more rapidly than would be observed clinically. After the initial abrupt degradation, the vessel remodels and the elastin begin to degrade throughout the vessel, resulting in a disperse degradation at later time points, similar to what has been reported previously.[9,10] However, given this region-specific initial degradation, the BAPN+Elastase model may not be an optimal model for small AAAs or when studying short-term changes. Even so, the relative ease of the surgical procedure, presence of large infrarenal aneurysms, and development of ILT in this BAPN+Elastase model make this a particularly intriguing murine AAA model for future studies.

In conclusion, we demonstrated that elastase concentration and BAPN are able to modulate aneurysm development in this relatively new murine AAA model. Lower concentrations of

elastase result in smaller aneurysms, while higher concentrations tend to lead to larger aneurysms. However, this concentration-dependent effect plateaued above 5 mg/ml, with both the 5 and 10 mg/ml groups developing similar aneurysm sizes with ILT formation. In addition, we demonstrated that BAPN could be used to "start" and "stop" aneurysm growth. Thus, elastase concentration and BAPN can be used in tandem to create complex aneurysms that vary in size, growth rate, and presence of ILT. Future work will be needed to elucidate specific reasons for the differences observed, potentially through studies of inflammatory cells and markers,[52] other cell types such as smooth muscle cells and endothelial cells,[53,54] production and activation of proteases, and the remodeling of various ECM components such as collagen and glycosaminoglycans.[55] Further studies with the BAPN+Elastase model may eventually help in the development of new pharmacological treatments, characterization of the role played by ILT, and improvement in our understanding of how hemodynamics contributes to AAA expansion.

3.7   Author Contributions

A.G.B. and C.J.G. designed study; A.G.B, D.J.R., and K.E.K. performed experiments; A.G.B, D.J.R., K.E.K., N.E.G., M.M.W., and A.D.C. analyzed data; A.G.B., D.J.R. and C.J.G. interpreted results of experiments; A.G.B prepared figures; A.G.B. drafted manuscript; A.G.B., D.J.R., S.S.P., E.A.F., A.D.C., and C.J.G. edited and revised manuscript; all authors approved final version of manuscript.

3.8   Conflicts of Interest

C.J.G. serves on the scientific advisory board for FUJIFILM VisualSonics Inc. However, FUJIFILM VisualSonics Inc. had no role in the design, execution, interpretation, or writing of the study.

3.9   References

1.   Johnston KW, Rutherford RB, Tilson MD, Shah DM, Hollier L, Stanley JC. 1991. Suggested standards for reporting on arterial aneurysms. J. Vasc. Surg. 13:452-8

2.   Sakalihasan N, Michel J-B, Katsargyris A, Kuivaniemi H, Defraigne J-O, et al. 2018. Abdominal aortic aneurysms. Nature Reviews Disease Primers 4:34

3.   Harter LP, Gross BH, Callen PW, Barth RA. 1982. Ultrasonic evaluation of abdominal aortic thrombus. J. Ultrasound Med. 1:315-8

4.   Piechota-Polanczyk A, Jozkowicz A, Nowak W, Eilenberg W, Neumayer C, et al. 2015. The abdominal aortic aneurysm and intraluminal thrombus: current concepts of development and treatment. Frontiers in cardiovascular medicine 2:19

5.   Poulsen JL, Stubbe J, Lindholt J. 2016. Animal models used to explore abdominal aortic aneurysms: a systematic review. Eur. J. Vasc. Endovasc. Surg. 52:487-99

6.   Anidjar S, Salzmann JL, Gentric D, Lagneau P, Camilleri JP, Michel JB. 1990. Elastase-induced experimental aneurysms in rats. Circ. 82:973-81

7.   Pyo R, Lee JK, Shipley JM, Curci JA, Mao D, et al. 2000. Targeted gene disruption of matrix metalloproteinase-9 (gelatinase B) suppresses development of experimental abdominal aortic aneurysms. J. Clin. Invest. 105:1641-9

8.   Bhamidipati CM, Mehta GS, Lu G, Moehle CW, Barbery C, et al. 2012. Development of a novel murine model of aortic aneurysms using peri-adventitial elastase. Surg. 152:238-46

9.   Romary DJ, Berman AG, Goergen CJ. 2019. High-frequency murine ultrasound provides enhanced metrics of BAPN-induced AAA growth. Am. J. of Physiol.-Heart and Circ. Physiol. 317:H981-H90

10.   Lu G, Su G, Davis JP, Schaheen B, Downs E, et al. 2017. A novel chronic advanced stage abdominal aortic aneurysm murine model. J. Vasc. Surg. 66:232-42. e4

11.   Kagan HM, Li W. 2003. Lysyl oxidase: properties, specificity, and biological roles inside and outside of the cell. J. Cell. Biochem. 88:660-72

12. Anderson JL, Niedert EE, Patnaik SS, Tang R, Holloway RL, et al. 2021. Animal Model Dependent Response to Pentagalloyl Glucose in Murine Abdominal Aortic Injury. J. Clin. Med. 10:219

13. Adelsperger AR, Phillips EH, Ibriga HS, Craig BA, Green LA, et al. 2018. Development and growth trends in angiotensin II-induced murine dissecting abdominal aortic aneurysms. Physiol. Rep. 6:e13668

14. Phillips EH, Chang MS, Gorman S, Qureshi HJ, Ejendal KFK, et al. 2018. Angiotensin II Infusion Does Not Cause Abdominal Aortic Aneurysms in Apolipoprotein E-Deficient Rats. J. Vasc. Res. 55:1-12

15. Goergen CJ, Azuma J, Barr KN, Magdefessel L, Kallop DY, et al. 2011. Influences of aortic motion and curvature on vessel expansion in murine experimental aneurysms. Arterioscler. Thromb. Vasc. Biol. 31:270-9

16. Updegrove A, Wilson NM, Merkow J, Lan H, Marsden AL, Shadden SC. 2017. SimVascular: An Open Source Pipeline for Cardiovascular Simulation. Ann. Biomed. Eng. 45:525-41

17. Schneider CA, Rasband WS, Eliceiri KW. 2012. NIH Image to ImageJ: 25 years of image analysis. Nat. Methods 9:671-5

18. Daugherty A, Cassis LA. 2004. Mouse models of abdominal aortic aneurysms. Arterioscler Thromb Vasc Biol 24:429-34

19. Daugherty A, Manning MW, Cassis LA. 2000. Angiotensin II promotes atherosclerotic lesions and aneurysms in apolipoprotein E–deficient mice. J. Clin. Invest. 105:1605-12

20. Trachet B, Fraga-Silva RA, Jacquet PA, Stergiopulos N, Segers P. 2015. Incidence, severity, mortality, and confounding factors for dissecting AAA detection in angiotensin II-infused mice: a meta-analysis. Cardiovasc. Res. 108:159-70

21. Trachet B, Aslanidou L, Piersigilli A, Fraga-Silva RA, Sordet-Dessimoz J, et al. 2017. Angiotensin II infusion into ApoE-/-mice: a model for aortic dissection rather than abdominal aortic aneurysm? Cardiovasc. Res. 113:1230-42

22. Chiou AC, Chiu B, Pearce WH. 2001. Murine Aortic Aneurysm Produced by Periarterial Application of Calcium Chloride. J. Surg. Res. 99:371-6

23. Wang Y, Krishna S, Golledge J. 2013. The calcium chloride-induced rodent model of abdominal aortic aneurysm. Atheroscler. 226:29-39

24. Ren W, Liu Y, Wang X, Jia L, Piao C, et al. 2016. β-Aminopropionitrile monofumarate induces thoracic aortic dissection in C57BL/6 mice. Sci. Rep. 6:1-7

25. Kurihara T, Shimizu-Hirota R, Shimoda M, Adachi T, Shimizu H, et al. 2012. Neutrophil-derived matrix metalloproteinase 9 triggers acute aortic dissection. Circ. 126:3070-80

26. Kanematsu Y, Kanematsu M, Kurihara C, Tsou T-L, Nuki Y, et al. 2010. Pharmacologically induced thoracic and abdominal aortic aneurysms in mice. Hypertension 55:1267-74

27. Kurobe H, Matsuoka Y, Hirata Y, Sugasawa N, Maxfield MW, et al. 2013. Azelnidipine suppresses the progression of aortic aneurysm in wild mice model through anti-inflammatory effects. J. Thorac. Cardiovasc. Surg. 146:1501-8

28. Fashandi AZ, Hawkins RB, Salmon MD, Spinosa MD, Montgomery WG, et al. 2018. A novel reproducible model of aortic aneurysm rupture. Surg. 163:397-403

29. Darling RC, Messina CR, Brewster DC, Ottinger LW. 1977. Autopsy study of unoperated abdominal aortic aneurysms. The case for early resection. Circ. 56:II161-4

30. Gharahi H, Zambrano BA, Lim C, Choi J, Lee W, Baek S. 2015. On growth measurements of abdominal aortic aneurysms using maximally inscribed spheres. Med. Eng. Phys. 37:683-91

31. Martufi G, Lindquist Liljeqvist M, Sakalihasan N, Panuccio G, Hultgren R, et al. 2016. Local diameter, wall stress, and thrombus thickness influence the local growth of abdominal aortic aneurysms. J. Endovasc. Ther. 23:957-66

32. Weiss D, Latorre M, Rego BV, Cavinato C, Tanski BJ, Berman AG, et al. 2021. Biomechanical consequences of compromised elastic fiber integrity and matrix cross-linking on abdominal aortic aneurysmal enlargement. Acta Biomaterialia.

33. Biasetti J, Gasser TC, Auer M, Hedin U, Labruto F. 2010. Hemodynamics of the normal aorta compared to fusiform and saccular abdominal aortic aneurysms with emphasis on a potential thrombus formation mechanism. Ann. Biomed. Eng. 38:380-90

34. Biasetti J, Spazzini PG, Swedenborg J, Gasser TC. 2012. An integrated fluid-chemical model toward modeling the formation of intra-luminal thrombus in abdominal aortic aneurysms. Front. Physiol. 3:266

35. Di Achille P, Tellides G, Figueroa C, Humphrey J. A haemodynamic predictor of intraluminal thrombus formation in abdominal aortic aneurysms. Proc. Proc. R. Soc. A, 2014, 470:20140163: The Royal Society

36. Pappu S, Dardik A, Tagare H, Gusberg RJ. 2008. Beyond fusiform and saccular: a novel quantitative tortuosity index may help classify aneurysm shape and predict aneurysm rupture potential. Ann. Vasc. Surg. 22:88-97

37. Fillinger MF, Racusin J, Baker RK, Cronenwett JL, Teutelink A, et al. 2004. Anatomic characteristics of ruptured abdominal aortic aneurysm on conventional CT scans: implications for rupture risk. J. Vasc. Surg. 39:1243-52

38. Wyss TR, Dick F, Brown LC, Greenhalgh RM. 2011. The influence of thrombus, calcification, angulation, and tortuosity of attachment sites on the time to the first graft-related complication after endovascular aneurysm repair. J. Vasc. Surg. 54:965-71

39. Goergen CJ, Barr KN, Huynh DT, Eastham-Anderson JR, Choi G, et al. 2010. In Vivo Quantification of Murine Aortic Cyclic Strain, Motion, and Curvature: Implications for Abdominal Aortic Aneurysm Growth. J. Magn. Reson. Imaging 32:847-58

40. Rodríguez C, Martínez-González J, Raposo B, Alcudia JF, Guadall A, Badimon L. 2008. Regulation of lysyl oxidase in vascular cells: lysyl oxidase as a new player in cardiovascular diseases. Cardiovasc. Res. 79:7-13

41. Lee VS, Halabi CM, Hoffman EP, Carmichael N, Leshchiner I, et al. 2016. Loss of function mutation in LOX causes thoracic aortic aneurysm and dissection in humans. Proc. Natl. Acad. Sci. 113:8759-64

42. Guo D-c, Regalado ES, Gong L, Duan X, Santos-Cortez RLP, et al. 2016. LOX mutations predispose to thoracic aortic aneurysms and dissections. Circ. Res. 118:928-34

43. Farrell K, Simmers P, Mahajan G, Boytard L, Camardo A, et al. 2019. Alterations in phenotype and gene expression of adult human aneurysmal smooth muscle cells by exogenous nitric oxide. Exp. Cell Res. 384:111589

44. Brüel A, Ørtoft G, Oxlund H. 1998. Inhibition of cross-links in collagen is associated with reduced stiffness of the aorta in young rats. Atheroscler. 140:135-45

45. Onoda M, Yoshimura K, Aoki H, Ikeda Y, Morikage N, et al. 2010. Lysyl oxidase resolves inflammation by reducing monocyte chemoattractant protein-1 in abdominal aortic aneurysm. Atheroscler. 208:366-9

46. Singh K, Bønaa KH, Jacobsen BK, Bjørk L, Solberg S. 2001. Prevalence of and Risk Factors for Abdominal Aortic Aneurysms in a Population-based Study : The Tromsø Study. Am. J. Epidemiol. 154:236-44

47. Vardulaki K, Walker N, Day N, Duffy S, Ashton H, Scott R. 2000. Quantifying the risks of hypertension, age, sex and smoking in patients with abdominal aortic aneurysm. Br. J. Surg. 87:195-200

48. Brown LC, Powell JT. 1999. Risk factors for aneurysm rupture in patients kept under ultrasound surveillance. UK Small Aneurysm Trial Participants. Ann. Surg. 230:289-96; discussion 96-7

49. Brown PM, Zelt DT, Sobolev B. 2003. The risk of rupture in untreated aneurysms: the impact of size, gender, and expansion rate. J. Vasc. Surg. 37:280-4

50. Okuyama M, Jiang W, Javidan A, Chen JZ, Howatt DA, et al. 2020. Lysyl Oxidase Inhibition Ablates Sexual Dimorphism of Abdominal Aortic Aneurysm Formation in Mice. Circ. 142:1993-5

51. Wilson K, Bradbury A, Whyman M, Hoskins P, Lee A, et al. 1998. Relationship between abdominal aortic aneurysm wall compliance and clinical outcome: a preliminary analysis. Eur. J. Vasc. Endovasc. Surg. 15:472-7

52. Shah PK. 1997. Inflammation, metalloproteinases, and increased proteolysis: an emerging pathophysiological paradigm in aortic aneurysm. Circ. 96(7):2115-7.

53. Henderson EL, Geng Y-J, Sukhova GK, Whittemore AD, Knox J, Libby P. 1999. Death of Smooth Muscle Cells and Expression of Mediators of Apoptosis by T Lymphocytes in Human Abdominal Aortic Aneurysms. Circ. 99(1):96-104. doi:doi:10.1161/01.CIR.99.1.96.

54. Sun J, Deng H, Zhou Z, Xiong X, Gao L. 2018. Endothelium as a potential target for treatment of abdominal aortic aneurysm. Oxid Med Cell Longev.

55. Didangelos A, Yin X, Mandal K, Saje A, Smith A, Xu Q, et al. 2011. Extracellular matrix composition and remodeling in human abdominal aortic aneurysms: a proteomics approach. Mol Cell Proteomics. 10(8):M111. 008128.

4. ULTRASOUND IMAGING OF *IN VIVO* VASCULAR GRAFT REMODELING

The previous chapter utilized ultrasound imaging to assess aneurysmal disease progression in a novel murine model. Here, we continue our exploration of tissue remodeling in the vascular system, but instead of investigating disease, we shift our focus to the remodeling that occurs after repair. We do this by implanting small-diameter tissue-engineered vascular grafts within the infrarenal aorta of mice and longitudinally assessing its growth with ultrasound. Our primary goal was to assess how varying the braiding parameters of tissue engineered grafts altered the remodeling response. At the end of the study, histology and mechanics were used to further assess the grafts. This work was done in collaboration with Dr. Christopher Breuer's lab (graft design, implantation, and histology) and Dr. Jay Humphrey's lab (mechanics).

4.1 Abstract

We developed tissue engineered vascular grafts (TEVGs) using scaffolds fabricated from braided poly(glycolic acid) (PGA) fibers coated with poly(glycerol sebacate) (PGS). Our approach relies on *in vivo* tissue engineering by which neotissue forms solely within the body after a scaffold has been implanted. Herein, we investigate the impact of altering scaffold braid design and scaffold coating on neotissue formation. Several combinations of braiding parameters were manufactured and evaluated in a Beige mouse model in the infrarenal abdominal aorta (IAA). Animals were followed with 4D ultrasound analysis, and 12-week explanted vessels were evaluated for biaxial mechanical properties as well as histological composition. Results show that scaffold parameters (i.e., braiding angle, braiding density, and presence of a PGS coating) have interdependent effects on the resulting graft performance, namely, alteration of these parameters influences levels of inflammation, extracellular matrix production, graft dilation, neovessel distensibility and overall survival. Coupling carefully designed *in vivo* experimentation with regression analysis, we uncovered critical relationships between the scaffold design and the resulting neotissue that enable

induction of favorable cellular and extracellular composition in a controlled manner. Such an approach provides a potential for fabricating scaffolds with a broad range of features and the potential to manufacture optimized TEVGs.

4.2 Introduction

There is a pressing clinical need for improved vascular conduits, particularly small caliber arterial grafts. Coronary and peripheral bypass procedures commonly utilize autologous vascular grafts, which have demonstrated 10-year patencies of 60-90% depending on the procedure and the vessel used.[1-3] However, about one-third of patients lack suitable autologous vessels due to pre-existing conditions or previous operations.[4,5] Tissue engineered vascular grafts (TEVGs) offer a unique solution, allowing fabrication of off-the-shelf vascular conduits that can develop into functional blood vessels within the body.[6,7] While several TEVGs have been translated to the clinic, performance has been mixed and design improvements have largely been based on empiricism rather than rational design, thus hindering clinical development.[7,8] An ideal TEVG needs to be readily available, easily implantable, biocompatible, resistant to thrombosis, stenosis and dilation, as well as capable of developing into a living functional neovessel.[9,10] These factors depend heavily on both the scaffold materials used and the manufacturing method.

Poly(glycerol sebacate) (PGS), also known as "biorubber," is the first biodegradable polymer designed specifically for fabricating TEVGs.[11] It is biocompatible, nonthrombogenic, and highly elastic, which is ideal for an artificial arterial conduit.[11] It also demonstrates a sufficient degradation profile to allow adequate time for neotissue formation without remaining so long as to cause a longstanding foreign body reaction; it undergoes complete degradation *in vivo* within approximately 6 weeks.[12] Despite the broad range of potential applications and scientific interest towards PGS, its difficulties in manufacturing and handling have hindered its entry to the clinic.[13] By contrast, poly(glycolic acid) (PGA) is a long-used biomaterial, particularly in TEVGs, which degrades within 12 weeks *in vivo*, though with loss of mechanical integrity occurring between 4 and 8 weeks.[14-16] Novel scaffolds can easily be envisioned that combine the advantages of each of these important biomaterials, but the question is, how best to design new scaffolds?

Computational modeling has shown promise for accelerating the optimization process of vascular grafts by determining potential mechanisms of neotissue formation and effects of altering scaffold parameters.[17,18] Recent models informed by experimental data have suggested that *in vivo*

neovessel formation is an inflammation-driven, mechano-mediated process.[15] Therefore, altering the design of the scaffold provides a two-fold means for optimizing *in vivo* performance. More specifically, the chemical, mechanical, and morphometric properties of a scaffold can be changed to modulate the degree of induced inflammation, with particularly critical properties including polymer chemistry, fiber size and alignment, pore size, porosity, and degradation rate.[19] The evolving mechanical properties are especially important as they can dictate the degree of stress shielding of cells within the developing neotissue, thus affecting mechanobiologically mediated extracellular matrix production, remodeling, and degradation.[20] Importantly, factors that define the inflammatory status and mechanical properties of a scaffold are strongly coupled, making selection of individual parameters more challenging and the creation of an optimized design elusive. Successful neovessel formation requires neotissue development to balance scaffold degradation. Lack of coordination between these processes can lead to pathologic remodeling or graft failure.

While computational modeling offers a potential way to predict optimal scaffold parameters, improvements in fabrication methods with a high degree of control and replication will similarly be necessary to realize optimal designs.[17,21] Textile manufacturing offers a well-established method for producing scaffolds from a broad array of biodegradable polymers that can be fabricated with a wide range of mechanical properties. Textile manufacturing allows certain degrees of decoupling of the chemical and mechanical properties of the scaffold, enabling a wide range of mechanical properties using the same polymer yarn. Braiding, in particular, offers a tunable platform for fabricating scaffolds, allowing precise selection of complex anisotropic mechanical profiles.[9] Increasing the braid angle relative to the axial direction increases the circumferential stiffness of the scaffold, while decreasing the axial stiffness. Picks per square inch (PPSI) and number of ends together determine the void space within the braid with increases of either parameter decreasing void space therefore increasing the bulk stiffness of the graft. Braiding also allows tissue-level mechanical properties to be decoupled from those at the cellular level by utilizing identical polymer fibers woven in different arrangements. In this study, we investigate braiding as a method for producing PGA scaffolds having different immunogenic and mechanical properties. These scaffolds were manufactured with and without PGS coating. Scaffolds were evaluated in a Beige mouse model and implanted in the infrarenal abdominal aorta (IAA). By selecting scaffold designs that represent current bounds of what is manufacturable/testable, we

demonstrate that, for the same polymer chemistry, differences in initial physical/mechanical properties can alter neotissue formation as well as graft performance. Such data will prove critical in informing the next computational models for accelerating design.

4.3 Materials and Methods

4.3.1 Graft Fabrication

Scaffold Braiding

Scaffolds were braided on a mandrel with an outer diameter of 0.66 mm by a 48-carrier braider (Steeger USA; Inman, SC) using 45 denier, 20 filament PGA yarn (Riverpoint Medical; Portland, OR). All scaffold designs were fabricated using a 1-ply design and a 0.3 mm tension spring setting and were scoured in 99% isopropyl alcohol at ambient temperature for 15 minutes. The 1x1 and 2x2 designs were heat set for 1.5 hours at 180°C and 1 hour at 130°C, respectively.

Poly(glycerol sebacate) Coating and Curing

PGS coating solutions were made by mixing 23 g of molten PGS (Regenerez® Secant Group, LLC; Telford, PA) with 77 g of ethyl acetate (Sigma 319902) in an 8 oz polypropylene jar (Uline; Pleasant Prairie, WI) using a stir bar and stir plate set to 500 RPM for 2 hours. The homogenous PGS coating solution was transferred to a 50 mL graduated cylinder and positioned under the arm of the Single Vessel dip coater (KSV NIMA; Gothenburg, Sweden). Approximately 20 cm lengths of each design were cut from their mandrels and fastened to the dip coating arm. Two rounds of dip coating in the PGS polymer solution were performed for the coated graft cohorts, with a 15-minute drying period between rounds. Grafts were cured in a vacuum oven (JEIO TECH OV-12) at 120°C and 10 torr for 18 hours. All grafts were sterilized by gamma irradiation (18-29 kGy dosage).

4.3.2 Scanning Electron Microscopy

Scaffold samples were prepped for scanning electron microscopy by mounting with carbon tape. Samples were then imaged under low vacuum using JEOL JSM 1060LA Scanning Electron Microscope under 10kV, a spot size of 60%, and a working distance of 10 mm

4.3.3 Implantation

All animal experiments were approved by the Nationwide Children's Hospital and Purdue University Institutional Animal Care and Use Committee all animals received humane care in compliance with the National Institutes of Health (NIH) Guide for the Care and Use of Laboratory Animals (NIH, Bethesda, MD, USA). Beige mice (C57BL/6J-Lystbg-J/J; The Jackson Laboratory, Bar Harbor, ME, USA) between 8-12 weeks of age, were used for surgery (n=10-15 per group). Scaffolds 3 mm long were implanted as IAA interposition grafts using standard microsurgical technique facilitated by an operating microscope with zoom magnification.[22] Briefly, a midline laparotomy incision was made from below the xyphoid to the suprapubic region, and a self-retaining retractor inserted. The intestines were wrapped in sterile saline-moistened gauze and retracted. The aorta was separated from the inferior vena cava and vascular control was obtained with microvascular clamps. The IAA was transected. Scaffolds were implanted, anastomosed proximally and distally with 10-0 polypropylene running suture. The skin was then closed in two layers by using a 6-0 black polyamide monofilament suture, and animals were moved to a recovery cage with a warming pad until becoming fully ambulatory.

4.3.4 Ultrasound Analysis

Mice (n=2-4 per group based on surgical survival) were imaged using high frequency ultrasound (Vevo3100; FUJIFILM VisualSonics Inc., Toronto, ON, Canada) before surgery, as well as 1, 2, 4, 6, 8, 10, and 12 weeks post-implantation. During imaging, mice were anesthetized with 1-3% isoflurane and placed supine on a heated stage. Hair was removed from the abdominal region using chemical depilatory cream (Nair, Church & Dwight, Ewing, NJ). A 22-55 MHz frequency linear transducer was used to acquire long- and short-axis brightness (B-) mode, motion (M-) mode, and ECG-gated Kilohertz Visualization images of the IAA at locations proximal, mid, and distal to the graft (MS550D, FUJIFILM VisualSonics). Additionally, a linear step motor was

used to collect sequential 2D short-axis images to create 3D datasets. The luminal and adventitial boundaries were segmented manually from the volumetric image data using the open source code SimVascular to create 3D representations of the grafts.[23] The segmentations were then imported into MATLAB (MathWorks, Natick, MA) to calculate the effective diameter at each z-slice location along the graft. In addition, thickness was determined from 2D short-axis images at the mid-graft location (VevoLAB, FUJIFILM VisualSonics). We calculated circumferential Green-Lagrange strain using the M-mode images by measuring systolic and diastolic diameters in triplicate.[24]

4.3.5 Blood Pressure Measurements

Blood pressure was measured at baseline before implantation, and again at 4, 8, and 12 weeks post-implantation using a CODA 2 Channel Standard Blood Pressure System (Kent Scientific, Torrington, CT). For each mouse (n=2-4 per group), at least 10 replicate measurements of systolic, diastolic, and mean arterial pressure were averaged per timepoint.

4.3.6 MMP Activity

To measure general MMP activity, 100µL of MMPSenseTM 680 (PerkinElmer, Waltham, MA) was injected via tail vein approximately 24 hours prior to euthanasia. After euthanasia, the graft and aorta were placed under near infrared light (625 nm excitation; 700 nm emission) to obtain fluorescent images from both the dorsal and ventral sides (4000mm Digital Imaging Station, Kodak). Using a custom MATLAB script, the intensity ratio for each image was calculated as the ratio of signal intensity in the graft relative to that of the healthy aorta.[25] Dorsal and ventral regions were averaged to give a single value per mouse (n=2-4 per group).

4.3.7 Biaxial Mechanical Testing

The entire IAA, including the graft, was explanted and stored in Hanks Balanced Salt Solution at 4°C until mechanical testing, performed within 72 hours of harvest. These composite vessels (n=2-4 per group), were cannulated and secured to paired glass pipettes using 6-0 suture.[26] The mounted vessels were placed in a custom computer-controlled biaxial testing system in Hanks Balanced Salt Solution and the unloaded dimensions (length and outer diameter) were recorded at

10 mmHg.[27] The preconditioning protocol is similar to that for the native IAA and included equilibration at 90 mmHg with low intraluminal flow at *in vivo* stretch for 15 mins, followed by pressurization from 10-140 mmHg for 4 cycles.[28] The unloaded dimensions of the vessels were measured again after preconditioning and the *in vivo* stretch of the composite vessels were estimated by identifying the axial stretch at which axial force was nearly constant in response to a change in pressure. The protocol for pressure-distension tests similarly involved cyclic pressurization of the vessels from 10-140 mmHg at a constant vessel-specific *in vivo* stretch, while the protocol for axial force-extension tests involved loading from 0 to 25 mN axial force at a fixed pressure. Distensibility calculations are based on external diameter measurements. Force and pressure were measured using standard transducers; axial stretch was controlled using a sub-micron resolution stepper motor, and diameter was tracked using a video-camera and custom software. Native IAAs of similar length from 20-week-old Beige mice were used for the control group.

4.3.8   Histology & Immunohistochemistry

Following either MMP-Sense or mechanical testing, grafts were segmented into transverse sections and samples were fixed in 10% formalin and paraffin-embedded. Sections 4 µm thick were stained using standard techniques. Hart's elastin stain was used to evaluate elastin density and thickness, Picro-Sirius Red was used to assess collagen density, and von Kossa and Alizarin Red were used to detect calcification, if any (n=4-13 per group, based on surgical survival).

For immunohistochemistry, tissue sections were deparaffinized, rehydrated, and blocked for endogenous peroxidase activity and non-specific protein adsorption prior to staining. Primary antibodies and associated concentrations were calponin (Abcam 203047, 1:100) and CD68 (Abcam 125212, 1:2000). Slides were stained with appropriate secondary antibodies at a concentration of 1:1500 followed by incubation in streptavidin horseradish peroxidase (Vector). Color development was performed with 3,3-diaminobenzidine (Vector) and tissue was counterstained with Gill's hematoxylin. Photomicrographs were acquired with a Zeiss AxioObserver.Z1 inverted microscope with a 20x objective and captured with a Zeiss Axiocam 105 (color) digital camera.

Image analysis was performed using ImageJ (National Institute of Health, MD, USA).[29,30] Images from two different segments of each graft were analyzed and averaged. Quantification

evaluated elastin layer thickness, elastin density, collagen density, calponin positive area fraction, and CD68 positive area fraction. Area measurements were obtained by pixel-specific thresholding based on specific values of hue, saturation, and brightness as well as size. The reported densities or area fractions correspond to the number of positively defined pixels over the total number of pixels in the vessel region.

4.3.9   Statistical Analysis

Results are presented as mean values ± standard deviations. Ultrasound data were analyzed using a repeated measures two-way ANOVA (main effects of graft and time) with a post-hoc Dunnett's test. For other data, statistical significance among groups was determined using ANOVA with post-hoc Dunnett's or Sidak's tests for multiple comparisons based the standard deviation of the data. We considered $p \leq 0.05$ to be statistically significant. Statistical analyses were performed with GraphPad Prism 8.0 (GraphPad Software, CA, USA).

Regressions were performed using STATA statistical software. Multiple linear regressions were performed for each histological analysis as well as for explanted vessel distensibility. Independent variables defining the scaffold designs were PPSI, Braiding Angle, and Presence of PGS coating (as a Boolean variable). Again, a $p \leq 0.05$ was used as a level of significance for each regression term. Logistic regression was used for each of the 5 implanted designs to determine the effect of scaffold parameters on survival. Independent variables were type of braid (2x2 vs 1x1), PPSI, braiding angle, and presence of PGS coating. Number of ends and mass/inch were initially included as independent variables but were determined to be covariate and subsequently removed from the analysis.

4.4   Results

4.4.1   Scaffold Fabrication

Parameters of each graft design are listed in **Table 4.1**. Braiding parameters included braiding angle, number of ends, and PPSI. Braiding angle is defined as the angle between the clockwise and counterclockwise fiber bundles, and the number of ends is the total number of fiber bundles used to create the braid. PPSI refers to the number of cross overs seen in a given surface area of the braid. 1x1 and 2x2 refer to the braiding style used, where a 1x1 braid has 1 clockwise

bundle crossing over a single counterclockwise bundle, and a 2x2 has 2 clockwise bundles crossing over 2 counterclockwise bundles. **Figure 4.1** provides an overview with representative scanning electron microscope (SEM) images of each scaffold design, gross images of a TEVG at implantation and explantation, and a timeline of measurements and testing.

Table 4.1. Manufacturing parameters for the braided TEVGs

Design	Braid Pattern	Number of Ends	Picks per Square Inch [PPSI]	Braiding Angle	Mass per Inch [mg]
1	1 x 1	24	19110	83	4.1
2	1 x 1	24	7350	38	3.2
3	1 x 1	12	7350	107	2.6
4	2 x 2	24	29400	107	5.1
5	2 x 2	32	13230	38	4.3
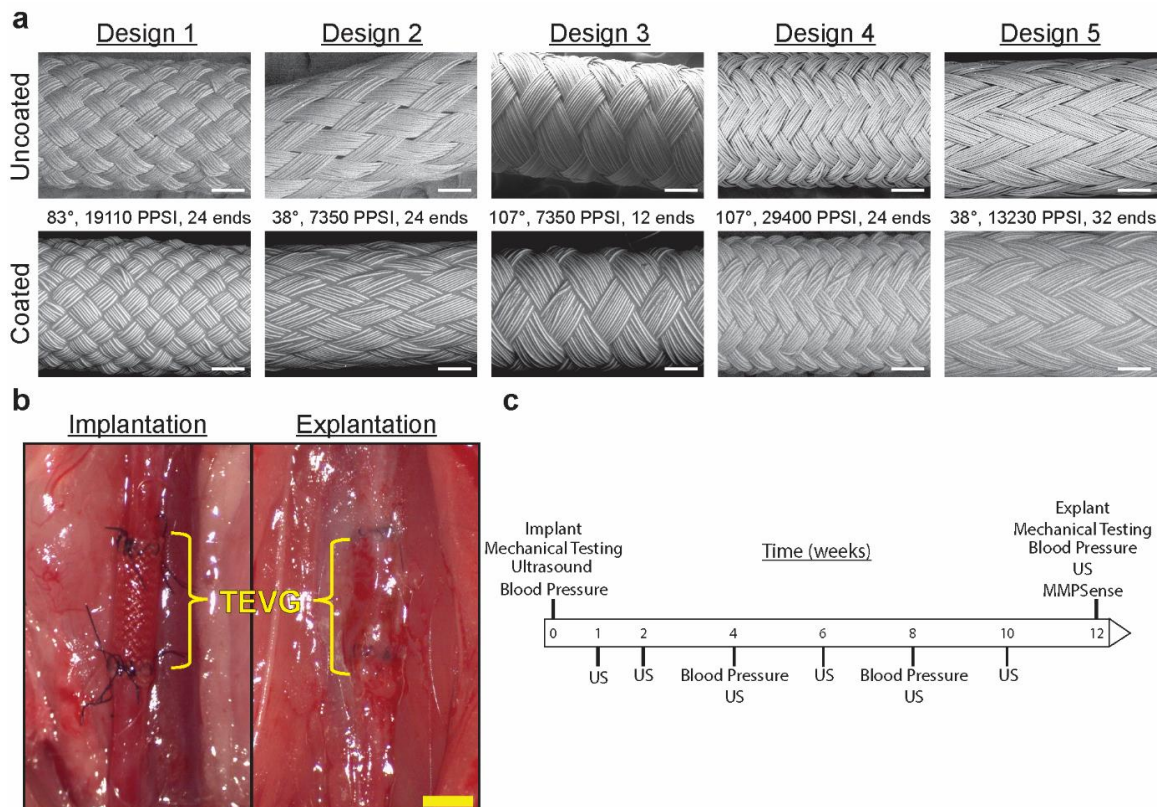
Figure 4.1. A) Representative SEM images of the five graft designs with the listed braiding parameters showing both PGS coated and uncoated cohorts. White scale bar = 200 µm. B) Images of the braided TEVG upon implantation in the infrarenal aorta and 12 weeks later upon explantation. Yellow scale bar = 2 mm. c) Experimental timeline.

4.4.2 Survival

The mechanism of failure differed across the different scaffold designs (**Table 4.2**). Within the 1x1 braiding designs, scaffolds with low PPSI, which results in looser braids, demonstrated higher rates of early death from surgical bleeding and early ruptures, often within the first week. The Design 1 cohorts, which have a denser braid (i.e., high PPSI), had only one bleeding death in each group, and no early ruptures. However, the uncoated Design 1 group had two mice die from a later rupture, at 28- and 46-days post-implantation. Due to the different incidences of graft failure modes, 12-week survival ranged from 29% to 93% depending on design, with the coated dense braid of Design 1 performing the best. There were no deaths in any group between 7 and 26 days (**Appendix B Figure 1**). At explant, all surviving animals demonstrated patent lumens with no evidence of thrombosis.

Table 4.2. Summary of the total number of implants performed and associated morbidity and mortality. Base scaffolds were PGA; coating was with PGS. * Implants of 2x2 designs were limited due to mortality events associated with the looseness of the braid.

Design	Coated [Y/N]	Number Implanted	Bleeding Deaths	Early Ruptures [≤1 Week]	Late Ruptures [>3 Weeks]	Survival at 12 Weeks
1	Y	14	1	0	0	93%
	N	14	1	0	2	79%
2	Y	14	3	3	0	57%
	N	15	3	2	0	67%
3	Y	14	6	4	0	29%
	N	15	5	3	0	47%
4*	Y	10	1	0	4	50%
	N	10	3	0	3	40%
5*	Y	10	1	7	0	20%
	N	0	-	-	-	-

Designs 4 and 5 were manufactured using a 2x2 braiding pattern, and 10 mice per cohort were initially implanted. Surgical deaths from anastomotic bleeding ranged from 1-3 animals per group (**Table 4.2**). The Design 4 cohort did not experience early rupture, but four coated and three uncoated grafts experienced aneurysmal dilation and rupture between days 27 and 38. With the

Design 5 cohort, 7 of 9 animals died due to bleeding through the graft within the first week. Due to the high mortality in this group, the uncoated version was not implanted. The high failure rates, and differential modes of failure, suggested a need for a tighter braid to prevent early bleeding and provide more structural support during degradation. As such, only the 1x1 braided designs were used for the remainder of the studies.

4.4.3   Serial Ultrasound & Blood Pressure Monitoring

Ultrasound analysis detected a rapid increase in diameter between weeks 4 and 8, with diameters remaining steady beyond 8 weeks (**Figure 4.2**). Design 2 grafts demonstrated earlier dilation than the other designs, possibly due to its looser, smaller angle braid. Representative 3D models for all graft designs can be seen in **Appendix B Figure 2**. All grafts demonstrated low compliance in comparison to baseline measurements of the native aorta. Compliance remained low over time, even following degradation of the scaffold (**Figure 4.3**). Proximal and distal anastomotic changes were minimal (**Appendix B Figure 3**). Blood pressure monitoring, performed on the ultrasound analysis cohorts, demonstrated no differences in blood pressure across groups or over time (**Appendix B Figure 4**).

4.4.4   MMP Activity and Inflammation

General matrix metalloproteinase (MMP) analysis, using an MMP-activatable fluorescent probe, demonstrated low signal in the grafts at 12 weeks (**Figure 4.4A**), with results similar across groups (**Figure 4.4B**). Inflammation was assessed by cluster of differentiation 68 (CD68) antibody staining (**Figure 4.4C**), a pan-macrophage marker. The effect of coating was found to be significant ($p = 0.0098$) on fractional area of CD68 staining, while direct statistical comparisons between groups were not significant. With the exception of the Design 3 coated and uncoated cohorts, all groups had significantly higher expression of CD68 compared to that the native aorta (**Figure 4.4D**).
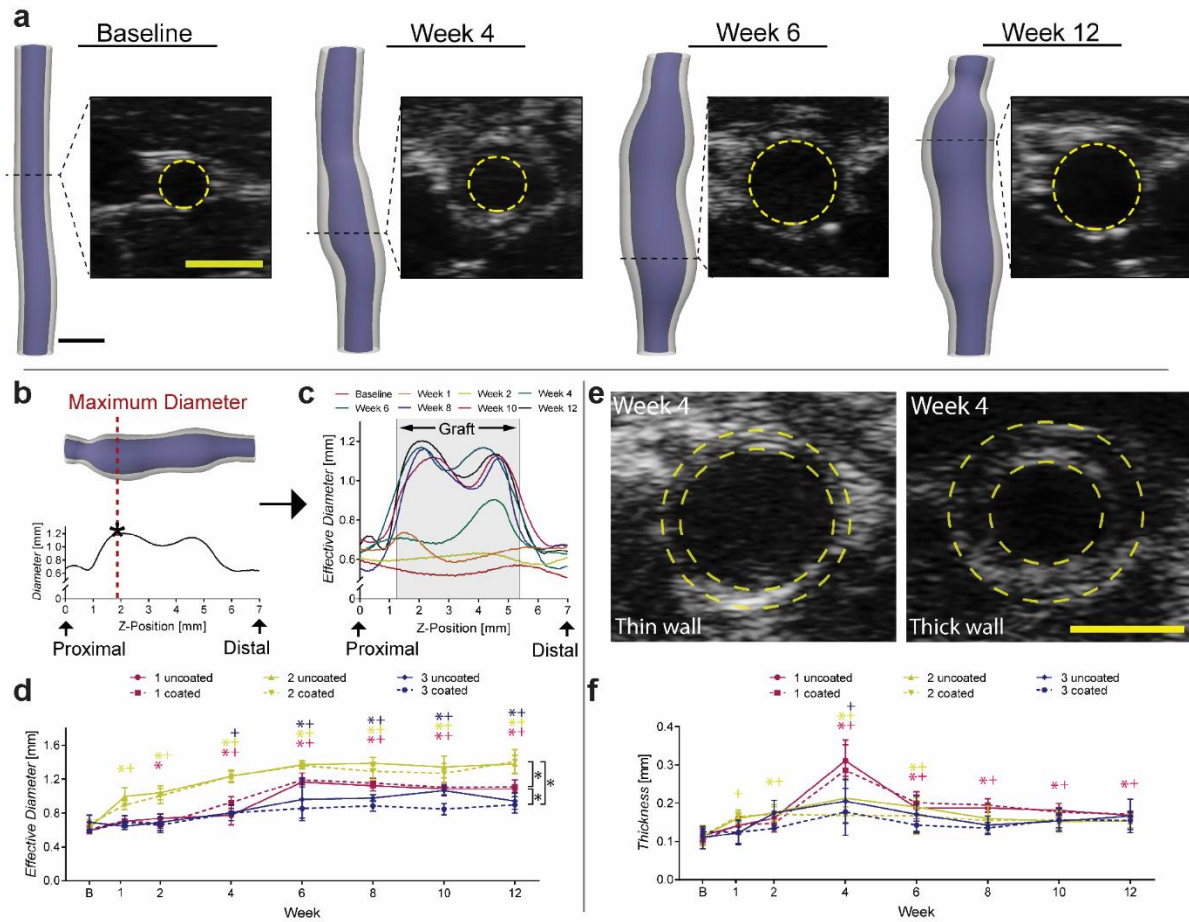
Figure 4.2. Ultrasound analysis of diameter and thickness. A) Representative segmentations were developed from 3D ultrasound images and highlight graft remodeling over time. This particular progression was for a mouse with a Design 1 coated graft. B) Segmentations were then used to calculate effective lumen diameter at every z-slice of the graft, and C) for each time point. D) Maximum lumen diameter varied per group, with Design 2 showing an early increase, while Design 1 had an abrupt increase between weeks 4 and 6. Design 3 had the smallest diameter at the end of study. E) In addition, representative ultrasound images show the difference between thin-walled (Design 2) and thick-walled (Design 1) grafts, as was quantified in (F). Dashed lines demarcate the luminal and abluminal boundaries of the graft and are shown for illustrative purposes. Actual measurements were performed in VevoLAB and SimVascular. An '*' refers to uncoated and a '+' refers to coated, with the color indicating the appropriate group ($p < 0.05$). All comparisons are relative to baseline. $n = 2$-4 per group. Data were compared using two-way ANOVA (main effects of graft and time) with a post-hoc Dunnett's test. Scale bars = 1 mm.
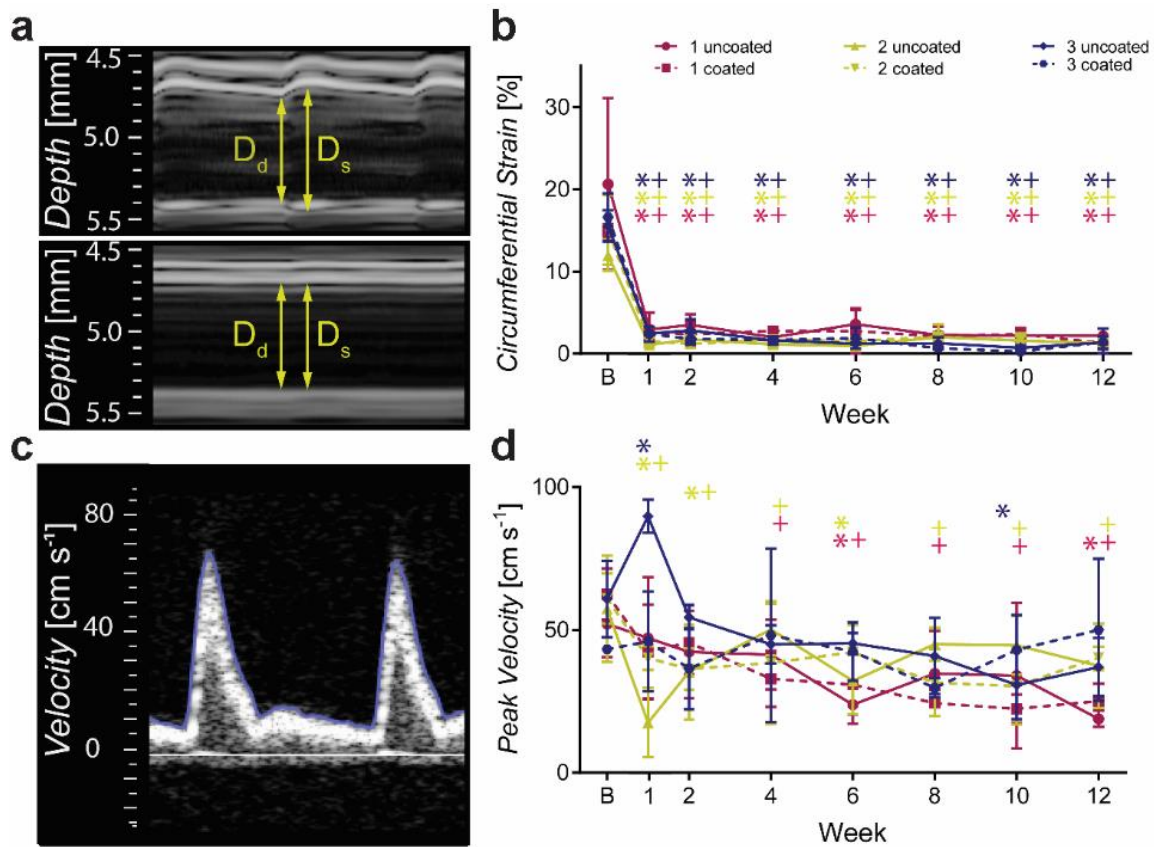
Figure 4.3. Ultrasound analysis of strain and velocity. A) In vivo cyclic circumferential Green-Lagrange strain was determined from M-mode images. B) All groups had an immediate reduction in strain following implantation of the scaffold that remained low throughout the study. C) Peak velocity was quantified from pulsed-wave Doppler ultrasound and d) showed some small changes, though highly variable. Representative images were taken from a Design 1 coated (for A) and uncoated (for C) graft, but similar results were observed for all graft types. An '*' refers to uncoated and a '+' refers to coated, with the color indicating the particular design ($p < 0.05$). All comparisons are relative to baseline. n = 2-4 per group. Comparisons were made with two-way ANOVA (main effects of graft and time) with a post-hoc Dunnett's test.
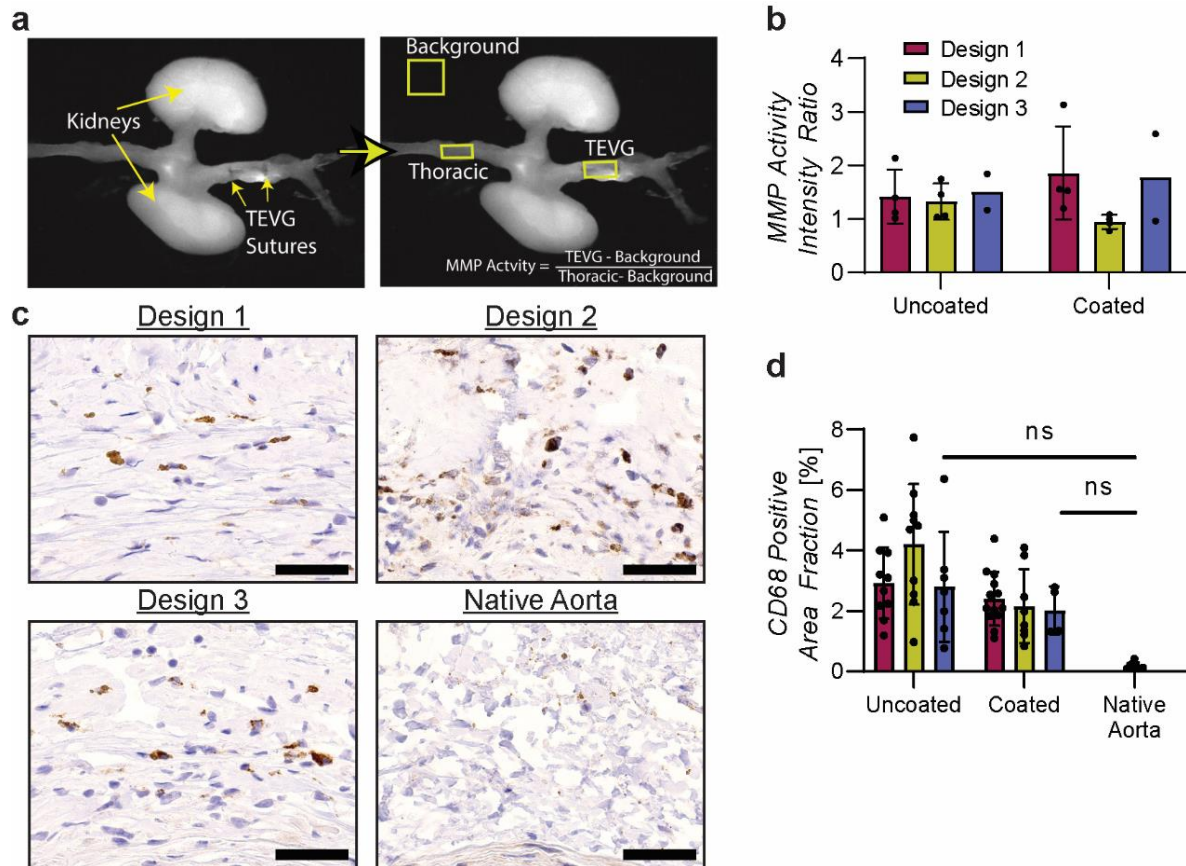
Figure 4.4. MMP activity and inflammation. A) Using near-infrared images of the explanted aorta/graft complex, MMP activity was calculated as the ratio of average TEVG intensity to thoracic intensity, after removing the effect of the background. These representative images were taken from a Design 1 uncoated mouse. B) Results indicated that MMP activity was not different between designs or coatings. n = 2-4 per group. Comparisons were made with ANOVA. C) Immunohistochemical staining using an antibody specific for CD68, a pan-macrophage marker. Representative images taken using a 63x objective. Scale bar = 40 µm. D) Results showed no significant differences between graft designs. Designs 1 and 2 both had significantly higher CD68 expression compared to the native aorta for both uncoated (D1; $p < 0.001$, D2; $p = 0.002$) and coated (D1; $p < 0.001$, D2; $p = 0.03$) grafts while Design 3 did not for uncoated ($p = 0.08$) and coated ($p = 0.11$). n=4-13 per group, based on survival. Comparisons were made with ANOVA with a post-hoc Dunnett's test.

4.4.5   Biaxial Mechanical Testing

Measured unloaded outer diameter and wall thickness were greater for all grafts than the age-matched native IAA. All varied significantly except for the diameter of coated grafts of Design 1 and 3 and the thickness of Design 3 coated grafts (**Figure 4.5B-C**). Both Design 2 uncoated and coated cohorts had significantly different *in vivo* axial stretch compared with the native aorta (p =

0.03, $p = 0.04$, respectively) (**Figure 4.5D**). All grafts had a significantly different measure of distending elastic energy (energy associated with loading the vessel from 10 to 140mmHg, at *in vivo* axial stretch) ($p = 0.03$ for D1 coated, $p = 0.04$ for the other groups) (**Figure 4.5E**). The grafts also had significantly different measures of distensibility compared to the native aorta ($p < 0.001$ for all) (**Figure 4.5F**). While significant differences in mechanical and morphological properties were observed between all graft designs and the native IAA, no significant differences were observed among the different grafts. Finally, despite the relatively large increase in compliance compared to the scaffolds at implantation, all the explants remained much stiffer structurally than the age-matched native IAA.
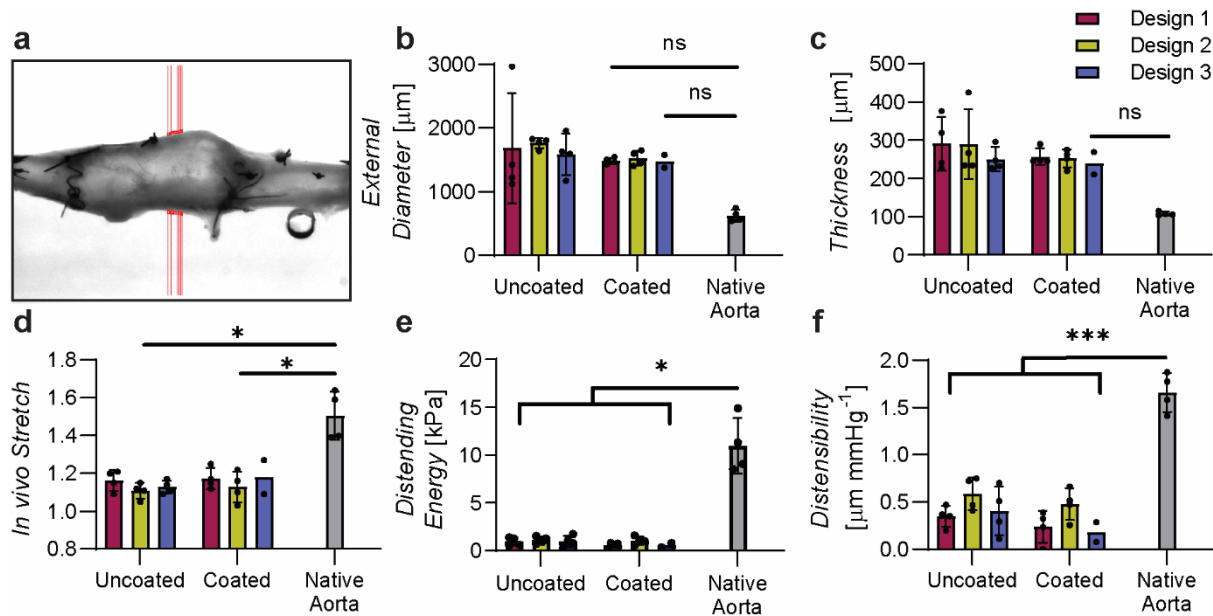
Figure 4.5. Biaxial mechanical properties. A) External diameter tracking of a representative explanted TEVG during biaxial mechanical testing upon explantation at 12 weeks. This representative image was taken from a Design 1 coated mouse. B-F) Summary of mechanical properties of graft designs (n = 4 for all groups except Design 3 coated which had n = 2). For external diameter, coated Design 1 and 3 were the only groups found to not be significantly different than the native aorta (p = 0.06, p = 0.22 respectively). Similarly, the coated Design 3 group was the only one found not significantly thicker than the native aorta (p = 0.1). Design 2 uncoated and coated cohorts had significantly different values of in vivo stretch compared to the native aorta (p = 0.03, p = 0.04 respectively). All groups had significantly different measures of distending energy (that due to distension alone) and distensibility compared to the native aorta. While significant differences in mechanical and morphological properties were observed between all graft designs and the native IAA, no significant differences were observed across graft designs. Comparisons were made with ANOVA with a post-hoc Sidak's or Dunnett's test depending on standard deviation. (* < 0.05, ** <0.01, *** <0.001)

4.4.6 Structural Histology Quantification

Figure 4.6A shows representative images of sections stained using techniques for Hart's, Picro-Sirius Red (viewed under polarized light), and calponin. Quantification of the positive area fraction of Hart's elastin (**Figure 4.6B**) showed differential effects of scaffold design on elastin density, which were significant ($p < 0.001$) while the effect of coating was not ($p = 0.294$). Specifically, significant differences in elastin density were seen between Design 2 (low braiding angle) and the other two designs (both high braiding angles) for both uncoated and coated cohorts. All groups, except Design 2 uncoated and coated cohorts, had significantly lower elastin densities compared to the native aorta. Measurements of the overall thickness of elastic laminae provided further insight into elastin deposition.[31] The effect of graft design was also significant ($p < 0.001$), and like elastin density, Design 2 uncoated and coated cohorts were significantly thicker compared to the other designs (**Figure 4.6C**). Interestingly, Design 2 had a thicker elastic lamina compared to the native aorta, with significant differences seen between the Design 2 uncoated cohort and the native aorta ($p = 0.0031$).

The effect of graft design on Picro-Sirius Red staining for collagen fibers was marked. Design 1 had a significantly greater collagen density compared to Design 2 for both uncoated ($p < 0.001$) and coated ($p < 0.001$) cohorts (**Figure 4.6D**). Design 2 samples also had a significantly lower collagen density in comparison to the native aorta for both uncoated ($p < 0.001$) and coated ($p = 0.003$) cohorts. The effect of scaffold design was significant regarding mature smooth muscle cell density ($p = 0.0022$) as reflected by the fractional area of calponin staining but showed no significant differences between any groups (**Figure 4.6E**). This also includes comparison between the TEVGs and the native aorta. All quantified measurements were normalized to total areas to account for differences in size between grafts and native aortas samples. Non-normalized data can be found in the supplement (**Appendix B Figure 5**). These data show similar differences between graft designs. Finally, only one sample, a Design 2 uncoated graft, was positive for calcification, seen with both von Kossa and Alizarin red staining (**Appendix B Figure 6**).
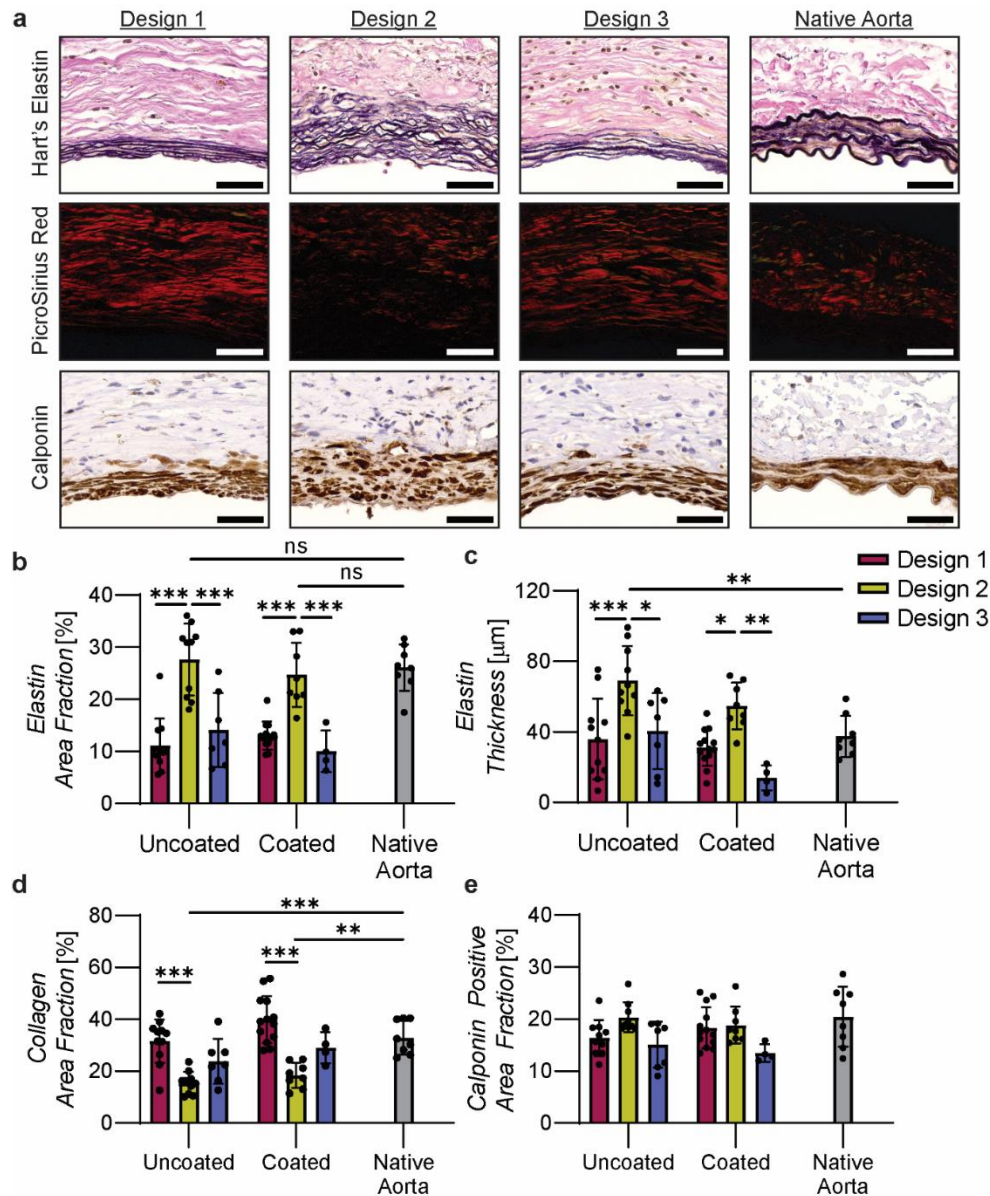
Figure 4.6. Histological analysis. A) Representative histological and immunohistological images of all graft designs followed by images of a native aorta. Stains include Hart's for elastin, Picro-Sirius Red for collagen, and calponin for smooth muscle cells. Images were taken using a 63x objective. Scale bars = 40 µm. B-C) evaluation of Hart's elastin showed differences in both elastin density and elastic lamina thickness between Design 2 and Designs 1 and 3 for coated and uncoated cohorts. Design 2 coated and uncoated cohorts were the only groups that did not have significantly decreased elastin density compared to the native aorta. Design 2 uncoated was the only group that had a significantly thicker band of elastin compared to the native aorta. D) Design 1 coated and uncoated cohorts had significantly higher densities of collagen when compared to the Design 2 cohorts. The Design 2 cohorts both had significantly lower collagen densities compared to the native aorta. E) No differences in smooth muscle positive area fraction were observed between any group or to the native aorta. n=4-13 per group. Comparisons were made with ANOVA with a post-hoc Sidak's test. (* < 0.05, ** <0.01, *** <0.001)

4.4.7 Statistical Relations

By logistic regression, the 2x2 scaffolds associated with a higher rate of overall mortality ($p > 0.001$). Increasing the braiding density of the scaffold by increasing the PPSI decreased mortality, whereas increasing the braiding angle resulted in higher mortality. Despite seeing an increase in mortality in some PGS coated groups, coating was not found to statistically affect survival beyond normal surgical variation. Multiple linear regression on the explanted 1x1 scaffolds (Designs 1, 2 and 3) evaluated the effect of scaffold braiding parameters on neovessel development. Increasing the PPSI correlated with decreased elastin and increased collagen density. Increasing the braiding angle towards a more circumferential braid correlated with a decrease in elastin, an increase in collagen, and a decrease in both calponin and CD68 positive cells. Increasing the angle also correlated with a decreased distensibility of the vessel by mechanical testing at explant. The addition of the PGS coating correlated with an increase in collagen and a decrease in inflammatory CD68 positive cells. Statistical details of these regressions can be found in **Appendix B Table 1**.

Regression analysis of the quantitative histology of the explanted vessels further demonstrated interesting relationships (**Appendix B Table 2**). Elastin and collagen were inversely related, as expected because area fractions, by definition, must sum to 1 and elastin and collagen are the primary constituents of the extracellular matrix. Elastin and calponin positive cells, elastin and CD68 positive cells, and calponin and CD68 positive cells correlated positively with each other. Comparing histology to mechanical testing data from the same animals demonstrated that there was no correlation between calponin or CD68 positive cells and distensibility. In contrast, elastin correlated positively with distensibility ($p = 0.029$) while collagen showed a near inverse correlation with distensibility ($p = 0.054$).

4.5 Discussion

We used 12-week implantations to evaluate specific bounds of the manufacturable parameter space for braided PGA scaffolds with and without a PGS coating. The differential temporal progressions of neovessel development and modes of graft failure (e.g., anastomotic bleeding, early or late rupture) remind us of the importance of evaluating degradable TEVGs across their full degradation time course as different mechanisms are likely operative at different times. Indeed,

previous computational simulations of short-term implants reinforced the importance of following the long-term performance of tissue engineered vascular grafts.[21,26]

In a study using electrospun scaffolds of poly-ε-caprolactone-co-L-lactic acid fibers (PCLA), all arterial grafts experienced sudden dilation and rupture at 14 weeks due to the sudden loss of mechanical strength of the scaffolds and inadequate tissue formation.[21] A study utilizing an electrospun PGS scaffold reinforced with an external poly(ε-caprolactone) (PCL) sheath only showed vascular architecture after 12 months *in vivo* while still exhibiting high levels of inflammation due to the slowly degrading PCL sheath and small pore sizes for the inner PGS layer.[26] Similar PGS-PCL scaffolds showed peri-operative mortality of over 30% thought to be due to defects in the outer sheath and the increased coagulability of wild-type mice.[32] In both studies of bilayered PGS-PCL scaffolds, mechanical testing after 12 weeks of implantation revealed low distensibilities in comparison to that of native vessels, as in the present study. Modification of the microstructural design of the PGS-PCL scaffolds in these studies required changes to the entire electrospinning protocol and were met with a number of challenges, including wrinkling and luminal occlusion due to swelling. The use of textile manufacturing methods in this study allowed finer control over graft parameters without major modifications to the fabrication process; use of faster degrading polymers, PGA and PGS, showed the capacity for swifter neovessel development.

The *in vivo* imaging methods used in this study included advanced volumetric ultrasound strategies that allowed us to better assess *in vivo* graft performance. For example, we collected 3D ultrasound images at multiple timepoints, through which we determined graft diameters and thicknesses. While diameter can be determined from standard 2D images,[33] the 3D datasets provide a more holistic view of graft development, as has been shown previously in murine aneurysm studies.[34,35] Of particular interest, we noted a thickened wall in Design 1 at week 4, which thinned by week 6 and remained stable for the rest of the study. Despite the thickened wall at week 4, we did not observe any narrowing of the lumen consistent with stenosis. These results were confirmed with histology at week 4, which showed little tissue formation on the luminal surface of the scaffolds but substantial collagen deposition surrounding the braided scaffolds (**Appendix B Figure 7**). We believe this initial adventitial collagen deposition is responsible for the increase in thickness seen on ultrasound at 4 weeks. This suggests that this graft design may be undergoing rapid remodeling between weeks 4 and 6. We also observed an increase in diameter at the proximal

and distal ends of some grafts, resulting in a barbell shape. While not observed in all animals, this may suggest faster graft degradation and neotissue formation at the anastomoses relative to the middle of the graft, consistent with infiltration of native vascular cells from the adjacent vessels.[36] Finally, using M-mode ultrasound, we calculated low strain within the graft while the native IAA proximal and distal to the graft remained highly pulsatile, indicating a relatively consistent strain gradient across the anastomoses. Given that this strain gradient likely changes throughout the remodeling process, future work with 4D ultrasound (3D+time) could enable noninvasive assessment of strain along the vessel.[35,37] Overall, the advanced 3D ultrasound metrics included in this study gave us greater insight into graft remodeling compared to standard imaging approaches.

Beige mutant mice were selected for their relative platelet storage pool deficiency compared to wild-type mice.[38] Previous studies by our laboratory showed benefits of using Beige mice to prevent early thrombosis in the small diameter vascular grafts evaluated in mice.[39-41] Higher thrombosis rates are expected in murine grafts compared to large animal grafts, as smaller arterial diameter greatly increases platelet shear stress.[42,43] Others have also shown that wild-type mice have hyperactive platelet responses compared to humans and larger animals such as rats.[44,45] The use of a mouse model with platelet storage pool deficiency thus allows examination of molecular and cellular mechanisms that drive neotissue formation without the confounding high thrombosis rates that would be seen in a wild-type mouse.

The explanted neovessels demonstrated high levels of elastin deposition. This result is notable as the vast majority of TEVGs, whether made from decellularized matrix or synthetic polymers, have difficulty in triggering elastin production.[46] Individual elastin fibers in the native aorta appear wavier than fibers seen in the neovessels due to the dilation of the grafts. The Design 2 cohorts had a similar elastin density to that of the native aorta. These cohorts also experienced steady dilation compared to the rapid dilation in other cohorts. Increasing (cyclic) wall tension associated with dilation could be one reason for increased elastin density in these groups.[47,48] However, these cohorts had thicker elastic laminae with thinner fibers in comparison to native vessels, which may suggest that the elastin fibers are immature or not organized fully. It is uncertain if they would develop further, though continued elastin deposition from 3 to 6 months has been observed.[32] The elastin in the grafts appears to be more organized than what has been seen in previous studies looking at the same time point in PGS-PCL grafts.[26,32,49] Nevertheless, the elastin in each of these graft designs is not serving its functional capacity due to the low energy

storage capacity observed in these stiff constructs. Smooth muscle cells also appear circular compared to the elongated cells of the native aorta which could indicate these cells are in a synthetic, noncontractile state, indicating ongoing extracellular matrix remodeling.[50] Notably, calponin-positive cells were only present within the neotissue closest to the lumen. Previous studies have also observed contractile cells within the neointima of tissue engineered vessels.[51]

Statistical regression analysis comparing the implanted scaffold parameters to the explanted neovessel characteristics demonstrated that the PGS coating decreased inflammation and increased collagen accumulation. The lower inflammation and macrophage density seen at explant (12 weeks), in comparison to other polymer-based vascular grafts at similar time,[26,31,52] likely reflected the near complete degradation of polymer by 12 weeks. PGA fibers appear birefringent under polarized light,[53] and the fibers were seen in 4-week explants but not at 12-weeks, suggesting complete degradation of the polymer by 12 weeks (**Appendix B Figure 7**). While macrophages and inflammation are essential for neotissue formation, macrophage overabundance or prolonged inflammatory response associates with worse outcomes for tissue engineered vessels.[52] Slow degrading polymers, expectedly, associate with longer lasting inflammation and more foreign body giant cell formation.[54] Overall these findings suggest that the differences in scaffold designs affected the balance of immuno-driven and mechano-mediated matrix production in development of the neovessels. This aligns with our previous study that used computational modeling to demonstrate how you can change inflammation and alter neotissue in a predictable manner by altering scaffold morphometry.[19] The low incidence of calcification seen in this study is also likely related to the shorter polymer degradation times, as nondegradable conduits highly susceptible to calcification after long implantation.[55] In a previous study in rats, adding a PGS coating to a PGA arterial scaffold decreased the incidence of calcification and improved the inflammatory response seen with a shift in macrophage polarization.[31] While we have not specifically examined the molecular mechanism PGS may have on inflammation, for similar biodegradable scaffolds we have demonstrated this is a TGF-β mediated process.[56]

Our study further demonstrated that increasing the braiding angle towards the circumferential direction decreased distensibility at 12 weeks. Although one expects decreased distensibility with preferential circumferential polymer fiber alignment early on, this finding after degradation of polymer reinforces the thought that polymer orientation influences cell alignment, and thus, neotissue alignment. Notwithstanding the deposited elastin and the positive correlation

between elastin content and distensibility, the *in vivo* axial stretch and energy stored elastically upon pressurization were both considerably lower in the grafts than in native IAAs, consistent with the elastin not being fully functional, the presence of excessive, stiff collagen, or both. The non-native organization of the elastic laminae and the trend toward a negative correlation between collagen content and distensibility suggests that both are likely. The ability to store energy elastically is critical to the function of conduit vessels such as the aorta and remains an unmet need. While the grafts evaluated in this study did not reach the compliance of the native aorta, they developed to levels similar to those seen in aneurysmal murine arteries.[25,57,58] This may be due to the initial stiffness of the implanted scaffolds, thus a more compliant scaffold may have facilitated mechanical properties that better match the native vessel. Recall, also, that the more compliant scaffolds evaluated in this study, the 2x2 braided designs, were still significantly less compliant a than native vessel and had a high failure rate due to the lack of structural integrity, both initially and over the course of degradation. Thus, finding the appropriate balance between initial stiffness and strength remains a significant challenge.

Overall, statistical regression analysis of the relations between scaffold characteristics and neovessel outcomes highlights the complexity and importance of rational design in tissue engineering. While many tissue engineering design improvements are made empirically to improve a specific parameter, such as amount of collagen deposited or reduced inflammation, we can see from the statistical regressions (**Appendix B Tables 1 & 2**) that many of these parameters, such as survival, collagen deposition, and inflammation, are intertwined in both their relation to scaffold design parameters and their relations to each other. For example, increasing the density of a scaffold by increasing the PPSI served to improve survival, but it also decreased elastin production. Similarly, decreasing the braiding angle towards the axial direction improved distensibility and survival, but led to early dilation as seen by ultrasound. In addition, changing of braiding parameters can have unintended consequences, such as loosening of the overall braiding structure, which can lead to a higher rate of bleed through as was seen in Designs 4 and 5 with the 2x2 braiding pattern. Careful balancing of the relative importance of multiple desired parameters will be necessary to determine a proposed ideal scaffold with optimized performance in both the short and long-term after implantation in a patient.[17]

4.6   Conclusion

In this work, braided small-diameter arterial grafts of PGA with and without PGS coating were manufactured at the edges of the braidable parameter space and evaluated for failure mode and performance within a murine IAA implantation model. Braiding parameters, and the resulting physical properties of the scaffolds, had a substantial effect on the success and failure mode (i.e., bleeding, early rupture, late rupture) *in vivo*. Braiding parameters and PGS coating also affected the histological make-up of the resulting neovessels. Detailed ultrasound analysis allowed longitudinal *in vivo* evaluation of morphometric properties and explant biaxial testing allowed functional consequences of immunohistological findings to be contextualized. Statistical findings from this work will aid in the development of mathematical models to predict the outcomes of new scaffolds.

4.7   Acknowledgements

4.8   Conflicts of Interest

C.K.B. is an inventor on patent/patent applications [2015252805 (Australia), 2016565483 (Japan), 855,370, 9,446,175, 9,782,522, 10,300,082, 61/987,910, 62/266,309, 62/309,285, 62/209,990, 62/936,225] submitted by Yale University and/or Nationwide Children's Hospital that cover methods of improving the design, manufacturing, or performance of tissue-engineered vascular grafts. C.K.B. is a founder of Lyst Therapeutics.

4.9 References

1. Lytle BW, Loop FD, Cosgrove DM et al. 1985. Long-term (5 to 12 years) serial studies of internal mammary artery and saphenous vein coronary bypass grafts. J Thorac Cardiovasc Surg. 89(2):248-258.

2. Goldman S, Zadina K, Moritz T et al. 2004. Long-term patency of saphenous vein and left internal mammary artery grafts after coronary artery bypass surgery: Results from a department of veterans affairs cooperative study. J Am Coll Cardiol. 44(11):2149-2156.

3. Gooch KJ, Firstenberg MS, Shrefler BS, Scandling BW. 2018. Biomechanics and mechanobiology of saphenous vein grafts. J Biomech Eng. 140(2).

4. Harskamp RE, Lopes RD, Baisden CE et al. 2013. Saphenous vein graft failure after coronary artery bypass surgery: Pathophysiology, management, and future directions. Ann Surg. 257(5):824-833.

5. Veith FJ, Moss CM, Sprayregen S, Montefusco C. 1979. Preoperative saphenous venography in arterial reconstructive surgery of the lower extremity. Surgery. 85(3):253-256.

6. Pashneh-Tala S, MacNeil S, Claeyssens F. 2016. The tissue-engineered vascular graft—past, present, and future. Tissue Engineering Part B: Reviews. 22(1):68-100.

7. Matsuzaki Y, John K, Shoji T, Shinoka T. 2019. Bioprinting vasculature: Materials, cells and emergent techniques. Appl Sci. 9.

8. Carrabba M, Madeddu P. 2018. Current strategies for the manufacture of small size tissue engineering vascular grafts. Frontiers in bioengineering and biotechnology. 6:41.

9. Singh C, Wong CS, Wang X. 2015. Medical textiles as vascular implants and their success to mimic natural arteries. Journal of functional biomaterials. 6(3):500-525.

10. Wu J, Hu C, Tang Z et al. 2018. Tissue-engineered vascular grafts: Balance of the four major requirements. Colloid and Interface Science Communications. 23:34-44.

11. Wang Y, Ameer GA, Sheppard BJ, Langer R. 2002. A tough biodegradable elastomer. Nat Biotechnol. 20(6):602-606.

12. Wang Y, Kim YM, Langer R. 2003. In vivo degradation characteristics of poly (glycerol sebacate). Journal of Biomedical Materials Research Part A: An Official Journal of The Society for Biomaterials, The Japanese Society for Biomaterials, and The Australian Society for Biomaterials and the Korean Society for Biomaterials. 66(1):192-197.

13. Loh XJ, Karim AA, Owh C. 2015. Poly (glycerol sebacate) biomaterial: Synthesis and biomedical applications. Journal of Materials Chemistry B. 3(39):7641-7652.

14. Naito Y, Williams-Fritze M, Duncan DR et al. 2012. Characterization of the natural history of extracellular matrix production in tissue-engineered vascular grafts during neovessel formation. Cells Tissues Organs. 195(1-2):60-72.

15. Szafron J, Khosravi R, Reinhardt J et al. 2018. Immuno-driven and mechano-mediated neotissue formation in tissue engineered vascular grafts. Ann Biomed Eng. 46(11):1938-1950.

16. Agarwal R, Blum KM, Musgrave A et al. 2019. Degradation and in vivo evaluation of polycaprolactone, poly (ε-caprolactone-co-l-lactide), and poly-l-lactic acid as scaffold sealant polymers for murine tissue-engineered vascular grafts. Regen Med. 14(7):627-637.

17. Szafron JM, Ramachandra AB, Breuer CK et al. 2019. Optimization of tissue-engineered vascular graft design using computational modeling. Tissue Engineering Part C: Methods. 25(10):561-570.

18. Tamimi EA, Ardila DC, Ensley BD et al. 2019. Computationally optimizing the compliance of multilayered biomimetic tissue engineered vascular grafts. J Biomech Eng. 141(6).

19. Miller KS, Khosravi R, Breuer CK, Humphrey JD. 2015. A hypothesis-driven parametric study of effects of polymeric scaffold properties on tissue engineered neovessel formation. Acta biomaterialia. 11:283-294.

20. Udelsman BV, Khosravi R, Miller KS et al. 2014. Characterization of evolving biomechanical properties of tissue engineered vascular grafts in the arterial circulation. J Biomech. 47(9):2070-2079.

21. Best CA, Szafron JM, Rocco KA et al. 2019. Differential outcomes of venous and arterial tissue engineered vascular grafts highlight the importance of coupling long-term implantation studies with computational modeling. Acta biomaterialia. 94:183-194.

22. Smith Jr RJ, Yi T, Nasiri B et al. 2019. Implantation of vegf-functionalized cell-free vascular grafts: Regenerative and immunological response. The FASEB Journal. 33(4):5089-5100.

23. Updegrove A, Wilson NM, Merkow J et al. 2017. Simvascular: An open source pipeline for cardiovascular simulation. Ann Biomed Eng. 45(3):525-541.

24. Humphrey JD, O'Rourke SL. 2015. Stress, strain, and constitutive relations. An introduction to biomechanics. Springer. p. 47-107.

25. Goergen CJ, Azuma J, Barr KN et al. 2011. Influences of aortic motion and curvature on vessel expansion in murine experimental aneurysms. Arterioscler Thromb Vasc Biol. 31(2):270-279.

26. Khosravi R, Best CA, Allen RA et al. 2016. Long-term functional efficacy of a novel electrospun poly (glycerol sebacate)-based arterial graft in mice. Ann Biomed Eng. 44(8):2402-2416.

27. Gleason R, Gray S, Wilson E, Humphrey J. 2004. A multiaxial computer-controlled organ culture and biomechanical device for mouse carotid arteries. J Biomech Eng. 126(6):787-795.

28. Ferruzzi J, Bersi M, Humphrey J. 2013. Biomechanical phenotyping of central arteries in health and disease: Advantages of and methods for murine models. Ann Biomed Eng. 41(7):1311-1330.

29. Rueden CT, Schindelin J, Hiner MC et al. 2017. Imagej2: Imagej for the next generation of scientific image data. BMC Bioinformatics. 18(1):1-26.

30. Schindelin J, Arganda-Carreras I, Frise E et al. 2012. Fiji: An open-source platform for biological-image analysis. Nature methods. 9(7):676-682.

31. Fukunishi T, Ong CS, Lui C et al. 2019. Formation of neoarteries with optimal remodeling using rapidly degrading textile vascular grafts. Tissue Engineering Part A. 25(7-8):632-641.

32. Wu Y-L, Szafron JM, Blum KM et al. 2020. Electrospun tissue-engineered arterial graft thickness affects long-term composition and mechanics. Tissue Engineering Part A.

33. Trachet B, Fraga-Silva RA, Londono FJ et al. 2015. Performance comparison of ultrasound-based methods to assess aortic diameter and stiffness in normal and aneurysmal mice. PLoS One. 10(5):e0129007.

34. Romary DJ, Berman AG, Goergen CJ. 2019. High-frequency murine ultrasound provides enhanced metrics of bapn-induced aaa growth. American Journal of Physiology-Heart and Circulatory Physiology. 317(5):H981-H990.

35. Cebull HL, Soepriatna AH, Boyle JJ et al. 2019. Strain mapping from four-dimensional ultrasound reveals complex remodeling in dissecting murine abdominal aortic aneurysms. J Biomech Eng. 141(6).

36. Hibino N, Villalona G, Pietris N et al. 2011. Tissue-engineered vascular grafts form neovessels that arise from regeneration of the adjacent blood vessel. The FASEB Journal. 25(8):2731-2739.

37. Boyle JJ, Soepriatna A, Damen F et al. 2019. Regularization-free strain mapping in three dimensions, with application to cardiac ultrasound. J Biomech Eng. 141(1).

38. Pratt H, Carroll R, Jones J, Lothrop Jr C. 1991. Platelet aggregation, storage pool deficiency, and protein phosphorylation in mice with chediak-higashi syndrome. Am J Vet Res. 52(6):945-950.

39. Kurobe H, Maxfield MW, Tara S et al. 2015. Development of small diameter nanofiber tissue engineered arterial grafts. PLoS One. 10(4):e0120328.

40. Tara S, Kurobe H, Maxfield MW et al. 2015. Evaluation of remodeling process in small-diameter cell-free tissue-engineered arterial graft. J Vasc Surg. 62(3):734-743.

41.	Nelson GN, Mirensky T, Brennan MP et al. 2008. Functional small-diameter human tissue–engineered arterial grafts in an immunodeficient mouse model: Preliminary findings. Arch Surg. 143(5):488-494.

42.	Shadden SC, Hendabadi S. 2013. Potential fluid mechanic pathways of platelet activation. Biomechanics and modeling in mechanobiology. 12(3):467-474.

43.	Greve JM, Les AS, Tang BT et al. 2006. Allometric scaling of wall shear stress from mice to humans: Quantification using cine phase-contrast mri and computational fluid dynamics. American Journal of Physiology-Heart and Circulatory Physiology. 291(4):H1700-H1708.

44.	Lemini C, Jaimez R, Franco Y. 2007. Gender and inter-species influence on coagulation tests of rats and mice. Thromb Res. 120(3):415-419.

45.	Nylander S, Mattsson C, Lindahl TL. 2006. Characterisation of species differences in the platelet adp and thrombin response. Thromb Res. 117(5):543-549.

46.	Patel A, Fine B, Sandig M, Mequanint K. 2006. Elastin biosynthesis: The missing link in tissue-engineered blood vessels. Cardiovasc Res. 71(1):40-49.

47.	Sutcliffe MC, Davidson JM. 1990. Effect of static stretching on elastin production by porcine aortic smooth muscle cells. Matrix. 10(3):148-153.

48.	Wanjare M, Agarwal N, Gerecht S. 2015. Biomechanical strain induces elastin and collagen production in human pluripotent stem cell-derived vascular smooth muscle cells. Am J Physiol Cell Physiol. 309(4):C271-281.

49.	Wu W, Allen RA, Wang Y. 2012. Fast-degrading elastomer enables rapid remodeling of a cell-free synthetic graft into a neoartery. Nat Med. 18(7):1148-1153.

50.	Louis SF, Zahradka P. 2010. Vascular smooth muscle cell motility: From migration to invasion. Exp Clin Cardiol. 15(4):e75.

51.	Reinhardt JW, Rosado JdDR, Barker JC et al. 2019. Early natural history of neotissue formation in tissue-engineered vascular grafts in a murine model. Regen Med. 14(5):389-408.

52.	Hibino N, Yi T, Duncan DR et al. 2011. A critical role for macrophages in neovessel formation and the development of stenosis in tissue-engineered vascular grafts. The FASEB Journal. 25(12):4253-4263.

53.	Drews JD, Pepper VK, Best CA et al. 2020. Spontaneous reversal of stenosis in tissue-engineered vascular grafts. Sci Transl Med. 12(537).

54.	Hashizume R, Hong Y, Takanari K et al. 2013. The effect of polymer degradation time on functional outcomes of temporary elastic patch support in ischemic cardiomyopathy. Biomaterials. 34(30):7353-7363.

55. Hagler DJ, Miranda WR, Haggerty BJ et al. 2019. Fate of the fontan connection: Mechanisms of stenosis and management. Congenit Heart Dis. 14(4):571-581.

56. Lee YU, Ruiz-Rosado JdD, Mahler N et al. 2016. Tgf-β receptor 1 inhibition prevents stenosis of tissue-engineered vascular grafts by reducing host mononuclear phagocyte activation. The FASEB Journal. 30(7):2627-2636.

57. Sangha GS, Busch A, Acuna A et al. 2019. Effects of iliac stenosis on abdominal aortic aneurysm formation in mice and humans. J Vasc Res. 56(5):217-229.

58. Phillips EH, Yrineo AA, Schroeder HD et al. 2015. Morphological and biomechanical differences in the elastase and angii apoe−/− rodent models of abdominal aortic aneurysms. BioMed research international. 2015.

5. CONCLUSION

Abdominal aortic aneurysms are a degenerative condition that carry a high risk of fatality if rupture occurs. While clinical assessments focus primarily on diameter and growth rate to assess rupture risk, the complex pathophysiology warrant improved metrics. However, our success in this area is highly dependent on our ever-increasing understanding of the disease. The work performed in this dissertation enhances our understanding of both disease and treatment by 1) probing the role of elastin and lysyl oxidase on aneurysm size and morphology in a relatively new murine model and 2) investigating our ability to alter the remodeling process of tissue engineered vascular grafts by varying specific design parameters.

With respect to the first area of research, we combined an elastase surgery with continuous oral administration of BAPN in mice to create a continuously growing aneurysm in which some mice had intraluminal thrombus. We then probed the model by altering the elastase concentration and the timing of BAPN administration. We demonstrated that aneurysm size could be modulated by changing the concentration of elastase, thus increasing applicability of this animal model to include both slow- and fast-growing aneurysms. We also found that, even after aneurysm formation, BAPN remained necessary for continued aneurysmal growth, demonstrating the role of lysyl oxidase in stabilizing the aneurysm. Lastly, we showed that female mice developed larger aneurysms than the males, demonstrating sexual dimorphism in this model.

With respect to the second area of research, we assessed vascular remodeling in mice that had a tissue engineered vascular graft implanted. We chose a variety of braiding patterns in order to understand the influencing role of graft design on its patency. We found that many key outcomes such as collagen and elastin deposition, inflammation, and overall survival were often intertwined. As a result, we demonstrated that changing parameters may improve one outcome and yet worsen another and that finding a way to balance outcomes in order to optimize performance is key. In this way, the work in this dissertation enhance both our understanding of the disease and that of treatment options.

The potential future directions from this dissertation are extensive. With respect to aneurysm research, much remains unknown about thrombus deposition and its role in rupture risk. Building on the current work, future studies could use computational fluid dynamics or fluid-structure interactions to probe the hemodynamics that lead to thrombus deposition. Employing multiple

sessions of ultrasound imaging combined with computational modelling may even enable delineation of the staccato vs continuous layering process. Thrombus mechanics and inflammation – along with their role in rupture – is yet another large area of research that could build on the work performed in this dissertation. Lastly, the sexual dimorphism observed in this model warrants future research. For example, as a future study, castration and ovariectomy could be performed in male and female mice, respectively, prior to the BAPN+Elastase surgery, to assess the role of sex hormones on aneurysm growth. Moreover, to build on the current graft research, we could pursue our optimized graft design in a larger animal species to confirm results. Some of the graft designs resulted in early bleed-out, which may be improved by alternate types or amounts of coating. In these ways, we could extend the work performed here and further our ability to both understand and treat aneurysms.

APPENDIX A. SUPPLEMENTAL DATA FOR CHAPTER 3

This section provides supplemental tables and figures for Chapter 3 "Ultrasound Imaging of Vascular Tissue Remodeling during Repair."

Methods

Microscopic examination was performed by a board-certified pathologist. To evaluate aorta pathology of H&E stained slides, a semi-quantitative scoring system was applied that assessed four morphological aspects: 1) mononuclear cell infiltrate; 2) polymorphonuclear cell infiltrate; 3) circumferential involvement; and 4) elastin quality. The infiltration of cells was graded on four levels: 0, normal; 1, mild increase in cell numbers; 2, moderate increase in cell numbers; 3, marked increase in cell numbers. The circumferential involvement was graded on four levels: 0, normal; 1, <10% of aorta circumference infiltrated by cells; 2, 10%-50% of aorta circumference; 3, 50% or greater of the aorta circumference. The elastin quality of MPC slides was graded on 4 levels and included qualitative assessment of disorderly arrangement of fibers, disruption in continuity, and/or distorted form. The elastin quality grades were: 0, normal; 1, <25% aorta circumference has distorted elastin; 2, 25%-75% of aorta circumference; 3, 75% or greater of aorta circumference.

MMP Analysis
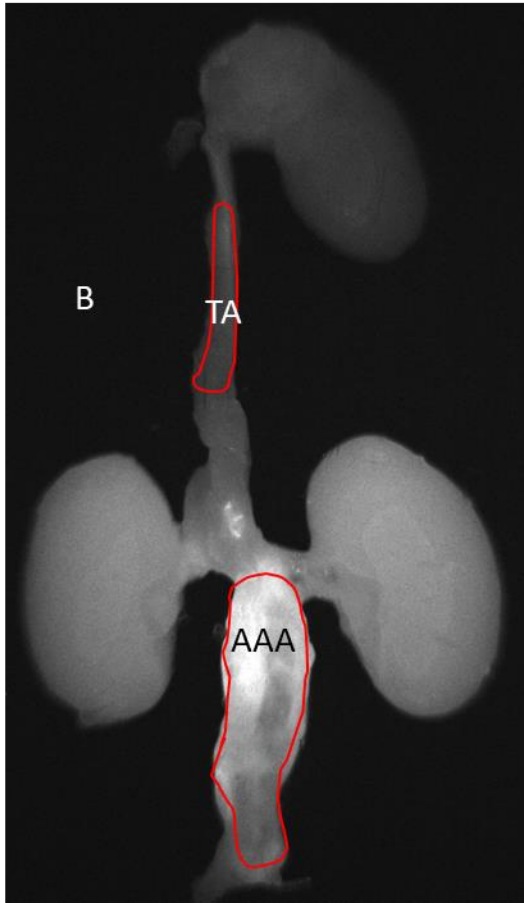
$$Intensity\ Ratio = \frac{\bar{I}_{AAA} - \bar{I}_B}{\bar{I}_{TA} - \bar{I}_B}$$

where I is the average pixel intensity

Appendix A Figure 1. Representative schematic showing the analysis method used to assess MMP activity. Regions of aneurysmal aorta, thoracic aorta, and background were hand-drawn, and the average pixel intensity calculated for each region. A ratio of aneurysmal intensity to thoracic intensity (after removing the effects of background noise) was used to determine MMP activity.

Timecourse of Representative Mice from the Concentration Study

Day 0 7 14 21 28 35 42 49 56

2.5 mg/ml

5 mg/ml

10 mg/ml

5 mm
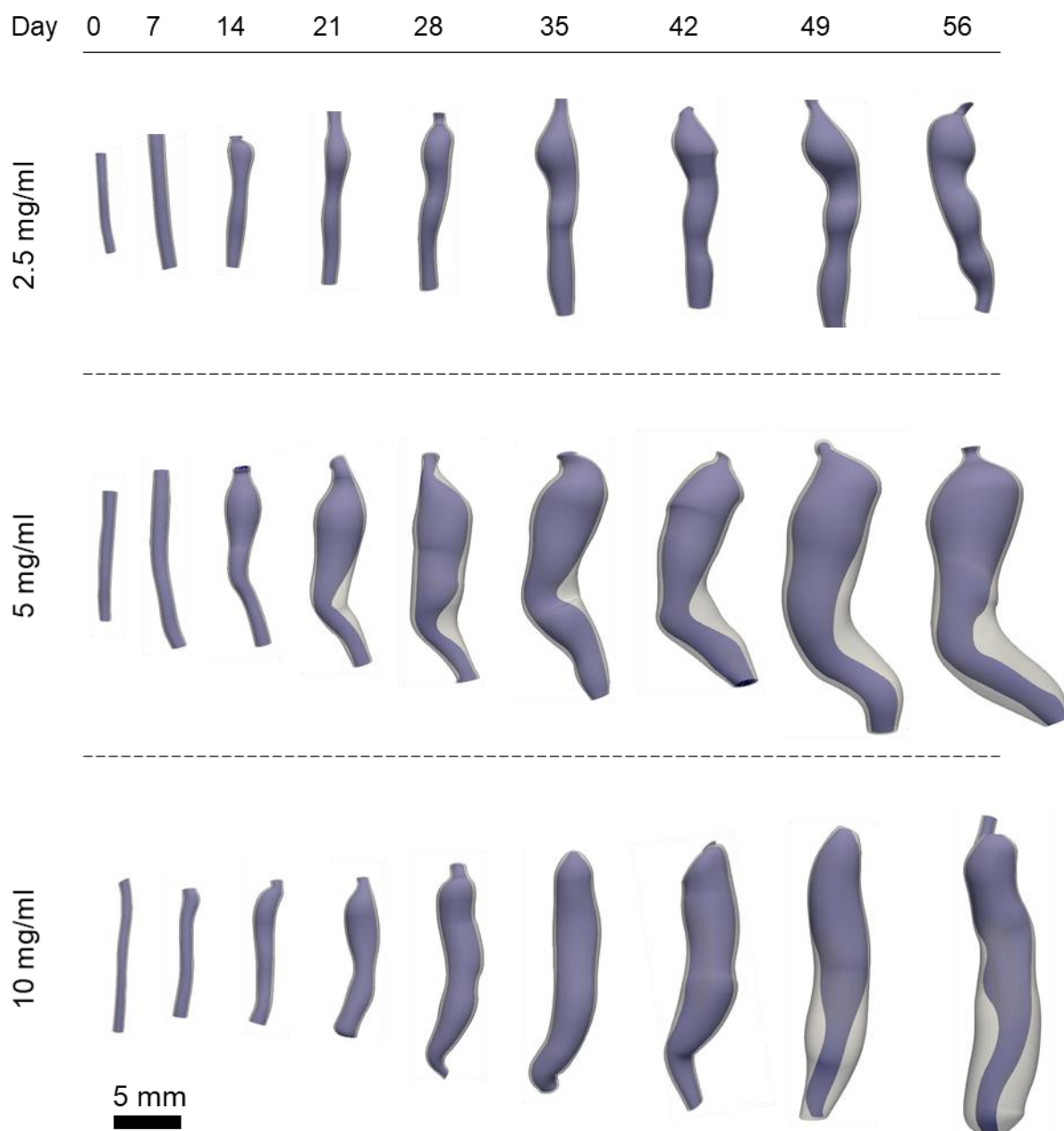
Appendix A Figure 2. Representative time course for mice treated with 2.5 mg/ml, 5 mg/ml, and 10 mg/ml of elastase. The purple is lumen and the white is outer wall. Locations of thick wall grey in color indicate thrombus.

Day 56 Models

5 mm
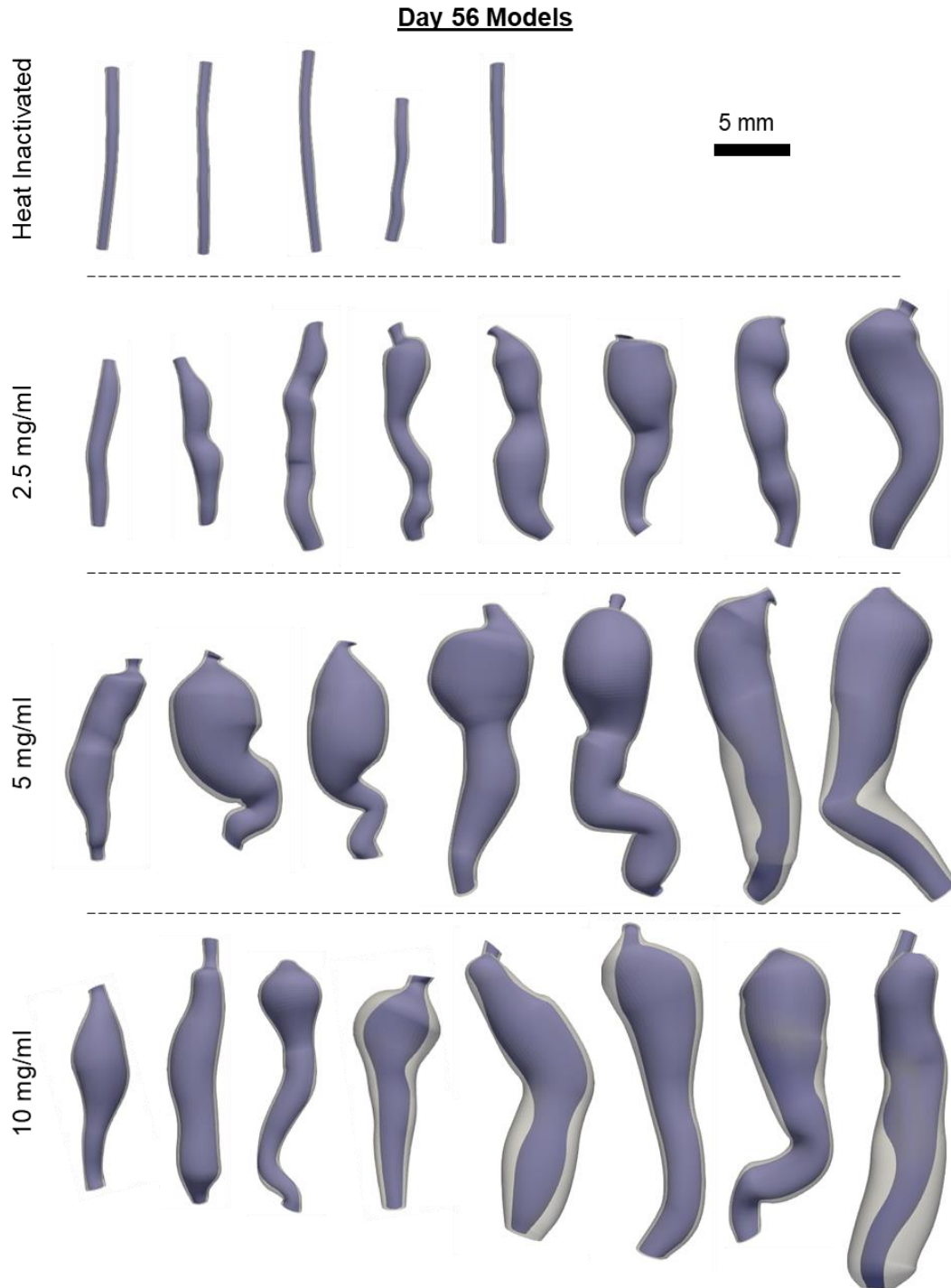
Appendix A Figure 3. 3D ultrasound-based segmentations of mice 56 days post-surgery. Mice treated with 2.5 mg/ml generally appear smaller and lack the thrombus observed in the 5 mg/ml and 10 mg/ml groups. In the 5 mg/ml group, two mice had thrombus, which was lower than the five mice who had thrombus in the 10 mg/ml group, as indicated by the thicker walls in the segmentations.

Appendix A Figure 4. Hematoxylin and Eosin (H&E) staining of mice treated with 10 mg/ml elastase. Mice were euthanized 56 days post-surgery.

Movat's Pentachrome of Chronic Concentration Study – 10 mg/ml Group
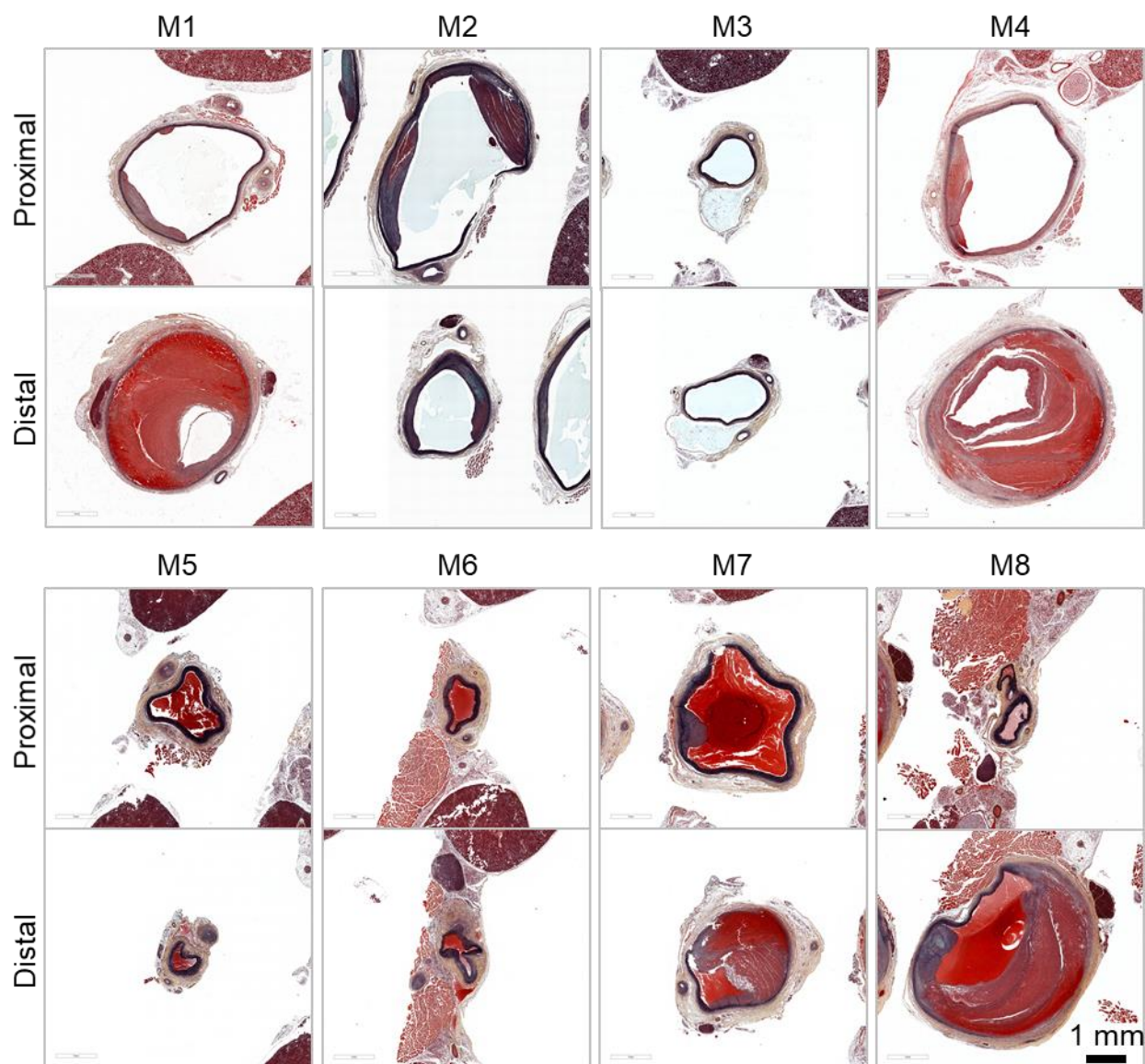
Appendix A Figure 5. Movat's Pentachrome (MPC) staining of mice treated with 10 mg/ml elastase. Mice were euthanized 56 days post-surgery.

H&E of Chronic Concentration Study – 5 mg/ml Group
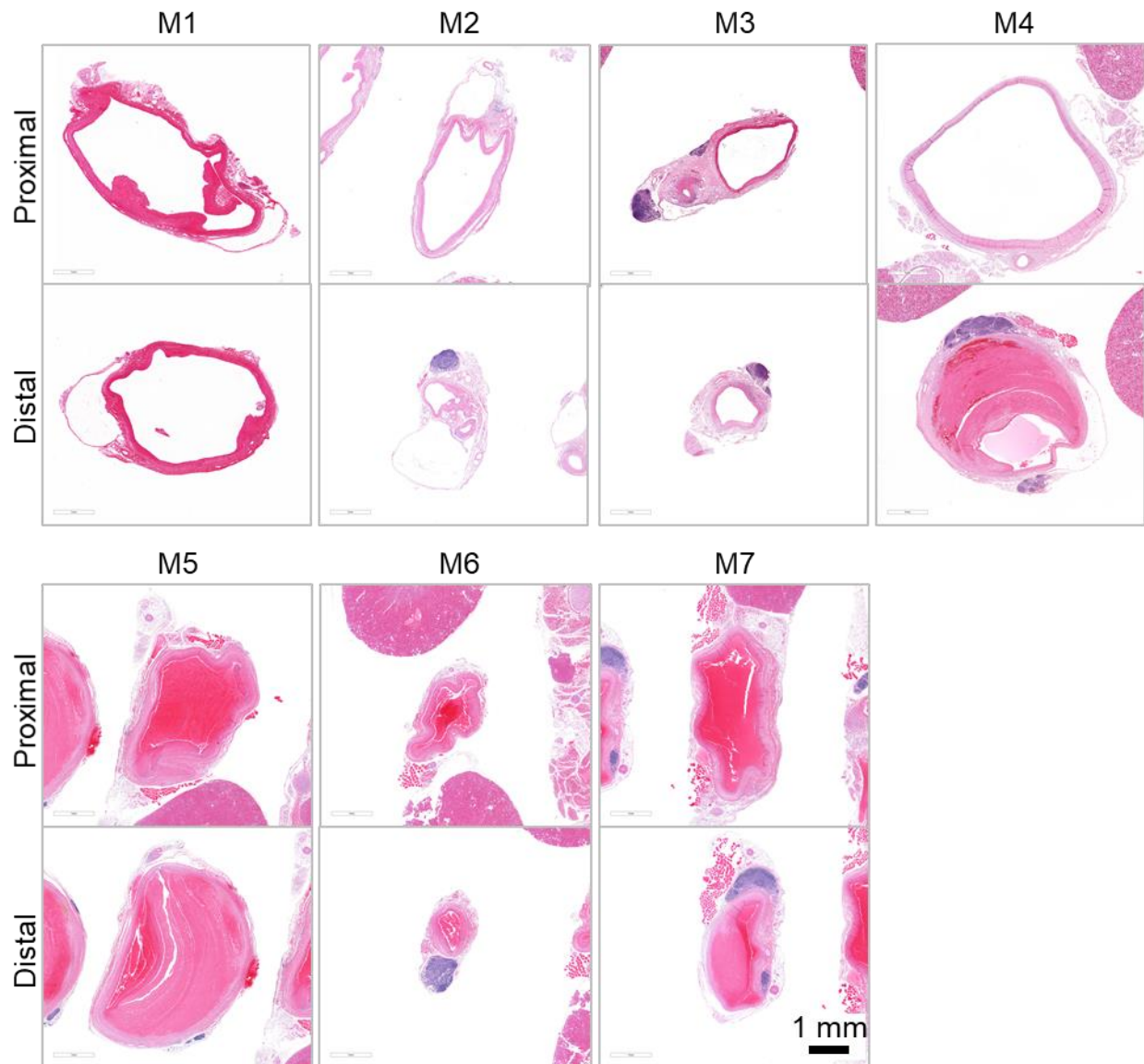
Appendix A Figure 6. Hematoxylin and Eosin (H&E) staining of mice treated with 5 mg/ml elastase. Mice were euthanized 56 days post-surgery.

Movat's Pentachrome of Chronic Concentration Study – 5 mg/ml Group
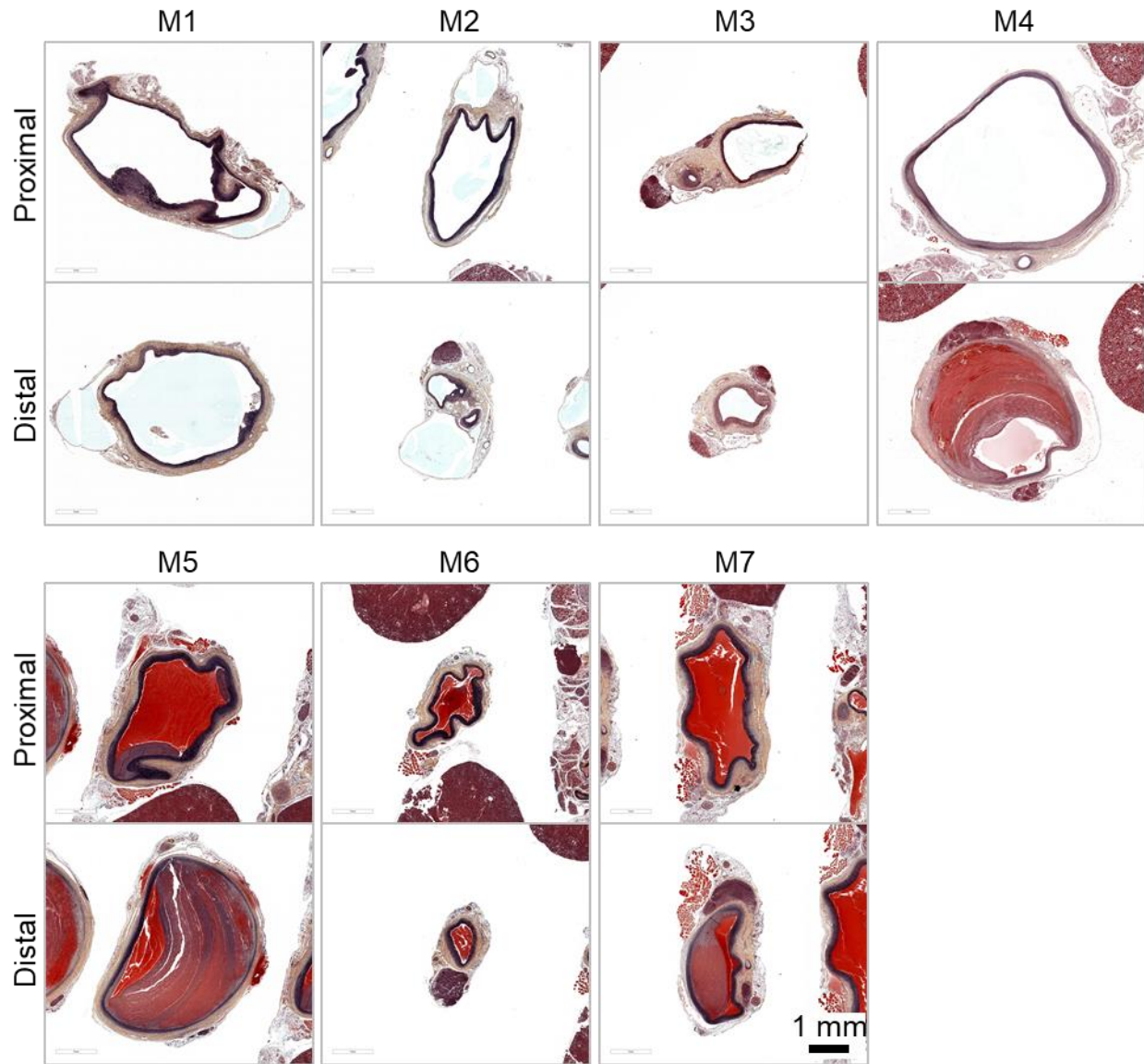
Appendix A Figure 7. Movat's Pentachrome (MPC) staining of mice treated with 5 mg/ml elastase. Mice were euthanized 56 days post-surgery.
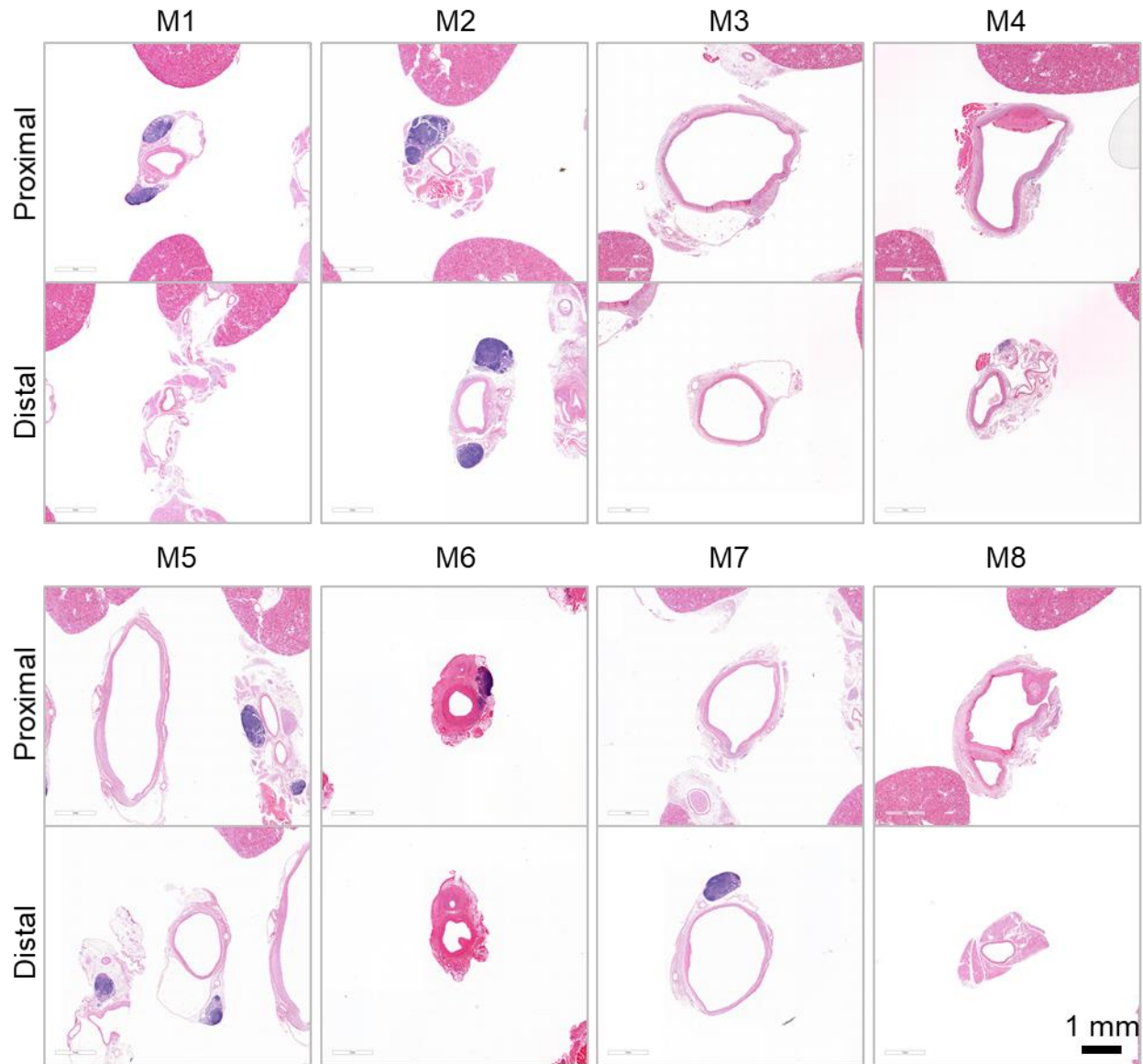
Appendix A Figure 8. Hematoxylin and Eosin (H&E) staining of mice treated with 2.5 mg/ml elastase. Mice were euthanized 56 days post-surgery.
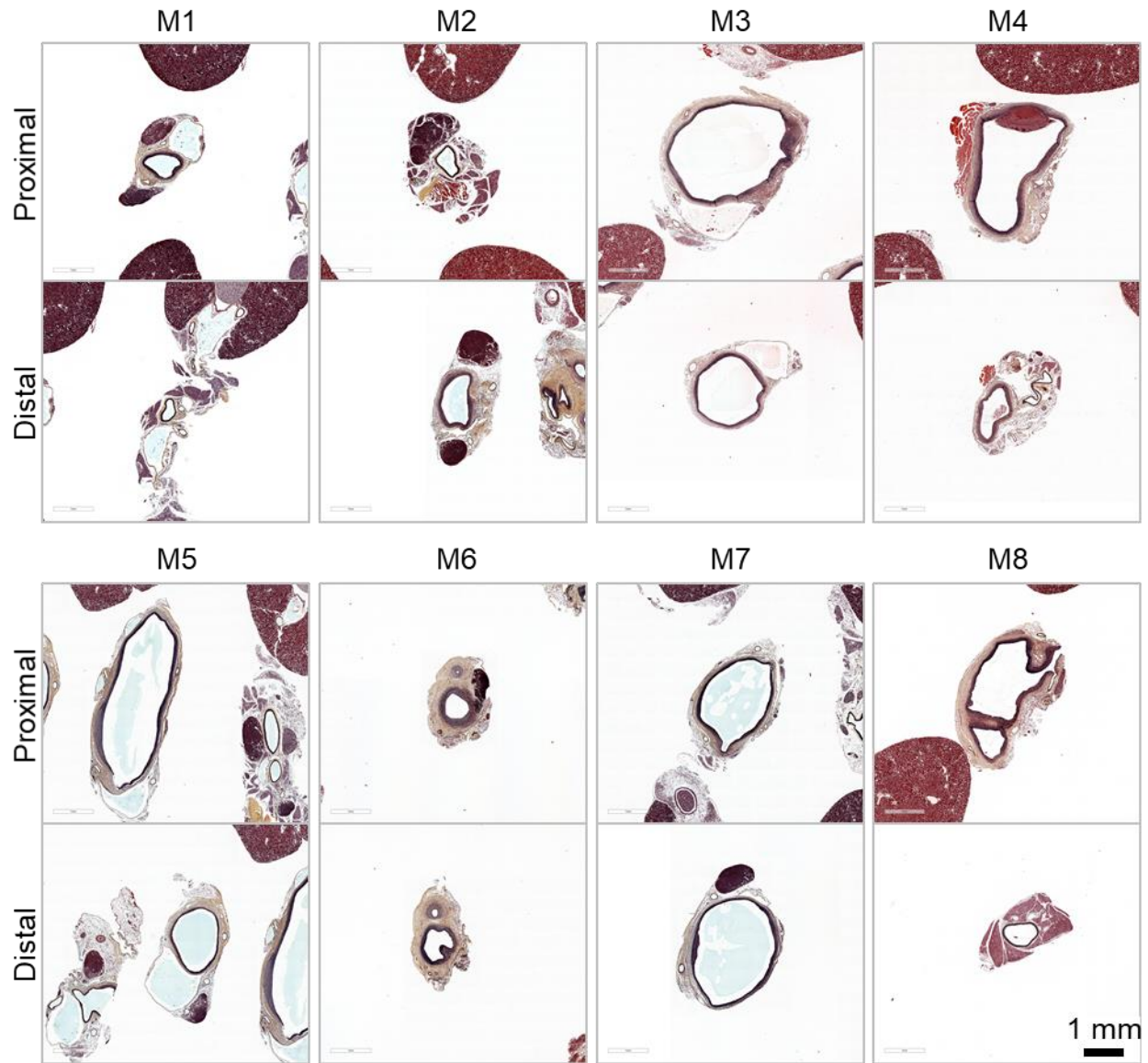
Appendix A Figure 9. Movat's Pentachrome (MPC) staining of mice treated with 2.5 mg/ml elastase. Mice were euthanized 56 days post-surgery.

H&E of Chronic Concentration Study – Heat Inactivated Group
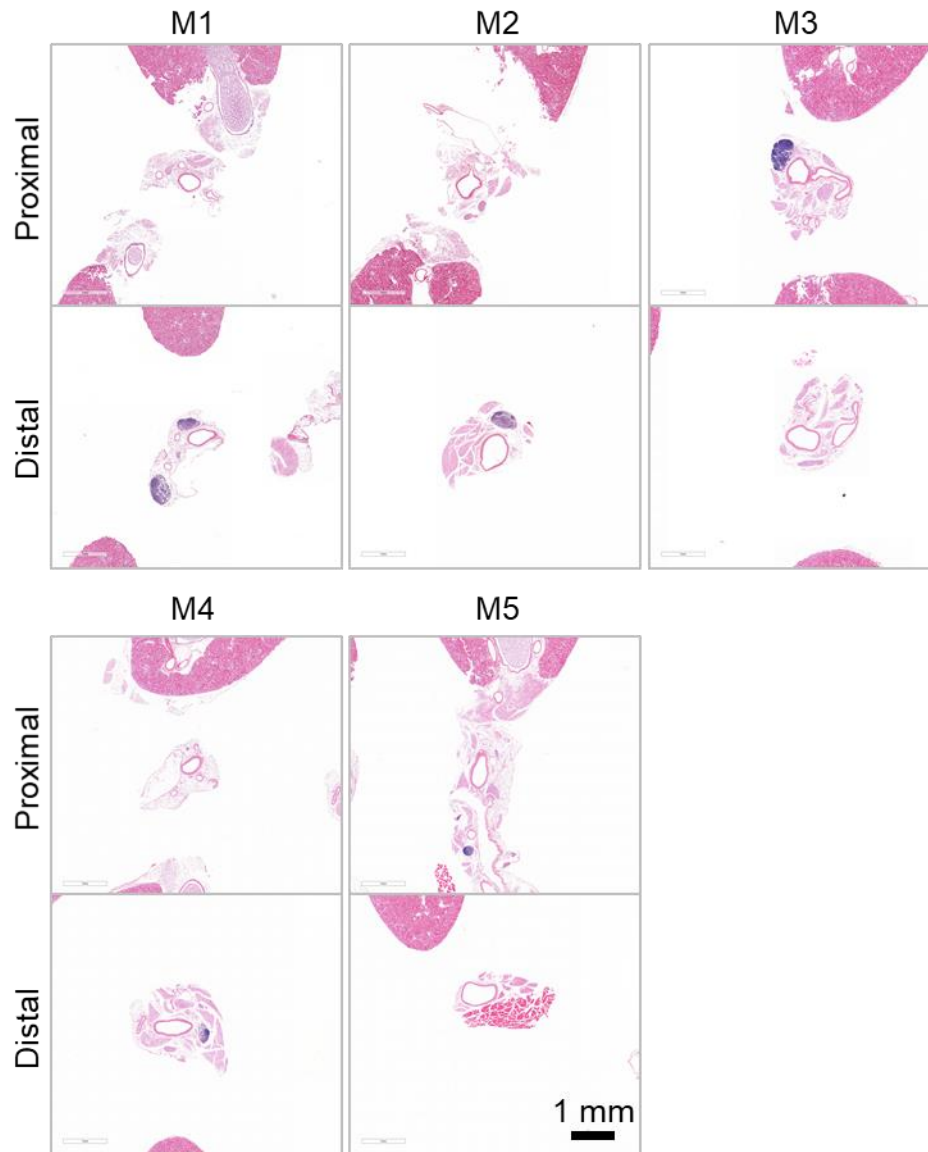
Appendix A Figure 10. Hematoxylin and Eosin (H&E) staining of mice treated with heat-inactivated elastase. Mice were euthanized 56 days post-surgery.

Movat's Pentachrome of Chronic Concentration Study – Heat Inactivated Group
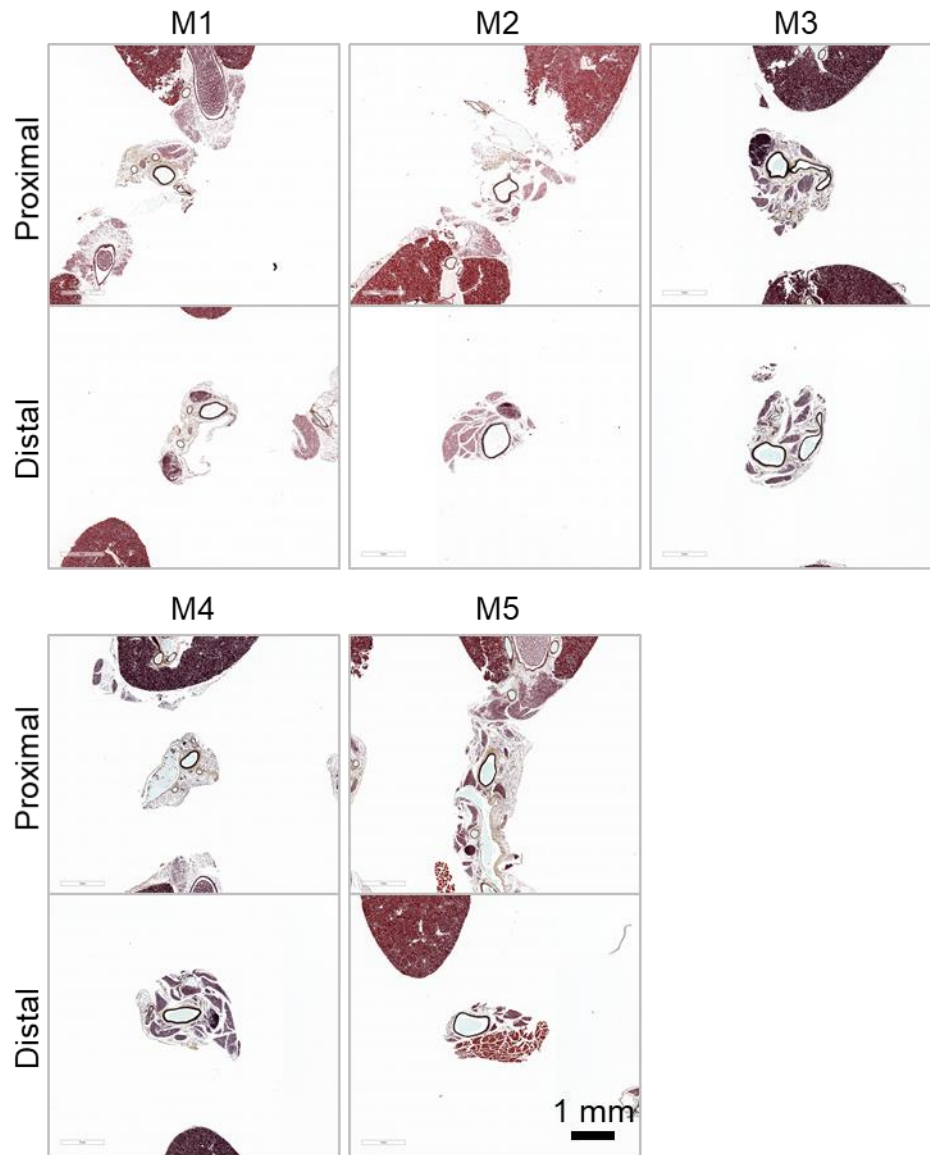
Appendix A Figure 11. Movat's Pentachrome (MPC) staining of mice treated with heat-inactivated elastase. Mice were euthanized 56 days post-surgery.

H&E of Terminal Concentration Study
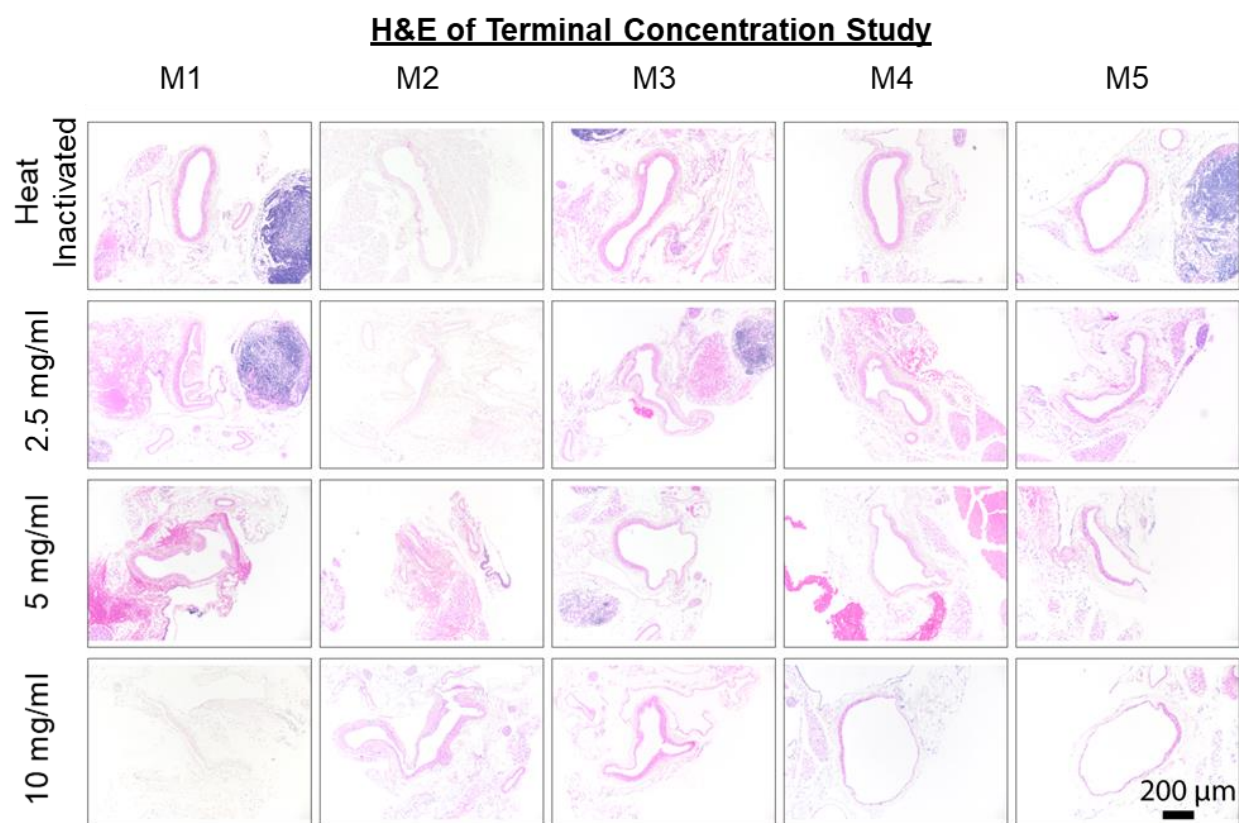
Appendix A Figure 12. Hematoxylin and Eosin (H&E) staining of mice euthanized immediately post-surgery. The concentrations are of elastase applied to the aorta.
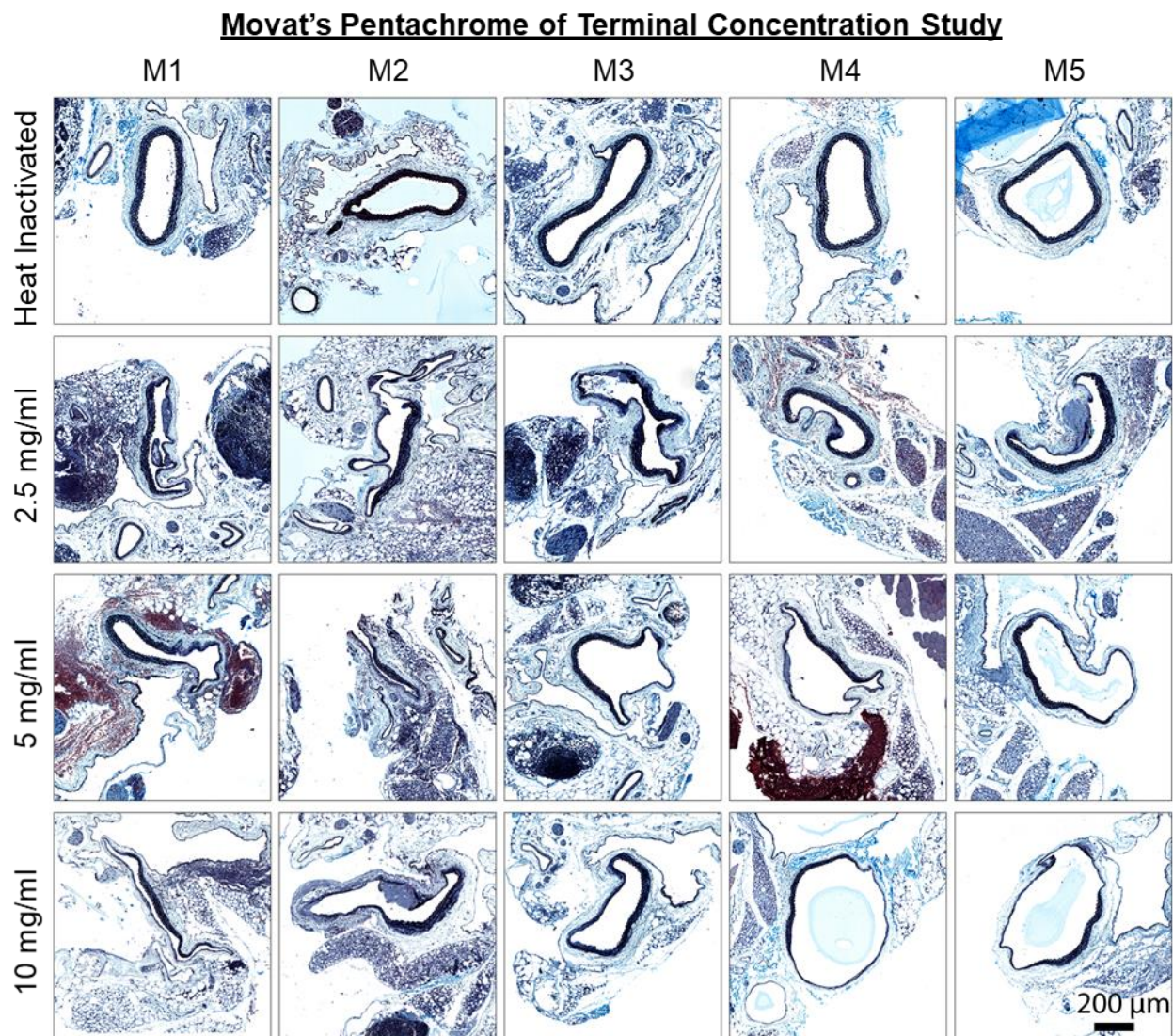
Appendix A Figure 13. Movat's Pentachrome (MPC) staining of mice euthanized immediately post-surgery. The concentrations are of elastase applied to the aorta.

H&E of 7-day Concentration Study
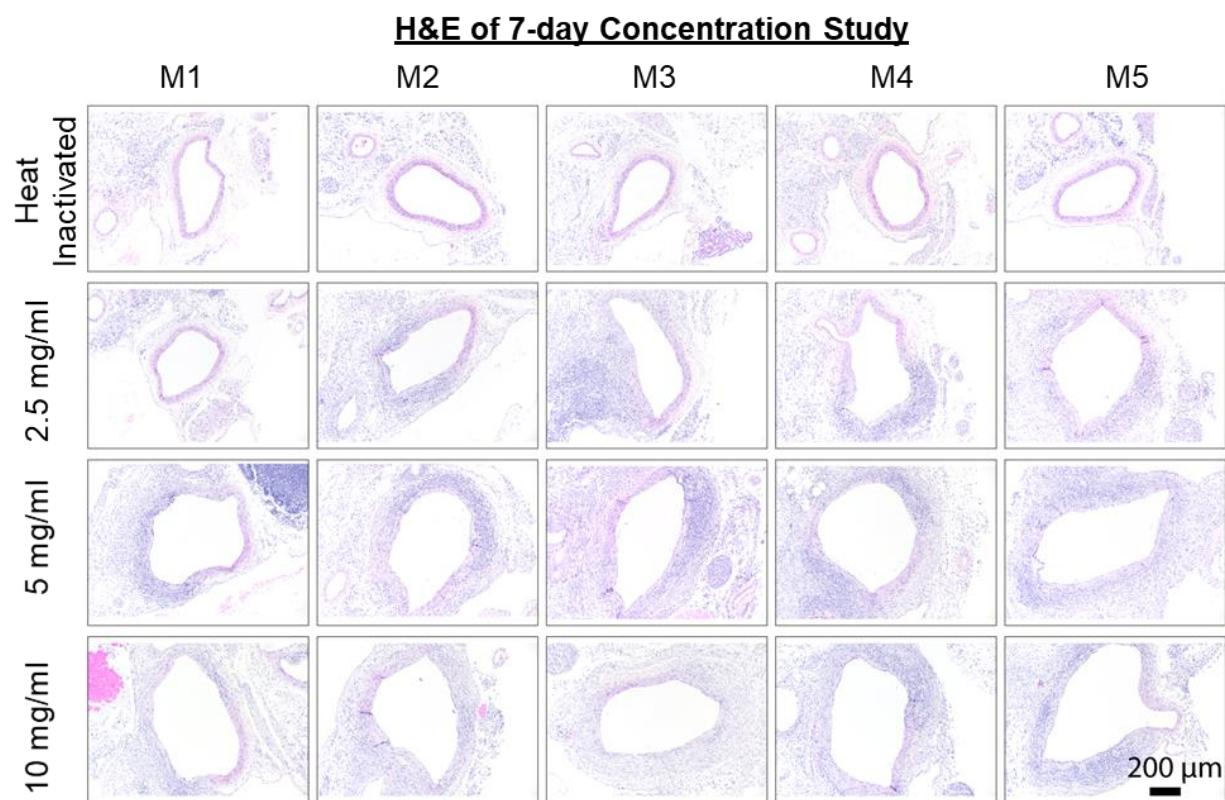
Appendix A Figure 14. Hematoxylin and Eosin (H&E) staining of mice euthanized 7 days post-surgery. The concentrations are of elastase applied to the aorta.
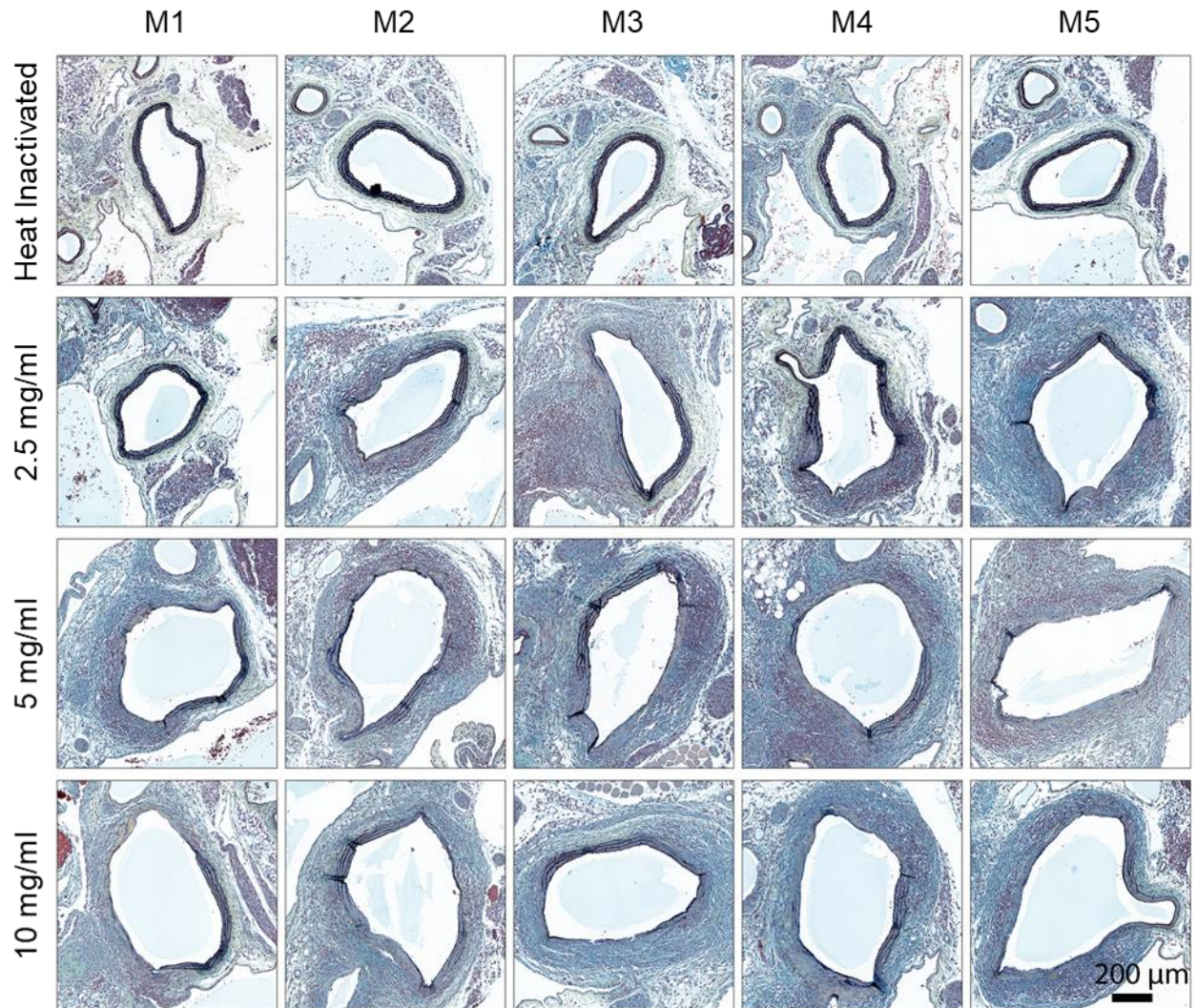
Appendix A Figure 15. Movat's Pentachrome (MPC) staining of mice euthanized immediately post-surgery. The concentrations are of elastase applied to the aorta.
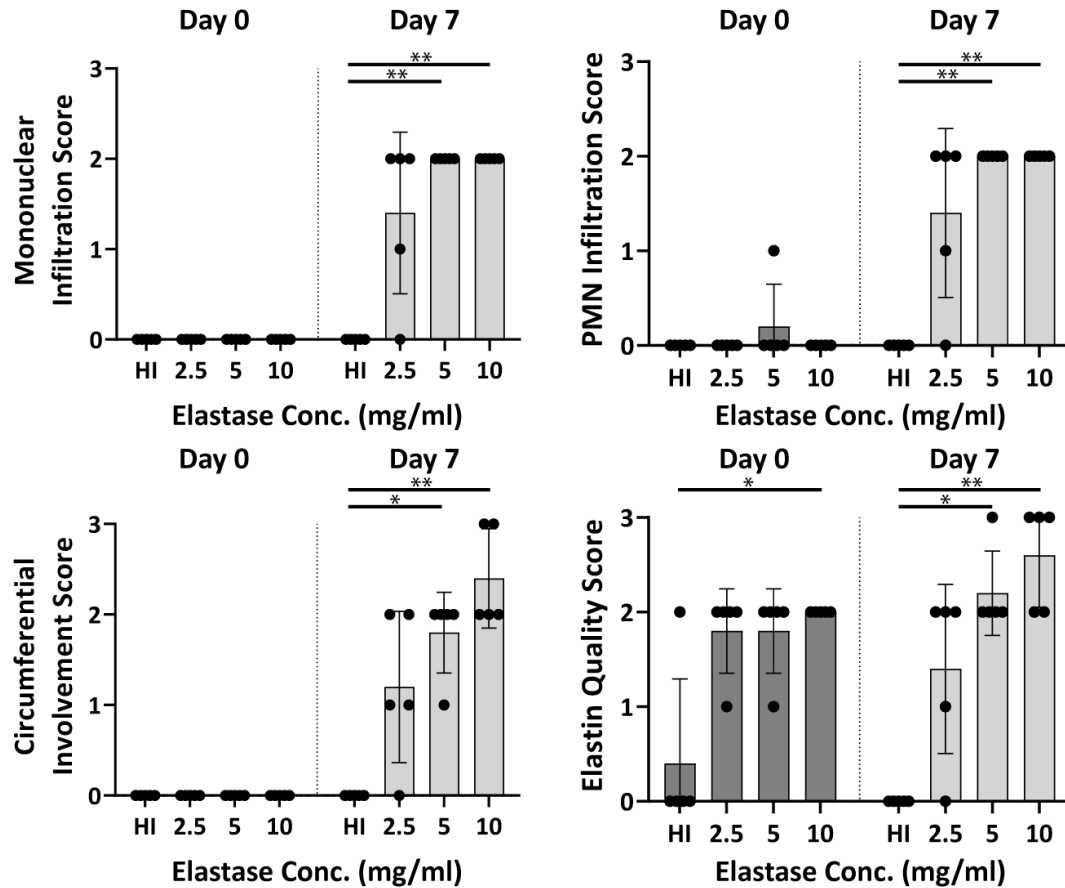
Appendix A Figure 16. Semi-quantitative scoring of the H&E slides indicated mononuclear and polymorphonuclear leukocytes infiltration in the elastase-treated mice by day 7. Additionally, the infiltration was spread throughout more of the circumference of the aorta in the 5 and 10 mg/ml groups. Lastly, elastin quality was immediately reduced post-surgery, which continued through day 7. Due to the non-parametric nature of the scoring, a Kruskal-Wallis test was performed within each time point with a post-hoc Dunn's test. *p<0.05, **p<0.01*
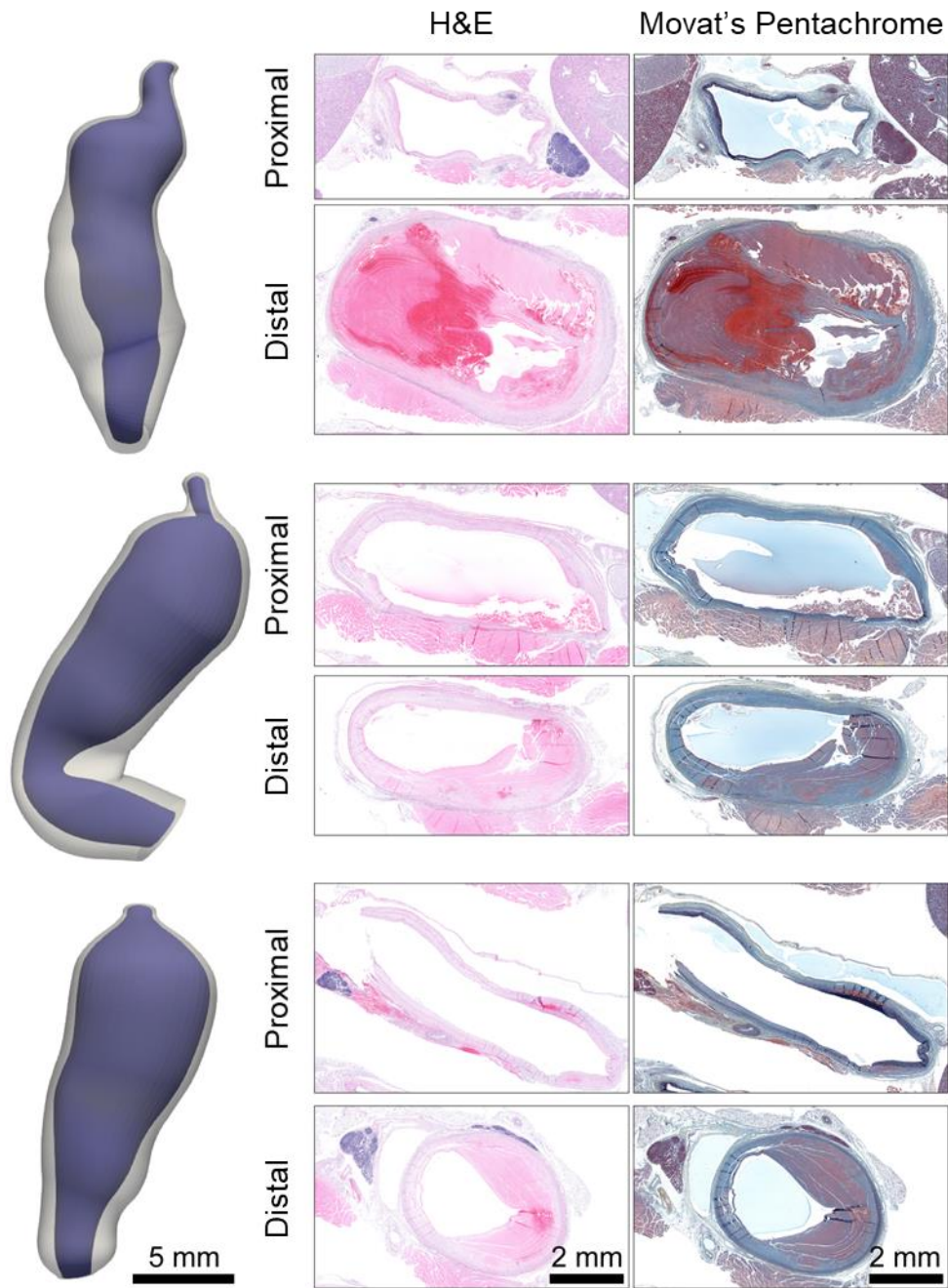
Appendix A Figure 17. 3D ultrasound-based segmentations of female mice 56 days post-surgery. The aneurysms in these female mice were larger than that of the males at the same timepoint, and all female mice developed thrombus. Also shown is Hematoxylin and Eosin (H&E) and Movat's Pentachrome (MPC) staining in the proximal and distal sections.
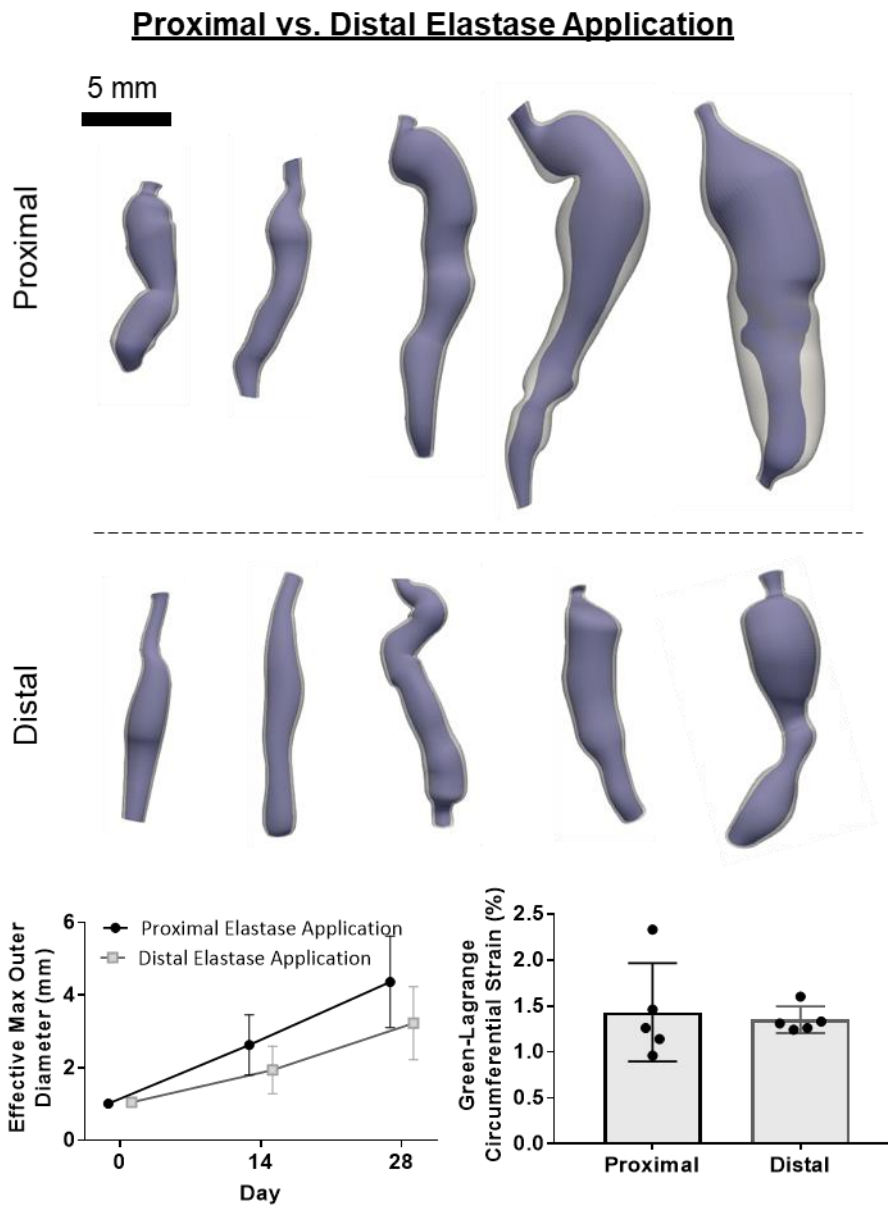
Appendix A Figure 18. 3D ultrasound-based segmentations demonstrating the effects of applying elastase more proximally (i.e. closer to the renal arteries) compared to distally (i.e. closer to the trifurcation). Although diameter is not significantly different between groups, animals that received a proximal elastase application typically resulted in larger aneurysms.
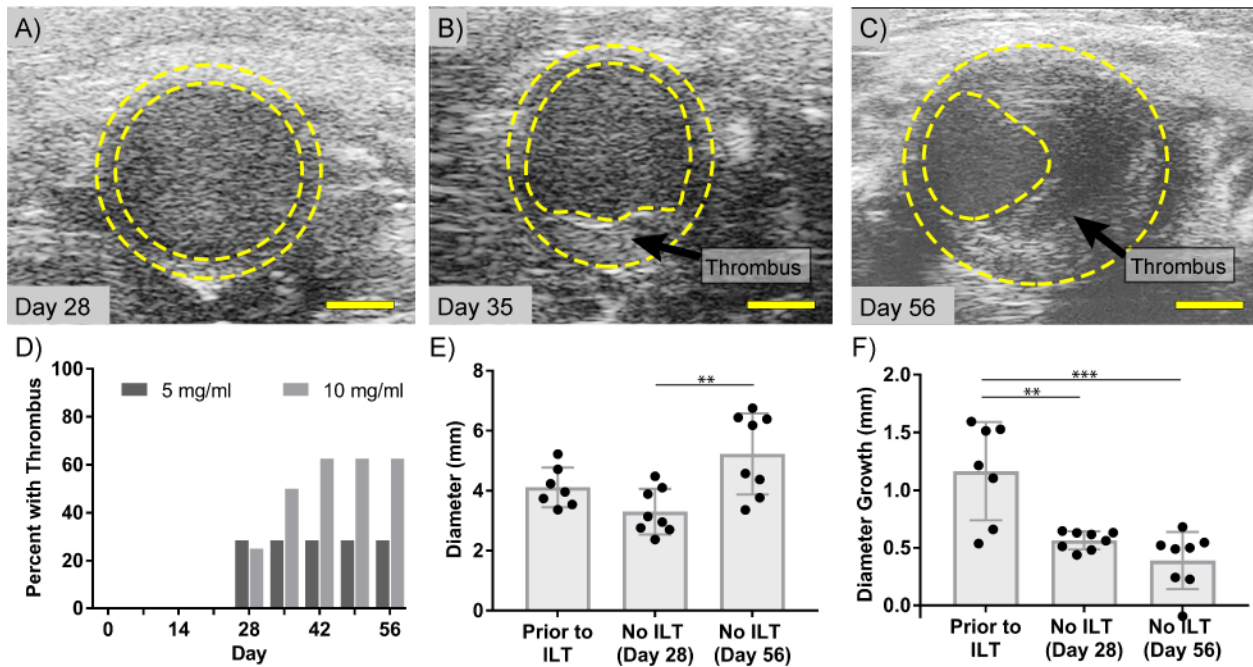
Appendix A Figure 19. Presence of thrombus was noted in some of the 5 mg/ml and 10 mg/ml elastase-treated mice. A) Ultrasound images of a representative mouse show no thrombus on day 28, B) compared to day 35. C) Over time, the thrombus continued to grow and develop, resulting in a much higher thrombus burden by day 56. D) The percentage of mice with thrombus was greater in the 10 mg/ml group than the 5 mg/ml group, though results were non-significant. E) Combining mice in the 5 mg/ml and 10 mg/ml groups, we found that measurements of diameter from the week prior to observing thrombus were not significantly different from mice that had no thrombus at days 28 or 56. F) In contrast, mice that formed thrombus had a significantly higher diameter growth rate compared to mice that had no thrombus. Scale bars are 1 mm. $*p<0.05$; $**p<0.01$; $***p<0.001$
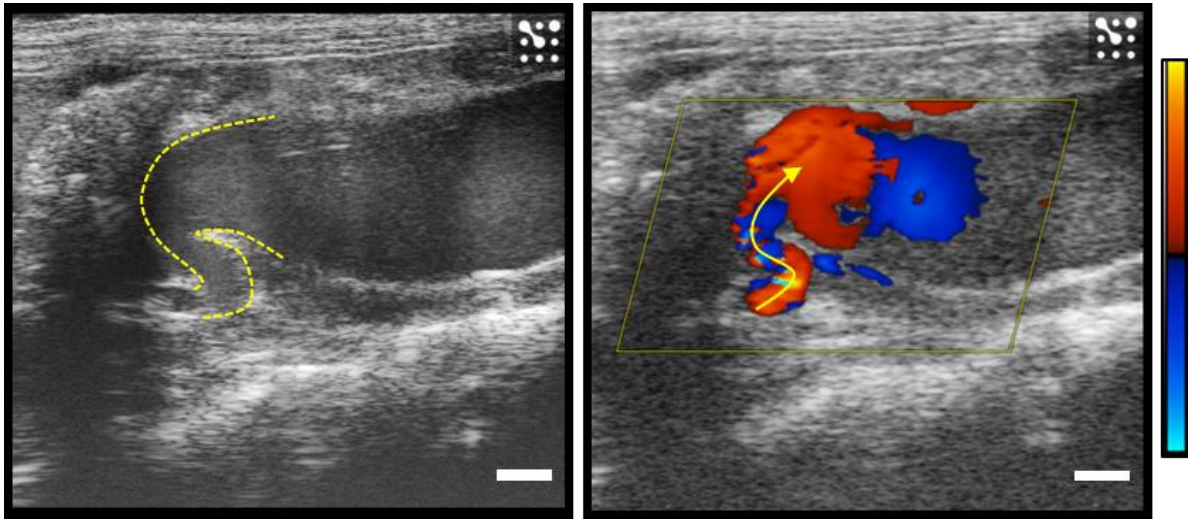
Appendix A Figure20. Long-axis EKV and Color Doppler images of a mouse the week prior to thrombus formation. Yellow dotted lines show the outline of the proximal portion of the vessel, while the yellow arrow indicates the path of blood flow. Overall, these images show a tortuous proximal non-aneurysmal region that causes a small jet inflow of blood into the abdominal aorta. Scale bar is 1 mm.
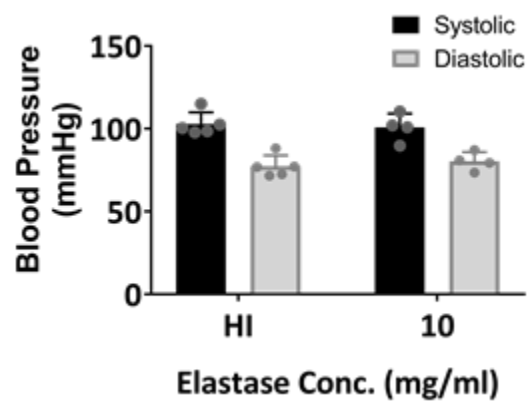
Appendix A Figure 21. The blood pressure of 5 mice from the heat-inactivated and 4 mice from the 10 mg/ml groups were measured on Day 56. Results demonstrate that the mice were normotensive.

APPENDIX B. SUPPLEMENTAL DATA FOR CHAPTER 4

This section provides supplemental tables and figures for Chapter 4 "Ultrasound Imaging of *In Vivo* Vascular Graft Remodeling."

Appendix B Table 1. Regression outcomes. Each regression is plotted as a specific row, with independent variables in separate columns. (+) and (-) denote a relation being significant with a direct or inverse relation, with the associated p-value in parentheses. ns denotes Not Significant (p>0.05).

	2X2	PPSI	Angle	PGS
Survival	- (<0.001)	+ (<0.001)	- (0.04)	ns
Elastin	N/A	- (0.003)	- (<0.001)	ns
Collagen	N/A	+ (<0.001)	+ (0.002)	+ (0.006)
Calponin	N/A	ns	- (0.004)	ns
CD68	N/A	ns	ns	- (0.007)
Distensibility	N/A	ns	- (0.027)	ns

Appendix B Table 2. Histological comparisons. Direct regressions of row and column histological findings for all explanted vessels. (+) and (-) denote a relation being significant with a direct or inverse relation, with the associated p-value in parentheses. ns denotes Not Significant (p>0.05). Duplicate and blank columns removed for clarity.

	Collagen	Elastin	Calponin
Elastin	- (<0.001)		
Calponin	ns	+ (<0.001)	
CD68	ns	+ (0.011)	+ (0.009)
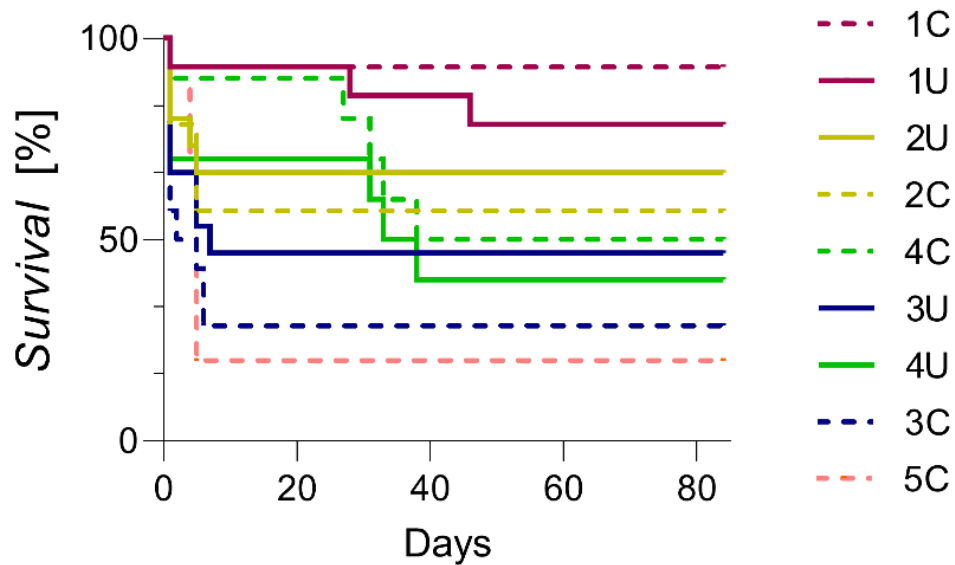
Appendix B Figure 20. Survival curve. Survival varied over time. Three time points showed the greatest drops in survival, all due to different modes of graft failure. The initial deaths (< 0 days) were found to be due to anastomotic bleeding. Other early deaths (1-7 days) were due to grafts dilating slightly, which created an opening between braids and resulted in internal bleeding. Later deaths (>26 days) were caused by rapid dilation of the graft upon degradation, which resulted in graft rupture and internal bleeding.
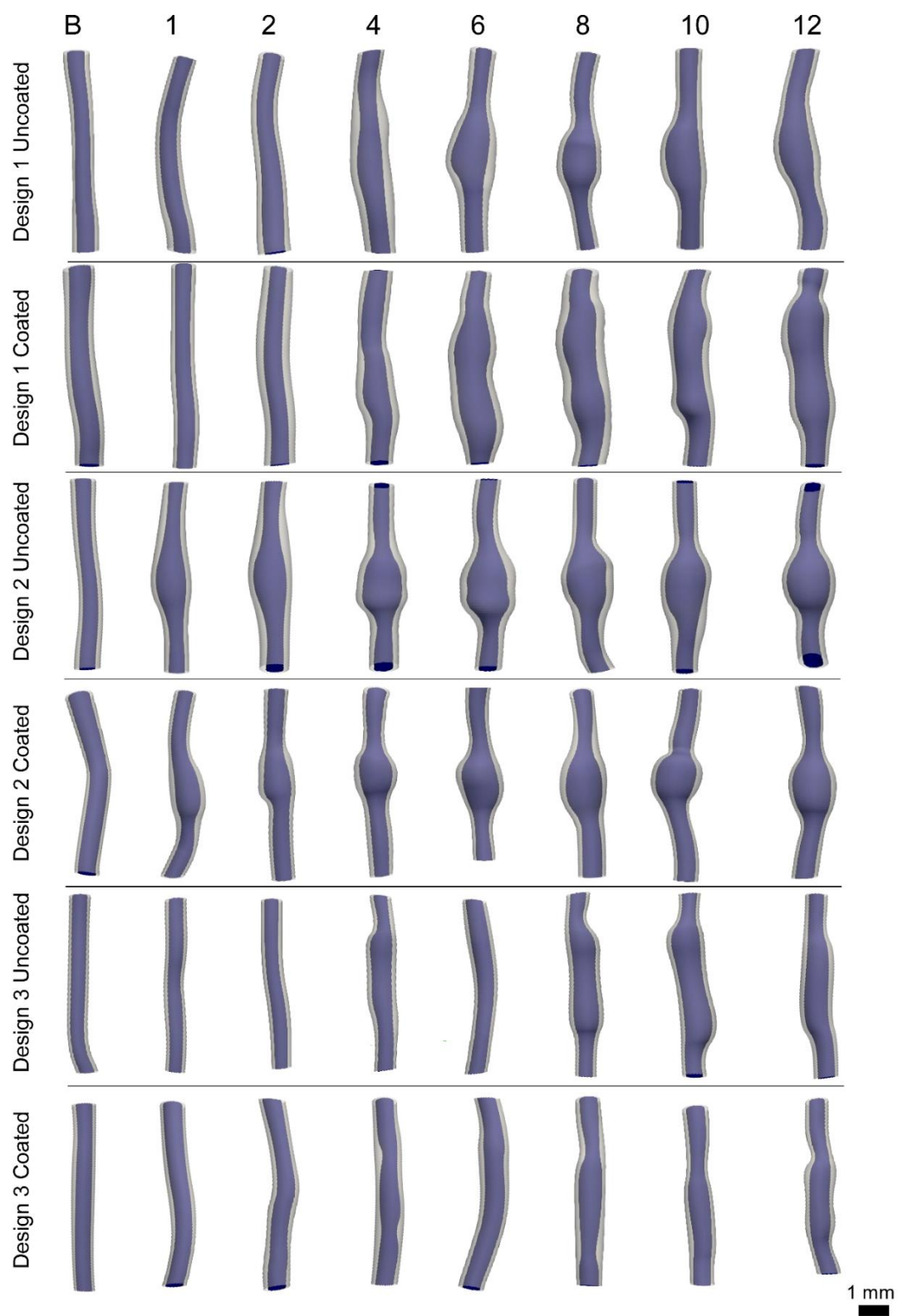
Appendix B Figure 21. Representative 3D segmentations. Volumetric representations from each vessel show the remodeling process of each graft type over 12 weeks.
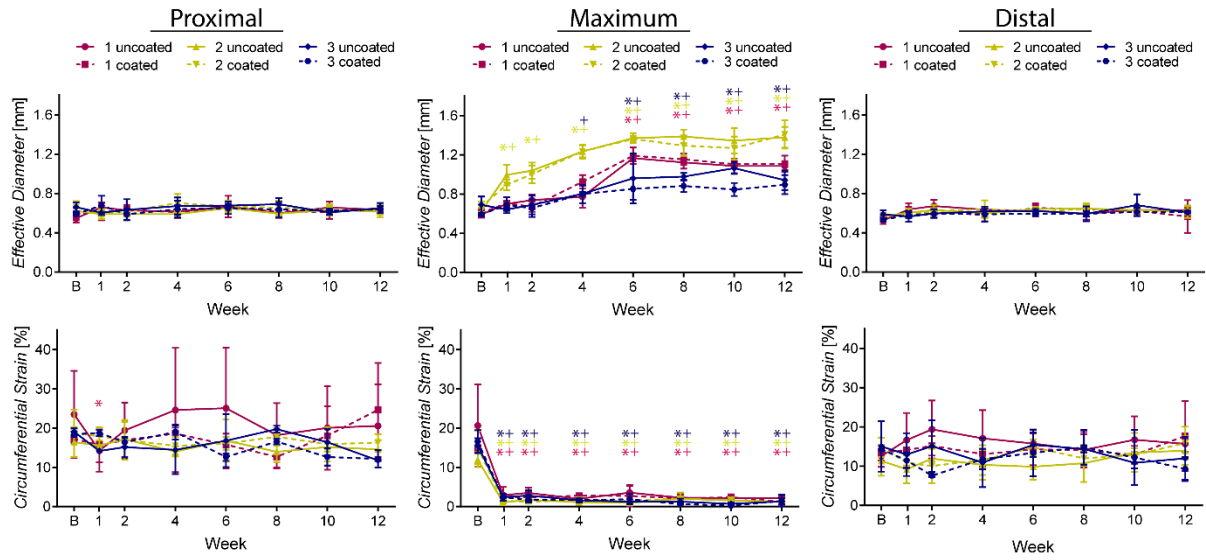
Appendix B Figure 22. Ultrasound-based diameters and strains. Diameter and strain were measured from the ultrasound images at locations proximal and distal to the graft, as well as at the location of the maximum diameter within the graft. An '*' refers to uncoated and a '+' refers to coated, with the color indicating the appropriate group (*p* < 0.05). All comparisons are relative to baseline.
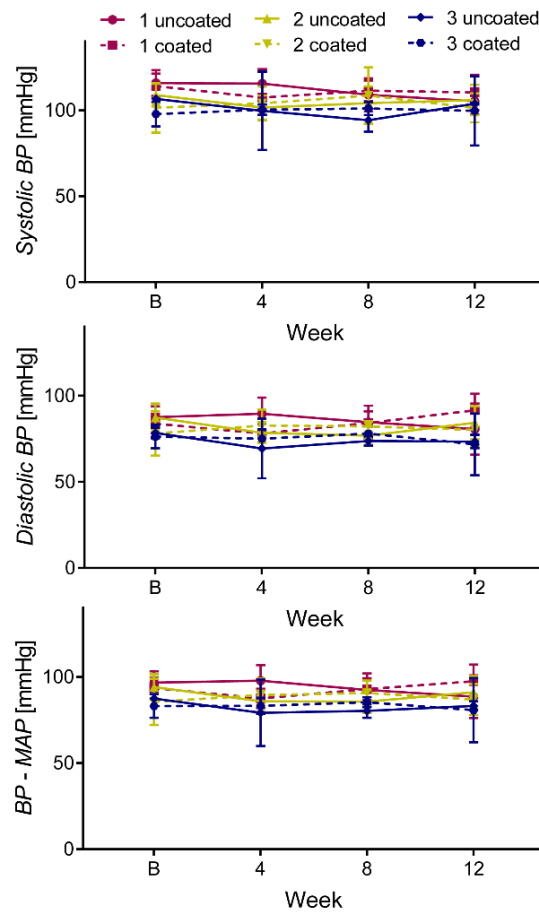
Appendix B Figure 23. Blood pressure measurements. Systolic, diastolic, and mean arterial blood pressure were unaffected by graft implantation, as demonstrated by the lack of significant differences among groups or compared to baseline.
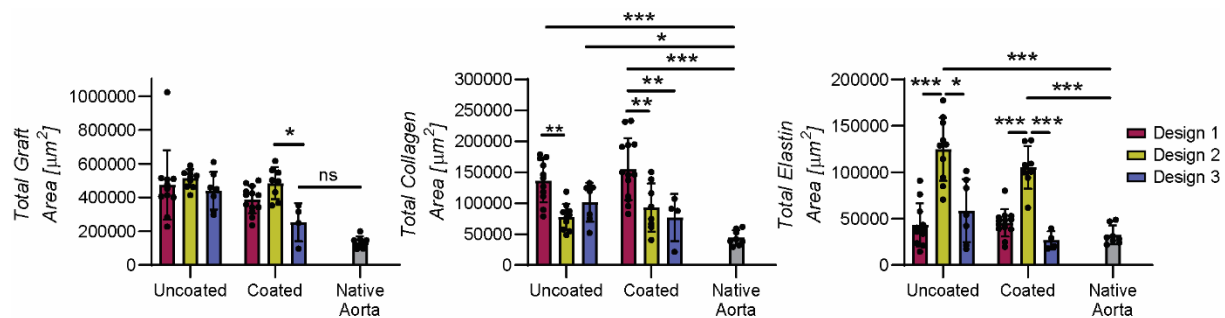
Appendix B Figure 24. Total area histological analysis. Graphs show total area measurements from histological samples. The first graph is the total tissue area of the vessels stained with Picro-Sirius Red and imaged with brightfield microscopy. Design 2 and 3 coated were the only Designs to differ significantly (p =0.03). Design 3 coated was also the only group to not significantly vary from the native aorta ($p = 0.78$). All other grafts had significantly greater tissue area ($p < 0.001$ for all groups). The second graph shows the collagen area measurements from vessels stained with Picro-Sirius Red and imaged with polarized light. Design 1 grafts contained significantly greater amounts of collagen compared to Design 2 for both uncoated ($p = 0.006$) and coated ($p = 0.004$) cohorts. Similar results were seen between Design 1 and 3 but only for the coated cohort ($p = 0.04$). Design 1 grafts, both uncoated and coated, as well as Design 3 uncoated grafts had significantly greater amounts of collagen compared to the native samples ($p < 0.001$, $p < 0.001$, $p = 0.04$ respectively). The last graph shows the total elastin area measurements from the Hart's elastin stain. Design 2 uncoated and coated groups had greater amounts of elastin compared to the other designs and the native aorta ($p = 0.02$ between D2 and D3 coated, $p < 0.001$ for all other groups). n=4-13 per group. Comparisons were made with ANOVA with a post-hoc Sidak's or Dunnett's test. (* < 0.05, ** <0.01, *** <0.001)
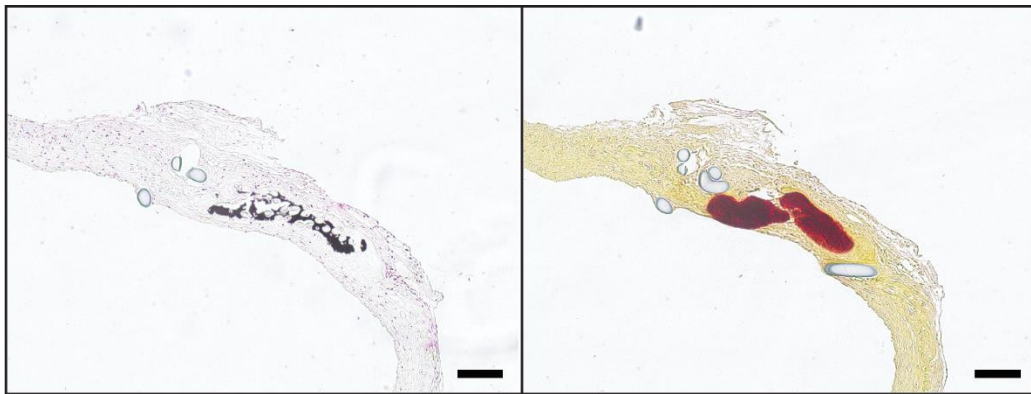
Appendix B Figure 25. Calcification. Representative image of calcification from von Kossa and Alizarin Red staining. The graft is from the Design 2 uncoated cohorts. Images were taken using a 20x objective. Scale bar = 100 µm.
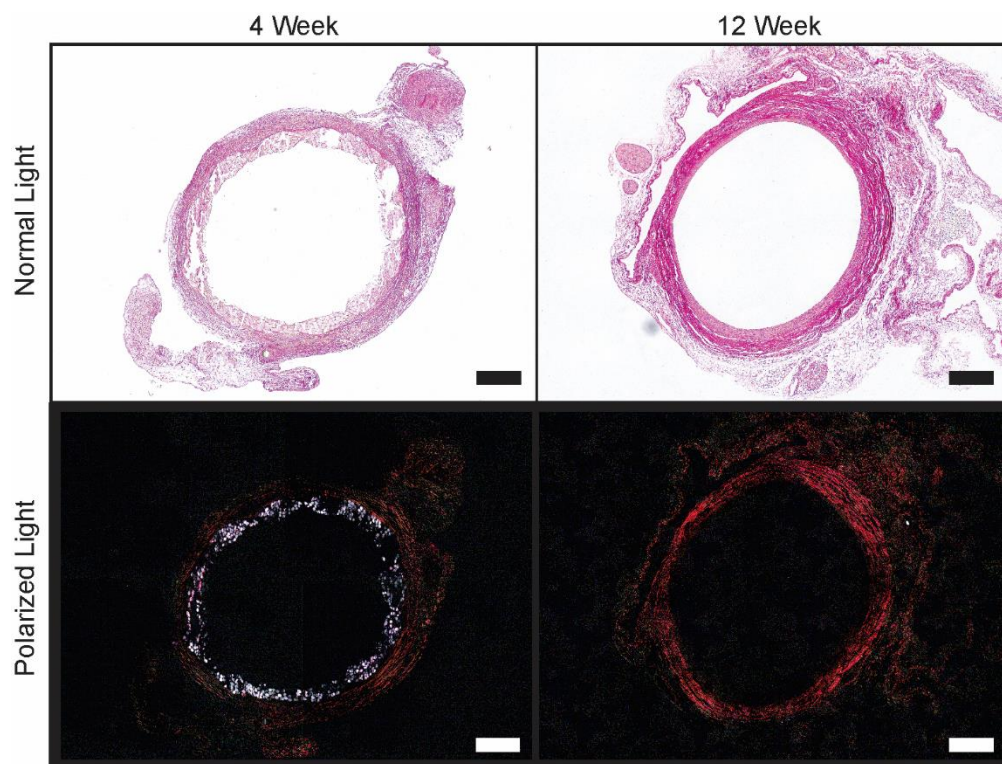
Appendix B Figure 26. Fiber degradation. Representative images of grafts at 4 and 12 weeks stained with Picro-Sirius Red and imaged with normal and polarized light. These are Design 1 coated grafts. At 4 weeks, PGA fibers show up clearly under polarized light due to their birefringence. At 12 weeks there is no indication of fibers remaining upon examination with polarized light. It is possible that PGA polymer still exists in the wall but there does not appear to be any large fibers providing mechanical support. Images were taken using a 20x objective. Scale bar = 200 µm.

APPENDIX C. A SECOND LAB - MANUSCRIPTS IN BONE BIOMECHANICS

While the majority of my dissertation research has focused on vascular imaging with ultrasound, a substantial amount of work has also been performed in the area of bone biomechanics. In this section, the first-author publications completed during my graduate studies are highlighted.

C.1   Muscle Contraction Induces Osteogenic Levels of Cortical Bone Strain despite Muscle Weakness in a Mouse Model of Osteogenesis Imperfecta

Abstract

Mechanical interactions between muscle and bone have long been recognized as integral to bone integrity. However, few studies have directly measured these interactions within the context of musculoskeletal disease. In this study, the osteogenesis imperfecta murine model (oim/oim) was utilized because it has both reduced bone and muscle properties, allowing direct assessment of whether weakened muscle is able to engender strain on weakened bone. To do so, a strain gauge was attached to the tibia of healthy and oim/oim mice, muscles within the posterior quadrant of the lower hind limb were stimulated, and bone strain during muscle contraction was measured. Results indicated that the relationship between maximum muscle torque and maximum engendered strain is altered in oim/oim bone, with less torque required to engender strain compare to wild-type and heterozygous mice. Maximum muscle torque at 150 Hz stimulation frequency was able to engender ~1500 $\mu\varepsilon$ in oim/oim animals. However, even though the strain engendered in the oim/oim mice was high relative to historical bone formation thresholds, the maximum strain values were still significantly lower than that of the wild-type mice. These results are promising in that they suggest that muscle stimulation may be a viable means of inducing bone formation in oim/oim and potentially other disease models where muscle weakness/atrophy exist.

Introduction

Muscle and bone are intricately linked, both physically and chemically. From a strictly mechanical perspective, muscles attach to bone and use these bone attachment sites as the lever arms by which they enable movement. In fact, the relatively small distance between the muscle attachment site and the joint creates an unfavorable lever arm, implying that during movement, the muscle must exert a much larger force on bone compared to ground reaction forces. Lu et al. found that less than 30% of the forces transmitted through the femur during normal gait were derived from the ground reaction force, with a much higher 70% driven from muscle contraction.[1] Similarly, Wehner et al. calculated the internal loads in the human tibia during gait and found that the forces were up to 4.7 times the body weight.[2] For this reason, some have suggested that muscle may be a primary means of mechanically stimulating bone.[3]

Mechanical loading has been well-established as integral to maintaining bone integrity. Below a strain threshold, bone loss will occur while above a different strain threshold, bone formation will occur.[4,5] Given the importance of mechanical loading to bone health, and considering the ability of muscle to engender significant forces on bone, it follows that muscle health is likely also critical to bone health. Indeed, correlative relationships between muscle and bone have been well-documented.[6,7] For example, in situations of long-term bedrest, low bone mass and poor muscle tone occur together.[8] Similarly, osteoporosis is often associated with sarcopenia.[9,10] A number of studies have even shown that skeletal muscle mass can be a predictor of bone mass[11] or bending stiffness.[12] Interestingly, these correlations also occur with genetic diseases that primarily impact only one aspect of the musculoskeletal system (i.e. directly impacting only bone or only muscle).

Osteogenesis Imperfecta (OI) is a bone disease driven by a mutation to the genes involved in the Type I collagen synthesis pathway.[13] Patients with OI show skeletal weakness, ranging from mild to severe to perinatal lethal.[14] Despite OI being considered a "bone disease," muscle is often also impacted in OI patients,[15–18] with the degree of impact dependent on the severity of the disease.[19] In the preclinical realm, one commonly used mouse model of OI is the Osteogenesis Imperfecta Murine (oim/oim) model. Oim/oim results from a single G nucleotide deletion in the COL1A2 gene. This change causes a frameshift in the final 48 amino acids at the C terminus, resulting in an extra amino acid which renders the α2 chain non-functional. The end result is the accumulation of homotrimeric collagen instead of the normal heterotrimeric molecule.[20] In its

homozygous form, oim/oim mice show significant skeletal weakness and spontaneous fractures, while the heterozygous form is milder.[20–24] Also similar to the human condition, oim/oim mice have muscular weakness.[25] In the homozygous mice, muscle size and strength are significantly reduced, while the heterozygous mice show a milder, non-significant reduction.[25]

Given that muscle and bone are both impacted by OI, it is unclear how efficiently weakened muscle is able to engender strain on the bone. In other words, if only muscle were affected, then weaker muscle would imply lower forces (and thereby lower strain) on bone. In contrast, if only bone were affected, then the muscle force would remain the same, but the bone strain would presumed to be increased because the bone is weaker. To address this uncertainty, we attached a strain gauge to the anteromedial mid-diaphysis of the tibia of both wild-type and oim/oim mice and then conducted *in vivo* muscle stimulation to induce plantar flexion. This setup enabled us to collect muscle ankle torque and bone strain simultaneously. In addition, *ex vivo* morphological analyses of bone and muscle by micro-computed tomography (CT) were used to assess bone mass and muscle area. Our hypothesis was that the muscle-bone unit would find an equilibrium such that engendered bone strain would be conserved across mouse strains.

Methods

Experimental Overview

Wild-type (WT), heterozygous (Het), and homozygous (oim/oim) oim mice were bred in-house and maintained on a C57BL/6J background.[26] Mice were group housed in a facility with 12-hour light/dark cycles and access to food and water *ad libitum*. At 16 weeks of age, male mice (n= 7-9/group; Appendix C.1 Table 1) from each genotype underwent surgery to attach a strain gauge to the anteromedial portion of the mid-diaphysis of the right tibia. After attachment of the gauge, but while still under anesthesia, the mouse was moved to a muscle testing machine and the tibial nerve was stimulated to induce plantarflexion. After collection of torque and strain data, the mouse was euthanized. The strain gauge was manually checked to ensure firm attachment, and then the right limb was dissected out, wrapped in saline, and stored at −20 °C until imaging by micro-computed tomography (micro-CT). This initial imaging session was used to assess any obvious bone abnormalities (broken or bent bones, etc.) and to estimate muscle cross-sectional area. Soft tissue was then dissected away, and the tibia was imaged again by micro-CT for bone structural

information. All procedures were conducted with prior approval from Indiana University School of Medicine IACUC.

Appendix C.1 Table 1. Number of animals per group.

	WT	HET	OIM
Initial Group Numbers	8	9	7
Broken Tibia or Woven Bone (excluded from all analysis)	0	1	1
Poor Strain Gauge Placement (excluded from strain)	3	2	2

Strain Gauge Attachment

Mice were anesthetized with 1-3% isoflurane and chemical depilatory cream was applied to the lower right hind limb to remove hair. An incision was then made through the skin and fascia, exposing the anteromedial portion of the midshaft tibia. The surface of the bone was degreased, and a single-element strain gauge with gauge dimensions of 2.54 mm L x 0.51 mm W (EA-06-015DJ-120, Vishay Precision Group, Shelton, CT) was aligned with the long axis of the tibia and attached using a cyanoacrylate-based adhesive (Loctite Super Glue, Henkel-Adhesives, Düsseldorf, Germany). During strain measurement, the gauge was attached to a strain gauge conditioner (2100 Signal Conditioning Amplifier System, Micro-Measurements, Vishay Precision Group, Shelton, CT) via a quarter-bridge completion. Calibration to ensure accurate conversion from volts to strain was performed by adjusting the signal gain based on the gauge factor, per manufacturer instructions.

Muscle Stimulation

Isometric muscle stimulation was performed using an *in vivo* setup (Aurora Scientific Inc., Ontario, Canada). The mouse's foot was taped to the machine's footplate (a torque transducer) which was used to measure ankle torque during plantarflexion. Two sterile shielded monopolar needle electrodes were inserted on either side of the tibial nerve, slightly proximal to the mid-calf level, and were adjusted to ensure maximum twitch response. This setup of the electrodes primarily stimulates the gastrocnemius and soleus muscles to induce plantarflexion, but also has some

contributions from the plantaris, flexor hallucis longus, flexor digitorium longus, and tibialis posterior. The muscles were then stimulated (0.5 msec pulse width), beginning at 25 Hz and extending to 300 Hz in 25-Hz increments. The muscles were stimulated at each frequency for 200 msec, followed by 45 seconds of rest before moving to the next frequency. During stimulation, both muscle torque and bone strain were recorded (Appendix C.1 Figure 1). Data were analyzed using a custom Matlab script to determine maximum torque and strain at each stimulation frequency. In addition, the torque-time slope at each stimulation frequency was calculated by fitting a linear regression to the maximum rising slope of each torque-time graph.
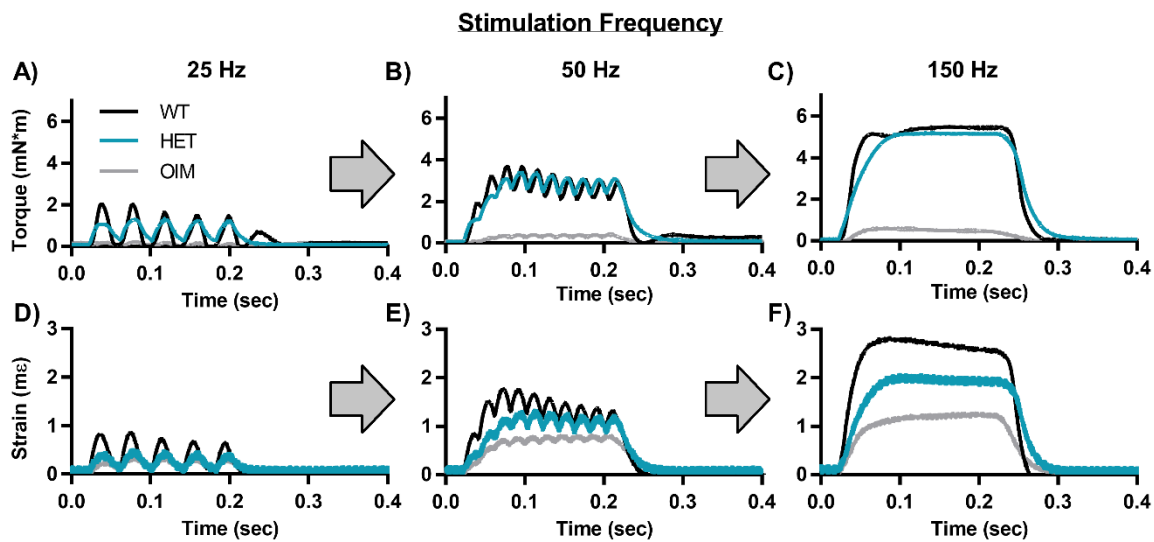
Appendix C.1 Figure 1. Example torque (A-C) and strain (D-F) curves during muscle stimulation of WT, Het, and oim/oim at 25 Hz (A,D), 50 Hz (B,E), and 150 Hz (C,F) stimulation frequency. Note tetanic muscle contraction occurred by 150 Hz.

Micro-Computed Tomography

Whole right limbs were scanned by high resolution micro-CT (Skyscan 1176; Bruker, Kontich, Belgium) at an 8.4 μm resolution (V = 50 kV; I = 500 μA; Step size = 0.9°; no averaging).[27] Projection images were used to assess the presence of broken bones and/or calcified tendon. After reconstruction and rotation, a 1-mm region of interest at the tibial mid-diaphysis was used to estimate total soft-tissue volume and bone volume. These volumes were converted to averaged areas by dividing the volume by the length of the region of interest (1 mm). Muscle area

was then calculated as the difference between the total soft-tissue area and the area of the bone and marrow.

The soft tissue was then removed in order to acquire a more crisp image set, and the tibia was scanned again by high resolution micro-CT (Skyscan 1172; Bruker, Kontich, Belgium) using the following parameters: 10 μm resolution, 60 kV tube voltage, 167 μA current, 0.7-degree increment angle, and 2-frame averaging. To convert gray-scale images to mineral content, hydroxyapatite calibration phantoms (0.25 and 0.75 g/cm3 CaHA) were also scanned. After reconstruction and rotation (nRecon and DataViewer, Bruker), 1-mm regions of interest were selected in the proximal metaphysis (Appendix C.1 Supplemental Text and Figure 1) and mid-diaphysis for analysis. In the mid-diaphysis, the cortical shaft was analyzed using a custom Matlab script (MathWorks, Inc. Natick, MA) to determine areas (total cross sectional area and marrow area), periosteal and endocortical bone surface, maximum principal moment of inertia, and tissue mineral density.

Statistical Analysis

All statistics were performed in Prism (Graphpad Software, San Diego, CA). For torque and strain data, a two-way ANOVA was performed to assess the main effects of stimulation frequency and genotype. A post-hoc Tukey HSD test was then performed at each stimulation frequency to assess individual differences between genotypes ($p<0.05$). For CT data, we used a one-way ANOVA with a post-hoc Tukey HSD test to determine effects of genotype ($p<0.05$). For the strain-torque regression, a linear regression was used to assess correlations between variables. Comparison of the linear regression slopes was assessed by ANCOVA with post-hoc Tukey HSD test ($p<0.05$). All data are presented as mean ± standard deviation.

Results

General Animal Information

Animal numbers for each group are shown in Appendix C.1 Table 1. One oim/oim mouse had a broken right tibia at the time of surgery and one Het mouse showed a large area of woven bone. Both were excluded from all analysis. In addition, difficulties with strain gauge attachment such as a non-secure gauge, off-axis placement, or a break in the wire or gauge precluded some

mice from strain analysis (Appendix C.1 Table 1). Note that the mice with strain gauge attachment errors were still included in other analyses (micro-CT and muscle torque).

A significant difference in body weight was noted for oim/oim (18.7±2.6 g) compared to both Het (28.4±2.1 g; p<0.001) and WT (28.4±1.7 g; p<0.001) mice. Tibial length was also significantly lower in oim/oim (16.2±0.8 mm) compared to Het (17.8±0.4 mm; p<0.001) and WT (18.1±0.2 mm; p<0.001). There were no significant differences in weight or tibial length between WT and Het.

Muscle Contractile Force and Cross Sectional Area

Measurements of maximum torque at each stimulation frequency showed significant muscle weakness in oim/oim in all but the lowest stimulation frequency (Appendix C.1 Figure 2A). To further explore maximum torque during tetanic contraction, data was plotted at the 150 Hz stimulation frequency (Appendix C.1 Figure 2B–C). Maximum torque was significantly lower in oim/oim by 77% (p<0.001) and 74% (p<0.001) compared to the WT and Het, respectively (Appendix C.1 Figure 2B). There was also a marked suppression in the rising slope of the torque-time curves in the Het compared to the WT (p=0.03) and in the oim/oim compared to both the WT (p<0.001) and Het (p<0.001) (Appendix C.1 Figure 2C). Similar to the functional muscle assessment, muscle cross-sectional area estimated by micro-CT indicated that oim/oim had 46% (p<0.001) and 49% (p<0.001) less muscle area compared to WT and Het (Appendix C.1 Figure 2D). No significant differences were noted between WT and Het for any muscle parameters.
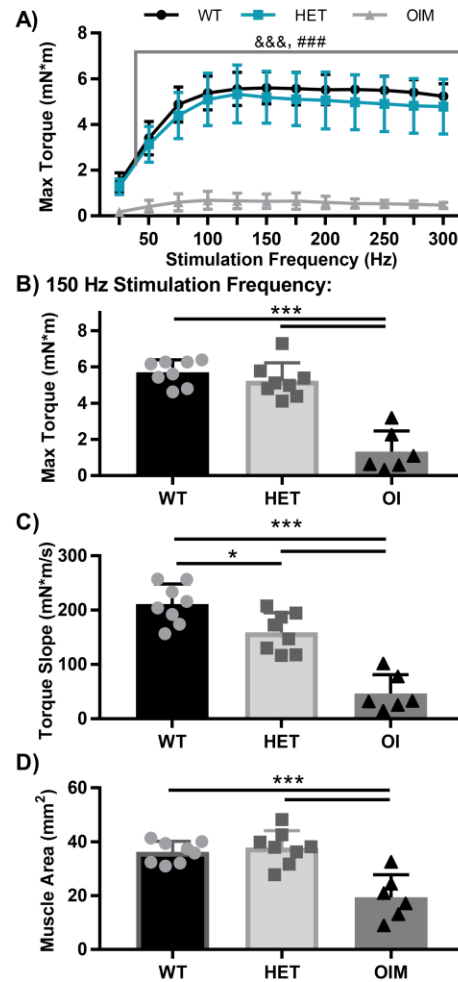
Appendix C.1 Figure 2. Functional and area-based muscle analysis indicated significant muscle weakness in oim/oim, but not Het. A) Frequency-based analysis showed reduced maximum torque in oim/oim at all but the lowest stimulation frequency (25 Hz). B) Maximum torque at a single frequency (150 Hz) further demonstrates this reduction. C) Interestingly, we also noticed that the rising torque-time slope was reduced, with oim/oim having the shallowest slope and Het having an intermediate slope. D) CT analysis of muscle area also indicated muscle weakness in oim/oim. In panel A, "&" indicates comparison between WT and oim/oim and "#" between Het and oim/oim (p<0.001 for both). In panels B-D, *p<0.05, **p<0.01, ***p<0.001 with the bars showing comparisons.

Cortical Bone Structural Parameters

Oim/oim mice also had significantly smaller bones compared to both WT and Het (Appendix C.1 Figure 3A–C). Oim/oim showed a 24% lower cross-sectional area compared to both WT and Het (both p<0.01; Appendix C.1 Figure 3D). A similar difference was observed in marrow area

(−22% vs WT, −19% vs Het; both p<0.01; Appendix C.1 Figure 3E). Measurements of periosteal and endocortical perimeters corroborated these results, with both showing significantly smaller values in oim/oim mice (Appendix C.1 Figure 3G–H). This smaller geometry led to 43% and 46% lower maximum moment of inertia in oim/oim compared to WT (p<0.05) and Het (p<0.01), respectively (Appendix C.1 Figure 3F). Similarly, minimum moment of inertia was 45% and 43% lower in oim/oim compared to WT (p<0.01) and Het (p<0.01), respectively. Interestingly, oim/oim had significantly higher tissue mineral density than WT (p<0.01) and Het (p<0.05), suggesting increased mineralization (Appendix C.1 Figure 3I). No significant differences were noted between WT and Het for any cortical parameters.
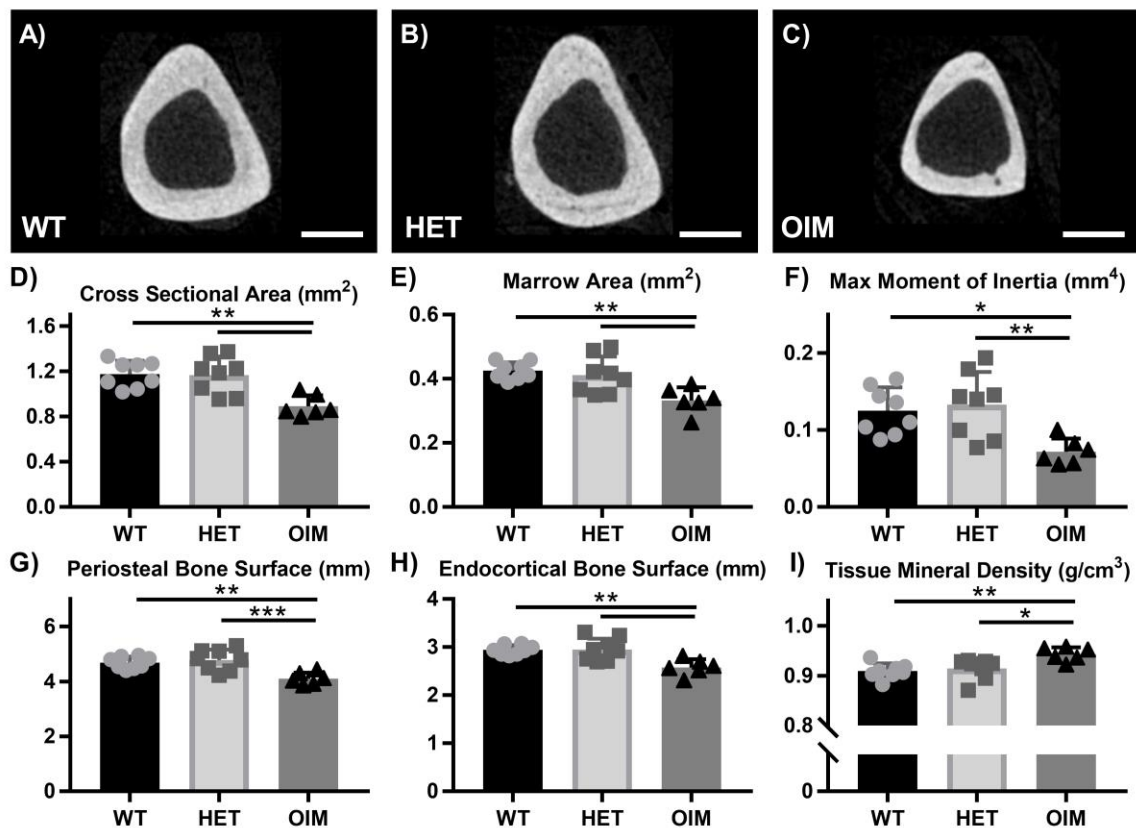
Appendix C.1 Figure 3. Functional Example cortical micro-CT images at the mid-diaphysis of A) WT, B) Het, and C) oim/oim. Oim/oim had smaller bones as indicated by D) reduced cross-sectional area, E) marrow area, G) periosteal bone surface and H) endocortical bone surface. F) Together, these resulted in a reduced cross-sectional maximum moment of inertia, suggesting that oim/oim bones have reduced resistance to bending. I) Tissue mineral density was increased in oim/oim. White scale bars: 0.5 mm. *p<0.05, **p<0.01, ***p<0.001 with the bars showing comparisons.

Bone Strain and Torque-Strain Interaction

Despite the significant muscle weakness noted in the oim/oim mice, the engendered tensile strain during maximum tetanic contraction at the 150 Hz stimulation frequency was 1488±416 με, which is within the range of strains shown to induce a bone formation response in this age of mouse.[4,5] This value was 41% lower compared to WT (p=0.03). Het values of strain induced at 150 Hz were intermediate and not significantly different from either WT or oim/oim (Appendix C.1 Figure 4B). Similar results were observed at the other frequencies, with all but the lowest two frequencies showing significantly lower strain in the oim/oim mice compared to wild-type mice at a matched frequency (Appendix C.1 Figure 4A).

To further demonstrate the relationship between bone and muscle, bone strain per unit of muscle torque was calculated. Oim/oim had significantly higher strain per torque compared to both WT and Het at all frequencies (Appendix C.1 Figure 4C). At 150 Hz stimulation frequency, oim/oim had a 441% greater ratio than WT and a 558% greater ratio than Het (both p<0.001; Appendix C.1 Figure 4D). Similarly, when all stimulation frequencies and mice were plotted to examine correlations between strain and torque (Appendix C.1 Figure 4E), oim/oim had a significantly steeper slope than either WT or Het (both p<0.001).

Tendon Calcification and Broken Calcaneus

As assessed by CT (Appendix C.1 Figure 5), oim/oim had the greatest number of mice with calcification of the Achilles tendon, though calcification was also observed in some Het. In addition, over half of the oim/oim had a broken right calcaneus, with large callus formation indicating a fracture that had occurred before the muscle stimulation and that had started to heal. These mice (n=4) had 76% lower maximum muscle torque than oim/oim with intact calcaneus (n=2). Given that the transmission of force from the muscle goes through the tendon and calcaneus, the tendon and calcaneus are likely important contributors to muscle-bone interactions.
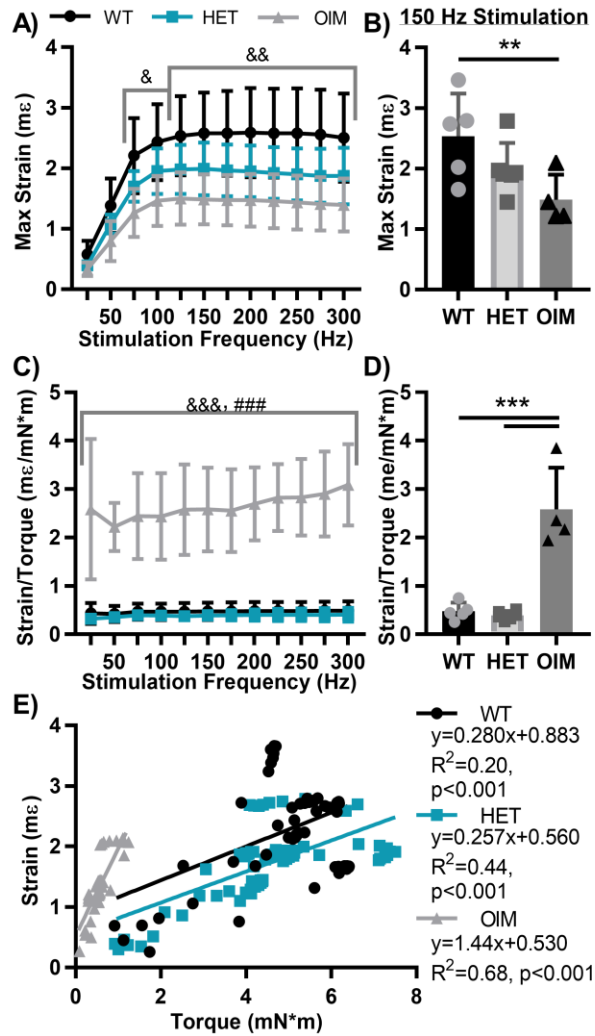
Appendix C.1 Figure 4. A) Maximum strain was reduced in oim/oim at stimulation frequencies greater than 50 Hz. B) Maximum strain at a single frequency (150 Hz) further demonstrates this reduction. C) After normalizing strain to torque, oim/oim showed higher strain relative to toque at all frequency, and D) further demonstrated at 150 Hz. E) Similarly, grouping all frequencies and all mice of a genotype together also demonstrates a higher strain vs torque slope in oim/oim. In panels A and C, "&" indicates comparison between WT and oim/oim and "#" between Het and oim/oim. In panels B and D, *p<0.05, **p<0.01, ***p<0.001 with the bars showing comparisons.
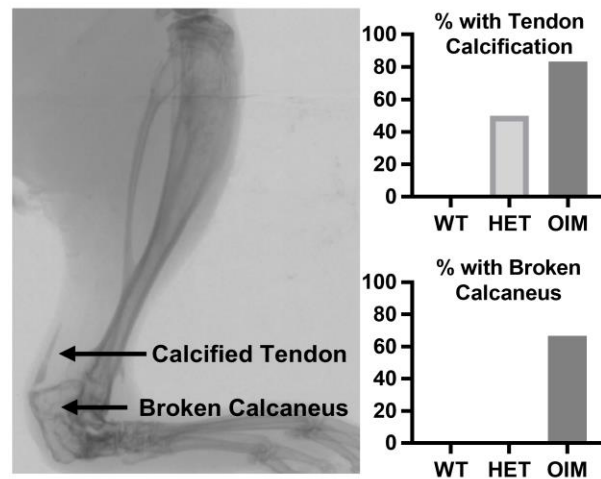
Appendix C.1 Figure 5. Micro-CT image showing calcified tendon and broken calcaneus. The percentage of each genotype with either a calcified tendon or broken calcaneus are also shown.

Discussion

Mechanical interactions between muscle and bone have long been recognized as integral to bone integrity. However, few studies have directly measured these interactions within the context of musculoskeletal disease. In this study, we attached a strain gauge to the tibia of healthy and OI mice and measured bone strain during muscle contraction. Our primary results showed that oim/oim muscle was able to engender an average of ~1500 µε on bone despite muscle weakness. Even so, this strain value was significantly lower than the ~2500 µε engendered by WT mice.

The first finding was that the oim/oim mice required less muscle torque to engender a given bone strain, as may be expected given the reduction in bone properties observed in this model. Previous studies have shown that oim/oim have reduced bone mass and bone mechanical properties, including stiffness [24,28–30] Although we did not measure mechanical properties in the current study, measurements of cortical and cancellous bone geometry and density (Appendix C.1 Supplemental Text and Figure 1) indicated that oim/oim animals had significantly smaller bones with a drastically lower cross sectional moment of inertia. Moment of inertia is a measure of a bone's structural ability to resist bending. Therefore, although moment of inertia is not a direct mechanical measurement, a lower moment of inertia would indicate that a bone can more easily deform under a given load, similar to what has been reported previously.

The reduction in bone properties was paired with reductions in estimated muscle cross-sectional area and function. Muscle weakness is often observed clinically,[16–18,31] and can even be considered the presenting sign of OI.[32,33] A study by Veilleux *et. al* showed that OI Type I patients had lower average peak force, even after normalizing to muscle cross-sectional area. Similar results were noted in the pre-clinical realm, with Gentry *et al.* showing that the maximum contractile force and specific contractile force were lower in the plantaris, gastrocnemius, and tibialis anterior of oim/oim mice.[25] In the current study, oim/oim mice had reduced maximum muscle torque during plantarflexion and lower estimated muscle cross-sectional area.

Despite the significant muscle weakness, and presumably due to oim/oim bone's increased propensity to bending, the strain engendered on the oim/oim bone during maximum muscle contraction was above historical osteogenic strain thresholds,[4,5] suggesting at least partial conservation in the muscle-bone relationship, even in disease. The implication of this is that muscle stimulation, although lower than normal, may be able to mechanically induce bone formation in OI. This idea—using muscle to improve OI bone—has been previously explored. In a study by Oestreich *et al.*, myostatin deficiency in Het mice resulted in improved bone strength.[34] Similarly, administration of a soluble activin receptor 2B to increase muscle mass in Het also increased bone mass.[35] Our study suggests that the improvements to bone may be driven—at least partially—by the mechanical loading of the bone during muscle contraction.

Although strain levels in the oim/oim were high relative to historical osteogenic strain thresholds, they were still lower than WT, suggesting that even at maximum muscle contraction, oim/oim would likely have a reduced bone formation effect. In other words, as Sugiyama et al. demonstrated, the bone's response to mechanical stimulation is linear within the anabolic strain region.[4] Thus, even though the strain level is anabolic in WT, Het, and oim/oim, the bone formation effects would likely be diminished in oim/oim. Similarly, oim/oim may have to exert greater forces relative to their maximum contractile force in order to have a desired effect. This finding suggests that it may require more "effort" to induce a bone formation response in oim/oim than in WT. For example, if we consider ~1000 $\mu\varepsilon$ as the threshold for bone formation,[4,5] then a WT mouse—which engenders a maximum of ~2500 $\mu\varepsilon$ on bone—may only have to exert ~40% of its maximum muscle force in order to be above the strain threshold for bone formation. In contrast, an oim/oim mouse—which only engenders a maximum of ~1500 $\mu\varepsilon$ on bone—may need to exert nearly 70% of its maximum muscle force to have the same effect. Thus, even though

oim/oim had both weaker muscle and weaker bone, the relationship between muscle and bone was not fully conserved in this model in that the oim/oim have to exert more "effort" to obtain the same strain response.

It is also important to note that, during standard locomotion, a person rarely exerts maximum muscle force. We chose muscle stimulation in the current experiment because it afforded greater control over muscle contraction properties, but care must be taken in the interpretation of our data. Maximum contraction during muscle stimulation is much higher than observed during normal activity. For example, strain values during walking in healthy mice have been reported as approximately 200 με of tension,[36] which is much lower than the ~2500 με engendered in the WT mice during maximum muscle contraction. Despite these differences, the fact that maximum muscle stimulation can cause ~1500 με of tensile strain in oim/oim is encouraging, and would suggest an interesting avenue for further exploration.

One important observation in this study was that the Achilles tendon had some calcification in most of the oim/oim and half of the Het animals. Previous work have also noted Achilles tendon calcification in oim/oim,[37,38] and studies of oim/oim tail tendon have indicated that oim/oim had reduced mechanical integrity[39] and altered structure.[40,41] In our study, Het mice with calcification of the tendon as determined by the bright streak in the micro-CT had a non-significant reduction in maximum muscle torque. In addition, the calcaneus in nearly half of the oim/oim was broken, but the presence of a callus indicates that the break occurred prior to muscle stimulation. As might be expected, the mice with a broken calcaneus had a much lower maximum muscle torque compared to oim/oim with intact bone. Clearly, the tendon and calcaneus are important to force transmission from muscle to bone. Although we did not explore this further, additional research into the role of the tendon and calcaneus are warranted.

A few limitations should be noted. First, this study only assessed mechanical interactions of muscle and bone, and did not explore chemical interactions, even though those are likely impacted as well. A growing body of literature has indicated the importance of muscle-bone molecular and biochemical interactions, as demonstrated by an increased number of reviews on the topic.[42–44] However, we have limited our scope to purely mechanical interactions, as could be assessed by strain gauging. Second, we also used imaging to estimate muscle cross-sectional area, which does not allow us to differentiate skeletal muscle, connective tissue, and adipose. Our estimates show differences among groups that are consistent with previous literature using more traditional

histological measures. Lastly, the OI murine model used in this study has an α2 chain mutation, which is less common in humans. In addition, presence of spontaneous fractures in the long bones limits the mice available for studies. Despite these limitations in the mouse model, oim/oim does show both muscle and bone weakness as is common in human patients and is the primary reason this model was chosen.

In summary, we have demonstrated that oim/oim mice require less muscle torque to engender strain on bone. As a result, although the oim/oim have extreme muscle weakness, maximum muscle contraction was still able to engender ~1500 με. This engendered strain was still lower in oim/oim than in the WT. Even so, these results are promising in that they show that muscle stimulation induces strains above historical bone formation thresholds in oim/oim.

Supplemental Material

Cancellous Analysis Methods

Within the proximal metaphysis, the cancellous bone was automatically segmented from its surrounding cortical shell (CTAn, Bruker) and then checked to ensure accuracy of the segmentation. Poor segmentations were re-segmented manually. Data were then analyzed to determine bone volume fraction (BV/TV), trabecular thickness (Tb.Th), number (Tb.N), separation (Tb.Sp), bone mineral density (BMD), and tissue mineral density (TMD).

Cancellous Results

As was observed in the mid-diaphysis, oim/oim also had lower bone mass in the metaphysis while the difference between WT and Het were statistically indistinguishable. Bone volume fraction was 51% and 52% lower in oim/oim compared to WT and Het, respectively (both p<0.001; Appendix C.1 Supplemental Figure 1A). Bone mineral density was similarly lower (p<0.01 vs WT and Het; Appendix C.1 Supplemental Figure 1F). This difference was predominately driven by the 49% and 48% lower trabecular number and the 93% and 89% higher trabecular separation compared to WT and Het, respectively (all p<0.001; Appendix C.1 Supplemental Figure 1C-D). Trabecular thickness was statistically indistinguishable between groups (Appendix C.1 Supplemental Figure 1B). Unlike in cortical analysis, there was no difference observed in tissue mineral density (Appendix C.1 Supplemental Figure 1E).
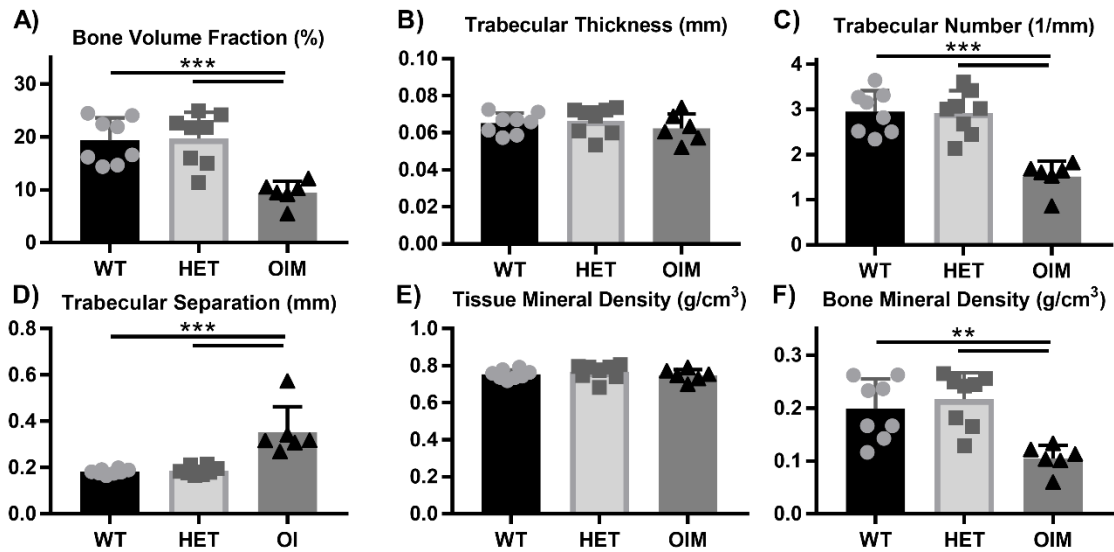
Appendix C.1 Supplemental Figure 1. Micro-CT image showing calcified tendon and broken calcaneus. The percentage of each genotype with either a calcified tendon or broken calcaneus are also shown.

References

1. Lu T-W, Taylor SJ, O'Connor JJ, Walker PS. 1997. Influence of muscle activity on the forces in the femur: An in vivo study. *J Biomech*. 30(11-12):1101–1106.

2. Wehner T, Claes L, Simon U. 2009. Internal loads in the human tibia during gait. *Clinical Biomechanics*. 24(3):299–302.

3. Robling AG. 2009. Is bone's response to mechanical signals dominated by muscle forces? *Med Sci Sports Exerc*. 41(11):2044.

4. Sugiyama T, Meakin LB, Browne WJ et al. 2012. Bones' adaptive response to mechanical loading is essentially linear between the low strains associated with disuse and the high strains associated with the lamellar/woven bone transition. *J Bone Miner Res*. 27(8):1784–1793.

5. Turner CH, Forwood MR, Rho JY, Yoshikawa T. 1994. Mechanical loading thresholds for lamellar and woven bone formation. *J Bone Miner Res*. 9(1):87–97.

6. Burr DB. 1997. Muscle strength, bone mass, and age-related bone loss. *J Bone Miner Res*. 12(10):1547–1551.

7. Kaye M, Kusy RP. 1995. Genetic lineage, bone mass, and physical activity in mice. *Bone*. 17(2):131–135.

8. Rittweger J, Frost HM, Schiessl H et al. 2005. Muscle atrophy and bone loss after 90 days' bed rest and the effects of flywheel resistive exercise and pamidronate: Results from the ltbr study. *Bone*. 36(6):1019–1029.

9. Sjöblom S, Suuronen J, Rikkonen T et al. 2013. Relationship between postmenopausal osteoporosis and the components of clinical sarcopenia. *Maturitas*. 75(2):175–180.

10. Verschueren S, Gielen E, O'neill T et al. 2013. Sarcopenia and its relationship with bone mineral density in middle-aged and elderly european men. *Osteoporos Int*. 24(1):87–98.

11. Blain H, Jaussent A, Thomas E et al. 2010. Appendicular skeletal muscle mass is the strongest independent factor associated with femoral neck bone mineral density in adult and older men. *Exp Gerontol*. 45(9):679–684.

12. Myburgh KH, Charette S, Zhou L et al. 1993. Influence of recreational activity and muscle strength on ulnar bending stiffness in men. *Med Sci Sports Exerc*. 25(5):592–596.

13. Gajko-Galicka A 2002. Mutations in type i collagen genes resulting in osteogenesis imperfecta in humans. *ACTA BIOCHIMICA POLONICA-ENGLISH EDITION-*. 49(2):433–442.

14. Sillence D, Senn A, Danks D. 1979. Genetic heterogeneity in osteogenesis imperfecta. *J Med Genet*. 16(2):101–116.

15. Takken T, Terlingen HC, Helders PJ et al. 2004. Cardiopulmonary fitness and muscle strength in patients with osteogenesis imperfecta type i. *The Journal of pediatrics*. 145(6):813–818.

16. Pouliot-Laforte A, Veilleux LN, Rauch F, Lemay M. 2015. Physical activity in youth with osteogenesis imperfecta type i. *J Musculoskelet Neuronal Interact*. 15(2):171–176.

17. Veilleux L-N, Lemay M, Pouliot-Laforte A et al. 2014. Muscle anatomy and dynamic muscle function in osteogenesis imperfecta type i. *The Journal of Clinical Endocrinology & Metabolism*. 99(2):E356–E362.

18. Veilleux L-N, Pouliot-Laforte A, Lemay M et al. 2015. The functional muscle–bone unit in patients with osteogenesis imperfecta type i. *Bone*. 79:52–57.

19. Engelbert R, Van Der Graaf Y, Van Empelen R, Beemer F, Helders P. 1997. Osteogenesis imperfecta in childhood: Impairment and disability. *Pediatrics*. 99(2):e3–e3.

20. Chipman SD, Sweet HO, McBride DJ et al. 1993. Defective pro alpha 2 (i) collagen synthesis in a recessive mutation in mice: A model of human osteogenesis imperfecta. *Proceedings of the National Academy of Sciences*. 90(5):1701–1705.

21. Saban J, Zussman M, Havey R et al. 1996. Heterozygous oim mice exhibit a mild form of osteogenesis imperfecta. *Bone*. 19(6):575–579.

22. McBride D Jr, Shapiro J, Dunn M. 1998. Bone geometry and strength measurements in aging mice with the oim mutation. *Calcif Tissue Int*. 62(2):172–176.

23. Phillips CL, Bradley DA, Schlotzhauer CL et al. 2000. oim mice exhibit altered femur and incisor mineral composition and decreased bone mineral density. *Bone*. 27(2):219–226.

24. Bart ZR, Hammond MA, Wallace JM. 2014. Multi-scale analysis of bone chemistry, morphology and mechanics in the oim model of osteogenesis imperfecta. *Connect Tissue Res*. 55(sup1):4–8.

25. Gentry BA, Ferreira AJ, McCambridge AJ, Brown M, Phillips CL. 2010. Skeletal muscle weakness in osteogeneis imperfecta mice. *Matrix Biol*. 29(7):638–644.

26. Carleton SM, McBride DJ, Carson WL et al. 2008. Role of genetic background in determining phenotypic severity throughout postnatal development and at peak bone mass in col1a2 deficient mice (oim). *Bone*. 42(4):681–694.

27. Bouxsein ML, Boyd SK, Christiansen BA et al. 2010. Guidelines for assessment of bone microstructure in rodents using micro–computed tomography. *J Bone Miner Res*. 25(7):1468–1486.

28. Vanleene M, Porter A, Guillot P-V et al. 2012. Ultra-structural defects cause low bone matrix stiffness despite high mineralization in osteogenesis imperfecta mice. *Bone*. 50(6):1317–1323.

29. Miller E, Delos D, Baldini T, Wright TM, Camacho NP. 2007. Abnormal mineral-matrix interactions are a significant contributor to fragility in oim/oim bone. *Calcif Tissue Int*. 81(3):206–214.

30. Yao X, Carleton SM, Kettle AD et al. 2013. Gender-dependence of bone structure and properties in adult osteogenesis imperfecta murine model. *Ann Biomed Eng*. 41(6):1139–1149.

31. Caudill A, Flanagan A, Hassani S et al. 2010. Ankle strength and functional limitations in children and adolescents with type i osteogenesis imperfecta. *Pediatr Phys Ther*. 22(3):288–295.

32. Pavone V, Mattina T, Pavone P, Falsaperla R, Testa G. 2017. Early motor delay: An outstanding, initial sign of osteogenesis imperfecta type 1. *Journal of orthopaedic case reports*. 7(3):63–66.

33. Boot AM, De Coo RF, Pals G, de Muinck Keizer-Schrama SM. 2006. Muscle weakness as presenting symptom of osteogenesis imperfecta. *Eur J Pediatr*. 165(6):392–394.

34. Oestreich A, Carleton S, Yao X et al. 2016. Myostatin deficiency partially rescues the bone phenotype of osteogenesis imperfecta model mice. *Osteoporos Int*. 27(1):161–170.

35. DiGirolamo DJ, Singhal V, Chang X, Lee S-J, Germain-Lee EL. 2015. Administration of soluble activin receptor 2b increases bone and muscle mass in a mouse model of osteogenesis imperfecta. *Bone research*. 3:14042.

36. De Souza RL, Matsuura M, Eckstein F et al. 2005. Non-invasive axial loading of mouse tibiae increases cortical bone formation and modifies trabecular organization: A new model to study cortical and cancellous compartments in a single loaded element. *Bone*. 37(6):810–818.

37. Landis WJ. 1995. Tomographic imaging of collagen-mineral interaction: Implications for osteogenesis imperfecta. *Connect Tissue Res*. 31(4):287–290.

38. Landis WJ. 1995. The strength of a calcified tissue depends in part on the molecular structure and organization of its constituent mineral crystals in their organic matrix. *Bone*. 16(5):533–544.

39. Misof K, Landis WJ, Klaushofer K, Fratzl P. 1997. Collagen from the osteogenesis imperfecta mouse model (oim) shows reduced resistance against tensile stress. *The Journal of clinical investigation*. 100(1):40–45.

40. McBride DJ, Choe V, Shapiro JR, Brodsky B. 1997. Altered collagen structure in mouse tail tendon lacking the α2(i) chain. *J Mol Biol*. 270(2):275–284.

41. Sims T, Miles C, Bailey A, Camacho N. 2003. Properties of collagen in oim mouse tissues. *Connect Tissue Res*. 44(1):202–205.

42. Brotto M, Bonewald L. 2015. Bone and muscle: Interactions beyond mechanical. *Bone*. 80:109–114.

43. Brotto M, Johnson ML. 2014. Endocrine crosstalk between muscle and bone. *Current Osteoporosis Reports*. 12(2):135–141.

44. Phillips CL, Jeong Y. 2018. Osteogenesis imperfecta: Muscle–bone interactions when bi-directionally compromised. *Current osteoporosis reports*.1–12.

C.2 Effects of Raloxifene and Tibial Loading on Bone Mass and Mechanics in Male and Female Mice

Abstract

Purpose: Raloxifene (RAL) is a selective estrogen receptor modulator (SERM) that has previously been shown to cause acellular benefits to bone tissue. Due to these improvements, RAL was combined with targeted tibial loading to assess if RAL treatment during periods of active bone formation would allow for further mechanical enhancements. Methods: Structural, mechanical, and microstructural effects were assessed in bone from C57BL/6 mice that were treated with RAL (0.5 mg/kg), tibial loading, or both for 6 weeks, beginning at 10 weeks of age. Results: Ex vivo microcomputed tomography (CT) images indicated RAL and loading work together to improve bone mass and architecture, especially within the cancellous region of males. Increases in cancellous bone volume fraction were heavily driven by increases in trabecular thickness, though there were some effects on trabecular spacing and number. In the cortical regions, RAL and loading both increased cross-sectional area, cortical area, and cortical thickness. Whole-bone mechanical testing primarily indicated the effects of loading. Further characterization through Raman spectroscopy and nanoindentation showed load-based changes in mineralization and micromechanics, while both loading and RAL caused changes in the secondary collagen structure. In contrast to males, in females, there were large load-based effects in the cancellous and cortical regions, resulting in increased whole-bone mechanical properties. RAL had less of an effect on cancellous and cortical architecture, though some effects were still present. Conclusion: RAL and loading work together to impact bone architecture and mechanical integrity, leading to greater improvements than either treatment individually.

Introduction

Raloxifene (RAL) is an FDA-approved selective estrogen receptor modulator (SERM) used to reduce fracture risk in post-menopausal women. It is a nonsteroidal benzothiophene that causes anti-resorptive effects in bone, which has been suggested *in vitro* to occur by both preventing osteoclastic and promoting osteoblastic activity.[1] These anti-resorptive effects occur without also

stimulating proliferation of the breast and endometrium.[2,3] The efficacy of RAL in reducing vertebral fracture risk has been well demonstrated[4,5] and is comparable to that of bisphosphonates.[6] Despite this reduction in fracture risk, improvements in bone quantity due to RAL are modest, with a meta-analysis indicating that RAL increased bone mineral density (BMD) of the lumbar spine by only 2.5%, as compared to the 4.5-7.5% increase due to risedronate or alendronate.[6] Moreover, a logistic regression model indicated that changes in vertebral BMD only accounted for 4% of the measured reduction in fracture risk,[7] suggesting additional non-mass based effects.

Although the exact mechanism by which RAL reduces fracture risk is unknown, pre-clinical studies have demonstrated that RAL improves material-level properties in bone independent of BMD.[8-10] Further *ex vivo* work has shown that, during mechanical loading, RAL alters the transfer of load between the collagen and hydroxyapatite, leading to reduced strains in the mineral and increased whole-bone toughness[11] and fatigue life.[12] These data suggest that RAL modifies the bone matrix independent of BMD, thus improving material-level properties of bone. For this reason, treatment with RAL during periods of active bone formation may allow for further mechanical enhancements due its potential ability to more readily access and thereby modify the collagen in the time period preceding mineralization.

One means of inducing active bone formation is mechanical stimulation. Clinically, this has been demonstrated through high-impact exercise such as running or jumping.[13-16] The exercise causes loading of the bone, which results in increased bone mass. *In vivo* non-invasive mechanical loading of the murine tibia has become a common means of loading bone.[17-21] In this model, the limb of the anesthetized animal is placed in a mechanical tester and cyclically loaded, causing a bone formation response. We have demonstrated a 15% increase in cortical thickness in mice that were loaded to 2050 $\mu\epsilon$ for two weeks.[22]

Due to the mass-based improvements associated with loading and the material-level improvements associated with RAL, it was hypothesized that treatment with RAL during loading would improve bone mechanics beyond either treatment individually. In this study, this concept was tested in young male and female mice by treating them with RAL while simultaneously loading their right tibia. While tibial loading is not as clinically relevant as exercise, it often leads to larger mass-based gains.[23] Given that the primary goal of this study was to assess the effects of RAL during situations in which bone is being actively formed, tibial loading was utilized. For similar reasons, young mice were used due to their greater responsiveness to loading.[24] After

treatment was completed, computed tomography and mechanical testing to failure were used to investigate changes in bone structure and function, respectively. In addition, material-level changes in the new bone tissue were assessed by Raman spectroscopy and nanoindentation.

Methods

Experimental Overview

Male and female C57BL/6 mice from an in-house colony were randomly separated into two groups: control (CON) and raloxifene (RAL). Beginning at 10 weeks of age, RAL mice were injected subcutaneously 5x/week with 0.5 mg/kg RAL. At the same time, both CON and RAL mice underwent compressive loading of the right tibia 3x/week. The contralateral limb served as a non-loaded control. Based on the sample sizes used in previous studies,[22,25,26] one cohort (n=11-12/group/sex) was allocated to micro-computed tomography (micro-CT) and mechanical testing, while a second cohort (n=8/group; male only) was allocated to Raman spectroscopy and nanoindentation. Based on the results from cohort 1, only males were included in the second cohort so as to reduce the total number of mice. In this group, to enable detection of new bone growth for Raman spectroscopy and nanoindentation, the second cohort received a single subcutaneous calcein injection (0.15 mL) at the end of the first week. At 16 weeks of age, mice were euthanized by CO_2 asphyxiation and their tibiae were harvested and stored in phosphate-buffered saline (PBS)-soaked gauze at -20°C until use. Mouse numbers and groups are detailed in Appendix C.2 Table 1. These procedures and subsequent analyses were performed without blinding. All procedures were performed with prior approval from the Indiana University School of Medicine Institutional Animal Care and Use Committee (IACUC Protocol 11069).

Appendix C.2 Table 1. Number of mice used for each cohort. For each mouse, both right and left tibiae were analyzed (loaded versus non-loaded).

	COHORT 1		COHORT 2		TOTAL
	CON	RAL	CON	RAL	
MALE	11	12	8	8	39
FEMALE	12	12	N/A	N/A	24

In vivo Compressive Loading

Mice were anesthetized (2% Isoflurane) and their right tibiae were cyclically loaded in compression to a peak force of 10.6 N[22] for both males and females.[27] The loading profile consisted of 2 cycles at 4 Hz followed by a 1-second rest at 2 N, repeated 110 times for a total of 220 compressive cycles per loading day (3x/week).

Computed Tomography (CT)

The frozen, harvested tibiae were scanned by high resolution micro-CT (Skyscan 1172; Bruker, Kontich, Belgium) at a nominal isotropic resolution of 10 μm (V = 60 kV, I = 167 μA; 0.7-degree increment angle; 2 frame averaging). Hydroxyapatite calibration phantoms (0.25 and 0.75 g/cm3 CaHA) were used to convert gray-scale images to mineral content and to prevent day-to-day variation from becoming a potential confounding variable. After scanning, the tibiae were re-frozen at -20 C until mechanical testing.

The CT scans were then reconstructed (nRecon) and rotated (DataViewer) to enable consistent selection of the cancellous and cortical regions of interest. For cancellous analysis, a 1-mm thick region of interest in the proximal metaphysis was selected, beginning just distal to the growth plate and extending distally.[28] The cancellous bone was automatically segmented from the surrounding cortical shell in CTAn (Bruker) and then manually checked for accuracy. Each region of interest was then analyzed to determine bone volume fraction (BV/TV), trabecular thickness (Tb.Th), trabecular number (Tb.N), trabecular separation (Tb.Sp), bone mineral density (BMD), and tissue mineral density (TMD).

For cortical analysis, two 1-mm thick regions were selected. The first was centered at the mid-diaphysis (50% bone length) and the second at a proximal-mid location (37% of bone length) projected to be the site of highest tensile strain.[23,29] The mid-diaphysis was selected because it is the primary region that was mechanically tested, while the proximal-mid location was selected because it is the site of highest tensile strain and therefore, the chosen location for Raman spectroscopy and nanoindentation. A consistent grayscale threshold was used to segment bone from non-bone. These cortical regions of interest were analyzed in Matlab (MathWorks, Inc. Natick, MA) to determine areas (total cross sectional area, cortical area, and marrow area), cortical thickness, principal moments of inertia (maximum and minimum), and tissue mineral density.[22,23]

Mechanical Testing

Following micro-CT, tibiae were monotonically tested to failure using four-point bending (3 mm inner loading span; 9 mm outer span) at a rate of 0.025 mm/sec. Tibiae were positioned with the loading fixture centered on the mid-diaphysis with the medial side in tension.[22] During testing, samples were kept hydrated by dripping PBS on the bone. From the load-displacement data, forces (yield and maximum), displacements (yield, post-yield, and total), work (yield, post-yield, and total), and stiffness were calculated. Load-displacement data were normalized to stress-strain using cortical mid-diaphyseal CT data in conjunction with standard four-point bending equations as described previously.[22] From the stress-strain data, stresses (yield and maximum), strains (yield, post-yield, and total), resilience, toughness, and elastic modulus were determined. To plot representative curves, the force-displacement and stress-strain values were averaged for each group at yield, maximum force, and failure locations.

Raman Spectroscopy

To prepare for Raman spectroscopy and nanoindentation, intact tibia from the second cohort were embedded vertically in individual glass tubes using a fast-curing methyl methacrylate (MMA) resin (Koldmount; SPI Supplies, West Chester, PA). After curing, embedded tibiae were carefully extracted from the glass tubes and mounted into a hydrated low-speed sectioning saw (IsoMet Low Speed Precision Cutter, Buehler, Lake Bluff, IL). Embedded tibiae were sectioned at 37% of the bone length measured from the proximal end,[23] and polished using a 3 µm diamond suspension. After polishing, sections were rinsed with PBS and stored frozen in PBS-soaked gauze until use.

Raman spectroscopy was performed using an InVia Raman Spectrometer (Renishaw, Wotton-under-Edge, United Kingdom). A 785 nm laser was focused on the bone surface using a 50X objective to a spot size of ~1 µm. Using fluorescent calcein labels as guides, five regions of new bone spaced at least 10 µm apart in the posterior bone quadrant were assessed. For CON and RAL, new bone was assessed in the area inside the endocortical label while for LOAD and LOAD+RAL, new bone was assessed outside of the loading-induced periosteal label. The endocortical region was selected for CON and RAL samples because neither of these non-loaded groups exhibited periosteal calcein labelling as opposed to their loaded counterparts. Spectra were

acquired following a 12s exposure at 5% laser power and were averaged across 10 accumulations. Baselines were corrected using Renishaw WiRE intelligent fitting software, utilizing an 11th order polynomial fit, and cosmic rays were removed. Data was subsequently smoothed using a 2nd order Savitzky-Golay filter across 7 data points. Band intensities were calculated for v_1-PO_4^{3-} (959 cm^{-1}), v_1-CO_3^{2-} (1071 cm^{-1}), amide III (1246 cm^{-1}), CH_2 wag (1450 cm^{-1}), and amide I (1665 cm^{-1}) using GRAMS/AI (Thermo Fisher Scientific, Waltham, MA)Relative mineralization was determined by the mineral-to-matrix ratio, calculated as band intensity ratios of v_1-PO_4^{3-}/Amide I, v_1-PO_4^{3-}/CH_2 wag, and v_1-PO_4^{3-}/Amide III as previously described.[30] Mineral maturity/crystallinity was calculated as the inverse of the full width at half max of the v_1-PO_4^{3-} band. Type B carbonate substitution was calculated as the band intensity ratio of v_1-PO_4^{3-}/v_1-CO_3^{2-}. Relative collagen maturity was determined by fitting subpeaks within the amide I band via second derivative spectroscopy. 1660 cm^{-1} and 1690 cm^{-1} fitted beneath the amide I band. The spectral parameters calculated for each sample region were averaged, yielding a single value for each parameter for analysis.

Nanoindentation

Following Raman spectroscopy, samples underwent nanoindentation using a Hysitron TI 980 TriboIndenter (Bruker, Billerica, MA) equipped with a diamond Berkovich probe. Analysis was performed in the same regions of new bone as assessed by Raman spectroscopy. The loading profile consisted of a 30s loading period, a 120s hold at 1,000 µN, and a 30s unloading period. The resulting load-displacement curves were analyzed for reduced modulus and hardness as reported previously.[31] The data (N=5 per region) were averaged to produce a single value for each parameter per region.

Statistics

Data are presented as mean ± standard deviation, unless otherwise noted. In addition, each sex was statistically analyzed separately. Data were checked for normality of the residuals, and any violations were corrected with transformations. Extreme outliers (> 3*IQR) were removed. For CT and mechanical testing, a two-way repeated measures ANOVA was then used. Within this ANOVA model, the limb (right versus left) was considered the repeated measure and the treatment

(RAL versus none) was considered the non-repeated measure. For Raman spectroscopy and nanoindentation, the two-way ANOVA was non-repeated due to the loss of some samples during processing. Main effects of treatment (between-subject effect), loading (within-subject effect), and their interaction ($p<0.05$) were analyzed. If the interaction term was significant, the two-way ANOVA was deemed invalid and instead, a one-way ANOVA was performed. If the one-way ANOVA was significant, a post-hoc Tukey's HSD test was used to assess differences between groups. All statistics were performed in Matlab (MathWorks, Inc. Natick, MA) using a custom script. In addition, Cohen's d was calculated for each group (loading, RAL, and combination) relative to the non-loaded control to assess relative effect sizes.

Results

Cancellous Bone Mass Show Improvements due to Loading and RAL in Male Mice and Primarily due to Loading in Female Mice

Loading and RAL both caused improvements to trabecular architecture in male and female mice (Appendix C.2 Figure 1A-B). In male mice, improvements to BMD and bone volume fraction were additive, with the combined treatment having greater effects than either treatment individually ($p<0.001$ for all comparisons; Appendix C.2 Figure 1C-D). Assessment of statistical effect size further demonstrate this additive response. For BMD, the statistical effect size was 1.00, 1.46, and 2.42 for loading, RAL, and the combined group, respectively, while for bone volume fraction, it was 1.13, 1.48, and 2.84, respectively. These improvements to bone volume fraction were driven, in part, by large increases in trabecular thickness ($p<0.001$ for loading and RAL; Appendix C.2 Figure 1E). While both loading and RAL improved trabecular thickness, only loading decreased trabecular separation ($p<0.01$; Appendix C.2 Figure 1F), and only RAL improved trabecular number ($p<0.01$; Appendix C.2 Figure 1G), suggesting differing mechanisms. Lastly, TMD was greater in the loaded mice ($p<0.01$; Appendix C.2 Figure 1H). A noteworthy observation was that, with the exception of trabecular thickness and TMD, the effect size due to RAL was larger than that due to loading. In addition, for all measurements, the combined effect size was greater than either loading or RAL individually.

Similar to the males, the females had positive effects due both loading and RAL. BMD and bone volume fraction were significantly improved by loading ($p<0.001$ for both), though RAL

may also have had some effect on bone volume fraction given that the statistical effect size for the combination (2.64) was much larger than either that of loading (1.95) or RAL (1.07) individually (p=0.06; Appendix C.2 Figure 1C-D). In addition, both loading and RAL increased trabecular thickness, though the effects of loading were much greater (Appendix C.2 Figure 1E). Loading also reduced trabecular separation (p=0.01; Appendix C.2 Figure 1F) and increased trabecular number (p=0.04; Appendix C.2 Figure 1G). Although RAL did not have a significant impact on trabecular separation and number, the statistical effect sizes suggest that the combination treatment resulted in greater improvements than loading alone. Namely, for trabecular separation, the statistical effect size was -0.27 and -0.23 for loading and RAL, respectively, while in the combined group it was -0.62. Even more apparent, for trabecular number, the statistical effect size due to loading was only 0.28, while due to RAL was 0.68 and due to the combination was 0.88. Both loading and RAL influenced TMD (Appendix C.2 Figure 1H). For all properties except trabecular thickness and TMD, the combined effect size was larger than either loading or RAL individually.

Cortical Bone Mass in the Proximal-Mid and Mid Regions Show Effects of Loading and RAL in Males, but Primarily of Loading in Females

Similar to the cancellous region, the proximal-mid location showed additive effects of loading and RAL in the male mice, while in the female mice, the effects of loading were more pronounced than that of RAL (Appendix C.2 Figure 2A). In the male mice, total cross-sectional area, cortical area, and cortical thickness were improved by both loading (p=0.02, p<0.01, and p<0.001, respectively) and RAL (p<0.001 for all), with both treatments having similar effect sizes. When the treatments were combined, the gains were largest (Appendix C.2 Figure 2B-D). Loading also significantly increased the maximum moment of inertia (p<0.001; Appendix C.2 Figure 2E), while both treatments increased the minimum moment of inertia (p<0.001 and p<0.01 for loading and RAL, respectively; Appendix C.2 Figure 2F). While TMD in the cancellous region was significantly impacted by loading, there was no effect in the proximal-mid location.

In the females, both loading and RAL had a significant impact on cross-sectional area and cortical thickness (Appendix C.2 Figure 2B, D). Loading also significantly increased cortical area (p<0.001; Appendix C.2 Figure 2C) and maximum moment of inertia (Appendix C.2 Figure 2E). Both loading and RAL significantly increased minimum moment of inertia (Appendix C.2 Figure 2F). TMD was also significantly increased with loading (p<0.001; Appendix C.2 Figure 2G).
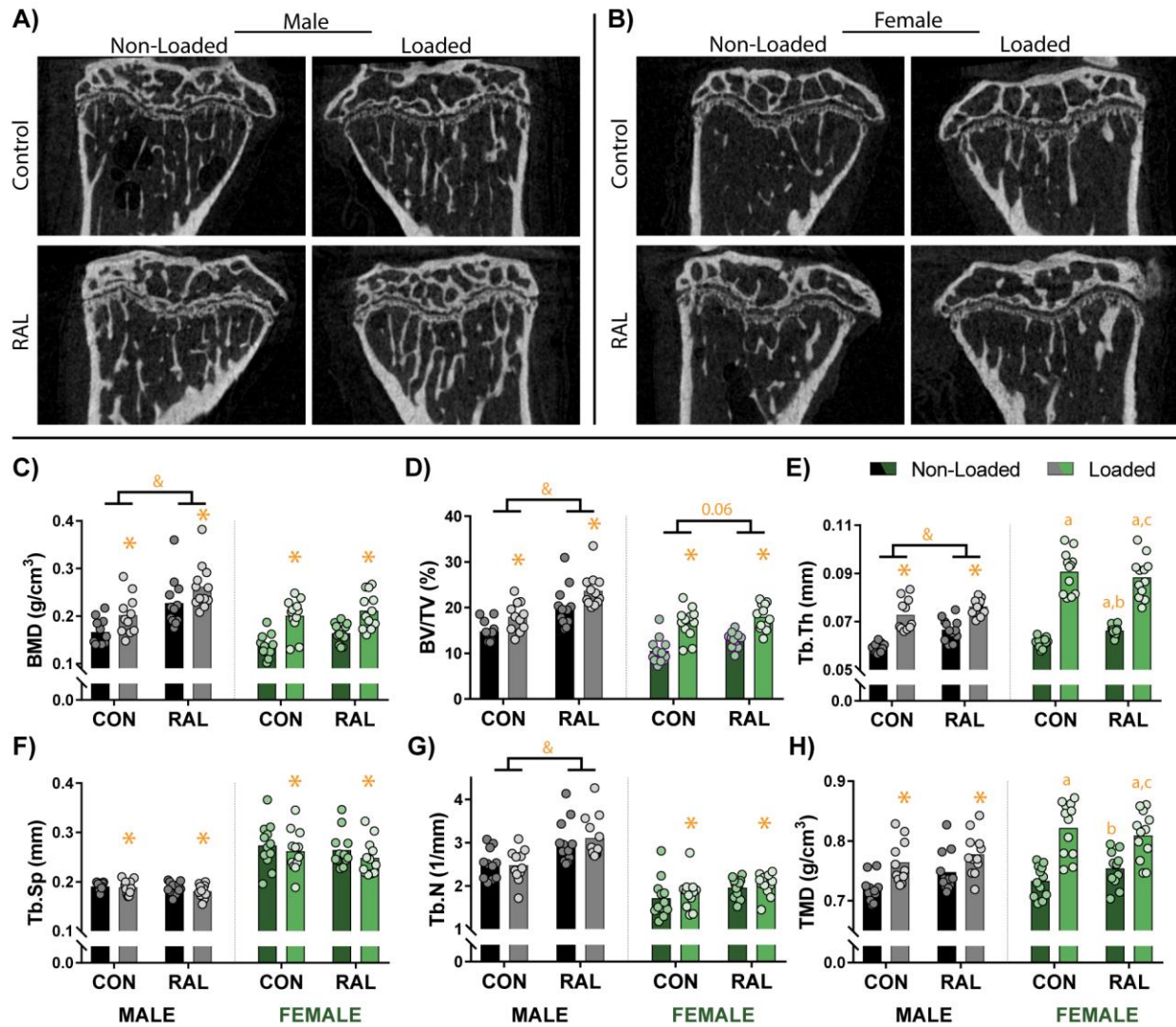
Appendix C.2 Figure 1. Sagittal CT images of the proximal tibia from (A) male and (B) female mice qualitatively show increased cancellous bone due to loading and RAL. (C) Quantitative measures of bone mineral density (BMD) and (D) bone volume fraction (BV/TV) similarly indicate additive mass-based effects due to loading and RAL in males. In females, the loading had the more prominent effect than RAL. (E) These improvements were driven by load- and RAL-based increases to trabecular thickness (Tb.Th), (F) load-based decreases to trabecular spacing (Tb.Sp), and (G) load- and RAL-based increases in trabecular number (Tb.N). (H) In addition, tissue mineral density (TMD) was increased due to loading in both males and females. For a two-way ANOVA, a '&' indicates a main effect of RAL and an '*' indicates a main effect of loading. If the interaction term was significant, an 'a' indicates a significant difference from non-loaded control, 'b' indicates a significant difference from loaded control, and 'c' indicates a significant difference from non-loaded RAL.

160
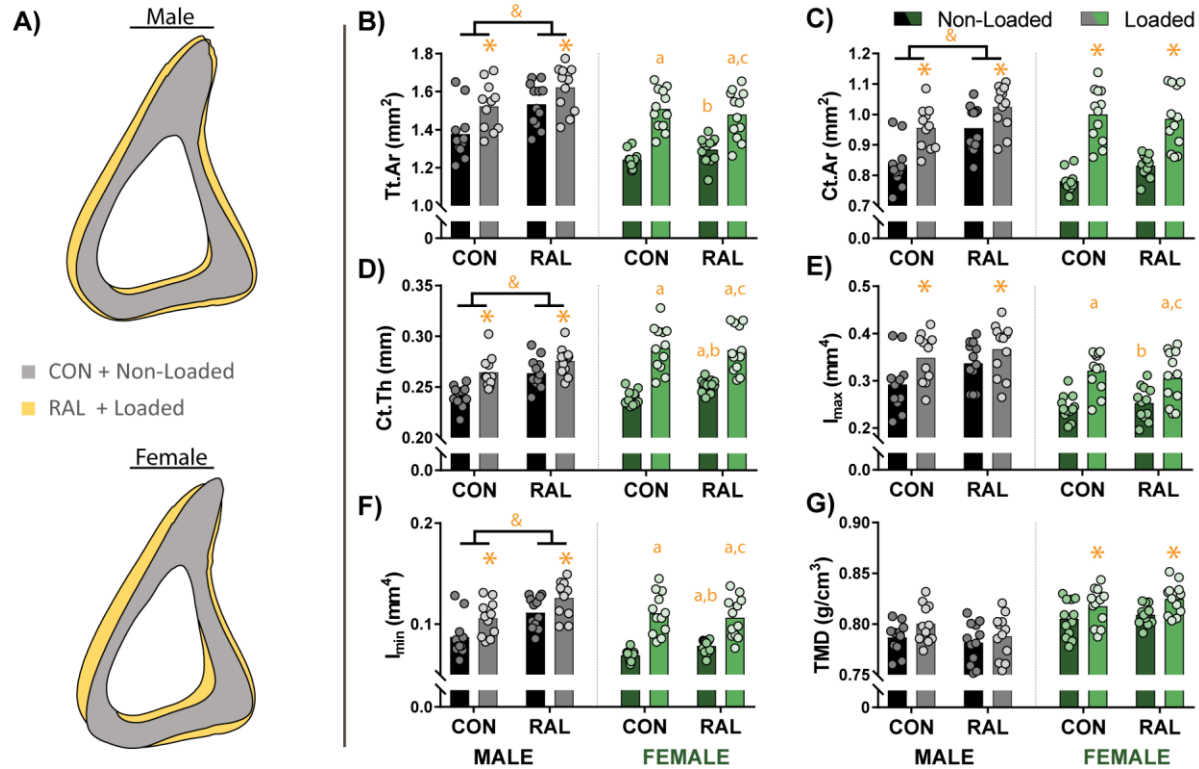
Appendix C.2 Figure 2. (A) Averaged cortical profiles of male and female mice at the proximal-mid position show improvements due to loading and RAL. (B) Measures of the total cross-sectional area (Tt.Ar), (C) cortical area (Ct.Ar), and (D) cortical thickness (Ct.Th) were significantly impacted by both load and RAL in males, resulting in a graded response. In contrast, in females, while there was some effects of RAL, the robust increases were primarily driven by load. (E) Maximum moment of inertia (I_{max}) was impacted by loading in both sexes, while (F) minimum moment of inertia (I_{min}) was positively influenced by RAL as well as the loading. (G) Tissue mineral density (TMD) showed no response in males, while it was significantly increased with loading in females. For a two-way ANOVA, a '&' indicates a main effect of RAL and an '*' indicates a main effect of loading. If the interaction term was significant, an 'a' indicates a significant difference from non-loaded control, 'b' indicates a significant difference from loaded control, and 'c' indicates a significant difference from non-loaded RAL.

As was shown for the cancellous and proximal-mid regions, within the mid-cortical region, loading and RAL had similar effects in the males, while in females, loading had a greater effect than RAL (Appendix C.2 Figure 3A). In males, cross-sectional area showed a graded response, only reaching significance in the combined treatment group (Appendix C.2 Figure 3B), whereas for cortical area and cortical thickness, the loading, RAL, and combined treatment were all significantly different from the non-loaded control (Appendix C.2 Figure 3C-D). Maximum moment of inertia showed similar trends as cross-sectional area, with results trending upward for loading and RAL but only reaching significance in the combined group (Appendix C.2 Figure 3E).

For minimum moment of inertia, RAL had the greater effect (Appendix C.2 Figure 1F). For TMD, both RAL groups were significantly lower than the loaded control mice, but not the non-loaded control mice (Appendix C.2 Figure 3G).

For the female mice, cross-sectional area, cortical area, and cortical thickness were all improved with both loading and RAL (Appendix C.2 Figure 3B-D), while maximum and minimum moments of inertia were only impacted by loading (Appendix C.2 Figure 3E-F). There was no effect of either loading or RAL on TMD.
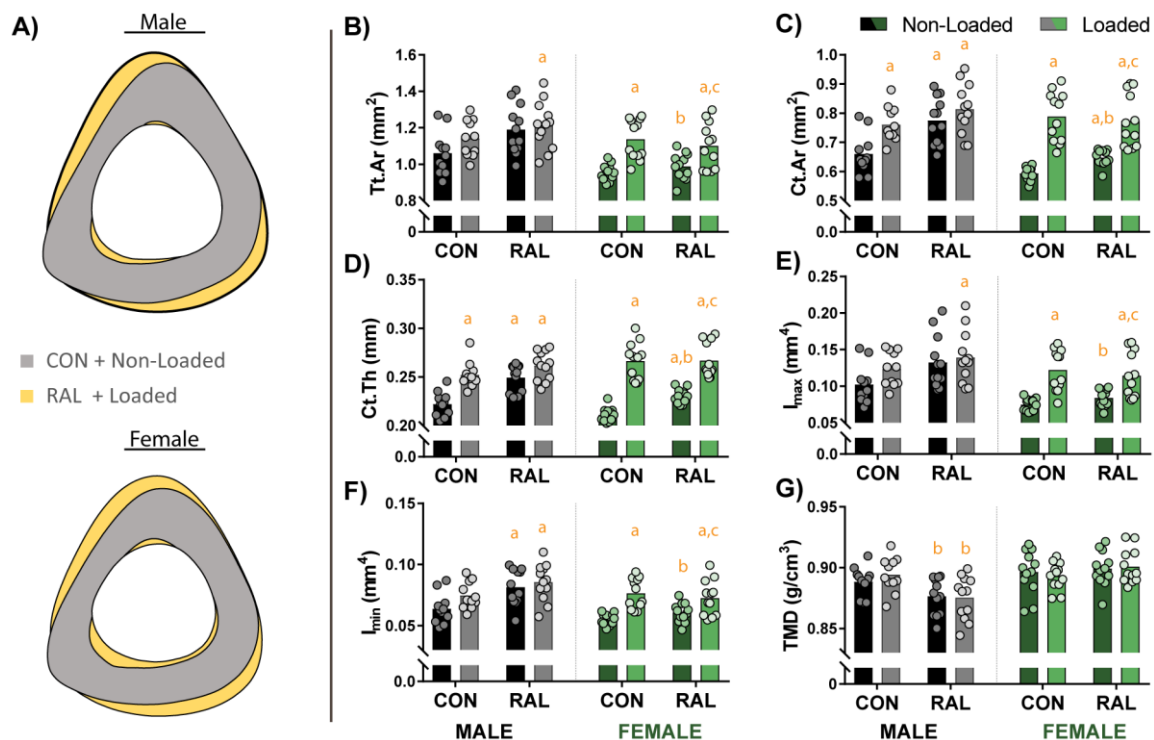
Appendix C.2 Figure 3. (A) Averaged cortical profiles of male and female mice at the mid location show large improvements due to loading (both males and females) and RAL (primarily males). (B) Measures of total cross-sectional area (Tt.Ar) indicate a graded response in males, only reaching significance in the combined treatment. In contrast, in females, the robust increases in CSA were driven by load. (C) Cortical area (Ct.Ar) and (D) cortical thickness (Ct.Th) were increased due to both load and RAL. However, the load-response was more robust than the RAL response in females. (E) Maximum and (F) minimum moments of inertia were both increased due to loading and RAL in both sexes. (G) Tissue mineral density (TMD) showed very little effects. For a two-way ANOVA, a '&' indicates a main effect of RAL and an '*' indicates a main effect of loading. If the interaction term was significant, an 'a' indicates a significant difference from non-loaded control, 'b' indicates a significant difference from loaded control, and 'c' indicates a significant difference from non-loaded RAL.

Mechanics Primarily Show an Effect of Loading in Both Males and Females

Four-point bending to failure, which primarily tests the mechanical integrity of the mid-cortical region, showed a similar response to loading and RAL as was observed by CT. Namely, in males, loading and RAL both improved the structural-level mechanics, though there was no additive effect of the combined treatment, while in females, loading alone drove the improvements (Appendix C.2 Figure 4A-C; Appendix C.2 Table 2). After normalizing to bone size, estimated material-level mechanics indicated significant improvements due only to loading in male and female mice (Appendix C.2 Figure 4D-F; Appendix C.2 Table 2). Although non-significant, total work and toughness both trended upward with the combined treatment in females. Analysis of effect size highlighted this observation in that Load, RAL, and RAL+Load had increasing effect sizes for total work (0.628, 0.709, and 0.865, respectively) and toughness (0.368, 0.651, and 0.665).
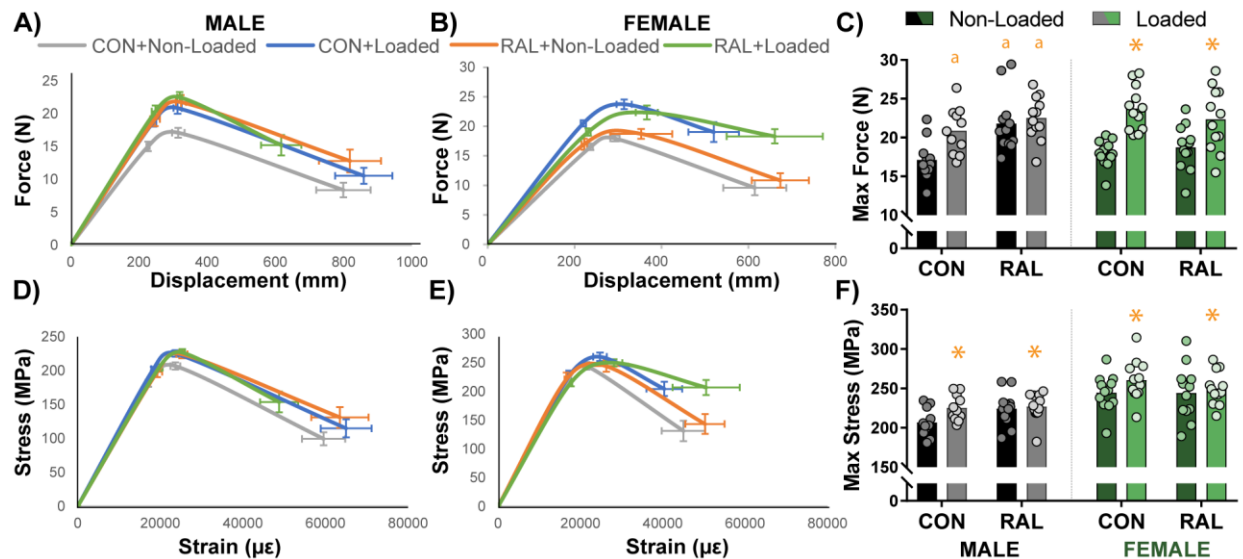
Appendix C.2 Figure 4. (A) Averaged force-displacement plots for male mice show an upward shift in the strength of tibiae that received loading, RAL, and both. (B) In female mice, improvements in mechanical properties was primarily driven by loading, as can be observed in (C) maximum force. After normalizing to cross-sectional area, stress-strain plots for (D) male and (E) female showed similar results as the force-displacement plots, as can also be observed in (F) maximum stress. Plots are shown as average ± SEM. For a two-way ANOVA, a '&' indicates a main effect of RAL and an '*' indicates a main effect of loading. If the interaction term was significant, an 'a' indicates a significant difference from non-loaded control, 'b' indicates a significant difference from loaded control, and 'c' indicates a significant difference from non-loaded RAL.

Appendix C.2 Table 2. Mechanical properties for male and female mice. A '*' indicates a significant effect of load and a '+' indicates a significant effect of treatment (p<0.05). In the case of significant interaction term, a one-way ANOVA with post-hoc Tukey HSD test was performed. An 'a' indicates a significant difference from CON, a 'b' indicates a significant difference from LOAD, and a 'c' indicates a significant difference from RAL (p<0.05).

	CON	LOAD	RAL	RAL+LOAD
MALE	**(n=11)**	**(n=11)**	**(n=12)**	**(n=12)**
Yield Force (N) *+	15.0±2.5	18.8±2.5	18.3±1.9	20.1±3.0
Maximum Force (N)	17.1±2.6	20.9±3.0 [a]	21.8±3.7 [a]	22.5±2.8 [a]
Displacement to Yield (µm)	227±17	250±16 [a]	233±5	238±14
Postyield Displacement (µm)	572±260	616±294	571±324	369±206
Total Displacement (µm)	799±265	859±278	819±315	617±205
Stiffness (N/mm) *	75.4±13.1	89.3±23.7	86.3±11.5	92.2±12.8
Work to Yield (mJ)	1.87±0.32	2.48±0.27 [a]	2.34±0.24 [a]	2.51±0.28 [a]
Postyield Work (mJ)	6.12±2.81	9.17±5.64	8.21±3.84	6.35±3.34
Total Work (mJ)	7.99±2.71	11.64±5.56	10.83±3.88	9.12±3.45
Yield Stress (MPa) *	181±18	203±10	198±27	204±17
Maximum Stress (MPa) *	207±18	225±17	224±21	227±17
Strain to Yield (mε)	17.1±1.4	18.4±2.0	18.1±0.6	18.8±0.6
Total Strain (mε)	59.5±18.2	65.0±21.4	63.5±24.0	48.8±16.0
Modulus (GPa)	12.0±0.8	12.7±2.2	11.8±2.1	12.0±0.9
Resilience (MPa) *	1.71±0.27	2.03±0.19	1.94±0.15	2.06±0.19
Toughness (MPa)	7.39±2.72	9.44±3.92	8.73±3.11	7.34±2.93
FEMALE	**(n=12)**	**(n=12)**	**(n=12)**	**(n=12)**
Yield Force (N) *	16.5±1.9	20.5±1.9	17.0±3.3	19.0±2.1
Maximum Force (N) *	17.9±1.7	23.7±2.9	18.7±2.9	22.3±4.1
Displacement to Yield (µm)	237±18	220±20	222±21	231±18
Postyield Displacement (µm)	378±252	300±205	451±232	429±373
Total Displacement (µm)	615±251	520±201	673±227	661±383
Stiffness (N/mm)	79.3±11.9	107.3±19.9 [a]	87.9±21.2 [b]	93.5±12.3
Work to Yield (mJ) *	2.14±0.27	2.46±0.17	2.07±0.38	2.41±0.32
Postyield Work (mJ)	4.13±2.22	6.06±4.60	6.13±3.32	8.30±6.78

Appendix C.2 Table 2 continued.

Total Work (mJ)	6.27±2.09	8.53±4.62	8.20±3.23	10.71±6.94
Yield Stress (MPa)	225±29	227±33	221±40	215±22
Maximum Stress (MPa) *	245±23	260±26	244±34	250±21
Strain to Yield (mε)	17.3±1.4	17.2±1.3	16.6±1.5	17.7±1.1
Total Strain (mε)	45.0±18.3	40.4±14.9	50.3±16.5	50.5±28.3
Modulus (GPa)	14.8±2.4	15.1±3.3	15.3±3.2	13.8±1.5
Resilience (MPa)	2.14±0.28	2.13±0.25	2.02±0.38	2.09±0.28
Toughness (MPa)	6.25±1.99	7.41±3.99	7.96±3.15	8.92±5.32

Loading and Raloxifene Treatment alter Matrix Composition in Newly Formed Bone

Regions of new bone growth were determined using fluorescent calcein labels (Appendix C.2 Figure 5A-D). For the loaded bones, the periosteal surface was assessed, while for the non-loaded bones, the endocortical surface was assessed due to the lack of periosteal labelling. Raman spectroscopic measures of relative mineralization, as described by both the $v1\text{-}PO_4^3$/Amide I and $v1\text{-}PO_4^3$/Amide III band intensity ratios, were not significantly impacted by loading or RAL treatment. However, when calculated as the $v1\text{-}PO_4^3$/CH$_2$ wag band intensity ratio, relative mineralization was significantly increased by loading ($p < 0.001$), but not RAL (Appendix C.2 Figure 5E). Similarly, mineral crystallinity was also significantly increased in loaded limbs ($p = 0.04$) but was not affected by RAL treatment (Appendix C.2 Figure 5F). Both loading and RAL did cause an increase in Type B carbonate substitution as determined by the $v_1\text{-}CO_3^{2-}/v_1\text{-}PO_4^3$ band intensity ratio ($p = 0.02$ and $p < 0.01$, respectively; Appendix C.2 Figure 5G). Finally, relative collagen maturity was significantly increased by both loading and RAL treatment (Appendix C.2 Figure 5H).

Loading Increases Reduced Modulus and Hardness in Newly Formed Bone

In an effort to understand the local mechanics of the newly formed bone, we calculated hardness and reduced elastic modulus from nanoindentation curves (Appendix C.2 Figure 6). Results showed that both were significantly increased in limbs that underwent loading ($p < 0.01$ and $p < 0.01$, respectively), but not significantly altered by RAL treatment.
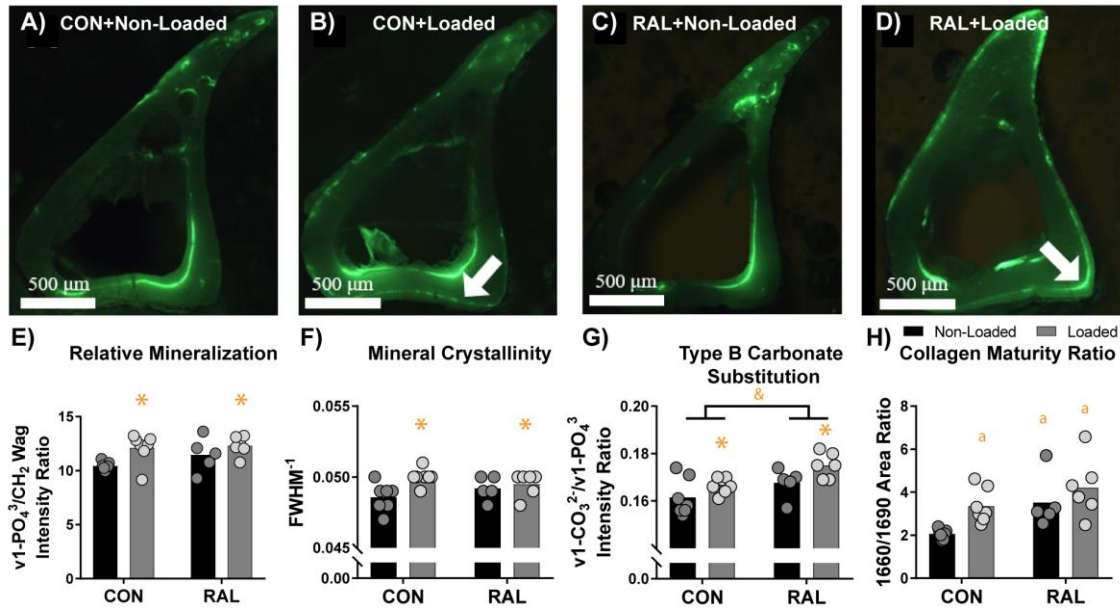
Appendix C.2 Figure 5. Raman spectra of newly formed bone were acquired in (A) non-loaded control, (B) loaded control, (C) non-loaded RAL, and (D) loaded RAL tibiae using fluorescent calcein labelling for visualization. White arrows show regions of periosteal bone growth in the loaded limbs. (E) Relative mineralization and (F) mineral crystallinity were both elevated due to loading, while (G) Type B carbonate substitution was increased due to RAL. (H) Collagen maturity ratio indicated increased collagen maturity due to both loading and RAL. For a two-way ANOVA, a '&' indicates a main effect of RAL and an '*' indicates a main effect of loading. If the interaction term was significant, an 'a' indicates a significant difference from non-loaded control, 'b' indicates a significant difference from loaded control, and 'c' indicates a significant difference from non-loaded RAL. Arrows indicate locations of new bone growth.
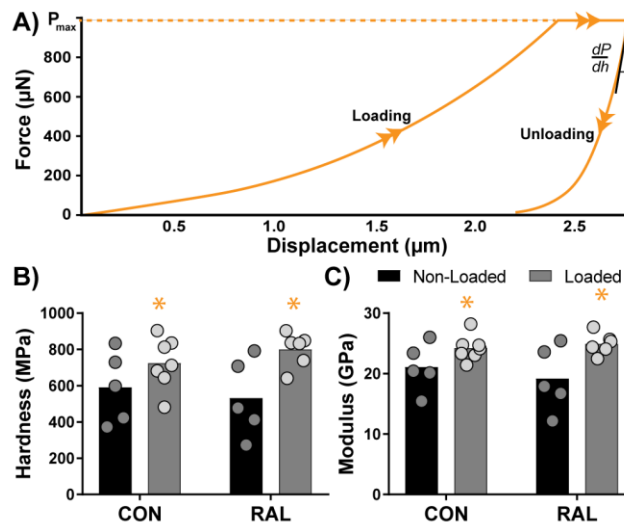
Appendix C.2 Figure 6. (A) Representative indentation plot showing loading and unloading curves. (B) Hardness and (C) modulus both showed increases due to loading, but not due to RAL.

Discussion

Raloxifene is a selective estrogen receptor modulator (SERM) that has been shown to reduce fracture risk in osteoporosis patients[11,32] through both quantity- and quality-based improvements. We therefore hypothesized that the presence of RAL during periods of active bone formation (i.e. prior and during mineralization) would enable tissue-based improvements to a greater degree than during periods of little bone formation. In addition, while previous work has demonstrated that adding aerobic exercise during RAL treatment can further increase BMD,[33] little work has been performed to assess the individual and combined impacts of RAL and mechanical stimulation, especially as it relates to metrics beyond that of BMD. Results in males demonstrate that loading and RAL have distinct impacts on the bone tissue, making the combination treatment a consideration to provide additional improvements beyond either treatment alone.

Tibial loading is a common method used to induce a robust bone formation response.[17-23] While physical exercise, such as running, is more clinically relevant, tibial loading has the advantage of a more robust bone-formation response.[23] Previous work from our group has shown that loading female C57BL/6 mice to 10.6 N for only 2 weeks (9 total loading bouts) can increase cortical thickness by 15%.[22] In the current study, we extended the loading to 6 weeks to provide additional time to observe the effects of RAL, and noted an average mid-cortical thickness increase of 26% in females. For the males, we chose to use the same peak load level as for females (10.6 N), given previous work that showed similar adaptive response in the cancellous region for both sexes.[27] Our work, in general, showed less responsiveness in the males than females (although the comparison was not statistically analyzed). In the cortical region, this difference in responsiveness is demonstrated by the 12% increase in cortical thickness observed with loading in the CON males compared to the 26% increase observed in CON females. In the same way, in the cancellous region, loading resulted in a 22% increase in bone volume fraction in CON males, compared to the 58% increase in females. One potential reason for this discrepancy could be an increase in background activity (e.g. cage fighting) among the group-housed males.[34] Alternatively, there may have been differences in load level and profile; however, since we did not verify strain levels induced in the bone prior to this study, direct comparisons are challenging. Even so, our primary objective in loading the tibiae was to induce a robust bone formation response which did occur in both males and females.

During this period of active bone formation, RAL was given to the mice. Previous work with RAL has demonstrated its ability to improve post-yield behavior in bone.[11] In addition, the mere presence of RAL *ex vivo* alters the transfer of load between the collagen and hydroxyapatite during mechanical loading.[11] Since the studies were shown in mineralized bone where access to the collagen may be inhibited, we hypothesized that RAL during tibial loading would create an environment whereby bone could be further improved. In this regard, we did observe some beneficial effects of RAL and loading, though the most pronounced effects were the mass-based outcomes observed within the cancellous region. In the clinic, RAL is known to only modestly improve bone mass, making these preclinical results interesting. Even so, these results do align with other preclinical work.[28,35] While cancellous effects were additive, effects in the mid-cortical region appeared to plateau. RAL and loading both had a positive impact, but their combination provided only modest further benefit.

RAL, like loading, improved maximum mechanical force. However, in the combination group, the effect plateaued such that loading, RAL, and the combination treatment all showed similar improvements. In females, the RAL+loading seemed to recover post-yield properties, increasing the effect size of total work and toughness versus non-loaded control bones, though results were non-significant. A previous study exploring the combination of RAL and a bisphosphonate treatment showed similar modest effects of RAL on mechanical properties.[35] Of particular interest is that, in that study, the effect of treatment on diseased bone was greater than that of healthy bone in the osteogenesis imperfecta murine model. While it is unclear why there were few whole-bone mechanical effects due to RAL in the current study, the previous work does suggest that bone may reach a point such that it is hard to make the already healthy bone any better.[35] As such, applying this combined treatment strategy in diseased bone is an important next step.

While whole-bone mechanical improvements were primarily loading-based, the secondary goal of this study was to assess if the newly deposited bone matrix was materially different among the treatment groups. For this sub-study, the decision to use only male mice was driven by a concern that the large loading-based effects in females would obscure the effects of RAL in the combined treatment group. In contrast, the mass-based effects in males at the proximal-mid location was graded, showing clear contributions of both loading and RAL. Others have reported that although bone size and shape are heavily affected by sex, the tissue-level material properties

are less dependent.[36] For these reasons, we chose to focus the Raman spectroscopy and nanoindentation on male mice.

When normalizing phosphate peak intensity by that of the amide I or amide III bands, relative mineralization remained unchanged. However, since this metric is relative, it may be that the osteoblasts deposited both mineral and collagen, resulting in no change in the mineral-to-matrix ratio. This finding is further supported by the increased modulus and hardness in bone that underwent loading, which is most likely due to increased local mineralization.[37] Like loading, RAL has been shown to increase osteoblast collagen deposition, as well as slightly increase or preserve bone mineral density,[38] which may have similarly resulted in a zero net change in these mineral/matrix ratios. Interestingly, a significant effect of loading was found when comparing the phosphate peak intensity to that of the CH_2 wag peak. In bone, the CH_2 wag peak originates primarily from the side chains of glycine, proline, and hydroxyproline found in collagen.[39] It is therefore possible that mechanical loading led to increased non-collagenous proteins (NCPs) in the bone matrix that contribute to the amide peaks, but due to their smaller CH_2 content compared to collagen, contribute little to the CH_2 wag peak.

Loading also significantly increased mineral crystallinity which is interesting given the lack of effect on type B carbonate substitution. In synthetic HA, increasing carbonate substitution typically decreases crystal perfection as carbonate substitutes for phosphate, increasing the length of the c-axis while decreasing the a-axis.[40,41] However, it should be noted that crystallinity also assesses the size and shape of the mineral crystals and not just perfection, which may have driven these effects. In addition, while the inverse relationship between carbonate substitution and crystallinity has been observed in bone, several studies examining the effects of aging on matrix composition have noted that crystallinity and carbonate content each tend to increase with age.[37,42] While the change in crystallinity was modest, it is possible that loading induced additional changes in crystal substitution that normalized the overall crystallinity measure. Further studies are needed to assess the contribution of additional ionic substitutions to the Raman crystallinity parameter.

Although loading did not increase type B carbonate substitution, RAL treatment did, which may be indicative of less mature bone tissue that has not yet undergone remodeling to remove carbonate. Two studies have examined the response of osteoblastic cells to carbonated hydroxyapatite in comparison to pure hydroxyapatite (HA). When considered together, these studies demonstrate that osteoblasts produce more mineral and proliferate more rapidly when in

contact with carbonated HA.[43,44] Therefore, RAL-induced bone formation on the periosteal surface may utilize increased carbonation to enhance the capacity for osteoblasts to lay new bone. In terms of mechanical properties, previous studies have demonstrated a negative correlation between carbonate substitution and fracture toughness on the whole bone level and reduced modulus and hardness on the tissue level.[45,46] Interestingly, no correlation was seen with structural mechanical properties including modulus and ultimate strength.[47] Decreased tissue-level properties are thought to be related to internal strains created by carbonate within the bone matrix that result in altered crystal formation and elongation.[48] In our study, we did not observe changes in reduced modulus or hardness in RAL-treated samples in regions with increased relative carbonate content. We hypothesize that RAL may interact with the matrix and stabilize mineral crystals that contain carbonate substitutions, normalizing the mechanical properties of the region, a process that may also involve increased matrix-bound water.

It was further observed that RAL increased the relative collagen maturity of newly formed bone tissue. This parameter, measured as the $1660 \text{ cm}^{-1}/1690 \text{ cm}^{-1}$ subpeak area ratios, likely represents changes in the secondary structure of collagen due to changes in content or shape driven by increased mineralization.[49] In general, proper collagen structure and alignment is responsible for providing bone tissue with toughness and post-yield mechanical integrity.[50] Thus, given these direct changes in the secondary structure of collagen, fatigue and fracture toughness testing may better reflect the mechanical outcome of these changes as compared to the monotonic test to failure that was performed in this study. Future work involving dynamic mechanical analysis can provide information on how collagen and RAL treatment impact the viscoelastic properties of bone on the microscale.

As a limitation, we note that in order to cut and polish bone samples for Raman spectroscopy and nanoindentation, bones were embedded in Koldmount, a fast-curing methyl methacrylate (MMA) resin. This method of embedding was selected because it does not require the bone to be dehydrated and it cures rapidly. A previous study demonstrated that embedding bone in polymethylmethacrylate (PMMA) significantly altered the mineral/matrix ratio normalized to the CH_2 wag peak.[51] However, this process utilized a slow-curing method that involved dehydration and soaking the bone in xylenes before undergoing a 7-day infiltration with MMA. In this case, bone composition is altered by dehydration and matrix infiltration which could result in increased free radical release deep into the bone matrix during polymerization. While the effects of

Koldmount embedding on bone Raman signatures and other matrix properties have not been directly studied, this method does not require dehydration or infiltration and likely preserves hydration of the bone tissue and limits free radical infiltration to the bone surface. Therefore, alterations in the CH_2 wag peak area are less likely to have been caused by the method of embedding and may reflect actual changes in the protein content of the bone matrix.

In summary, it was demonstrated that RAL and loading work together to improve bone size and architecture, especially within the cancellous region. In the cortical regions, there were some combination effects in the males, even at the microstructural-level which showed load-based changes in mineralization and RAL-based changes in the secondary collagen structure. In females, the large load-based effects in the cortical region obscured many effects of RAL, though some effects were still present. Future work will aim to explore the response of combined treatment in diseased tissue, which may provide a platform to observe even greater effects and potentially reverse the negative quality-based impacts of disease.

Supplemental Material
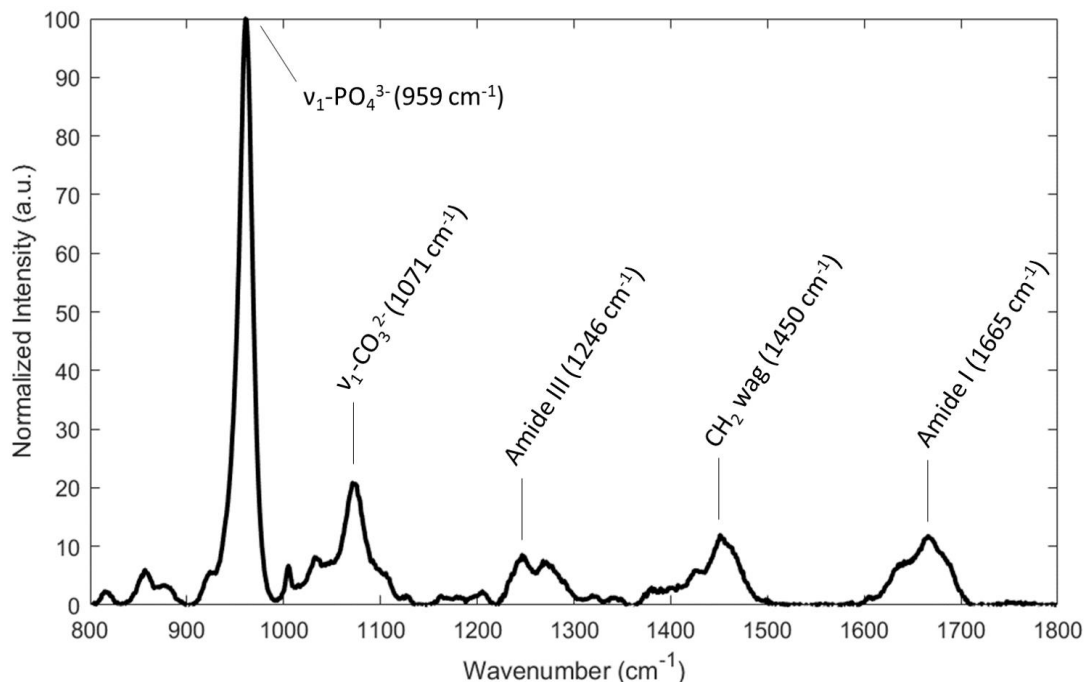
Appendix C.2 Supplemental Figure 1. Representative Raman spectra show the locations of the peaks used in the calculation of Raman parameters.

Appendix C.2 Supplemental Table 1. Cancellous bone analysis as assessed by CT. A '*' indicates a significant effect of load and a '+' indicates a significant effect of treatment (p<0.05). In the case of significant interaction term, a one-way ANOVA with post-hoc Tukey HSD test was performed. An 'a' indicates a significant difference from CON, a 'b' indicates a significant difference from LOAD, and a 'c' indicates a significant difference from RAL (p<0.05).

	CON	LOAD	RAL	RAL+LOAD
MALE	**(n=11)**	**(n=11)**	**(n=12)**	**(n=12)**
Bone Mineral Density (g/cm^3) *+	0.166±0.028	0.202±0.042	0.227±0.052	0.262±0.048
Bone Volume Fraction (%) *+	14.8±2.4	18.0±3.2	20.1±4.5	23.7±3.7
Trabecular Thickness (µm) *+	58.9±2.0	72.8±6.6	66.7±4.6	76.3±3.3
Trabecular Spacing (µm) *	190±8	189±14	188±12	181±13
Trabecular Number (1/mm) +	2.51±0.35	2.47±0.38	3.00±0.50	3.11±0.50
Tissue Mineral Density (g/cm^3) *	0.719±0.022	0.764±0.036	0.748±0.034	0.778±0.035
FEMALE	**(n=12)**	**(n=12)**	**(n=12)**	**(n=12)**
Bone Mineral Density (g/cm^3) *	0.137±0.023	0.201±0.037	0.164±0.021	0.212±0.038
Bone Volume Fraction (%) *	10.5±2.8	16.6±3.4	13.0±1.7	18.0±2.8
Trabecular Thickness (µm)	61.3±2.0	90.7±8.6 [a]	66.3±2.2 [a,b]	88.4±8.4 [a,c]
Trabecular Spacing (µm) *	274±45	262±42	264±36	249±36
Trabecular Number (1/mm) *	1.72±0.45	1.83±0.37	1.96±0.23	2.04±0.25
Tissue Mineral Density (g/cm^3)	0.733±0.026	0.822±0.045 [a]	0.754±0.029 [b]	0.809±0.041 [a,c]

Appendix C.2 Supplemental Table 2. Cortical bone analysis of the proximal-mid region as assessed by CT. A '*' indicates a significant effect of load and a '+' indicates a significant effect of treatment ($p<0.05$). In the case of significant interaction term, a one-way ANOVA with post-hoc Tukey HSD test was performed. An 'a' indicates a significant difference from CON, a 'b' indicates a significant difference from LOAD, and a 'c' indicates a significant difference from RAL ($p<0.05$).

	CON	LOAD	RAL	RAL+LOAD
MALE	**(n=11)**	**(n=11)**	**(n=12)**	**(n=12)**
Total Cross-Sectional Area (mm^2) *+	1.38±0.14	1.52±0.13	1.53±0.11	1.62±0.12
Cortical Area (mm^2) *+	0.834±0.075	0.956±0.070	0.955±0.075	1.025±0.072
Cortical Thickness (mm) *+	0.241±0.011	0.265±0.016	0.264±0.015	0.276±0.013
Maximum Moment of Inertia (mm^4) *	0.292±0.059	0.348±0.052	0.337±0.047	0.367±0.055
Minimum Moment of Inertia (mm^4) *+	0.087±0.020	0.106±0.017	0.111±0.016	0.126±0.017
Tissue Mineral Density (g/cm^3)	0.787±0.015	0.800±0.019	0.782±0.020	0.788±0.021
FEMALE	**(n=12)**	**(n=12)**	**(n=12)**	**(n=12)**
Total Cross-Sectional Area (mm^2)	1.24±0.04	1.51±0.11 [a]	1.30±0.07 [b]	1.48±0.13 [a,c]
Cortical Area (mm^2) *	0.781±0.032	1.000±0.089	0.832±0.037	0.985±0.100
Cortical Thickness (mm)	0.239±0.007	0.289±0.022 [a]	0.252±0.006 [a,b]	0.286±0.022 [a,c]
Maximum Moment of Inertia (mm^4)	0.244±0.026	0.322±0.042 [a]	0.253±0.035 [b]	0.306±0.056 [a,c]
Minimum Moment of Inertia (mm^4)	0.069±0.005	0.111±0.020 [a]	0.078±0.007 [a,b]	0.106±0.020 [a,c]
Tissue Mineral Density (g/cm^3) *	0.805±0.018	0.817±0.018	0.809±0.010	0.825±0.016

Appendix C.2 Supplemental Table 3. Cortical bone analysis of the mid-diaphysis as assessed by CT. A '*' indicates a significant effect of load and a '+' indicates a significant effect of treatment (p<0.05). In the case of significant interaction term, a one-way ANOVA with post-hoc Tukey HSD test was performed. An 'a' indicates a significant difference from CON, a 'b' indicates a significant difference from LOAD, and a 'c' indicates a significant difference from RAL (p<0.05).

	CON	LOAD	RAL	RAL+LOAD
MALE	**(n=11)**	**(n=11)**	**(n=12)**	**(n=12)**
Total Cross-Sectional Area (mm^2)	1.060±0.118	1.141±0.100	1.190±0.134	1.213±0.130 [a]
Cortical Area (mm^2)	0.660±0.068	0.761±0.060 [a]	0.774±0.080 [a]	0.813±0.087 [a]
Cortical Thickness (mm)	0.223±0.012	0.249±0.008 [a]	0.249±0.014 [a]	0.262±0.015 [a]
Maximum Moment of Inertia (mm^4)	0.102±0.026	0.124±0.024	0.132±0.036	0.139±0.036 [a]
Minimum Moment of Inertia (mm^4)	0.064±0.012	0.075±0.011	0.081±0.015 [a]	0.085±0.015 [a]
Tissue Mineral Density (g/cm^3)	0.888±0.012	0.894±0.014	0.876±0.015 [b]	0.875±0.018 [b]
FEMALE	**(n=12)**	**(n=12)**	**(n=12)**	**(n=12)**
Total Cross-Sectional Area (mm^2)	0.955±0.044	1.137±0.109 [a]	0.988±0.072 [b]	1.101±0.125 [a,c]
Cortical Area (mm^2)	0.593±0.022	0.788±0.085 [a]	0.647±0.027 [a,b]	0.773±0.092 [a,c]
Cortical Thickness (mm)	0.211±0.007	0.266±0.019 [a]	0.230±0.007 [a,b]	0.267±0.018 [a,c]
Maximum Moment of Inertia (mm^4)	0.075±0.008	0.122±0.028 [a]	0.084±0.012 [b]	0.114±0.031 [a,c]
Minimum Moment of Inertia (mm^4)	0.056±0.005	0.076±0.012 [a]	0.061±0.008 [b]	0.073±0.014 [a,c]
Tissue Mineral Density (g/cm^3)	0.896±0.018	0.893±0.011	0.899±0.014	0.901±0.014

Appendix C.2 Supplemental Table 4. Raman spectroscopy measures of new bone. A '*' indicates a significant effect of load and a '+' indicates a significant effect of treatment (p<0.05). In the case of significant interaction term, a one-way ANOVA with post-hoc Tukey HSD test was performed. An 'a' indicates a significant difference from CON, a 'b' indicates a significant difference from LOAD, and a 'c' indicates a significant difference from RAL (p<0.05).

	CON	LOAD	RAL	RAL+LOAD
MALE	**(n=7)**	**(n=5)**	**(n=7)**	**(n=6)**
$v1$-PO_4^3/CH_2 Wag Intensity Ratio *	10.4±0.4	12.6±0.5	11.5±1.6	12.3±0.9
Mineral Crystallinity (FWHM^{-1}) *	0.0488±0.0011	0.0500±0.0000	0.0492±0.0008	0.0495±0.0008
$v1$-CO_3^{2-}/$v1$-PO_4^3 Intensity Ratio *+	0.161±0.008	0.167±0.003	0.168±0.006	0.175±0.005
1660/1690 Area Ratio	2.06±0.22	3.36±0.80 [a]	3.52±1.25 [a]	4.21±1.38 [a]

Appendix C.2 Supplemental Table 5. Nanoindentation measures of new bone. A '*' indicates a significant effect of load and a '+' indicates a significant effect of treatment (p<0.05).

	CON	LOAD	RAL	RAL+LOAD
MALE	**(n=5)**	**(n=7)**	**(n=5)**	**(n=6)**
Hardness (MPa) *	591±196	724±141	532±214	800±94
Modulus (GPa) *	21.1±4.0	24.2±2.1	19.2±5.4	24.9±1.8

References

1. Taranta A, Brama M, Teti A et al. 2002. The selective estrogen receptor modulator raloxifene regulates osteoclast and osteoblast activity in vitro. Bone. 30(2):368-376.

2. Delmas PD, Bjarnason NH, Mitlak BH et al. 1997. Effects of raloxifene on bone mineral density, serum cholesterol concentrations, and uterine endometrium in postmenopausal women. N Engl J Med. 337(23):1641-1647.

3.	Gizzo S, Saccardi C, Patrelli TS et al. 2013. Update on raloxifene: Mechanism of action, clinical efficacy, adverse effects, and contraindications. Obstet Gynecol Surv. 68(6):467-481.

4.	Ettinger B, Black DM, Mitlak BH et al. 1999. Reduction of vertebral fracture risk in postmenopausal women with osteoporosis treated with raloxifene: Results from a 3-year randomized clinical trial. JAMA. 282(7):637-645.

5.	Seeman E, Crans GG, Diez-Perez A, Pinette KV, Delmas PD. 2006. Anti-vertebral fracture efficacy of raloxifene: A meta-analysis. Osteoporos Int. 17(2):313-316.

6.	Cranney A, Guyatt G, Griffith L et al. 2002. Ix: Summary of meta-analyses of therapies for postmenopausal osteoporosis. Endocr Rev. 23(4):570-578.

7.	Sarkar S, Mitlak BH, Wong M et al. 2002. Relationships between bone mineral density and incident vertebral fracture risk with raloxifene therapy. J Bone Miner Res. 17(1):1-10.

8.	Allen MR, Iwata K, Sato M, Burr DB. 2006. Raloxifene enhances vertebral mechanical properties independent of bone density. Bone. 39(5):1130-1135.

9.	Allen MR, Hogan HA, Hobbs WA et al. 2007. Raloxifene enhances material-level mechanical properties of femoral cortical and trabecular bone. Endocrinology. 148(8):3908-3913.

10.	Aref M, Gallant MA, Organ JM et al. 2013. In vivo reference point indentation reveals positive effects of raloxifene on mechanical properties following 6 months of treatment in skeletally mature beagle dogs. Bone. 56(2):10.1016/j.bone.2013.1007.1009.

11.	Gallant MA, Brown DM, Hammond M et al. 2014. Bone cell-independent benefits of raloxifene on the skeleton: A novel mechanism for improving bone material properties. Bone. 61:191-200.

12.	Allen MR, Aref MW, Newman CL, Kadakia JR, Wallace JM. 2016. Raloxifene neutralizes bone brittleness induced by anti-remodeling treatment and increases fatigue life through non-cell mediated mechanisms. Actualizaciones en Osteologia. 12(3):169-179.

13.	Dalen N, Olsson KE. 1974. Bone mineral content and physical activity. Acta Orthop Scand. 45(2):170-174.

14.	Wolman RL, Faulmann L, Clark P, Hesp R, Harries MG. 1991. Different training patterns and bone mineral density of the femoral shaft in elite, female athletes. Ann Rheum Dis. 50(7):487-489.

15.	Brewer V, Meyer BM, Keele MS, Upton SJ, Hagan RD. 1983. Role of exercise in prevention of involutional bone loss. Med Sci Sports Exerc. 15(6):445-449.

16.	Fuchs RK, Bauer JJ, Snow CM. 2001. Jumping improves hip and lumbar spine bone mass in prepubescent children: A randomized controlled trial. J Bone Miner Res. 16(1):148-156.

17. De Souza RL, Matsuura M, Eckstein F et al. 2005. Non-invasive axial loading of mouse tibiae increases cortical bone formation and modifies trabecular organization: A new model to study cortical and cancellous compartments in a single loaded element. Bone. 37(6):810-818.

18. Fritton JC, Myers ER, Wright TM, van der Meulen MCH. 2005. Loading induces site-specific increases in mineral content assessed by microcomputed tomography of the mouse tibia. Bone. 36(6):1030-1038.

19. Weatherholt AM, Fuchs RK, Warden SJ. 2013. Cortical and trabecular bone adaptation to incremental load magnitudes using the mouse tibial axial compression loading model. Bone. 52(1):372-379.

20. Yang H, Embry RE, Main RP. 2017. Effects of loading duration and short rest insertion on cancellous and cortical bone adaptation in the mouse tibia. PLoS One. 12(1):e0169519.

21. Sun D, Brodt MD, Zannit HM, Holguin N, Silva MJ. 2018. Evaluation of loading parameters for murine axial tibial loading: Stimulating cortical bone formation while reducing loading duration. Journal of Orthopaedic Research®. 36(2):682-691.

22. Berman AG, Clauser CA, Wunderlin C, Hammond MA, Wallace JM. 2015. Structural and mechanical improvements to bone are strain dependent with axial compression of the tibia in female c57bl/6 mice. PLoS One. 10(6):e0130504.

23. Berman AG, Hinton MJ, Wallace JM. 2019. Treadmill running and targeted tibial loading differentially improve bone mass in mice. Bone reports. 10:100195.

24. Willie BM, Birkhold AI, Razi H et al. 2013. Diminished response to in vivo mechanical loading in trabecular and not cortical bone in adulthood of female c57bl/6 mice coincides with a reduction in deformation to load. Bone. 55(2):335-346.

25. Hammond MA, Laine TJ, Berman AG, Wallace JM. 2016. Treadmill exercise improves fracture toughness and indentation modulus without altering the nanoscale morphology of collagen in mice. PLoS One. 11(9):e0163273.

26. Hammond MA, Berman AG, Pacheco-Costa R et al. 2016. Removing or truncating connexin 43 in murine osteocytes alters cortical geometry, nanoscale morphology, and tissue mechanics in the tibia. Bone. 88:85-91.

27. Lynch ME, Main RP, Xu Q et al. 2010. Cancellous bone adaptation to tibial compression is not sex dependent in growing mice. J Appl Physiol (1985). 109(3):685-691.

28. Powell KM, Brown AP, Skaggs CG et al. 2020. 6′-methoxy raloxifene-analog enhances mouse bone properties with reduced estrogen receptor binding. Bone Reports. 12:100246.

29. Sugiyama T, Price JS, Lanyon LE. 2010. Functional adaptation to mechanical loading in both cortical and cancellous bone is controlled locally and is confined to the loaded bones. Bone. 46(2):314-321.

30. Hammond MA, Gallant MA, Burr DB, Wallace JM. 2014. Nanoscale changes in collagen are reflected in physical and mechanical properties of bone at the microscale in diabetic rats. Bone. 60:26-32.

31. Newman CL, Creecy A, Granke M et al. 2016. Raloxifene improves skeletal properties in an animal model of cystic chronic kidney disease. Kidney Int. 89(1):95-104.

32. Bivi N, Hu H, Chavali B et al. 2016. Structural features underlying raloxifene's biophysical interaction with bone matrix. Bioorg Med Chem. 24(4):759-767.

33. Zhao C, Hou H, Chen Y, Lv K. 2016. Effect of aerobic exercise and raloxifene combination therapy on senile osteoporosis. Journal of physical therapy science. 28(6):1791-1794.

34. Meakin LB, Sugiyama T, Galea GL et al. 2013. Male mice housed in groups engage in frequent fighting and show a lower response to additional bone loading than females or individually housed males that do not fight. Bone. 54(1):113-117.

35. Powell KM, Skaggs C, Pulliam A et al. 2019. Zoledronate and raloxifene combination therapy enhances material and mechanical properties of diseased mouse bone. Bone. 127:199-206.

36. Tommasini SM, Nasser P, Jepsen KJ. 2007. Sexual dimorphism affects tibia size and shape but not tissue-level mechanical properties. Bone. 40(2):498-505.

37. Akkus O, Adar F, Schaffler MB. 2004. Age-related changes in physicochemical properties of mineral crystals are related to impaired mechanical function of cortical bone. Bone. 34(3):443-453.

38. Johnston CC, Jr., Bjarnason NH, Cohen FJ et al. 2000. Long-term effects of raloxifene on bone mineral density, bone turnover, and serum lipid levels in early postmenopausal women: Three-year data from 2 double-blind, randomized, placebo-controlled trials. Arch Intern Med. 160(22):3444-3450.

39. Sato ET, Martinho H. 2018. First-principles calculations of raman vibrational modes in the fingerprint region for connective tissue. Biomed Opt Express. 9(4):1728-1734.

40. Zapanta-LeGeros R. 1965. Effect of carbonate on the lattice parameters of apatite. Nature. 206(982):403-404.

41. McElderry J-DP, Zhu P, Mroue KH et al. 2013. Crystallinity and compositional changes in carbonated apatites: Evidence from (31)p solid-state nmr, raman, and afm analysis. J Solid State Chem. 206:10.1016/j.jssc.2013.1008.1011.

42. Yerramshetty JS, Lind C, Akkus O. 2006. The compositional and physicochemical homogeneity of male femoral cortex increases after the sixth decade. Bone. 39(6):1236-1243.

43. Germaini MM, Detsch R, Grunewald A et al. 2017. Osteoblast and osteoclast responses to a/b type carbonate-substituted hydroxyapatite ceramics for bone regeneration. Biomed Mater. 12(3):035008.

44. Uskokovic V, Janković-Častvan I, Wu V. 2019. Bone mineral crystallinity governs the orchestration of ossification and resorption during bone remodeling. ACS Biomaterials Science & Engineering. 5.

45. Makowski AJ, Granke M, Ayala OD et al. 2017. Applying full spectrum analysis to a raman spectroscopic assessment of fracture toughness of human cortical bone. Applied spectroscopy. 71(10):2385-2394.

46. Unal M, Uppuganti S, Timur S et al. 2019. Assessing matrix quality by raman spectroscopy helps predict fracture toughness of human cortical bone. Sci Rep. 9(1):1-13.

47. Bi X, Patil CA, Lynch CC et al. 2011. Raman and mechanical properties correlate at whole bone-and tissue-levels in a genetic mouse model. J Biomech. 44(2):297-303.

48. Bala Y, Farlay D, Boivin G. 2013. Bone mineralization: From tissue to crystal in normal and pathological contexts. Osteoporos Int. 24(8):2153-2166.

49. Farlay D, Duclos ME, Gineyts E et al. 2011. The ratio 1660/1690 cm(-1) measured by infrared microspectroscopy is not specific of enzymatic collagen cross-links in bone tissue. PLoS One. 6(12):e28736.

50. Wang X, Shen X, Li X, Agrawal CM. 2002. Age-related changes in the collagen network and toughness of bone. Bone. 31(1):1-7.

51. Yeni YN, Yerramshetty J, Akkus O, Pechey C, Les CM. 2006. Effect of fixation and embedding on raman spectroscopic analysis of bone tissue. Calcif Tissue Int. 78(6):363-371.

C.3 Treadmill Running and Targeted Tibial Loading Differentially Improve Bone Mass in Mice

Abstract

Treadmill running and tibial loading are two common modalities used to assess the role of mechanical stimulation on the skeleton preclinically. The primary advantage of treadmill running is its physiological relevance. However, the applied load is complex and multiaxial, with observed results influenced by cardiovascular and musculoskeletal effects. In contrast, with tibial loading, a direct uniaxial load is applied to a single bone, providing the advantage of greater control but with less physiological relevance. Despite the importance and wide-spread use of both modalities, direct comparisons are lacking. In this study, we compared effects of targeted tibial loading, treadmill running, and their combination on cancellous and cortical architecture in a murine model. We show that tibial loading and treadmill running differentially improve bone mass, with tibial loading resulting in thicker trabeculae and increased cortical mass, and exercise resulting in greater number of trabeculae and no cortical mass-based effects. Combination of the modalities resulted in an additive response. These data suggest that tibial loading and exercise may improve mass differentially.

Introduction

Bone is a dynamic structure that can alter its mass and architecture to accommodate a changing environment. Increases in load result in increased bone mass, and conversely, decreases in load result in decreased bone mass. This theory of bone adaption, referred to as mechanostat, has been well-established in both clinical[1,2] and preclinical[3] studies. Within the preclinical realm, studies can often be broadly separated into two groups: 1) exercise-based and 2) external mechanical stimulation.

For exercise studies, animals undergo some form of physical activity, such as running,[4-6] jumping,[7,8] or swimming,[9,10] causing stimulation of the bone and thereby inducing a bone formation response. The primary advantage of these models is their physiological relevance and translatability. However, this is also the primary disadvantage in that systemic effects are difficult,

if not impossible, to fully account for. Loads are multiaxial, and the observed results are influenced by cardiovascular and muscular effects, in addition to the applied mechanical strains engendered on bone. In general, most running studies have shown positive influence on cancellous bone mass and cortical mechanical integrity, though these results are heavily influenced by sex,[5] age,[11] and analysis location.[4] While these studies are important, the lack of control over the loading profile has made it difficult to assess the effect of specific alterations to loading stimulus or to target specific mechanotransduction pathways.

More recently, external mechanical stimulation protocols have been developed, providing researchers with the advantage of greater control but with less physiological relevance. These protocols apply a direct, predominately uniaxial, load to a single bone or limb, enabling control over the precise stimulus delivered to the bone.[12-14] Although a variety of external mechanical stimulation protocols have been utilized, one increasingly popular method is tibial loading, in which the tibia of an anesthetized rodent is placed within a mechanical test device and non-invasively loaded with a cyclic waveform.[14] The increased control in these models has enabled researchers to explore types of loads that are anabolic. For example, bone formation is both strain[15] and strain rate[16,17] dependent. Mechanistic studies have also been conducted, with targeted loading used to tease out the role of various molecules in mechanotrasduction pathways.[18,19] Despite these advantages, the physiological relevance of this model is less clearly defined.

While both types of models engender strain stimulus on bone and induce a bone formation response, previous data in our lab has suggested that exercise and tibial loading may differentially improve bone mass; however, few studies have assessed this question. Results drawn from one type are often used to interpret findings from a different type of loading. The primary goal of this study was to explicitly show some of these differences. Moreover, if mechanisms of bone formation are different, it would imply that the combined effects of exercise and tibial loading should increase bone's response in an additive manner. To test this hypothesis, we compared effects of targeted tibial loading, treadmill running, and their combination on cancellous and cortical architecture in a murine model.

Methods

Experimental Overview

All procedures were performed with prior approval from the Indiana University School of Science Institutional Animal Care and Use Committee (IACUC). Male C57Bl/6J mice were purchased from Jackson Laboratory (Bar Harbor, ME) and separated into two groups: exercise (EX; n=12) and sedentary control (SED; n=12). All mice were housed individually to prevent cage fighting which may mask effects of loading,[20] but we did not measure the background loading between groups. Beginning at 8 weeks of age, both exercise and sedentary mice underwent compressive loading of the right tibia (details below) for two consecutive days every other week (i.e. Mon/Tues of weeks 1, 3, and 5). The contralateral limb was used as an internal non-loaded control.[21] On the remaining days of each week and on the alternating weeks, the exercise mice ran on a treadmill (details below). At 14 weeks of age, mice were euthanized and their tibiae stored wrapped in phosphate-buffered saline (PBS)-soaked gauze at -20 °C. This study design resulted in four groups (n=12/group): 1) no exercise and non-loaded, 2) no exercise and loaded, 3) exercise and non-loaded, and 4) exercise and loaded (Figure 1).

Appendix C.3 Figure 1. Experimental overview showing A) groups and B) loading and exercise schedule.

In vivo Tibial Loading

Mice were anesthetized (2% Isoflurane) and their right limb cyclically loaded in compression. Each loading profile consisted of 2 cycles at 4 Hz to 11.9 N, followed by a 1-second rest at 2 N, repeated 110 times for a total of 220 compressive cycles per day. This profile differs from that previously reported from our group[22] due to the observation of limping in later cohorts of mice (data unpublished). We found that increasing the frequency to 4 Hz and holding the load

at 2 N during the rest period reduced limping. In the current study, limping was not observed. Moreover, the load level is within the range of loads shown to induce a bone formation response.[14,15,22] Note that although we did not perform histology, we did not observe any signs of woven bone from micro-computed tomography (micro-CT).

Treadmill Running

On exercise days, the exercise group ran on a treadmill (Animal Treadmill: Exer 3/6; Columbus Instruments, Columbus, OH, USA) at a 5° incline for 30 min. Over the first few days of exercise, mice were acclimated to the treadmill, beginning at a rate of 6 m/min and slowly building up to 12 m/min. By the second week, all mice maintained a 12 m/min rate for the duration of the running bout.

Computed Tomography (CT)

Harvested tibiae were scanned by high resolution micro-CT (Skyscan 1172; Bruker, Kontich, Belgium) using the following parameters: 10 μm resolution, 60 kV tube voltage, 167 μA current, 0.7-degree increment angle, and 2-frame averaging. To convert gray-scale images to mineral content, hydroxyapatite calibration phantoms (0.25 and 0.75 g/cm^3 CaHA) were also scanned. After reconstruction and rotation using Bruker software (nRecon and DataViewer), regions of interest were selected in the proximal metaphysis, proximal-mid diaphysis, and mid-diaphysis for analysis.

The proximal metaphysis was selected as a 2-mm region of interest, beginning at the distal end of the proximal growth plate and extending distally. Cancellous bone was then automatically segmented from its surrounding cortical shell in CTAn (Bruker) and manually checked for accuracy of segmentation. The region of interest was then analyzed in CTAn to determine bone volume fraction (BV/TV), trabecular thickness (Tb.Th), number (Tb.N), separation (Tb.Sp), bone mineral density (BMD), and tissue mineral density (TMD).

For the proximal-mid and mid-diaphysis locations, a 1-mm region of interest was selected at 37% and 50% of the bone length, respectively, measured from the top of the bone. The cortical shaft was analyzed (Matlab, MathWorks, Inc. Natick, MA) to determine areas (total cross sectional area [Tt.Ar], cortical area [Ct.Ar], and marrow area [Ma.Ar]), cortical thickness (Ct.Th), cortical

area fraction (Ct.Ar/Tt.Ar), perimeters (periosteal [Ps.Pm] and endocortical [Ec.Pm]), principal moments of inertia (I_{max} and I_{min}), and tissue mineral density (TMD).

Statistics

Main effects of exercise and tibial loading were assessed in Prism (v7.03, Graphpad) by repeated measures two-way ANOVA to assess the main effects of loading (within-subject effect), exercise (between-subject effect), and their interaction ($p < 0.05$). No significant interaction terms were noted for these data and, therefore, no post hoc analyses were performed. Data are presented as mean ± standard deviation.

Results

Body Weight and Tibial Length

At the beginning of the study, mice were weight-matched into sedentary (23.15 ± 1.56 g) and exercise (23.17 ± 1.56 g) groups. At the end of the study, body weights remained statistically indistinguishable (SED: 26.6±1.4 g, EX: 26.0±1.0 g; p=ns). In contrast, tibial length, as measured with calipers at the end of the study, was significantly increased due to loading (p=0.02) but not exercise. Despite its significance, differences in tibial length were modest (SED Non-Loaded: 18.2±0.6 mm, SED Loaded: 18.3±0.5 mm, EX Non-Loaded: 17.9±0.3, EX Loaded: 18.2±0.4 mm).

Tibial Loading and Exercise Differentially Improve Cancellous Bone Mass

A 2-mm metaphyseal region of interest was analyzed to assess cancellous bone properties (Figure 2). Results indicated that tibial loading (+7.9%; p=0.01) and exercise (+7.2%; p<0.001) similarly improved bone volume fraction (BV/TV) compared to the non-loaded sedentary bones. Combined effects of the two modalities were additive, showing a 17.2% improvement in bone volume fraction. Similar results were also observed for bone mineral density (BMD), with tibial loading resulting in an 8.3% improvement (p<0.001), exercise resulting in a 7.3% improvement (p<0.01), and their combined effect additive (+16.5%).

Despite similar increases in bone volume fraction and bone mineral density for tibial loading and exercise, the mechanism by which mass was increased varied for the two modalities. Tibial

loading primarily improved trabecular thickness (+18.3%; p<0.001) with detrimental impacts to trabecular number (-8.7%; p<0.001) and separation (+5.8%; p<0.001). In contrast, exercise predominately improved bone mass through greater trabecular number (+6.4%; p<0.05) with modest non-significant changes in trabecular separation and thickness. In combination, additive effects were noted for all three properties (+19.6% for thickness, +3.2% for separation, and -2.0% for number).

Interestingly, although both modalities improved bone mass, only tibial loading significantly impacted tissue mineral density (+6.2%; p<0.001). Exercise modestly improved the value (+1.5%), but results were non-significant.
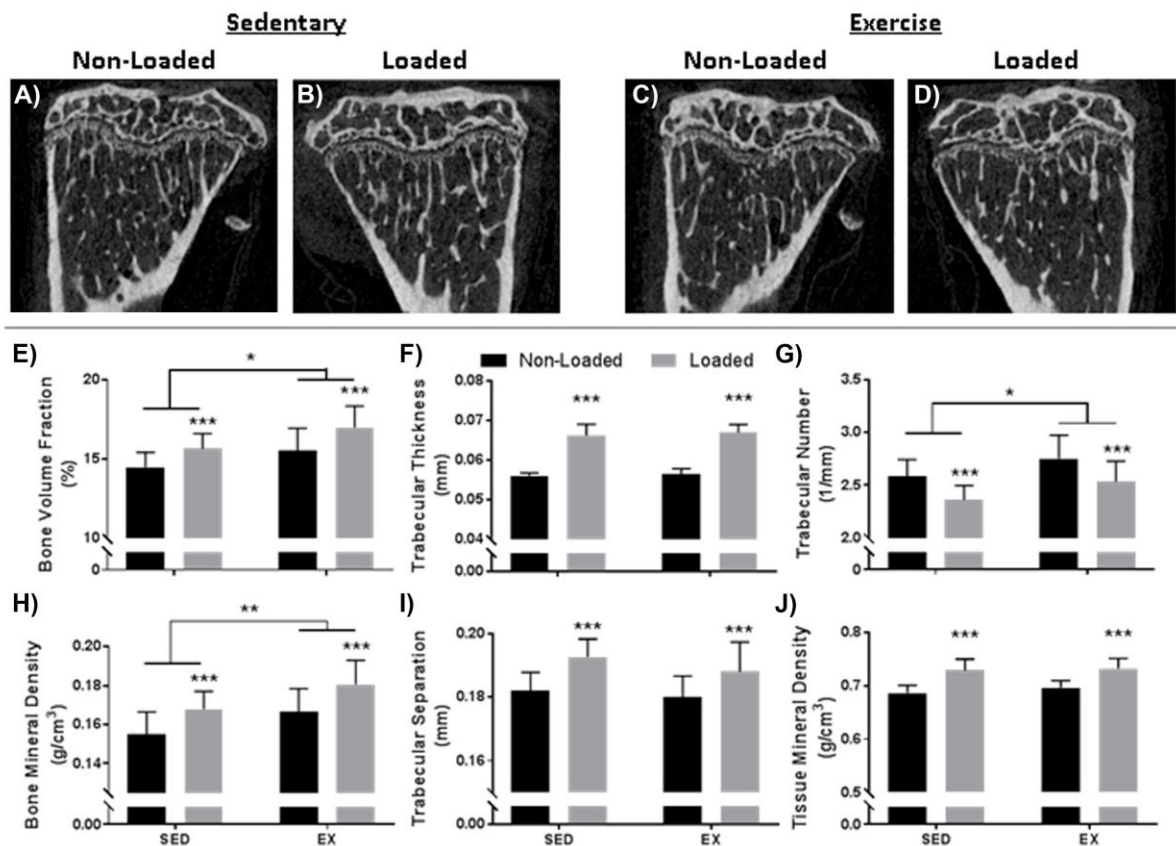
Appendix C.3 Figure 2. Cancellous properties within the tibial metaphysis are shown qualitatively (A-D) and quantitatively (E-J). Results indicate improved bone volume fraction (E) and bone mineral density (H) due to both tibial loading and exercise. Combined effects were additive. Tibial loading predominately improved trabecular thickness (F) with detrimental impacts to trabecular separation (I), while exercise predominately improved trabecular number (G). Only tibial loading improved tissue mineral density (J). *p < 0.05, **p < 0.01, ***p < 0.001

Tibial Loading, but not Exercise, Improves Cortical Bone Mass

In contrast to the cancellous region, only tibial loading improved bone mass in the cortical proximal-mid and mid-diaphysis locations. At the proximal-mid location, loading resulted in both periosteal and endocortical expansion, with the loaded bones having a thicker cortex than their non-loaded controls. Similarly, at the mid-diaphysis, loading also resulted in periosteal expansion, as noted by a significantly greater cross-sectional area. Marrow area and endosteal bone surface were reduced, suggesting endocortical contraction at this location. With the exception of periosteal bone surface at the mid-diaphysis location, all structural parameters measured at both the proximal-mid and mid-diaphysis were significantly altered due to loading whereas no properties were significantly changed due to exercise (Figure 3 and Table 1). Similar to the cancellous region, the proximal-mid location showed increased tissue mineral density with loading. Interestingly, unlike the cancellous and mid-proximal regions, tissue mineral density at the mid-diaphysis was not significantly improved due to loading.

Discussion

Tibial loading and exercise are two common modalities used to assess the effects of mechanical stimulation on the skeleton. However, direct comparisons of the two modalities are lacking. In this study, we show that tibial loading and treadmill running differentially improve bone mass, with tibial loading resulting in thicker trabeculae and increased cortical mass, and treadmill running resulting in greater number of trabeculae and no cortical mass-based effects.

To the authors' knowledge, only one paper to date has utilized both exercise and tibial loading; however, their exercise protocol was mild (3 days/week for 2 weeks) with the aim of supplementing the tibial loading rather than comparing it with tibial loading.[23] In addition, they used female mice at 16 weeks of age, compared to our 8 week old male mice. As a result, although the mass-based effects of their tibial loading were similar to our study (e.g. increased bone volume fraction and cortical cross-sectional area), the exercise portion of their results showed no effects, making it difficult to compare the structural changes driven by treadmill running and tibial loading. In contrast, we exercised mice 3-5 times per week for 6 weeks in order to induce an osteogenic response, enabling us to directly compare bone formation due to both exercise and tibial loading.
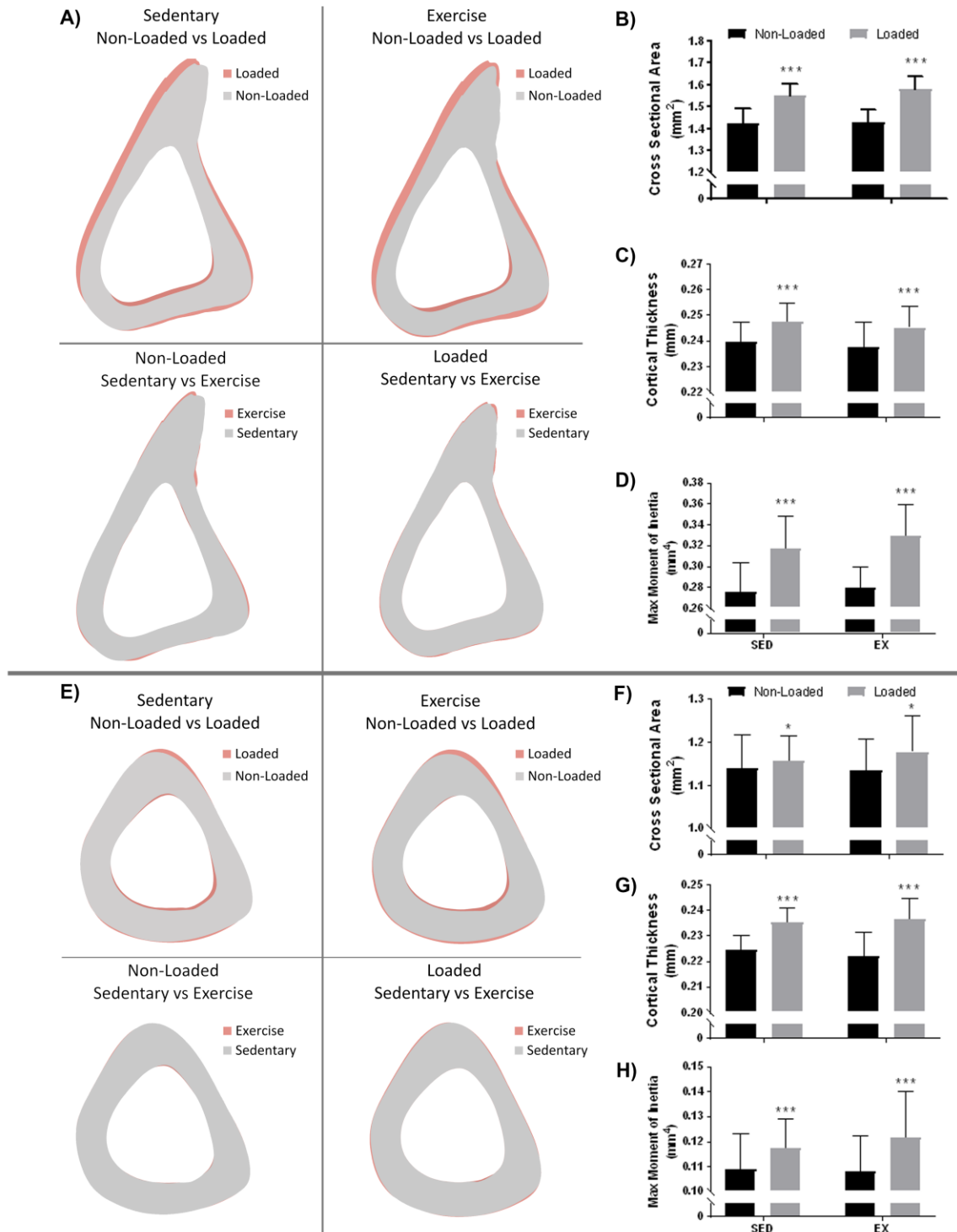
Appendix C.3 Figure 3. Cortical analysis at the proximal-mid (A-D) and mid (E-H) locations indicated a strong bone formation response due to loading (A and E, top panels) but not exercise (A and E, bottom panels). These effects can be observed quantitatively through significantly improved cross sectional area (B, F), cortical thickness (C, G), and maximum moment of inertia (D, H) in the loaded limb. *p < 0.05, **p < 0.01, ***p < 0.001

Appendix C.3 Table 1: Quantified cortical parameters from proximal-mid and mid locations indicate improved bone mass due to loading but not exercise. *p < 0.05, **p < 0.01, ***p < 0.001

	Sedentary		Exercise		Two-Way ANOVA		
	Non-Loaded	Loaded	Non-Loaded	Loaded	Exercise	Load	Interaction
Proximal-Mid Location (37%)							
Cross Sectional Area (mm^2)	1.421 (0.072)	1.551 (0.052)	1.428 (0.059)	1.581 (0.058)	ns	***	ns
Cortical Area (mm^2)	0.839 (0.031)	0.917 (0.029)	0.836 (0.033)	0.921 (0.031)	ns	***	ns
Marrow Area (mm^2)	0.582 (0.050)	0.635 (0.039)	0.592 (0.043)	0.660 (0.045)	ns	***	ns
Cortical Thickness (mm)	0.240 (0.008)	0.247 (0.007)	0.237 (0.010)	0.245 (0.009)	ns	***	ns
Periosteal Bone Surface (mm)	6.067 (0.171)	6.164 (0.150)	6.132 (0.173)	6.221 (0.184)	ns	*	ns
Endosteal Bone Surface (mm)	3.679 (0.149)	3.816 (0.125)	3.700 (0.132)	3.892 (0.150)	ns	***	ns
Max Moment of Inertia (mm^4)	0.275 (0.028)	0.317 (0.031)	0.279 (0.020)	0.329 (0.031)	ns	***	ns
Min Moment of Inertia (mm^4)	0.092 (0.012)	0.109 (0.010)	0.093 (0.012)	0.112 (0.010)	ns	***	ns
Tissue Mineral Density (g/cm^3)	0.780 (0.015)	0.788 (0.012)	0.777 (0.020)	0.783 (0.019)	ns	**	ns
Mid Location (50%)							
Cross Sectional Area (mm^2)	1.139 (0.077)	1.155 (0.061)	1.134 (0.074)	1.176 (0.085)	ns	*	ns
Cortical Area (mm^2)	0.693 (0.038)	0.727 (0.030)	0.686 (0.038)	0.738 (0.038)	ns	***	ns
Marrow Area (mm^2)	0.445 (0.043)	0.428 (0.035)	0.448 (0.049)	0.439 (0.056)	ns	*	ns
Cortical Thickness (mm)	0.224 (0.006)	0.235 (0.006)	0.222 (0.009)	0.236 (0.008)	ns	***	ns
Periosteal Bone Surface (mm)	4.608 (0.144)	4.639 (0.129)	4.593 (0.144)	4.664 (0.171)	ns	ns	ns
Endosteal Bone Surface (mm)	3.007 (0.159)	2.937 (0.124)	3.001 (0.174)	2.956 (0.195)	ns	*	ns
Max Moment of Inertia (mm^4)	0.109 (0.014)	0.117 (0.012)	0.108 (0.014)	0.122 (0.019)	ns	***	ns
Min Moment of Inertia (mm^4)	0.075 (0.010)	0.077 (0.008)	0.074 (0.008)	0.080 (0.009)	ns	**	ns
Tissue Mineral Density (g/cm^3)	0.891 (0.017)	0.886 (0.013)	0.883 (0.017)	0.885 (0.021)	ns	ns	ns

The tibial loading profile used in this study was similar to profiles reported previously (cyclic, rest-inserted loading),[14,24,25] though the presence of rest between cycles has recently been suggested to be unnecessary.[26] The load, 11.9 N, is within the range of common load levels that have been shown to increase bone volume fraction.[14,15,22,27] Interestingly, despite the plethora of papers utilizing tibial loading, a rarely discussed point is the observation that the increase in cancellous bone mass due to tibial loading is often predominately driven by increases in trabecular thickness rather than trabecular number and spacing,[22,25-29] though this is not always the case.[21,24] The current study showed similar results, with a 7.9% increase in bone volume fraction due to an 18.3% increase in trabecular thickness, while the number of trabeculae was significantly decreased. In contrast to tibial loading, the exercise increased bone volume fraction and BMD primarily by increasing trabecular number, suggesting a different mechanism. Based on these results, although tibial loading still can and does provide a wealth of information regarding mechanotransduction, care must be taken in translating observed results due to tibial loading to expected results due to treadmill running.

One potential reason for these observed effects may be differences in strain (both magnitude and direction) between tibial loading and exercise. Previous studies have shown that low load levels during tibial loading are insufficient to induce a bone formation response.[14,15,22] For that reason, we chose a higher load value that was within the range of loads shown to induce a formation response. However, by doing so, we also presumably selected a strain level that was much higher than is typically observed during treadmill running. For example, in 12 week old mice, walking was found to engender approximately 200 $\mu\varepsilon$ of tension, but in the same study, the authors found that approximately 1500 $\mu\varepsilon$ (i.e. 10 N) was required to engender a bone formation response during tibial loading.[14] Thus, the 11.9 N load that we used in the current study likely engenders much higher strain than treadmill running.

Another important difference to note is that, during tibial loading, the loading direction is more uniform. Although the natural curvature of the tibia causes eccentric loading (i.e. bending) that leads to regions of compression and tension,[30] the load is still applied in a more uniform, predominately uniaxial, direction without the influence of off-axis muscle and ground reaction forces. This may enable increased alignment of bone formation, causing greater trabecular thickness. Given these differences, it is unlikely that there would be a perfect profile that would mimic the response observed due to exercise.

Within the cortex, differences in bone formation were also noted, with tibial loading causing improved cortical area and exercise having no mass-based effect. Both results are similar to those observed previously.[22,31,32] However, it should be noted that this study only explored microstructural mass-based changes, and did not assess histology or quality-based changes to the tissue. Thus, the lack of bone mass response observed in the exercised mice does not imply that the matrix is unaffected. Previous work has demonstrated that treadmill running (both with and without changes in mass) can improve aspects of bone quality, predominately the collagen components.[5,6,31,33] Recent work has corroborated that these changes in tissue quality can have positive effects on mechanical properties associated with bone ductility[11] and toughness.[32] Similarly, tissue-level changes have been observed due to tibial loading, with short-term loading altering the mineralization of the matrix in both an age-dependent[34] and bone site-specific manner,[35] leading to improvements in tissue-level mechanics.[22]

In summary, we have shown that, in the cancellous region, tibial loading led to greater trabecular thickness while exercise led to greater number. Both improved bone volume fraction, with their combined effects resulting in an additive bone mass response. In the cortical region, only tibial loading resulted in increased bone mass, though that does not preclude the presence of non-mass based effects. These data suggest that tibial loading and exercise may improve mass differentially.

Acknowledgements

References

1. Wolman RL, Faulmann L, Clark P et al. 1991. Different training patterns and bone mineral density of the femoral shaft in elite, female athletes. Ann Rheum Dis. 50(7):487-489.

2. Warden SJ, Mantila Roosa SM, Kersh ME et al. 2014. Physical activity when young provides lifelong benefits to cortical bone size and strength in men. Proc Natl Acad Sci. 111(14):5337-5342.

3. Turner C. 1998. Three rules for bone adaptation to mechanical stimuli. Bone. 23(5):399-407.

4. Iwamoto J, Yeh JK, Aloia JF. 1999. Differential effect of treadmill exercise on three cancellous bone sites in the young growing rat. Bone. 24(3):163-169.

5. Wallace JM, Rajachar RM, Allen MR et al. 2007. Exercise-induced changes in the cortical bone of growing mice are bone and gender specific. Bone. 40(4):1120-1127.

6. Wallace JM, Ron MS, Kohn DH. 2009. Short-term exercise in mice increases tibial post-yield mechanical properties while two weeks of latency following exercise increases tissue-level strength. Calcif Tissue Int. 84(4):297-304.

7. Umemura Y, Ishiko T, Yamauchi T et al. 1997. Five jumps per day increase bone mass and breaking force in rats. J Bone Miner Res. 12(9):1480-1485.

8. Ju Y-I, Sone T, Okamoto T, Fukunaga M. 2008. Jump exercise during remobilization restores integrity of the trabecular architecture after tail suspension in young rats. J Appl Physiol. 104(6):1594-1600.

9. Swissa-Sivan A, Azoury R, Statter M et al. 1990. The effect of swimming on bone modeling and composition in young adult rats. Calcif Tissue Int. 47(3):173-177.

10. Hart KJ, Shaw JM, Vajda E et al. 2001. Swim-trained rats have greater bone mass, density, strength, and dynamics. J Appl Physiol. 91(4):1663-1668.

11. Gardinier JD, Rostami N, Juliano L, Zhang C. 2018. Bone adaptation in response to treadmill exercise in young and adult mice. Bone reports. 8:29-37.

12. Turner CH, Akhter MP, Raab DM et al. 1991. A noninvasive, in vivo model for studying strain adaptive bone modeling. Bone. 12(2):73-79.

13. Lee KC, Maxwell A, Lanyon LE. 2002. Validation of a technique for studying functional adaptation of the mouse ulna in response to mechanical loading. Bone. 31(3):407-412.

14. De Souza RL, Matsuura M, Eckstein F et al. 2005. Non-invasive axial loading of mouse tibiae increases cortical bone formation and modifies trabecular organization: A new model to study cortical and cancellous compartments in a single loaded element. Bone. 37(6):810-818.

15. Sugiyama T, Meakin LB, Browne WJ et al. 2012. Bones' adaptive response to mechanical loading is essentially linear between the low strains associated with disuse and the high strains associated with the lamellar/woven bone transition. J Bone Miner Res. 27(8):1784-1793.

16. Turner CH, Owan I, Takano Y. 1995. Mechanotransduction in bone: Role of strain rate. American Journal of Physiology - Endocrinology and Metabolism. 269(3):E438-E442.

17. Mosley JR, Lanyon LE. 1998. Strain rate as a controlling influence on adaptive modeling in response to dynamic loading of the ulna in growing male rats. Bone. 23(4):313-318.

18. Saxon LK, Jackson BF, Sugiyama T et al. 2011. Analysis of multiple bone responses to graded strains above functional levels, and to disuse, in mice in vivo show that the human lrp5 g171v high bone mass mutation increases the osteogenic response to loading but that lack of lrp5 activity reduces it. Bone. 49(2):184-193.

19. Morse A, McDonald MM, Kelly NH et al. 2014. Mechanical load increases in bone formation via a sclerostin-independent pathway. J Bone Miner Res. 29(11):2456-2467.

20. Meakin LB, Sugiyama T, Galea GL et al. 2013. Male mice housed in groups engage in frequent fighting and show a lower response to additional bone loading than females or individually housed males that do not fight. Bone. 54(1):113-117.

21. Sugiyama T, Price JS, Lanyon LE. 2010. Functional adaptation to mechanical loading in both cortical and cancellous bone is controlled locally and is confined to the loaded bones. Bone. 46(2):314-321.

22. Berman AG, Clauser CA, Wunderlin C et al. 2015. Structural and mechanical improvements to bone are strain dependent with axial compression of the tibia in female c57bl/6 mice. PLoS One. 10(6):e0130504.

23. Meakin LB, Udeh C, Galea GL et al. 2015. Exercise does not enhance aged bone's impaired response to artificial loading in c57bl/6 mice. Bone. 81:47-52.

24. Lynch ME, Main RP, Xu Q et al. 2010. Cancellous bone adaptation to tibial compression is not sex dependent in growing mice. J Appl Physiol (1985). 109(3):685-691.

25. Willie BM, Birkhold AI, Razi H et al. 2013. Diminished response to in vivo mechanical loading in trabecular and not cortical bone in adulthood of female c57bl/6 mice coincides with a reduction in deformation to load. Bone. 55(2):335-346.

26. Yang H, Embry RE, Main RP. 2017. Effects of loading duration and short rest insertion on cancellous and cortical bone adaptation in the mouse tibia. PLoS One. 12(1):e0169519.

27. Lynch ME, Main RP, Xu Q et al. 2011. Tibial compression is anabolic in the adult mouse skeleton despite reduced responsiveness with aging. Bone. 49(3):439-446.

28. Holguin N, Brodt MD, Sanchez ME et al. 2013. Adaptation of tibial structure and strength to axial compression depends on loading-history in both c57bl/6 and balb/c mice. Calcif Tissue Int. 93(3):211-221.

29. Weatherholt AM, Fuchs RK, Warden SJ. 2013. Cortical and trabecular bone adaptation to incremental load magnitudes using the mouse tibial axial compression loading model. Bone. 52(1):372-379.

30. Yang H, Butz KD, Duffy D et al. 2014. Characterization of cancellous and cortical bone strain in the in vivo mouse tibial loading model using microct-based finite element analysis. Bone. 66:131-139.

31. Kohn DH, Sahar ND, Wallace JM et al. 2009. Exercise alters mineral and matrix composition in the absence of adding new bone. Cells Tissues Organs. 189(1-4):33-37.

32. Hammond MA, Laine TJ, Berman AG, Wallace JM. 2016. Treadmill exercise improves fracture toughness and indentation modulus without altering the nanoscale morphology of collagen in mice. PLoS One. 11(9):e0163273.

33. Hammond MA, Wallace JM. 2015. Exercise prevents [beta]-aminopropionitrile-induced morphological changes to type i collagen in murine bone. BoneKEy Rep. 4.

34. Aido M, Kerschnitzki M, Hoerth R et al. 2015. Effect of in vivo loading on bone composition varies with animal age. Exp Gerontol. 63:48-58.

35. Bergstrom I, Kerns J, Tornqvist A et al. 2018. Compressive loading of the murine tibia reveals site-specific micro-scale differences in adaptation and maturation rates of bone. Osteoporos Int. 29(9):2161-2161.

PUBLICATIONS

The following provides a list of publications. An '*' indicates co-first authorship.

1. Weiss D, Latorre M, Rego BV, Cavinato C, Tanski BJ, **Berman AG,** Goergen CJ, Humphrey JD. Biomechanical consequences of compromised elastic fiber integrity and matrix cross-linking on abdominal aortic aneurysmal enlargement. Acta Biomaterialia. 2021 Jul.

2. **Berman AG***, Damrath JG*, Hatch J, Pulliam AN, Powell KM, Hinton M, Wallace JM. Effects of Raloxifene and Targeted Tibial Loading on Bone Mass and Mechanics in Male and Female Mice. Connective Tissue Research. 2021 Jan. 10; 1-3

3. Zbinden JC*, Blum KM*, **Berman AG***, Bangalore AB, Szafron JM , Kerr KE, Anderson JL, Sangha GS, Earl CC, Nigh NR, Mirhaidari GJM, Reinhardt JW, Chang YC, Yi T, Smalley R, Gabriele PD, Harris JJ, Humphrey JD, Goergen CJ, Breuer CK. Effects of Braiding Parameters on Tissue Engineered Vascular Graft Development. Advanced Healthcare Materials. 2020 Dec; 9(24):2001093.

4. **Berman AG**, Organ JM, Allen MR, Wallace JM. Muscle contraction induces osteogenic levels of cortical bone strain despite muscle weakness in a mouse model of Osteogenesis Imperfecta. Bone. 2020 Mar 1; 132:115061.

5. Powell KM, Brown AP, Skaggs CG, Pulliam AN, **Berman AG**, Deosthale P, Plotkin LI, Allen MR, Williams DR, Wallace JM. 6′-Methoxy Raloxifene-analog enhances mouse bone properties with reduced estrogen receptor binding. Bone reports. 2020 Jun 1; 12:100246.

6. Romary DJ, **Berman AG**, Goergen CJ. High-frequency murine ultrasound provides enhanced metrics of BAPN-induced AAA growth. American Journal of Physiology-Heart and Circulatory Physiology. 2019 Nov 1; 317(5):H981-90.

7. Powell KM, Skaggs C, Pulliam A, **Berman AG**, Allen MR, Wallace JM. Zoledronate and Raloxifene combination therapy enhances material and mechanical properties of diseased mouse bone. Bone. 2019 Oct 1; 127:199-206.

8. Sangha GS, Busch A, Acuna A, **Berman AG**, Phillips EH, Trenner M, Eckstein HH, Maegdefessel L, Goergen CJ. Effects of Iliac Stenosis on Abdominal Aortic Aneurysm Formation in Mice and Humans. Journal of vascular research. 2019; 56(5):217-29.

9. Dhowan B, Lim J, MacLean MD, **Berman AG**, Kim MK, Yang Q, Linnes J, Lee CH, Goergen CJ, Lee H. Simple minimally-invasive automatic antidote delivery device (A2D2) towards closed-loop reversal of opioid overdose. Journal of Controlled Release. 2019 Jul 28; 306:130-7.

10. **Berman AG**, Hinton MJ, Wallace JM. Treadmill running and targeted tibial loading differentially improve bone mass in mice. Bone reports. 2019 Jun 1; 10:100195.

11. Acuna A*, **Berman AG***, Damen FW*, Meyers BA*, Adelsperger AR, Bayer KC, Brindise MC, Bungart B, Kiel AM, Morrison RA, Muskat JC. Computational Fluid Dynamics of Vascular Disease in Animal Models. Journal of biomechanical engineering. 2018 Aug 1; 140(8).

12. Damen FW, **Berman AG**, Soepriatna AH, Ellis JM, Buttars SD, Aasa KL, Goergen CJ. High-frequency 4-dimensional ultrasound (4DUS): a reliable method for assessing murine cardiac function. Tomography. 2017 Dec; 3(4):180.

13. Pereyra AS, Hasek LY, Harris KL, **Berman AG**, Damen FW, Goergen CJ, Ellis JM. Loss of cardiac carnitine palmitoyltransferase 2 results in rapamycin-resistant, acetylation-independent hypertrophy. Journal of Biological Chemistry. 2017 Nov 10; 292(45):18443-56.

14. **Berman AG** and Wallace JM. Bone quality and quantity are mediated by mechanical stimuli. Clinical Reviews in Bone and Mineral Metabolism, 2016; 14(3):218-226.

15. Sugatani T, Agapova OA, Fang Y, **Berman AG**, Wallace JM, Malluche HH, Faugere MC, Smith W, Sung V, Hruska KA. A Ligand Trap of the Activin Receptor Type IIA Inhibits Osteoclast Stimulation of Bone Remodeling in Diabetic Mice with CKD. Kidney International, 2016; 91(1):86-95.

16. Abeysekera I, Thomas, J, Georgiadis TM, **Berman AG**, Hammond MA, Dria KJ, Wallace JM, Roper RJ. Differential effects of Epigallocatechin-3-gallate containing supplements on correcting skeletal defects in a Down syndrome mouse model. Molecular Nutrition and Food Research, 2016; 60(4):717-726.

17. Hammond MA, **Berman AG**, Laine TJ, Wallace JM. Treadmill Exercise Improves Fracture Toughness and Indentation Modulus without Altering the Nanoscale Morphology of Collagen in Mice. PloS One, 2016; 11(9): e0163273.

18. Hammond MA, **Berman AG**, Pacheco R, Davis HM, Plotkin LI, Wallace JM. Removing or Truncating Connexin 43 in Osteocytes Alters Nanoscale Composition and Microscale Mechanics. Bone, 2016; 88:85-91.

19. **Berman AG**, Wallace JM, Bart ZB, Allen MR. Raloxifene reduces skeletal fractures in an animal model of osteogenesis imperfecta. Matrix Biology, 2016; 52:19-28.

20. **Berman AG**, Clauser CC, Wunderlin CA, Hammond MA, Wallace JM. Cortical and Cancellous Structural Adaptation and Improvements to Mechanical Integrity are Strain Dependent with Axial Compression of the Tibia in Female C57BL/6 Mice. PloS One, 2015; 10(6): e0130504.